Collective Dynamics and Spectroscopy of Coupled Quantum Emitters

Dissertation
zur Erlangung des akademischen Grades
Doctor of Philosophy

eingereicht an der
Fakultät für Mathematik, Informatik und Physik
der Leopold-Franzens-Universität Innsbruck

von
David Plankensteiner, M.Sc.

Betreuer:
Univ.-Prof. Dr. Helmut Ritsch,
Institut für Theoretische Physik,
Universität Innsbruck

Zweitbetreuer:
Dr. Claudiu Genes,
Max Planck Institut für
die Physik des Lichts

Innsbruck, Mai 2019

Abstract

Quantum emitters are systems with discrete energy levels, such as atoms or molecules, which exhibit a nonvanishing dipole coupling to the electromagnetic field. The electromagnetic field is in turn modified by this coupling. One quantum emitter therefore feels the presence of others in a common radiation field. The behavior of multiple emitters placed close to one another thus changes drastically as they begin to act as a collective. Consequently, radiative processes and noise are of collective nature as well. This fact has to be taken into account in order to capture the full physical picture of a dense ensemble of quantum emitters.

A striking example for these interactions is spontaneous emission: The spontaneous decay of an excited emitter is induced by vacuum fluctuations of the electromagnetic field. In a compact collection of emitters, though, the radiated fields interfere with one another. This interference effect leads to modified spontaneous emission rates as well as energetic shifts of the emitters' energy levels. On the one hand, constructive interference can cause a substantial decrease in the lifetime of a collective excitation – a phenomenon known as superradiance. On the other hand, imprinting a certain phase difference between the emitters can lead to destructive interference of the radiated fields thereby inhibiting the spontaneous decay. Understanding the details behind this effect, which we call subradiance, enables us to greatly extend the lifetime of collectively excited states.

The preparation of subradiant states is not trivial and is investigated at length within the scope of this thesis. We show that, employing a magnetic field gradient, the phase differences required to suppress spontaneous emission are introduced in chains of quantum emitters. Furthermore, it turns out that the states prepared in this way feature high quantum correlations that are also robust.

More generally, collective decoherence can not only stem from the vacuum-mediated interactions. In laser spectroscopy, an ensemble of quantum emitters is addressed by a laser, which exhibits noise due to its fluctuating phase and amplitude. This noise is inevitably imprinted on the quantum emitters subsequently leading to effects such as dephasing. We investigate collective laser noise and ways to circumvent it in quantum metrological applications.

It is possible to use an optical cavity in order to enhance coherent light-matter interactions when addressing an ensemble of quantum emitters. Coupling dipole-dipole interacting quantum emitters to a single resonant mode enables us to observe the collective resonances featuring the modified linewidths and energies in the transmission spectrum of the cavity. Selecting subradiant states via the cavity mode profile, these resonance lines can be extremely narrow and entail a significant phase shift of the transmitted field. All those phenomena can be understood as a consequence of largely increased light-matter interactions due to the collective subradiant dipole preferentially radiating into the cavity instead of the surrounding free space.

The dipole-dipole interactions between emitters are greatly enhanced at nanoscale separations. In addition, quantum emitters forming rings display guided quasi-modes reminiscent of optical fibers. Combining these two facts, we investigate the properties of nanorings. It is shown that the spontaneous decay of a single ring decreases exponentially with its size. Consequently, almost lossless transport of excitations between two neighboring rings can occur.

The methods used to conduct the research presented in this thesis involve analytical, but also numerical techniques. The effort to implement the latter can be largely reduced by the use of a dedicated framework in the form of a toolbox, which contains predefined sets of functions specifically tailored towards the numerical simulation of open quantum systems. Such a toolbox, which was developed further by the author of this thesis, is presented in the following. It is built in the Julia programming language offering usability as well as performance.

Zusammenfassung

Quantenemitter sind Systeme mit diskreten Energieniveaus, wie etwa Atome oder Moleküle, die eine nichtverschwindende Dipolkopplung an das elektromagnetische Feld aufweisen. Das elektromagnetische Feld wird seinerseits durch diese Kopplung modifiziert. Ein Emitter fühlt daher die Nähe anderer, sofern sich diese im selben Strahlungsfeld befinden. Dadurch ändert sich das Verhalten von Quantenemittern, die sich in unmittelbarer Nähe zueinander befinden, drastisch, da sie sich wie ein kollektives Quantensystem verhalten. Daraus folgt, dass Strahlungsprozesse und Rauschen kollektiver Natur sind. Diese Tatsache muss in Betracht gezogen werden, um das volle physikalische Bild einer dichten Ansammlung von Quantenemittern einzufangen.

Ein einschlägiges Beispiel von solchen Wechselwirkungen sind spontane Emissionsprozesse. Im Allgemeinen wird spontaner Zerfall eines angeregten Emitters durch Vakuumfluktuationen des elektromagnetischen Feldes hervorgerufen. In einem kompakten Ensemble von Emittern interferieren die abgestrahlten Felder allerdings miteinander. Dieser Interfernzeffekt führt zu modifizierten spontanen Zerfallsraten sowie energetischen Verschiebungen der Energieniveaus der Emitter. Einerseits kann konstruktive Interferenz eine substantielle Verringerung der Lebensdauer einer kollektiven Anregung verursachen – ein Phänomen, welches gemeinhin als Superradianz bekannt ist. Andererseits kann ein Phasenunterschied zwischen nächsten Emittern zu destruktiver Interferenz der abgestrahlten Felder und somit zu einer Unterdrückung des spontanen Zerfalls führen. Ein detailliertes Verständnis dieses Effekts, den wir Subradianz nennen, erlaubt es uns, die Lebensdauer eines kollektiv angeregten Zustandes in großem Maße zu verlängern.

Die Präparation eines solchen subradianten Zustandes ist nicht trivial und wird daher im Rahmen dieser Dissertation ausführlich behandelt. Es wird im Folgenden gezeigt, dass man mithilfe eines Magnetfeldgradienten die für die Reduktion der spontanen Emission erforderlichen Phasendifferenzen in einer Kette von Quantenemittern einführen kann. Weiters stellt sich heraus, dass die auf diese Weise erzielten Zustände ein hohes Maß an Verschränkung aufweisen und diese ebenfalls robust gegenüber spontanem Zerfall ist.

Im Allgemeinen muss kollektive Dekohärenz allerdings nicht von den vom Vakuumfeld vermittelten Wechselwirkungen stammen. Bei Laserspektroskopie wird ein Ensemble von Quantenemittern von einem Laser adressiert, welcher unweigerlich jedwede Fluktuationen seiner Phase oder Amplitude auf die Emitter überträgt, was folglich zu Effekten wie Dephasierung führt. Wir untersuchen die Wirkung von solch kollektivem Laserrauschen und mögliche Arten es zu vermeiden im Zusammenhang mit quantenmetrologischen Anwendungen.

Unter Verwendung eines optischen Resonators ist es möglich kohärente Licht-Materie-Wechselwirkungen bei der Adressierung eines Ensembles bestehend aus Quantenemittern zu verstärken. Koppelt man Dipol-Dipol-wechselwirkende Quantenemitter an eine einzelne, resonante Mode, so ist es möglich die kollektiven Resonanzen und deren modifizierte Linienbreiten und Energien im Transmissionsspektrum des Resonatorfeldes zu beobachten. Selektiert man mittels des Modenprofils des Resonators subradiante Zustände, können diese Resonanzlinien extrem schmal sein und einen signifikanten Phasenversatz des transmittierten Feldes mit sich bringen. Diese Phänomene lassen sich als eine natürliche Konsequenz von verstärkten Licht-Materie Wechselwirkungen verstehen, da ein kollektiver, subradianter Dipol bevorzugt in den optischen Resonator strahlt, anstatt in den freien Raum.

Dipol-Dipol-Wechselwirkung wird bei einer Separation zwischen Emittern auf der Nanoskala in großem Maße verstärkt. Zusätzlich zeigen Ringe bestehend aus Quantenemittern geführte Quasimoden, ähnlich wie in optischen Fasern. Kombiniert man diese beiden Tatsachen, führt das zur Untersuchung von Nano-Ringen von Quantenemittern. Es wird gezeigt, dass die spontane Emission eines einzelnen Rings exponentiell mit dessen Größe abnimmt und aus Folge daraus praktisch verlustloser Transport von Anregungen zwischen zwei benachbarten Ringen stattfinden kann.

Die Methoden, welche in den wissenschaftlichen Untersuchungen in dieser Dissertation Anwendung finden, beinhalten sowohl analytische wie auch numerische Verfahren. Der Aufwand für Letztere lässt sich zu einem großen Teil verringern, indem man sich ein dediziertes Framework in Form einer Toolbox zunutze macht, die vordefinierte Funktionen speziell für die numerische Simulation von offenen Quantensystemen beinhaltet. Eine Toolbox dieser Art, die vom Autor dieser Arbeit weiterentwickelt wurde, wird im Folgenden präsentiert und ist in der Programmiersprache Julia verfasst, sodass sie sowohl einfache Nutzbarkeit als auch Effizienz bietet.

Danksagung

An dieser Stelle möchte ich mich herzlich bei all jenen bedanken, die mich während der Jahre, die ich dieser Arbeit gewidmet habe, begleitet und unterstützt haben.

Zuallererst bedanke ich mich bei Prof. Helmut Ritsch, der es mir ermöglichte, an faszinierenden Themen aktueller Forschung zu arbeiten, und gleichzeitig ein äußerst angenehmes Arbeitsklima schuf. Ein großes Dankeschön auch dafür, dass er mir die Freiheit ließ, meinen eigenen Forschungsfragen und Interessen nachzugehen.

Als Nächstes möchte ich mich ausdrücklich bei Claudiu Genes bedanken, der durch seine Faszination an der Arbeit meine Begeisterung immer wieder auf's Neue geweckt hat, ohne dabei den Humor zu verlieren.

Weiters bedanke ich mich bei allen Mitgliedern der Arbeitsgruppe Ritsch. Ich danke Laurin Ostermann für viele spannende Diskussionen, die nicht immer arbeitsbezogen waren. Danke an Valentin Torggler, Stefan Ostermann und Christoph Hotter. Vielen Dank auch an Sebastian Krämer, der meine Begeisterung zum Programmieren gefördert hat. Zuletzt noch einmal vielen Dank an die restlichen Mitglieder der Arbeitsgruppe, die ich nun nicht explizit erwähne. Ich hätte mir keine besseren Arbeitskollegen für die Zeit meiner Dissertation vorstellen können.

Ich bedanke mich bei meinen Freunden und Studienkollegen, auf die immer Verlass ist. Danke an meine Familie, die mich in allen Lebenslagen unterstützt. Speziell danke ich meiner Mutter, meinen beiden Schwestern, aber auch meiner Nichte und meinem Neffen, für die schönen Zeiten. Ebenfalls bedanke ich mich bei meiner Verwandtschaft in der Ackergasse.

Zuletzt bedanke ich mich von Herzen bei der Frau an meiner Seite, ohne die die letzten Jahre nicht annähernd so schön gewesen wären. Danke, Mona.

Contents

1 Introduction

It was in 1916 that Einstein introduced three fundamental interaction processes of light and matter [1.1]. In his seminal work, he described the processes of absorption and spontaneous emission, as well as the novel phenomenon of stimulated emission. To arrive at a proper theory, Einstein did not only describe the internal degrees of freedom of a molecule, but also the surrounding radiation field in a quantum mechanical sense; i.e., the exchange of energy between the electromagnetic field and a molecule was postulated to occur at discrete values only. The corresponding rates associated with these processes were only hypothesized by Einstein and left undetermined. To actually find the correct expressions of these rates, specifically the one at which spontaneous emission occurs, a full quantum mechanical derivation was required. This was first accomplished by Dirac [1.2] in 1927, when he derived Einstein's coefficients from first principles.

The considerations by Einstein and Dirac were aimed at gaining insight into the processes of emission and absorption of radiation by matter, which had remained largely inexplicable up until then. They sufficed to explain these phenomena for single quantum emitters (atoms or molecules) or, equivalently, for many independent quantum emitters. In the case of the latter one makes what is known as the *independent bath assumption*, in which each quantum emitter interacts with an independent set of thermal radiation modes. A natural question that still remained unanswered was how precisely atoms or molecules within a cloud behaved taking into account that each particle interacts with the same radiation field modes, such that the correlation length of the vacuum fluctuations is nonnegligible.

1.1 Interacting quantum emitters

In 1954, Dicke [1.3] considered the limiting case of a gas with such a high density, that the separation between particles was much less than the wavelength of the radiation field they were emitting. This renders the particles within the gas effectively indistinguishable and led Dicke to the description of the collection of emitters as a single point-like quantum system. The most prominent result of Dicke's work is *superradiance*. As he showed, a dense gas consisting of emitters that are initially in the upper level of an electronic transition, emits a short but intense pulse of light. In fact, the peak intensity of such a superradiant pulse of a gas consisting of N emitters is proportional to N^2, whereas its duration reduces with $1/N$. Numerous studies focused on superradiance [1.4], but it was not until the 1970s that it was observed experimentally [1.5]. This is a prominent example, where emitters behave like a single entity since they cannot be distinguished from one another by the surrounding light field. There are other cases, in which the independent bath assumption fails to capture the physics, and decoherence and noise have to be treated collectively (see, for example, chapter 4).

Moving away from the limiting case of negligible separations between particles to a configuration where they remain distinguishable but nevertheless interact with a common radiation field, required some more careful considerations. A basic theoretical description was developed by Lehmberg [1.6] in 1970, and is described at length within this thesis (see chapter 2).

1.2 Why bother with dense ensembles?

Interactions between quantum emitters, such as the ones discussed above, occur at high densities; i.e., when the separation between particles is small compared to a characteristic length scale. For example, note that the coherence length (inverse bandwidth) of a spontaneously emitted photon is given by the lifetime of the transition multiplied with the speed of light, and thus is much larger than its wavelength. Naturally, we may now ask why it is even of interest to look at ensembles of emitters with high densities. After all, what is keeping us from creating sufficiently dilute gases such that the particles within are essentially independent of one another?

For one, there is a number of reasons why maximizing the density of emitters is beneficial. In quantum metrological applications, such as optical atomic clocks [1.7], the fundamental shot noise is proportional to $1/\sqrt{N}$, with N being the number of emitters involved in the measurement. Furthermore, two-level quantum emitters are frequently employed in quantum computation as the quantum equivalent of bits - also called *qubits* - and, clearly, the amount of information that can be processed or stored is limited by the number of emitters involved. Additionally, interfaces between light and matter are vital tools for quantum computation and communication [1.8–1.10]. To minimize computational errors, faithful coherent interactions between the light and emitters are desirable. In cavity quantumelectrodynamics (CQED) applications [1.11], it is well-known that this coherent coupling is enhanced with the number of emitters [1.10]. Secondly, the characteristic length scale that governs the interactions may simply be too large, such that sufficiently separating the quantum emitters is not feasible. Consider, for example, that interactions mediated by optical fibers [1.12] or a standing wave cavity mode [1.13] are essentially of infinite range.

A theoretical understanding of the radiative interactions between densely packed quantum emitters is therefore crucial for the highly precise control required in applications such as the ones mentioned above.

1.3 Collective decoherence and how to avoid it

In ensembles of quantum emitters superradiant spontaneous emission can compensate for, or even surpass any collective enhancement of coherent processes, ultimately making matters worse. Thus, collectively enhanced decay can be a highly undesirable effect. One way to deal with this issue is to make use of the much less known phenomenon of *subradiance* [1.14]. Imprinting phases on the emitters such that their radiated fields interfere destructively leads to a collective decrease of the spontaneous emission rather than an increase. It is therefore possible to not only avoid superradiant decay, but even prolong the lifetime of excitations of the emitters in order to allow for longer interrogation times. An inherent property of this class of subradiant states is that they exhibit slow decay since they hardly couple to the environment. Consequently, not only spontaneous emission, but also addressing these states is inhibited. This is why subradiant states and their preparation are subject to on-going research (see, for example, chapter 3).

While at high densities collective spontaneous emission occurs, it is still governed by the natural linewidth of the employed quantum emitters. As such, it may not be the actual limiting factor in an application. For example, the world's currently most precise clock [1.15, 1.16] uses fermionic strontium isotopes (^{87}Sr), which feature an extremely narrow transition line. Other, more dominant noise sources are present, though. Depending on the inter-particle distance and the precise nature of the noise, these may also be *collective noise processes*. When a noisy laser is employed to address an ensemble of emitters, it imprints its own noise on the emitters which can dominate spontaneous emission processes. Even though lasers are often theoretically modeled as perfectly monochromatic light sources, this is of course not the case in reality. Rather, a laser exhibits fluctuations – albeit small ones – in its phase as well as its intensity. Given that many quantum emitters are placed within a space that is much smaller than the laser's coherence length, this phase and amplitude noise are of collective nature; i.e., all quantum emitters experience the same fluctuations by the laser instantaneously. Because the noise is collective, it is possible to engineer states within the emitter ensemble that renders them insensitive to this noise (see chapter 4).

1.4 Outline of this thesis

The collective behavior of an ensemble of quantum emitters that experience the same radiation field fluctuations forms the central theme of this thesis. Specifically, we aim to not only understand collective noise and decoherence, but find ways in which their effects can be suppressed or even exploited. To this end, we start out by highlighting the basic theoretical tools required to describe the phenomena we are interested in in chapter 2. The following chapters then contain the publications forming the main part of this thesis.

Previous research [1.17, 1.18] has shown the usefulness of subradiance in quantum metrological applications, specifically atomic clocks. Finding ways in which subradiant states can be addressed is therefore of interest. An approach that employs a magnetic field gradient along a chain of quantum emitters is investigated in chapter 3. Going further into the direction of collective noise reduction in metrological applications, we investigate the effects of laser phase and amplitude noise on Ramsey and Rabi spectroscopy in chapter 4.

In chapter 5 we show another way in which subradiance can be useful. We combine collective spontaneous emission and CQED in order to investigate enhanced light-matter interactions accompanied by extremely narrow antiresonance lines in the cavity transmission spectrum due to subradiance. These investigations are taken further in chapter 6, where we assess the quantum mechanical aspects of the problem raised in chapter 5 in great detail. Specifically, we highlight the application of quantum Langevin equations to ensembles of dipole-dipole interacting quantum emitters. This approach is then employed to find the quantum noise in the detection signal of the subradiant antiresonance lines.

Next, we move on to systems of emitters consisting of nanorings in chapter 7. As we show there, subradiant states play a crucial role in the efficient transport of excitations from one ring to another.

Finally, we take a methodological detour in chapter 8, in which we highlight a toolbox partially developed within the scope of this thesis. It is written in the Julia language [1.19] and allows for numerical simulations of open quantum systems in a straightforward yet efficient way.

After concluding remarks in chapter 9, we present an additional publication in chapter 10. This publication does not fall within the main part of the thesis, since the contribution by the author of the thesis was theoretical support for the implementation and interpretation of an experiment performed in Innsbruck.

2 Fundamental concepts of quantum optics

The aim of this chapter is to give a succinct description of the fundamental theoretical tools that are employed in the subsequent publications. As most basic principles can be found in a number of well-established textbooks [2.1–2.3], these will be introduced in scarce detail only.

2.1 Quantum mechanics of electric dipole transitions

Collective interactions of quantum emitters, specifically those considered here, stem from the interaction of the particles with a common radiation field. The very basis for these kinds of interactions is the coupling of each emitter to the electromagnetic field via a dipole transition. The considered quantum emitters feature a certain charge distribution, such that a single bound charge (electron) can interact with the electric field. More precisely, even though the eigenstates of an emitter do not have a dipole moment, the charge distribution of a superposition of two states of the emitter possesses a dipole, which oscillates at a frequency determined by the energy difference of the states.

The Hamiltonian function describing the energy of a single charge e at position $\mathbf{r}$ in an electric field written in the Coulomb gauge is [2.2]

$$H = \frac{(\mathbf{p} - e\mathbf{A}(\mathbf{r},t))^2}{2m} + e\phi(\mathbf{r}) + H_{\mathrm{F}}, \tag{2.1}$$

where $\mathbf{A}$ and ϕ are the vector and scalar potential of the electromagnetic field, respectively, m is the mass of the charge and $\mathbf{p}$ its momentum. The Hamiltonian H_{F} accounts for the energy of the free electromagnetic field and is not relevant for now. Assuming that the quantum emitter is much smaller than the typical wavelength of the fields it interacts with, we may perform the so-called dipole approximation [2.2] which amounts to setting $\mathbf{A}(\mathbf{r},t) \approx \mathbf{A}(\mathbf{0},t)$, where we chose our emitter to be located at the origin.

We now use the gauge invariance of the fields and perform a gauge transformation with the field $-\mathbf{r}\cdot\mathbf{A}(\mathbf{r},t)$, such that

$$\mathbf{A}(\mathbf{r},t) \to \mathbf{A}(\mathbf{r},t) - \nabla\left(\mathbf{r}\cdot\mathbf{A}(\mathbf{r},t)\right) = 0, \tag{2.2a}$$

$$\phi(\mathbf{r}) \to \phi(\mathbf{r}) + \frac{\partial}{\partial t}\left(\mathbf{r}\cdot\mathbf{A}(\mathbf{r},t)\right) = \phi(\mathbf{r}) - \mathbf{r}\cdot\mathbf{E}(\mathbf{r},t), \tag{2.2b}$$

where in the latter relation we excluded the electric field that stems from the static scalar potential. The Hamiltonian then becomes

$$H = H_0 + H_{\text{int}} + H_{\text{F}}, \tag{2.3}$$

where the first term includes the kinetic and potential energy of the charge, respectively, $H_0 := p^2/(2m) + e\phi(\mathbf{r})$. The second term describes the interaction between the electric field and the transition dipole of the quantum emitter. With the definition of the electric dipole moment $\mathbf{d} := -e\mathbf{r}$, we can write the interaction term as

$$H_{\text{int}} := \mathbf{d} \cdot \mathbf{E}(\mathbf{0}, t). \tag{2.4}$$

So far we did not specify the quantum nature of the interaction process. This is taken into account by considering the position $\mathbf{r}$ and subsequently $\mathbf{d}$ to be operators. In reality, we would have to account for all possible transitions. However, if we assume one specific transition of interest to be energetically separated far from all others, we can truncate the quantum emitter Hilbert space at the two levels which correspond to this transition. Thus, without further specifying the precise wave functions, consider only two states of the emitter labeled by $|g\rangle$ and $|e\rangle$, which span our reduced Hilbert space. Furthermore, they are eigenstates of the Hamiltonian describing the energy of the quantum emitter with corresponding eigenvalues E_g and E_e, respectively. The free energy part of the Hamiltonian is then

$$H_0 := \frac{p^2}{2m} + e\phi(\mathbf{r}) \approx E_e \left|e\right\rangle \left\langle e\right| + E_g \left|g\right\rangle \left\langle g\right|. \tag{2.5}$$

Note that we will from now on refer to $|e\rangle$ as the excited and $|g\rangle$ as the ground state. Accordingly, we choose $E_e > E_g$, i.e. the excited state is higher in energy.

If the potential ϕ has even parity with respect to the position $\mathbf{r}$ (such as the Coulomb potential of the nucleus in the case of an atom) then the Hamiltonian H_0 has even parity as well. Therefore, H_0 commutes with the parity transformation operator P, which has the property $P\mathbf{r}P^\dagger = -\mathbf{r}$. This means that H_0 and P have the same eigenstates, with a parity determined by the eigenvalues of the parity operator (± 1). Since the dipole moment operator, on the other hand, has odd parity in $\mathbf{r}$, its diagonal elements vanish and we have

$$\mathbf{d} = \mathbf{d}_{eg} \left|e\right\rangle \left\langle g\right| + \mathbf{d}_{eg}^* \left|g\right\rangle \left\langle e\right|, \tag{2.6}$$

where $\mathbf{d}_{eg}$ is the nonzero dipole matrix element associated with the transition. A more convenient notation allows us to write the interaction Hamiltonian as

$$H_{\text{int}} = \boldsymbol{\mu} \left(\sigma^\dagger + \sigma\right) \cdot \mathbf{E}(\mathbf{0}, t), \tag{2.7}$$

where $\boldsymbol{\mu} \equiv \mathbf{d}_{eg}$ is assumed to be real without loss of generality. The operator σ is given by

$$\sigma := \left|g\right\rangle \left\langle e\right| \tag{2.8}$$

and corresponds to the transition from the excited to the ground state. This operator can be expressed in terms of the well-known Pauli operators by substituting $\sigma = \sigma_x - i\sigma_y$ and $2\sigma^\dagger\sigma = \sigma_z + \mathbb{1}$. We can also write the free energy Hamiltonian in terms of these operators,

$$H_0 = \hbar\omega_0\sigma^\dagger\sigma, \tag{2.9}$$

where $\omega_0 = E_e/\hbar$ is the transition resonance frequency and we chose $E_g = 0$.

The description up to now takes the quantum mechanics of the internal degrees of freedom of the emitter into account. However, we also require a quantized formulation of the electric field in order to arrive at a full quantum mechanical model. It is generally convenient to separate the electric field into forward and backward propagating terms [2.1]; i.e.,

$$\mathbf{E}(\mathbf{r}, t) = \mathbf{E}^+(\mathbf{r}, t) + \mathbf{E}^-(\mathbf{r}, t), \tag{2.10}$$

where $\mathbf{E}^-(\mathbf{r}, t) = \left(\mathbf{E}^+(\mathbf{r}, t)\right)^\dagger$. Choosing an arbitrary region in space of volume $V = L^3$ [see Fig. 2.1(a)] that does not contain external sources and invoking periodic boundary conditions, we can write the free electric field in a mode expansion [2.1] as

$$\mathbf{E}^+(\mathbf{r}, t) = \sum_{\mathbf{k},\lambda} \sqrt{\frac{\hbar\omega_k}{2\epsilon_0 V}} \mathbf{e}_{\mathbf{k},\lambda} e^{i\mathbf{k}\cdot\mathbf{r}} a_{\mathbf{k},\lambda}(t). \tag{2.11}$$

Each mode with wave vector $\mathbf{k}$ features two different polarizations $\lambda = 1, 2$. The respective polarization unit vectors $\mathbf{e}_{\mathbf{k},\lambda}$ span a plane that is orthogonal to the propagation direction given by the wave vector. The frequency of each mode is $\omega_k = c|\mathbf{k}|$. If the electric field is classical, then the time-dependent amplitudes $a_{\mathbf{k},\lambda}$ are merely complex numbers. In the quantum mechanical description, though, these amplitudes are harmonic oscillator annihilation operators. As such, they fulfill the canonical commutation relation

$$\left[a_{\mathbf{k},\lambda}, a^\dagger_{\mathbf{k}',\lambda'}\right] = \delta_{\mathbf{k},\mathbf{k}'}\delta_{\lambda,\lambda'}\mathbb{1}. \tag{2.12}$$

The energy of the electromagnetic field can, accordingly, be written as the sum of number operators for each mode [2.1],

$$H_\mathrm{F} = \sum_{\mathbf{k},\lambda} \hbar\omega_k a^\dagger_{\mathbf{k},\lambda} a_{\mathbf{k},\lambda}. \tag{2.13}$$

Therefore, the full Hamiltonian of a quantum emitter interacting with a free electric field reads

$$H = \hbar\omega_0\sigma^\dagger\sigma + \sum_{\mathbf{k},\lambda} \hbar\omega_k a^\dagger_{\mathbf{k},\lambda} a_{\mathbf{k},\lambda} + \sum_{\mathbf{k},\lambda} \hbar g_{\mathbf{k},\lambda} \left(\sigma^\dagger + \sigma\right) \left(a^\dagger_{\mathbf{k},\lambda} + a_{\mathbf{k},\lambda}\right), \tag{2.14}$$

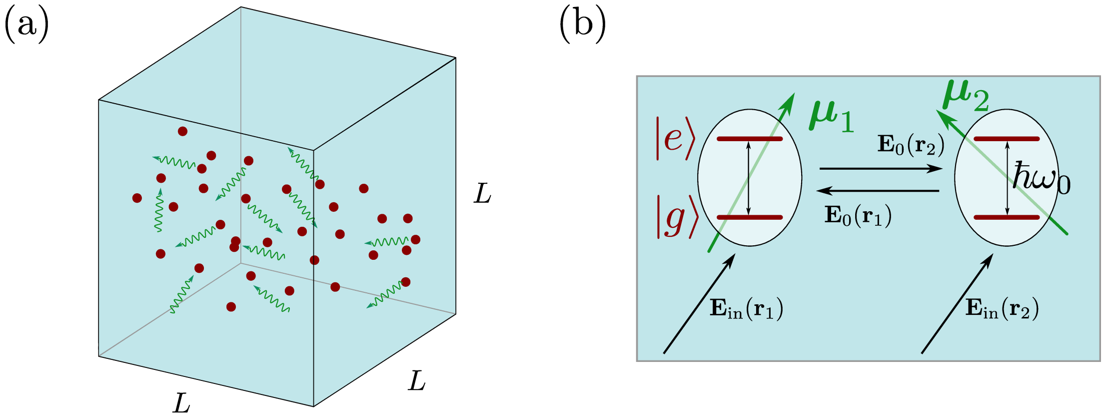

Figure 2.1: *Collective radiation of two-level quantum emitters.* (a) An ensemble of quantum emitters within the same quantization volume $V = L^3$. Each one of them experiences the fields emitted by all other present emitters leading to interference effects. (b) Two identical quantum emitters featuring an electric dipole transition with resonance energy $\hbar\omega_0$. The respective dipole moments associated with the transition are of the same magnitude but have arbitrary orientations. The emitters couple via the electric field emitted by each of them $[\mathbf{E}_0(\mathbf{r})]$. Additionally, they are subject to the input by the free electric field $[\mathbf{E}_{\text{in}}(\mathbf{r})]$.

where the strength of the dipole coupling is given by the frequency

$$g_{\mathbf{k},\lambda} = \sqrt{\frac{\omega_k}{2\hbar\epsilon_0 V}}\mathbf{e}_{\mathbf{k},\lambda} \cdot \boldsymbol{\mu}. \tag{2.15}$$

We proceed by making one final simplification, the so-called rotating-wave approximation (RWA). The Heisenberg equations for the operators of the emitter and the modes are given by the commutator with H. The solutions are dominated by oscillatory terms with the frequencies ω_0 and ω_k, respectively. Since these are optical frequencies, the products of these operators give rise to two greatly different timescales: The product $a^\dagger_{\mathbf{k},\lambda}\sigma$ oscillates in time with $\omega_k - \omega_0$, whereas $a_{\mathbf{k},\lambda}\sigma$ oscillates with $\omega_k + \omega_0$. The latter therefore oscillates on a much faster timescale, such that we can disregard those terms.

The final form of the Hamiltonian is

$$H = \hbar\omega_0\sigma^\dagger\sigma + \sum_{\mathbf{k},\lambda}\hbar\omega_k a^\dagger_{\mathbf{k},\lambda}a_{\mathbf{k},\lambda} + \sum_{\mathbf{k},\lambda}\hbar g_{\mathbf{k},\lambda}\left(\sigma^\dagger a_{\mathbf{k},\lambda} + a^\dagger_{\mathbf{k},\lambda}\sigma\right). \tag{2.16}$$

The above describes absorption and emission phenomena of a single quantum emitter in free space. However, this model also keeps track of the, in principle, infinite degrees of freedom of the surrounding field modes. It is therefore not a practical approach to use this Hamiltonian directly. Rather, in the following sections, we will show how the emitted field can be expressed in terms of emitter operators. This yields an effective description of the emitter as an open system taking loss to the environment into account.

2.2 Collectively emitted electric field

While the previously derived Hamiltonian in Eq. (2.16) suffices to investigate the field that is radiated by a single quantum emitter, we want to have something more general. Namely, we want to describe an ensemble of emitters that is dense, i.e. the emitters are sufficiently close to one another such that each of them experiences the field radiated by all others [see, for example, the schematic illustration of two coupled quantum emitters shown in Fig. 2.1(b)]. The aim of this section is to derive the electric field radiated by the entirety of the emitter ensemble where interference effects are taken into account. To this end, we follow a procedure similar to the one in Ref. [2.4].

First, we write the Hamiltonian of N identical emitters located at positions $\mathbf{r}_j$ (where $j = 1, ..., N$) interacting with a common radiation field. It is obtained by superimposing the Hamiltonian in Eq. (2.16) for each emitter,

$$H = \hbar\omega_0 \sum_j \sigma_j^\dagger \sigma_j + \sum_{\mathbf{k},\lambda} \hbar\omega_k a_{\mathbf{k},\lambda}^\dagger a_{\mathbf{k},\lambda} + \sum_{\mathbf{k},\lambda} \sum_j \hbar g_{\mathbf{k},\lambda}^{(j)} \left(\sigma_j^\dagger a_{\mathbf{k},\lambda} e^{i\mathbf{k}\cdot\mathbf{r}_j} + a_{\mathbf{k},\lambda}^\dagger \sigma_j e^{-i\mathbf{k}\cdot\mathbf{r}_j} \right). \tag{2.17}$$

Here, the coupling strength of the electric field to the transition dipole $\boldsymbol{\mu}_j$ of the jth emitter is given by

$$g_{\mathbf{k},\lambda}^{(j)} = \sqrt{\frac{\omega_k}{2\hbar\epsilon_0 V}} \mathbf{e}_{\mathbf{k},\lambda} \cdot \boldsymbol{\mu}_j \tag{2.18}$$

Note that, while the orientation of the dipoles is arbitrary, since the emitters are identical they are of the same magnitude, i.e. $|\boldsymbol{\mu}_j| = \mu$. The Heisenberg equation for the photon annihilation operator of a specific mode is

$$\dot{a}_{\mathbf{k},\lambda} = \frac{i}{\hbar}[H, a_{\mathbf{k},\lambda}] = -i\omega_k a_{\mathbf{k},\lambda} - i \sum_j g_{\mathbf{k},\lambda}^{(j)} e^{-i\mathbf{k}\cdot\mathbf{r}_j} \sigma_j. \tag{2.19}$$

Integrating the above leads to

$$a_{\mathbf{k},\lambda}(t) = a_{\mathbf{k},\lambda}(0) e^{-i\omega_k t} - i \sum_j g_{\mathbf{k},\lambda}^{(j)} e^{-i\mathbf{k}\cdot\mathbf{r}_j} \int_0^t dt' \sigma_j(t') e^{i\omega_k(t'-t)}. \tag{2.20}$$

As we can see, the field operator at time t depends on the emitter operators at previous times t'. Since the emitter operators in turn depend on the field modes, it is not possible to solve the time integral exactly. Recall from the RWA, though, that the dominating time dependence of the emitters is governed by an oscillation with their resonance frequency,

$$\sigma_j(t) \propto \sigma_j(0) e^{-i\omega_0 t}. \tag{2.21}$$

Thus, if we define an operator

$$s_j(t) := \sigma_j(t)e^{i\omega_0 t} \propto \sigma_j(0), \tag{2.22}$$

we can expect this to vary only slowly in time (compared to the timescale given by $1/\omega_0$). We can therefore approximate a time integration that involves this new operator replacing t' by t. With the above definition, we write

$$\int_0^t dt'\sigma_j(t') = \int_0^t dt' s_j(t')e^{-i\omega_0 t'} \approx s_j(t)\int_0^t dt' e^{-i\omega_0 t'} = \sigma_j(t)\int_0^t dt' e^{-i\omega_0(t'-t)}. \tag{2.23}$$

This is the so-called Markov approximation [2.4], which is commonly used in the description of open quantum systems. Our ultimate goal in this section is to obtain an expression of the emitted electric field that is fully determined by the emitters. Substituting Eq. (2.20) into the free electric field, Eq. (2.11), we can separate the total electric field into two terms,

$$\mathbf{E}^+(\mathbf{r},t) = \mathbf{E}^+_{\text{in}}(\mathbf{r},t) + \mathbf{E}^+_0(\mathbf{r},t). \tag{2.24}$$

The first term is just the free evolution of the initial electric field,

$$\mathbf{E}^+_{\text{in}}(\mathbf{r},t) = \sum_{\mathbf{k},\lambda}\sqrt{\frac{\hbar\omega_k}{2\epsilon_0 V}}\mathbf{e}_{\mathbf{k},\lambda}a_{\mathbf{k},\lambda}(0)e^{-i\omega_k t}e^{i\mathbf{k}\cdot\mathbf{r}}. \tag{2.25}$$

In the following, we will consider the initial field to be in a vacuum state, such that $\langle\mathbf{E}^+_{\text{in}}(\mathbf{r},t)\rangle = 0$. Even though it is tempting to argue that we can then neglect this term since it does not contribute to averages, this would not be entirely accurate. Specifically, as we will show in Sec. 2.3.1, the input field will give rise to quantum noise. For now, though, we will not bother with any further discussion of this term.

The field emitted by the ensemble, on the other hand, can be simplified further and, using Eq. (2.23), it reads

$$\mathbf{E}^+_0(\mathbf{r},t) = -i\sum_j\sum_{\mathbf{k},\lambda}\sqrt{\frac{\hbar\omega_k}{2\epsilon_0 V}}\mathbf{e}_{\mathbf{k},\lambda}g^{(j)}_{\mathbf{k},\lambda}e^{i\mathbf{k}\cdot(\mathbf{r}-\mathbf{r}_j)}\sigma_j(t)\int_0^t dt' e^{i(\omega_k-\omega_0)(t'-t)}. \tag{2.26}$$

We proceed with solving the sum over polarizations. The polarization unit vectors $\mathbf{e}_{\mathbf{k},\lambda}$ are orthogonal on $\mathbf{k}$ as well as mutually so. Therefore, together with the unit wave vector $\hat{\mathbf{k}}$ they form an orthonormal basis. This means their projectors add up to the three-dimensional identity matrix, or inversely

$$\sum_\lambda \mathbf{e}_{\mathbf{k},\lambda}g^{(j)}_{\mathbf{k},\lambda} = \sqrt{\frac{\omega_k}{2\hbar\epsilon_0 V}}\sum_\lambda(\mathbf{e}_{\mathbf{k},\lambda}\circ\mathbf{e}_{\mathbf{k},\lambda})\cdot\boldsymbol{\mu}_j = \sqrt{\frac{\omega_k}{2\hbar\epsilon_0 V}}\left(\mathbb{1}-\hat{\mathbf{k}}\circ\hat{\mathbf{k}}\right)\cdot\boldsymbol{\mu}_j, \tag{2.27}$$

where $\circ$ denotes the dyadic product. Since the density of modes in free space is high, we can replace the sum over wave vectors by an integral. Using this and substituting Eq. (2.27), the electric field becomes

$$\begin{aligned}\mathbf{E}_0^+(\mathbf{r},t) = \frac{-i}{2\epsilon_0(2\pi c)^3}\sum_j \sigma_j(t)\int d\omega_k\omega_k^3\int_0^t dt' e^{i(\omega_k-\omega_0)(t'-t)} \\ \times\int d\Omega_k\left(\mathbb{1}-\left(\hat{\mathbf{k}}\circ\hat{\mathbf{k}}\right)\right)\cdot\boldsymbol{\mu}_j e^{i\mathbf{k}\cdot(\mathbf{r}-\mathbf{r}_j)}.\end{aligned} \tag{2.28}$$

In order to solve the solid-angle integral, we rewrite the exponential in terms of the spatial gradient as

$$\left(\hat{\mathbf{k}}\circ\hat{\mathbf{k}}\right)e^{i\mathbf{k}\cdot(\mathbf{r}-\mathbf{r}_j)} = -\frac{1}{k^2}\left(\nabla_{\mathbf{r}}\circ\nabla_{\mathbf{r}}\right)e^{i\mathbf{k}\cdot(\mathbf{r}-\mathbf{r}_j)}, \tag{2.29}$$

and exchange the order of integration and derivatives. The task of integrating over the solid angle reduces to taking second-order derivatives of the simple integral

$$\int d\Omega_k e^{i\mathbf{k}\cdot(\mathbf{r}-\mathbf{r}_j)} = 2\pi\int_0^\pi d\theta\sin\theta e^{ik|\mathbf{r}-\mathbf{r}_j|\cos\theta} = 4\pi\frac{\sin\left(k|\mathbf{r}-\mathbf{r}_j|\right)}{k|\mathbf{r}-\mathbf{r}_j|}. \tag{2.30}$$

While tedious, the ensuing calculation of derivatives is straightforward and results in the electric field

$$\mathbf{E}_0^+(\mathbf{r},t) = \frac{-i}{4\pi^2c^3\epsilon_0}\sum_j\sigma_j(t)\int d\omega_k\omega_k^3\int_0^t dt' e^{i(\omega_k-\omega_0)(t'-t)}\mathrm{Im}\left\{\underline{\mathbf{G}}(k,\mathbf{r}-\mathbf{r}_j)\right\}\cdot\boldsymbol{\mu}_j, \tag{2.31}$$

where, with $\hat{\mathbf{r}}$ being the position unit vector, we defined

$$\underline{\mathbf{G}}(k,\mathbf{r}) := e^{ikr}\left[\left(\frac{1}{kr}+\frac{i}{(kr)^2}-\frac{1}{(kr)^3}\right)\mathbb{1}-(\hat{\mathbf{r}}\circ\hat{\mathbf{r}})\left(\frac{1}{kr}+\frac{3i}{(kr)^2}-\frac{3}{(kr)^3}\right)\right]. \tag{2.32}$$

The above expression corresponds to Green's tensor for a (classical) oscillating dipole source [2.5]. Using this definition will later prove convenient, as it will enable us to express the radiated electric field in terms of this propagator even though our calculation remains fully quantum mechanical.

Finally, we apply the Sokhotski-Plemelj formula [2.6] to the time integral,

$$\int d\omega_k\int_0^t dt' e^{i(\omega_k-\omega_0)(t'-t)} = \int d\omega_k\left(-\mathcal{P}\frac{i}{\omega_k-\omega_0}+\pi\delta(\omega_k-\omega_0)\right), \tag{2.33}$$

where $\mathcal{P}$ denotes the principal value. The part of the remaining integral proportional to the δ function is not difficult to solve, whereas solving the principal value integrals is a bit more involved. Nevertheless, standard methods of complex contour integration apply [2.4]. We will simply state the result here and refer to Ref. [2.7] for a more

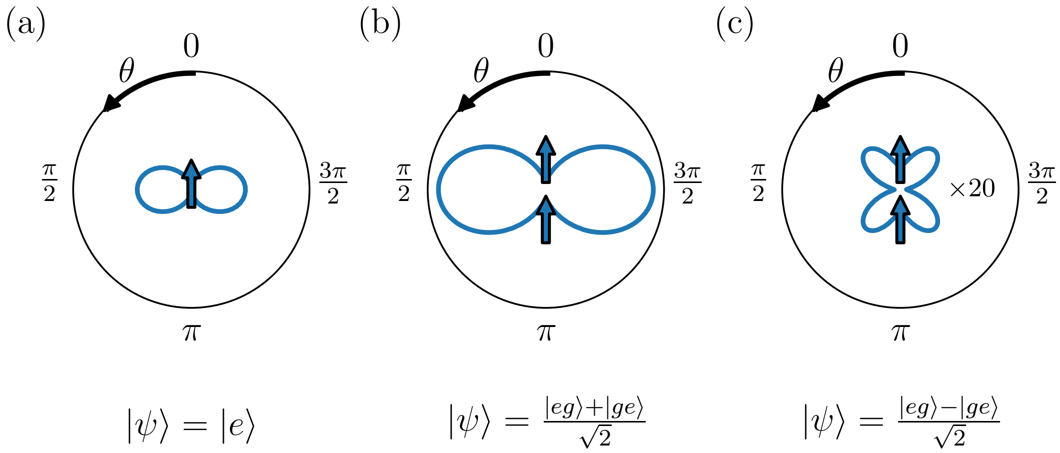

$|\psi\rangle = |e\rangle$ $\quad$ $|\psi\rangle = \frac{|eg\rangle+|ge\rangle}{\sqrt{2}}$ $\quad$ $|\psi\rangle = \frac{|eg\rangle-|ge\rangle}{\sqrt{2}}$

Figure 2.2: *Radial intensity profile of coupled dipole transitions.* The intensity $I(r)$ emitted by (a) a single quantum emitter, and by two quantum emitters in (b) a superradiant and (c) a subradiant state, respectively. The two emitters are separated by a fraction of the transition wavelength $|\mathbf{r}_1 - \mathbf{r}_2| = 0.1\lambda_0$ along the axis of their dipoles. The arrows schematically depict the transition dipole moment of each emitter. The intensities are calculated at a fixed distance $r = \lambda_0$ and are plotted as a function of the angle θ around the emitter(s) in the same plane in which the dipole moments lie. The intensity lines in (a) and (b) are to scale, whereas in (c) the subradiant state radiates so weakly that the intensity had to be scaled up by the factor indicated in the graph in order to be visible on the same scale.

rigorous treatment. In fact, the principal value integral yields precisely the real part of the tensor $\underline{\mathbf{G}}$ defined in Eq. (2.32), such that the electric field radiated by an ensemble of quantum emitters becomes

$$\mathbf{E}^{+}(\mathbf{r},t) = \mathbf{E}^{+}_{\text{in}}(\mathbf{r},t) - \frac{3\hbar\gamma}{4\mu}\sum_j \sigma_j(t)\underline{\mathbf{G}}(k_0, \mathbf{r}-\mathbf{r}_j)\cdot\hat{\boldsymbol{\mu}}_j. \tag{2.34}$$

Above, we have implicitly defined the transition wave number $k_0 = \omega_0/c$ as well as the rate $\gamma = \omega_0^3\mu^2/(3\pi c^3\epsilon_0\hbar)$, which, as we will also confirm later, is the spontaneous emission rate of a single quantum emitter. Let us again stress, that the emitted electric field under the assumptions made during the derivation is completely determined by the behavior of the quantum emitters. If the input field does not contribute (e.g. when computing average values), the degrees of freedom in the system are thus greatly reduced and further investigations are possible.

To gain some more insight into the physics, we can compute the radiated intensity,

$$\mathbf{I}(\mathbf{r},t) := \langle \mathbf{E}^{-}(\mathbf{r},t)\cdot\mathbf{E}^{+}(\mathbf{r},t)\rangle\,. \tag{2.35}$$

In Fig. 2.2, we plot the instantaneous ($t = 0$) intensity profile in the radial direction for a single and two closely spaced quantum emitters. We always consider a single excitation in a state $|\psi\rangle$ as specified in Fig. 2.2. As we can see, even though we keep the number of excitations in the system constant, the intensity in Fig. 2.2(b) is substantially larger. This is due to superradiance [2.8, 2.9] and we will later show the behavior of this effect when increasing the number of emitters further. On the other hand, in Fig. 2.2(c), we observe that the field profile is changed: For the antisymmetric superposition, the dipole radiation is suppressed and the system exhibits an extremely weak quadrupole. This contrary effect is called subradiance and comprises a large part of the investigations shown in the subsequent chapters.

The intensity as calculated above is also used in chapter 6 and chapter 7, respectively, to calculate the radiation patterns of ensembles of quantum emitters in different states.

2.3 Dipole-dipole interactions

The electric field derived in the previous section contains all the dynamics of an ensemble of dipole coupled quantum emitters. However, the field itself is often of little interest and it is more convenient to eliminate it completely. In the following we will develop such a description using the field from Eq. (2.34). The resulting effective dynamics forms the basis for many further investigations, which are the subject of the following chapters.

2.3.1 Quantum Langevin equations for dipole coupled quantum emitters

One possible way of solving for the dynamics of an ensemble of emitters is to work in the Heisenberg picture. While this approach is rather straightforward for energy-conserving systems, an effective description of open systems is generally a bit more involved. Specifically, we must account for quantum noise to avoid violating fundamental conservation laws, such as the canonical commutation relations. The emerging equation is known as the quantum Langevin equation (QLE) and is a well-known tool in quantum optics [2.10]. The peculiarity here is that the input noise features spatial correlations due to the dipole-dipole interactions of the quantum emitters.

We start by writing down the interaction Hamiltonian as given in Eq. (2.7) for many emitters,

$$H_{\text{int}} = \sum_j \mathbf{d}_j \cdot \mathbf{E}(\mathbf{r}_j) \approx \sum_j \left[\sigma_j^\dagger \left(\boldsymbol{\mu}_j \cdot \mathbf{E}^+(\mathbf{r}_j)\right) + \left(\boldsymbol{\mu}_j \cdot \mathbf{E}^-(\mathbf{r}_j)\right)\sigma_j\right], \tag{2.36}$$

where in the second step we performed the RWA. Now, let $\mathcal{O}$ be an arbitrary emitter operator, i.e. it commutes with the field operators at equal time. Its Heisenberg equation is

$$\dot{\mathcal{O}} = \frac{i}{\hbar}[H_0, \mathcal{O}] + \frac{i}{\hbar}\sum_j \left([\sigma_j^\dagger, \mathcal{O}]\left(\boldsymbol{\mu}_j \cdot \mathbf{E}^+(\mathbf{r}_j)\right) + \left(\boldsymbol{\mu}_j \cdot \mathbf{E}^-(\mathbf{r}_j)\right)[\sigma_j, \mathcal{O}]\right), \tag{2.37}$$

where $H_0 = \hbar\omega_0 \sum_j \sigma_j^\dagger \sigma_j$ is the free energy Hamiltonian. Using the expression for the electric field emitted by the ensemble, Eq. (2.34), we obtain after some manipulation

$$\begin{aligned}\dot{\mathcal{O}} = \frac{i}{\hbar}[H_0, \mathcal{O}] - \frac{3i\gamma}{4}\sum_{j,k}[\sigma_j^\dagger \sigma_k, \mathcal{O}] \left(\hat{\boldsymbol{\mu}}_j \cdot \mathrm{Re}\left\{\underline{\mathbf{G}}(k_0, \mathbf{r}_{jk})\right\} \cdot \hat{\boldsymbol{\mu}}_k\right) \\ + \sum_j [\sigma_j^\dagger, \mathcal{O}] \left(\frac{i}{\hbar}\left(\boldsymbol{\mu}_j \cdot \mathbf{E}_{\mathrm{in}}^+(\mathbf{r}_j, t)\right) + \frac{3\gamma}{4}\sum_k \left(\hat{\boldsymbol{\mu}}_j \cdot \mathrm{Im}\left\{\underline{\mathbf{G}}(k_0, \mathbf{r}_{jk})\right\} \cdot \hat{\boldsymbol{\mu}}_k\right)\sigma_k\right) \\ + \sum_j \left(\frac{i}{\hbar}\left(\boldsymbol{\mu}_j \cdot \mathbf{E}_{\mathrm{in}}^-(\mathbf{r}_j, t)\right) - \frac{3\gamma}{4}\sum_k \left(\hat{\boldsymbol{\mu}}_j \cdot \mathrm{Im}\left\{\underline{\mathbf{G}}(k_0, \mathbf{r}_{jk})\right\} \cdot \hat{\boldsymbol{\mu}}_k\right)\sigma_k^\dagger\right)[\sigma_j, \mathcal{O}].\end{aligned} \tag{2.38}$$

Here, we used the fact that the Green tensor has even parity in $\mathbf{r}$ and defined $\mathbf{r}_{jk} := \mathbf{r}_j - \mathbf{r}_k$. Note that the second term in the first line of Eq. (2.38) takes the form of a commutator and can thus be written as an additional term in the Hamiltonian. Physically, this corresponds to the process of coherent energy exchange between the coupled dipoles.

Finally, we need to consider the input fields. To this end, we define the operator

$$\xi_j(t) := \frac{i}{\hbar\sqrt{\gamma}}\left(\boldsymbol{\mu}_j \cdot \mathbf{E}_{\mathrm{in}}^+(\mathbf{r}_j, t)\right) = \frac{i}{\sqrt{\gamma}}\sum_{\mathbf{k},\lambda} g_{\mathbf{k},\lambda}^{(j)} a_{\mathbf{k},\lambda}(0) e^{-i\omega_k t} e^{i\mathbf{k}\cdot\mathbf{r}_j}, \tag{2.39}$$

which we identify as quantum noise operator. Assuming, as before, that the surrounding field is in a vacuum state, it is clear that the average of $\xi_j(t)$ vanishes. A more interesting quantity for the noise, though, is its correlation function or, equivalently, the canonical commutation relation. We consider the latter and with the definition of the free electric field from Eq. (2.25) write

$$\left[\xi_m(t), \xi_n^\dagger(t')\right] = \sum_{\mathbf{k},\lambda} \frac{\omega_k}{2\hbar\gamma\epsilon_0 V}\left(\boldsymbol{\mu}_m \cdot \mathbf{e}_{\mathbf{k},\lambda}\right)\left(\boldsymbol{\mu}_n \cdot \mathbf{e}_{\mathbf{k},\lambda}\right) e^{-i\omega_k(t-t')} e^{i\mathbf{k}\cdot\mathbf{r}_{mn}}, \tag{2.40}$$

where we already used the canonical commutator, Eq. (2.12), to resolve one of the arising sums. We use the relation from Eq. (2.27) to solve for the polarizations and proceed by replacing the sum over wave vectors by an integral. This leads to an integral over the solid angle, which has exactly the same form as before. Using the solution from Eq. (2.31) we can thus write

$$\left[\xi_m(t), \xi_n^\dagger(t')\right] = \int d\omega_k e^{i\omega_k(t-t')} \frac{\omega_k^3}{4\pi^2 c^3 \hbar\epsilon_0\gamma} \boldsymbol{\mu}_m \cdot \mathrm{Im}\left\{\underline{\mathbf{G}}(k, \mathbf{r}_{mn})\right\} \cdot \boldsymbol{\mu}_n. \tag{2.41}$$

Since we are only interested in relevant frequencies, i.e. where $\omega_k \approx \omega_0$, we may evaluate the argument in the Fourier transform above at this point [2.10], which leads to

$$\left[\xi_m(t), \xi_n^\dagger(t')\right] \approx \frac{3}{2}\delta(t - t')\ \hat{\boldsymbol{\mu}}_m \cdot \mathrm{Im}\left\{\underline{\mathbf{G}}(k_0, \mathbf{r}_{mn})\right\} \cdot \hat{\boldsymbol{\mu}}_n. \tag{2.42}$$

From this commutation relation it is clear that the quantum noise for dipole coupled quantum emitters is spatially correlated white noise (uncorrelated in time).

The quantum Langevin equation for dipole coupled quantum emitters is

$$\begin{aligned}\dot{\mathcal{O}} = \frac{i}{\hbar}[H_0 + H_{\text{dip}}, \mathcal{O}] + \sum_{j,k} [\sigma_j^\dagger, \mathcal{O}] \left(\delta_{jk} \sqrt{\gamma} \xi_j(t) + \frac{\gamma_{jk}}{2} \sigma_k \right) \\ - \sum_{j,k} \left(\delta_{jk} \sqrt{\gamma} \xi_j^\dagger(t) + \frac{\gamma_{jk}}{2} \sigma_k^\dagger \right) [\sigma_j, \mathcal{O}], \end{aligned} \tag{2.43}$$

where we defined the Hamiltonian describing the coherent excitation exchange as

$$H_{\text{dip}} := \sum_{j,k} \hbar \Omega_{jk} \sigma_j^\dagger \sigma_k. \tag{2.44}$$

Furthermore, we defined the coherent coupling and collective decay rates,

$$\Omega_{ij} := -\frac{3\gamma}{4} \, \hat{\boldsymbol{\mu}}_i \cdot \text{Re} \left\{ \underline{\mathbf{G}}(k_0, \mathbf{r}_{ij}) \right\} \cdot \hat{\boldsymbol{\mu}}_j, \tag{2.45a}$$

$$\gamma_{ij} := \frac{3\gamma}{2} \, \hat{\boldsymbol{\mu}}_i \cdot \text{Im} \left\{ \underline{\mathbf{G}}(k_0, \mathbf{r}_{ij}) \right\} \cdot \hat{\boldsymbol{\mu}}_j, \tag{2.45b}$$

respectively. Note that the shifts Ω_{ij} diverge at zero distance. Because of this, self-interaction terms are neglected, i.e. we set $\Omega_{ii} = 0$. In other words, we disregard the interaction of an emitter with itself.

The behavior of the rates defined above in the limits where $r_{ij} \ll \lambda_0$ (the so-called Dicke limit) and $r_{ij} \gg \lambda_0$ is of interest as well. In the first case, the interaction range is much larger than the separation such that it is effectively infinite. The coherent shifts then diverge, whereas $\gamma_{ij} \to \gamma$. In the second case, on the other hand, the separation between the emitters is so large that they become independent, i.e. $\Omega_{ij} \to 0$ and $\gamma_{ij} \to \delta_{ij}\gamma$.

Note that in terms of the collective decay rates the input noise correlations (and, similarly, their commutation relations) take the simple form

$$\langle \xi_j(t) \xi_k^\dagger(t') \rangle = \frac{\gamma_{jk}}{\gamma} \delta(t - t'). \tag{2.46}$$

The QLE as given in Eq. (2.43) allows for a number of analytical calculations in an approximate regime. Interesting quantities such as higher order correlations and frequency spectra can be directly calculated. This approach is thoroughly treated and used in chapter 6.

2.3.2 Collective input-output relation

It is possible to cast the QLE into an alternative form. To this end recall that when integrating the Heisenberg equation for the field operators $a_{\mathbf{k},\lambda}$ in Eq. (2.20), we chose the initial condition at time 0. However, it is also possible to use a boundary value at a time $t_1 > t$ [2.10]. The field operator is then given by

$$a_{\mathbf{k},\lambda}(t) = a_{\mathbf{k},\lambda}(t_1)e^{-i\omega_k(t-t_1)} + i\sum_j g_{\mathbf{k},\lambda}^{(j)} e^{-i\mathbf{k}\cdot\mathbf{r}_j} \int_t^{t_1} dt'\sigma_j(t')e^{i\omega_k(t'-t)}. \tag{2.47}$$

Proceeding as before by substituting this into the electric field, the arising calculation is mostly the same and we obtain

$$\mathbf{E}^+(\mathbf{r},t) = \mathbf{E}^+_{\text{out}}(\mathbf{r},t) - \frac{3\hbar\gamma}{4\mu}\sum_j \sigma_j(t)\underline{\mathbf{G}}(k_0,\mathbf{r}-\mathbf{r}_j)^* \cdot \hat{\boldsymbol{\mu}}_j. \tag{2.48}$$

Here, we defined the output field as

$$\mathbf{E}^+_{\text{out}}(\mathbf{r},t) = \sum_{\mathbf{k},\lambda}\sqrt{\frac{\hbar\omega_k}{2\epsilon_0 V}}\mathbf{e}_{\mathbf{k},\lambda}a_{\mathbf{k},\lambda}(t_1)e^{-i\omega_k(t-t_1)}e^{i\mathbf{k}\cdot\mathbf{r}}. \tag{2.49}$$

Of course the free electric field $\mathbf{E}^+$ at time t must be the same regardless of whether we express it in terms of the input field $\mathbf{E}^+_{\text{in}}$ or the output field $\mathbf{E}^+_{\text{out}}$. Equating Eq. (2.34) with Eq. (2.48), we can therefore deduce the relation between the input and output field,

$$\mathbf{E}^+_{\text{out}}(\mathbf{r},t) - \mathbf{E}^+_{\text{in}}(\mathbf{r},t) = -\frac{3i\hbar\gamma}{2\mu}\sum_j \sigma_j(t)\text{Im}\left\{\underline{\mathbf{G}}(k_0,\mathbf{r}-\mathbf{r}_j)\right\} \cdot \hat{\boldsymbol{\mu}}_j. \tag{2.50}$$

Using the definitions of the input noise operators $\xi_j(t)$ [Eq. (2.39)] and defining according output operators,

$$\xi_j^{\text{out}}(t) := \frac{i}{\hbar\sqrt{\gamma}}\left(\boldsymbol{\mu}_j \cdot \mathbf{E}^+_{\text{out}}(\mathbf{r}_j,t)\right), \tag{2.51}$$

we further derive

$$\xi_j^{\text{out}}(t) - \xi_j(t) = \sum_k \frac{\gamma_{jk}}{\sqrt{\gamma}}\sigma_k(t). \tag{2.52}$$

The above equation constitutes a generalized input-output relation for dipole coupled quantum emitters. It is useful when one is interested in the output of a system, as is the case, for example, in chapter 6. Furthermore, it is often vital for calculations to know the precise commutation relations between input noise operators and system operators. Arguing with causality, the input-output relation can be used to derive these [2.10] (see also Sec. 6.7).

2.3.3 Master equation for dipole coupled quantum emitters

If it is not feasible to directly use QLEs, e.g. if they are not soluble, there is another fundamental equation we can use, the so-called master equation. Basically, this description is equivalent to the QLE approach, but instead of working in the Heisenberg picture (time-dependent operators), we switch to the Schrödinger picture (time-dependent states).

We will now sketch how to find an equation for the density operator $\rho(t)$ which describes the state of the emitters. To this end, we start at the very beginning treating the full system consisting of the quantum emitters as well as the surrounding electric field modes. Assuming that at $t = 0$ there are no correlations between the electromagnetic field and the quantum emitters, the initial state is given by $\rho(0) \otimes \rho_{\mathrm{F}}(0)$. Here, ρ_{F} is the density matrix describing the state of the electromagnetic field. The time evolution of the composite density operator is determined by the unitary evolution operator $U(t) = \exp(-iHt/\hbar)$ with the Hamiltonian H from Eq. (2.17). Therefore, the state of the quantum emitters at time t is given by

$$\rho(t) = \mathrm{tr}_{\mathrm{F}} \left(U(t)\rho(0) \otimes \rho_{\mathrm{F}}(0) U^{\dagger}(t) \right), \tag{2.53}$$

where tr_{F} denotes the partial trace over the electromagnetic field.

The expectation value of an arbitrary emitter operator $\mathcal{O}$ behaves in time according to

$$\langle \mathcal{O}(t) \rangle = \mathrm{tr} \left(\mathcal{O}(t)\rho(0) \otimes \rho_{\mathrm{F}} \right) = \mathrm{tr} \left(\mathcal{O}(0)\rho(t) \right), \tag{2.54}$$

where we used the cyclic property of the trace to switch from the Heisenberg to the Schrödinger picture. In the last step we also used the fact that $\mathcal{O}(0)$ acts only on the emitter Hilbert space allowing us to trace out the state of the electromagnetic field. Taking the derivative of the above equation, we find

$$\mathrm{tr} \left(\dot{\mathcal{O}}(t)\rho(0) \otimes \rho_{\mathrm{F}}(0) \right) = \mathrm{tr} \left(\mathcal{O}(0)\dot{\rho}(t) \right). \tag{2.55}$$

Now, we insert the QLE for the operator $\mathcal{O}$, Eq. (2.43), on the left-hand side and again utilize the cyclic property of the trace,

$$\begin{aligned} \mathrm{tr}(\dot{\mathcal{O}}(t)\rho(0) \otimes \rho_{\mathrm{F}}(0)) = \mathrm{tr} \Bigg\{ \mathcal{O} \Big(&-\frac{i}{\hbar}[H_0 + H_{\mathrm{dip}}, \rho(t)] \\ &+ \sum_{j,k} \frac{\gamma_{jk}}{2} \left(2\sigma_j \rho(t) \sigma_k^{\dagger} - \sigma_j^{\dagger}\sigma_k \rho(t) - \rho(t)\sigma_j^{\dagger}\sigma_k \right) \Big) \Bigg\}. \end{aligned} \tag{2.56}$$

Here, we used the fact that the surrounding field is in a vacuum state, and thus

$$\xi_j(t)\rho_{\mathrm{F}}(0) = \rho_{\mathrm{F}}(0)\xi_j^{\dagger}(t) = 0, \tag{2.57}$$

so all terms proportional to the input noise vanish. Comparing Eq. (2.56) with Eq. (2.55)

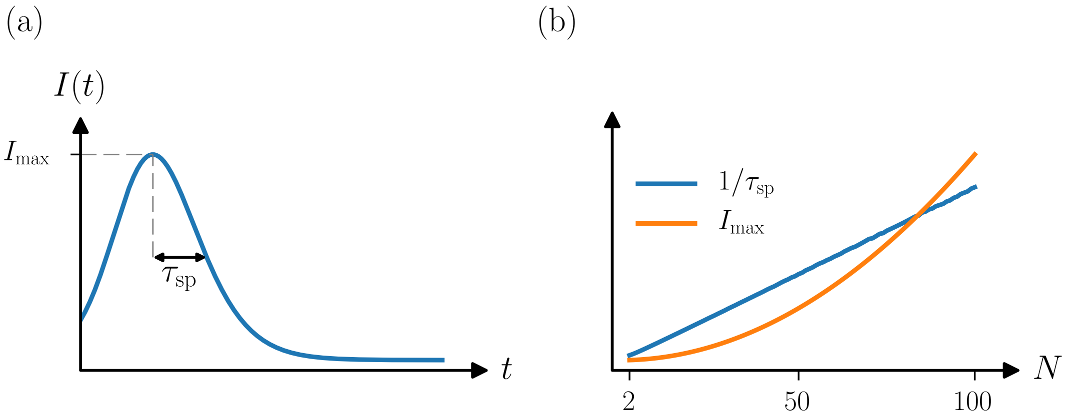

Figure 2.3: *Superradiant pulse of a dense ensemble.* (a) The intensity of the electric field emitted by a fully inverted ensemble consisting of $N = 25$ quantum emitters in the Dicke limit is shown as a function of time. After an initial build-up of coherences it reaches a maximum. The duration of this pulse is given by the half-width τ_{sp} (at half the maximum intensity). (b) The maximal intensity emitted scales with N^2, whereas the duration of the pulse is inversely proportional to the number of emitters, $\tau_{\mathrm{sp}} \propto 1/N$. In both graphs, the intensity was computed at a fixed distance from the emitter ensemble.

leads to the equation for the emitter density operator,

$$\dot{\rho} = -\frac{i}{\hbar}[H_0 + H_{\mathrm{dip}}, \rho] + \mathcal{L}[\rho], \tag{2.58}$$

where

$$\mathcal{L}[\rho] := \sum_{j,k} \frac{\gamma_{jk}}{2} \left(2\sigma_j \rho \sigma_k^\dagger - \sigma_j^\dagger \sigma_k \rho - \rho \sigma_j^\dagger \sigma_k\right), \tag{2.59}$$

is the Liouville operator in standard Lindblad form. Eq. (2.58) is the master equation for dipole-dipole interacting two-level emitters, as originally derived in Ref. [2.4] or later in e.g. Ref. [2.11]. The master equation is more convenient for numerical treatments (see also Sec. 2.6). As such it forms the basis of many theoretical investigations. For example, chapter 3 and chapter 7 are based on Eq. (2.58).

As an illustration of the master equation's versatility, we take a closer look at the Dicke limit [2.8]. In this limit, the density of the emitter ensemble is so high, that for any photon interacting with the emitters they appear to be located at the same point in space. If all dipoles have the same orientation, $\boldsymbol{\mu}_j \equiv \boldsymbol{\mu}$, the emitters behave identically and thus become completely indistinguishable. The interaction of any pair of emitters is then equal to all others (note that because of this we neglect the shifts as

$\Omega_{ij} = \Omega_{ii} = 0$), such that the Liouvillian in the master equation becomes

$$\mathcal{L}[\rho] = \frac{\gamma}{2}\left(2S\rho S^\dagger - S^\dagger S\rho - \rho S^\dagger S\right). \tag{2.60}$$

In the above, we defined the collective emitter lowering operator $S := \sum_j \sigma_j$. We can see that decay only occurs in a subspace of the collective state space where all states are invariant under particle exchange. Equivalently, we can say that for each number of excitations there is only one state that still couples to the environment, which exhibits maximal superradiance. All other states are completely decoupled, i.e. they are perfectly subradiant. This symmetrization of states also has the practical advantage that it reduces the size of the Hilbert space from 2^N states to $N+1$ relevant states.

The emitted electric field can also be expressed by the collective operators

$$\mathbf{E}_0^+(\mathbf{r},t) = -\frac{3\hbar\gamma}{4\mu}\underline{\mathbf{G}}(k_0, \mathbf{r}-\mathbf{r}_j)\cdot\hat{\boldsymbol{\mu}}\; S(t). \tag{2.61}$$

We can therefore compute the field in the reduced Hilbert space, also called the Dicke basis, as well. Using the master equation, we obtain the time evolution of the density operator and subsequently evaluate the expectation value for the intensity from Eq. (2.35). If we start with an ensemble that is initially in the fully inverted state, i.e. $|e\rangle^{\otimes N}$, we can observe a strong but short superradiant pulse. The pulse occurs after some initial build-up time [see Fig. 2.3(a)], which stems from the fact that an inverted emitter has no dipole moment. Thus, some time is required for the cumulation of a collective dipole, which then leads to a spontaneous emission cascade. The duration and maximal intensity of the pulse exhibit distinct scalings with the number of emitters, which is depicted in Fig. 2.3(b). The behavior shown in Fig. 2.3 is a well-known characteristic of superradiance [2.12].

2.4 Cavity QED with an ensemble of emitters

Ensembles of quantum emitters already exhibit rich phenomena on their own. However, coupling light to emitters in free space such that it faithfully interacts with them can be challenging. A well-established tool in quantum optics used to enhance coherent light-matter interactions is an optical cavity or optical resonator [2.13]. Such a cavity consists of two mirrors separated by a distance L_c (see Fig. 2.4). Due to the phase condition upon reflection from the mirrors, this creates a standing wave mode in the direction of the cavity axis. The only modes supported by the cavity are the ones with wave vectors $\mathbf{k} = 2\pi n\hat{\mathbf{z}}/L_\mathrm{c}$, where $n \in \mathbb{N}$ and we chose the axis of the cavity to be the z axis. Assuming that these modes are far separated in terms of their respective resonance frequencies, we can consider only a single mode to be of significance. The mirrors of the cavity are not perfect, but allow for some leakage into and out of the cavity. These effects are taken into account by an appropriate coupling term.

In the following we make two fundamental approximations: First, we assume that the cavity mode predominantly couples to modes which have wave vectors that are closely

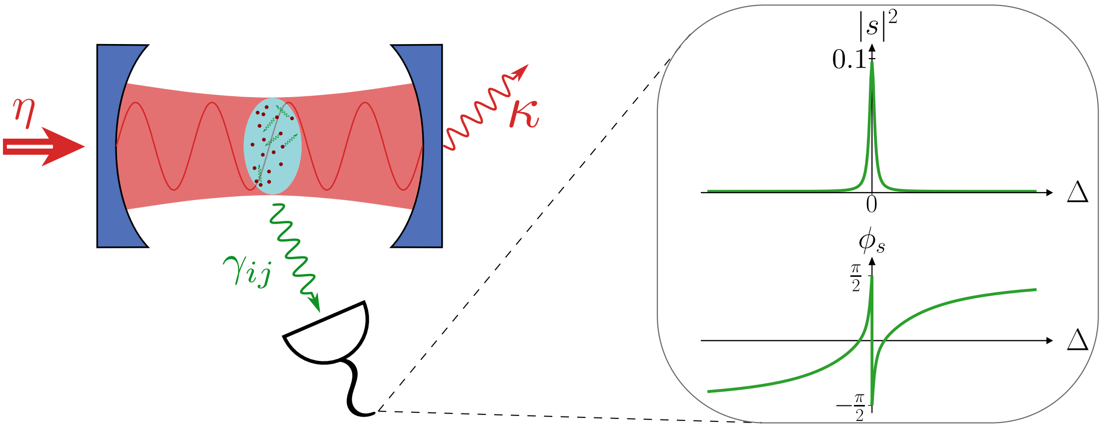

Figure 2.4: *Collective light scattering inside a Fabry-Pérot optical cavity.* An ensemble of interacting quantum emitters placed inside an optical cavity collectively emits light into but also out of the cavity. The cavity is driven coherently with an amplitude η and decays with the damping rate κ. In the bad-cavity ($g, \gamma \ll \kappa$) and weak-driving ($\eta \ll \kappa$) limit, the scattered amplitude $|s|^2$ remains small. The phase of the scattered field is maximal around the resonance point.

aligned with the cavity axis such that we can neglect any wave vectors that are not parallel to the z axis. This reduces the entire problem to one dimension. Secondly, we assume the free space modes that do couple to the cavity mode to do so equally with a constant rate ν; i.e., the mirror properties are frequency independent. Combining these assumptions, the Hamiltonian of an empty cavity coupling to the outside field reads

$$H = \hbar\omega_{\mathrm{c}} a^\dagger a + \sum_{k,\lambda} \hbar\omega_k b_{k,\lambda}^\dagger b_{k,\lambda} + \hbar\nu \sum_{k,\lambda} \left(b_{k,\lambda}^\dagger a + a^\dagger b_{k,\lambda} \right), \tag{2.62}$$

where ω_{c} is the resonance frequency of the cavity mode with the bosonic annihilation (creation) operator a ($a^\dagger$). The last term of the Hamiltonian describes the interaction between the cavity and the surrounding modes with the bath operators $b_{k,\lambda}$. The coupling to the environment is included via the process of destroying one photon in the cavity and creating one in a mode with wave number k and polarization λ, and vice-versa. The basic idea and method with which to continue is the exact same as before. Namely, we eliminate the bath operators $b_{k,\lambda}$ in order to obtain an effective equation for the cavity mode only. The integrals that arise when solving the Heisenberg equation of motion for the bath operators are considerably simpler. We therefore merely state the result.

The QLE for any cavity operator A, which commutes with the bath operators at equal times, is

$$\dot{A} = \frac{i}{\hbar}[H_{\mathrm{c}}, A] + [a^\dagger, A] \left(\sqrt{2\kappa} a_{\mathrm{in}}(t) + \kappa a \right) - \left(\sqrt{2\kappa} a_{\mathrm{in}}^\dagger(t) + \kappa a^\dagger \right) [a, A], \tag{2.63}$$

where $H_{\mathrm{c}} := \hbar\omega_{\mathrm{c}} a^\dagger a$. The damping rate κ is connected to the mirror coupling by $\kappa := \nu^2 L/c$. Note that here L is the length of the quantization volume ($L^3 = V$) from before. The input noise operator is given by the free part of the time evolution of the environment,

$$a_{\mathrm{in}}(t) = i\sqrt{\frac{c}{2L}} \sum_{k,\lambda} b_{k,\lambda}(0) e^{-i\omega_k t}. \tag{2.64}$$

We can follow the procedure shown in Sec. 2.3.2 and define a corresponding output operator, subsequently leading to the input-output relation

$$a_{\mathrm{out}}(t) - a_{\mathrm{in}}(t) = \sqrt{2\kappa} a(t). \tag{2.65}$$

The above equation can be used to investigate experimentally observable quantities such as the transmission and/or reflection of the cavity.

For our purposes, an empty cavity is of little interest. Consider, therefore, N quantum emitters that couple to the cavity via their transition dipoles. The interaction then takes the same form as in Eq. (2.7), where we described the coupling to many modes, just that now we only consider one specific (our cavity) mode. It reads

$$H_{\mathrm{TC}} = \sum_j \hbar g(\mathbf{r}_j) \left(a^\dagger \sigma_j + \sigma_j^\dagger a \right), \tag{2.66}$$

where $g(\mathbf{r}_j)$ is the dipole-interaction strength as given in Eq. (2.18) (substituting the cavity mode volume instead of the quantization volume) at the position of the jth emitter. This Hamiltonian corresponds to the well-known Jaynes-Cummings Hamiltonian describing the dipole-coupling of a standing-wave electric field and a single quantum emitter [2.14]. The generalization to N emitters, as in Eq. (2.66), is commonly known as the Tavis-Cummings (TC) Hamiltonian [2.15]. Note, that the coupling strength in Eq. (2.66) takes into account the standing wave as well as the transverse pattern of the cavity mode. The fact that the transverse mode profile can take very different shapes exhibiting phase shifts within a small area is used in chapter 5 in order to couple a cavity to subradiant states.

While the coherent coupling between quantum emitters and a cavity mode is quite intuitive, accounting for the precise system-bath coupling here is challenging. However, if we assume that the solid angle in which the emitters spontaneously decay into the cavity mode is small, we can neglect this part of the emitted field. Equivalently, we can say that the cavity mode does not significantly modify the bath for the quantum emitters, such that the baths for the cavity and the emitters can be considered independent. Thus, the respective bath operators $a_{\mathbf{k},\lambda}$ and $b_{k,\lambda}$ commute. This means, that we can separate the problems of describing the coupling to the environment for the cavity and the quantum emitters, respectively. Superimposing the results we obtained before then yields the proper QLE or master equation. Doing so enables a manifold of investigations. This very approach is studied in chapter 5 as well as more extensively in chapter 6.

As an example that showcases part of the rich physics, we can calculate the amplitude and phase of the field that is scattered out of the cavity by the emitters, when the cavity is driven. We add a cavity drive by including a coherent excitation in one mode, $a_{\mathrm{in}}(t) \rightarrow A_{\mathrm{in}}(t) = a_{\mathrm{in}}(t) + \eta/\sqrt{\kappa}e^{-i\omega_\ell t}$ (see also Sec. 2.5). The portion of the incident field that is scattered into free space by the emitters can then be computed by making use of the input-output relation, Eq. (2.52). It is defined as the sum over all emitter outputs normalized to the nonzero-average input,

$$s(t) := \sum_j \frac{\langle \xi_j^{\mathrm{out}}(t) \rangle}{\langle A_{\mathrm{in}}(t) \rangle} = \sum_{jk} \sqrt{\frac{\kappa}{\gamma}} \frac{\gamma_{jk}}{\eta} \langle \sigma_k(t) \rangle \,. \tag{2.67}$$

The scattered field intensity coefficient is $|s|^2$ and the phase of the field is given by

$$\phi_s(t) = \arctan\left(\frac{\mathrm{Im}\left\{s(t)\right\}}{\mathrm{Re}\left\{s(t)\right\}} \right). \tag{2.68}$$

While these expressions hold for any number of emitters, we only consider a single emitter in the following for simplicity. We would now proceed by using the emitter QLE, Eq. (2.43), to obtain an equation for the average of $\sigma(t)$. This couples to both the cavity annihilation operator as well as σ_z. For the latter, we make the approximation of a bad cavity ($g(\mathbf{r}), \gamma \ll \kappa$) and a weak drive ($\eta \ll \kappa$). This leads to $\langle \sigma_z \rangle \approx -1$. As for the cavity annihilation operator, we make use of Eq. (2.63) taking into account the coupling Hamiltonian, Eq. (2.66), in order to obtain an equation for its average. Under these conditions we find for the steady state,

$$s = \frac{-ig\sqrt{\kappa\gamma}}{(\kappa - i\Delta)\left(\frac{\gamma}{2} - i\Delta\right) + g^2}, \tag{2.69}$$

where $\Delta = \omega_\ell - \omega_{\mathrm{c}}$ and $\omega_{\mathrm{c}} = \omega_0$. In the above calculation we omitted most details since they are presented at length in chapter 6. Specifically, we substitute Eq. (6.13b) into Eq. (2.67) in order to obtain the above result.

The normalized intensity and the phase of the field are depicted in Fig. 2.4. This rather simple illustration suffices to highlight an important physical aspect. Namely, the phase of the field is $\pm\pi/2$ in the limit $\Delta \rightarrow 0^{\pm}$; i.e., the emitter induces a maximal phase shift around the resonance point. The same effect is responsible for the existence of so-called antiresonances: The phase shift induced by the emitter on the field inside the cavity causes partial destructive interference in the forward scattered part of the field. The transmission around the resonance is suppressed such that the emitter transition line is visible in the transmission spectrum of the cavity.

For many emitters, the linewidth of the collective transition is modified due to their mutual interactions. Very broad (superradiant) as well as sharp (subradiant) antiresonances can then be observed (see chapter 5 and chapter 6).

2.5 Collective laser spectroscopy

Many applications are based on addressing quantum emitters with laser light of a well-defined (single) frequency. Laser spectroscopy addresses the quantum emitters near their resonance frequency. A simplified model is this: Consider the free input electric field from Eq. (2.25). Now, let the mode with wave vector $\mathbf{k}_\ell$ and one specific polarization be the only one to significantly occupy a coherent state. Since the output of a phase-locked laser corresponds to a coherent state, we may replace the bosonic operators by classical complex amplitudes, $a_\ell(t) \to \alpha(t) = \alpha_0 \exp(-i\omega_\ell t)$. The interaction Hamiltonian describing the addressing with the electric field generated by the laser after making the RWA is

$$H_\ell := \hbar \sum_j \left(\eta e^{-i\omega_\ell t} e^{i\mathbf{k}_\ell \cdot \mathbf{r}_j} \sigma_j^\dagger + \eta^* e^{i\omega_\ell t} e^{-i\mathbf{k}_\ell \cdot \mathbf{r}_j} \sigma_j \right). \tag{2.70}$$

Here, $\eta := \sqrt{\omega_\ell/(2\hbar\epsilon_0 V)}\mu\alpha_0$ and we assumed all dipoles to be aligned with the polarization of the laser. Furthermore, we assumed $|\alpha_0| \gg 1$ such that the coupling to all other modes which are not driven by the laser is negligible.

The above Hamiltonian is conventionally used when modeling a coherent laser drive. It is based on the assumption that the laser mode is perfectly monochromatic and always supplies the exact same amount of photons. In reality, however, lasers have a finite linewidth and thus occupy more than a single mode [2.16]. Furthermore, the photon flux can fluctuate. The latter can quite intuitively be included in the model by introducing a random noise variable $\epsilon(t)$ which corresponds to a noisy laser amplitude, i.e. $\eta \to \eta + \epsilon(t)$. The amplitude noise here is white noise, so it has zero mean, $\{\epsilon(t)\}_{\text{cl}} = 0$, and is δ correlated, $\{\epsilon^*(t)\epsilon(t')\}_{\text{cl}} = \Gamma_{\text{a}}\delta(t-t')$. Here, $\{\cdot\}_{\text{cl}}$ denotes the average over infinitely many stochastic trajectories, and Γ_{a} is a frequency describing the characteristic magnitude of the amplitude noise.

The fact that a laser has a finite linewidth requires a more sophisticated description of H_ℓ. Consider that the spectrum of a laser has a Lorentzian shape [2.16], as depicted in Fig. 2.5(a). Thus, the first-order coherence function – which is the inverse Fourier transform of the spectrum – exhibits an exponential decay [see Fig. 2.5(b)],

$$g(\tau) := \langle a_\ell^\dagger(t+\tau) a_\ell(t) \rangle = |\alpha|^2 e^{-\Gamma\tau}, \tag{2.71}$$

where Γ is the linewidth (half-width at half the maximum) of the laser. We will now show that this linewidth can be modeled by a noisy phase of the laser. Instead of replacing the operator a_ℓ by a constant complex amplitude rotating at the laser frequency, we now make the Ansatz

$$a_\ell \to \alpha(t) = \alpha_0 e^{-i\omega_\ell t + i\phi(t)}, \tag{2.72}$$

where $\phi(t)$ accounts for the phase fluctuations of the laser. It is clear that to obtain the classical equivalent of the amplitude correlation in Eq. (2.71), it is not sufficient to

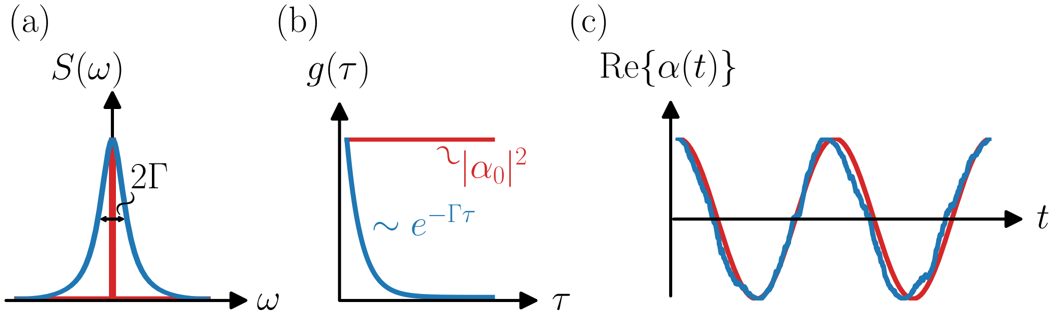

Figure 2.5: *Properties of the electric field radiated by a laser source.* (a) The Lorentzian spectrum of a laser with a half-width of zero (red) and Γ (blue). (b) The corresponding first-order coherence function of the perfectly monochromatic (red) and the imperfect laser (blue), respectively. While the coherence function of the zero-width laser is constant, i.e. it has infinite coherence time, the latter exhibits an exponentially decaying coherence function governed by its linewidth. (c) A single trajectory of the real electric field amplitude over multiple oscillation periods with frequency ω_ℓ. The finite linewidth (blue) leads to a fluctuating phase determined by its white-noise derivative.

describe $\phi(t)$ as a white-noise process. However, if its derivative is [2.10, 2.17, 2.18],

$$\left\{\dot\phi(t), \dot\phi(t')\right\}_{\mathrm{cl}} = 2\Gamma\delta(t-t'), \tag{2.73}$$

we can show that the above indeed leads to the correct amplitude correlation. The coherence function is

$$\{\alpha^*(t+\tau)\alpha(t)\}_{\mathrm{cl}} = |\alpha_0|^2 \left\{e^{i(\phi(t+\tau)-\phi(t))}\right\}_{\mathrm{cl}} = |\alpha_0|^2 \sum_m \frac{i^m}{m!} \left\{\left(\int_t^\tau dt'\dot\phi(t')\right)^m\right\}_{\mathrm{cl}}. \tag{2.74}$$

Since $\{\dot\phi\}_{\mathrm{cl}} = 0$, odd terms of the sum vanish. Using Isserlis' theorem [2.19], we can expand the correlation function of a product consisting of $2m$ terms into $(2m-1)!!$ two-point correlations. All remaining two-point correlations are equal, so we find

$$\left\{e^{i(\phi(t+\tau)-\phi(t))}\right\}_{\mathrm{cl}} = \sum_m \frac{(-1)^m}{m!2^m} \left(\int_t^{t+\tau} dt' \int_t^{t+\tau} dt'' \left\{\dot\phi(t')\dot\phi(t'')\right\}_{\mathrm{cl}}\right)^m = e^{-\Gamma\tau}. \tag{2.75}$$

In the last step, we used the white-noise correlation from Eq. (2.73). Substituting this result back into the amplitude correlation function, Eq. (2.74), we see that the fluctuating phase determined by its white-noise derivative perfectly models the finite linewidth of the laser,

$$\{\alpha^*(t+\tau)\alpha(t)\}_{\mathrm{cl}} = |\alpha_0|^2 e^{-\Gamma\tau}. \tag{2.76}$$

The effect of such a fluctuating phase on the oscillation of the field is shown in Fig. 2.5(c).

The laser imprints its noise on a quantum emitter it drives. As such, the laser noise processes can be mapped to emitter decoherence. More precisely, for a single emitter, the amplitude noise is described by a Liouville operator in standard Lindblad form with the damping operator σ_x and the rate Γ_a. Similarly, phase noise occurs with the damping operator σ_z at a rate Γ. These decoherence processes are also known as parallel and transverse noise, respectively. For more details on how this mapping is performed we refer to Sec. 4.7.

If the addressed ensemble of emitters is dense then all of the emitters experience the same amplitude and phase fluctuations, respectively. The noise processes derived here can then be described as collective noise of the quantum emitters. This is shown in chapter 4, where an effective model is derived and possible ways of making an ensemble insensitive to these noise processes are explored.

2.6 Numerical methods

Let us now, in the final part of this chapter, discuss some methodological aspects. Specifically, as the dynamics is nonlinear analytical solutions of quantum Langevin or master equations are often difficult to find, even in approximate regimes. Therefore, one has to resort to numerical solution methods. In general, we are interested in the dynamical behavior of a system, i.e. its time evolution, and the averages of observables. Since all average values can be obtained from a state vector or density matrix, the most practical approach is to work in the Schrödinger picture. Therefore, we aim to solve the master equation. Choosing an appropriate basis of the Hilbert space, we can work with the direct matrix representations of the operators. The numerical task at hand is then the solution of a system of first order ordinary differential equations.

As long as the considered quantum system obeys a master equation in standard Lindblad form, we simply have to implement the proper Hamiltonian and Liouvillian operators in order to solve for the dynamics. Additionally, the building blocks one uses (e.g. an optical cavity, two-level systems, etc.) often remain the same. Since composite systems are described by the product basis of the respective subspace bases, it makes sense, and is immensely useful, to predefine these fundamental building blocks as well as the algorithm which solves the master equation given the correct operators. This allows for comparably simple programs and is helpful in avoiding erroneous numerical calculations.

Toolboxes, which contain the according predefinitions, have a bit of a history. The first one that was widely successful was written in MATLAB [2.20]. A discussion of this toolbox and some of its successors [2.21, 2.22] can be found in the introduction of chapter 8. There, we also present a modernized version of such a toolbox, written in the Julia language [2.23, 2.24], which was developed further during the research conducted in the scope of this thesis.

It can be used to implement and simulate standard configurations in just a few lines of code. Consider, for example, the field scattered by a single quantum emitter placed inside an optical cavity, as shown in Fig. 2.4. While previously we provided an analytical treatment by assuming a weak drive and a bad cavity, using QuantumOptics.jl it is straightforward to numerically simulate the full system. This is shown in code sample 2.1, where we compute the steady state of the system without any approximations besides choosing a finite cutoff in the cavity photon number and the RWA. One can then use the input-output relation [Eq. (2.52)] to compute the scattered field amplitude. More examples such as code sample 2.1 are shown in chapter 8.

```julia
"""
Version info:
* Julia v1.1.0
* QuantumOptics.jl v0.6.5
"""

using QuantumOptics

# Parameters
Nc = 4
κ = 1.0
η = 0.01
γ = 0.1
g = 0.05
Δ = range(-3,stop=3,length=301)

# Hilbert space and operators
bf = FockBasis(Nc)
be = SpinBasis(1//2)
a = destroy(bf) ⊗ one(be)
σ = one(bf) ⊗ sigmam(be)

# Hamiltonian and damping operators
H0 = -dagger(a)*a - dagger(σ)*σ # ∝ Δ
H_int = g*(dagger(a)*σ + dagger(σ)*a)
H_p = 1.0im*η*(a - dagger(a))
J = [a, σ]

# Calculate β≡⟨σ⟩ for each Δ
β = []
for Δ1=Δ
    H = Δ1*H0 + H_int + H_p
    t, ρ = steadystate.master(H, J; rates=[2κ, γ], tol=1e-5)
    push!(β, expect(σ, ρ[end]))
end

# Calculate s from input-output relation
s = sqrt(κ*γ)/η .* β
```

Code sample 2.1: *Calculating the steady-state scattered field of a single quantum emitter inside a driven cavity. This bit of code produces the data behind the plots shown in Fig. 2.4.*

The main limitation of any numerical investigation of quantum physical models is the dimension of the Hilbert space under consideration. Consider, for example, our ensemble of N two-level quantum emitters. The corresponding number of possible states which span the Hilbert space is 2^N. Therefore, the matrices representing the emitter operators on this Hilbert space have 4^N complex elements. Obviously, this number becomes huge for even moderate numbers of emitters and the matrices are subsequently difficult to store due to the finite amount of memory available. Toolboxes such as the one presented in chapter 8 are therefore well suited to treat systems of sufficiently small size.

Another useful approach to treat Hilbert spaces of higher dimensions is the so-called Monte-Carlo wave function (MCWF) method [2.25, 2.26]. There, a time evolution according to a Schrödinger equation with a non-Hermitian Hamiltonian is performed. This results in a state described by a vector, whose norm decreases over time. With the decreasing norm, the probability that a quantum jump occurs increases. Once a quantum jump is performed, the state is renormalized. This leads to a stochastic wave function trajectory of the time evolution. Averaging over many such trajectories results in the same density operator as one obtains from a master equation. The big advantage here is that the state is at all times given by a vector. In the case of our quantum emitter ensemble, this would reduce the memory needed to store a state to 2^N. Even though this is a substantial reduction of the problem size, the memory remains the limiting factor here.

Another thing that one can exploit is the fact that strong quantum correlations (entanglement) are very fragile when incoherent processes are present. These processes can never be fully avoided in open quantum systems and coupling to the environment is always finite in reality. It can therefore be practical to truncate the Hilbert space to states with small quantum correlations between the subsystems. To lowest order, this is generally known as mean-field approach. It is often convenient to perform the truncation of the state space in the Heisenberg picture, i.e. by finding the correct QLEs for operators and expanding products of operators to low orders of quantum correlations. The resulting equations for the averages of (higher order) products or single operators can then be solved numerically or sometimes even analytically. This method is thoroughly discussed and used in chapter 6.

3 Publication

Scientific Reports **5**, 16231 (2015)

Selective protected state preparation of coupled dissipative quantum emitters[†]

D. Plankensteiner[1], L. Ostermann[1], H. Ritsch[1] and C. Genes[1]

[1]*Institut für Theoretische Physik, Universität Innsbruck,*
Technikerstraße 21a, A-6020 Innsbruck, Austria

Inherent binary or collective interactions in ensembles of quantum emitters induce a spread in the energy and lifetime of their eigenstates. While this typically causes fast decay and dephasing, in many cases certain special entangled collective states with minimal decay can be found, which possess ideal properties for spectroscopy, precision measurements or information storage. We show that for a specific choice of laser frequency, power and geometry or a suitable configuration of control fields one can efficiently prepare these states. We demonstrate this by studying preparation schemes for strongly subradiant entangled states of a chain of dipole-dipole coupled emitters. The prepared state fidelity and its entanglement depth is further improved via spatial excitation phase engineering or tailored magnetic fields.

doi: 10.1038/srep16231

[†] The author of this thesis performed most analytical and numerical computations presented in this work. L. Ostermann provided support and helpful discussions, specifically with the calculation concerning the depth of entanglement.

3.1 Introduction

Ensembles of effective two-level quantum emitters consisting of single atoms, ions, or defects in solids are employed ubiquitously in quantum optics and quantum information [3.1]. They are the basis for precision spectroscopy or atomic clock setups, as well as for experiments testing fundamental concepts of quantum physics or implementations of the strong coupling cavity QED (quantum electrodynamics) regime [3.2, 3.3]. In the absence of direct particle-particle interactions, larger ensembles allow for faster, more precise measurements [3.4] via a scaling of the effective single photon to matter coupling strength g by a factor $\sqrt{N}$ (with system size N) and a reduction of the quantum projection noise (by $1/\sqrt{N}$) [3.5, 3.6].

For any precise measurement one has to externally prepare, control and measure the particle dynamics. Hence, the emitters are almost unavoidably coupled to their environment. A suitable theoretical framework to model such experiments is open system dynamics with a coupling to a fluctuating thermal bath. At optical frequencies this can often be approximated by the zero effective temperature electromagnetic vacuum field [3.7, 3.8]. Still, extra perturbations by a thermal environment and background gas collisions cannot be avoided.

In a laboratory experiment the particles need to be confined in a finite spatial volume that can be addressed by laser beams. Thus, increasing particle numbers will lead to higher densities, where direct particle-particle interactions as well as environmentally induced collective decoherence can no longer be neglected. For optical transition frequencies a critical density is conventionally assumed at the point where the average particle separation is of the order of an optical wavelength [3.9]. Above this limit vacuum fluctuations tend to become uncorrelated and decay becomes independent. However, recent calculations have shown that collective states can exhibit superradiance and subradiance even at much larger distances [3.10] as long as the bandwidth of the emission is small enough.

In many typical configurations and in optical lattices in particular, the particle-particle interaction is dominated by binary dipole-dipole couplings, with its real part inducing energy shifts and its imaginary part being responsible for collective decay [3.11, 3.12]. Generally, this interaction is associated with dephasing and decay. However, recently it has been found that under special conditions also the opposite can be the case and these interactions can lead to a synchronization [3.13] or even a blockade of the decay [3.14]. Oftentimes it is assumed that while such states exist, they cannot be prepared by lasers as they are strongly decoupled from the radiation fields. However, it was recently proposed that individual instead of overall addressing of the atoms can push the many particle system to evolve towards subspaces protected from decay or dephasing [3.15]. When applied to Ramsey spectroscopy such states have been shown to exhibit frequency sensitivities superior even to those obtained from non-interacting ensembles [3.16]. However, apart from special cases with an optimal lattice size and excitation angle, it is not so obvious how to implement such precise a control.

In this work we highlight the surprising fact that interaction induced level shifts can be used to aid in preparing such states. In many cases the magnitude of the shifts a

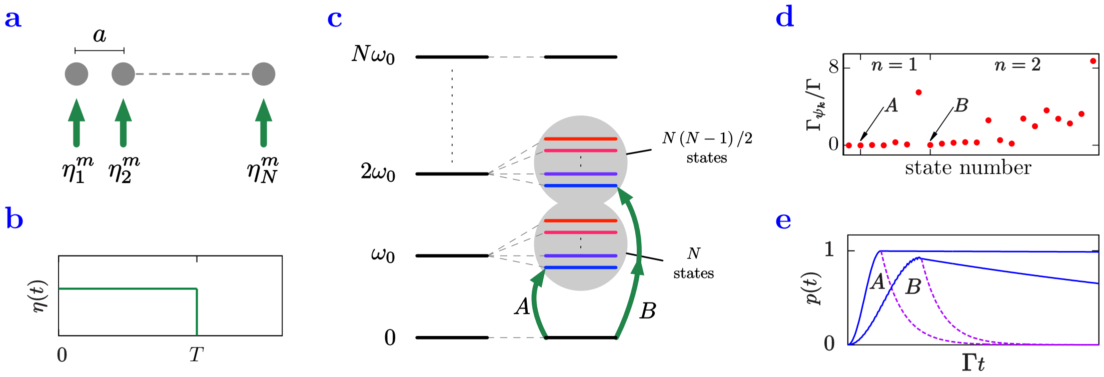

Figure 3.1: *Selective state preparation procedure.* a) A chain of N closely spaced quantum emitters (separation a with $ka \ll 1$, k being the laser wave number) are individually driven with a set of pumps $\{\eta_j^m\}$. b) The lasers are turned on for a time T, optimized such that an effective π-pulse into the desired subradiant target state is achieved. c) Level structure for the N systems where the C_n^N-fold degeneracy of a given n-excitation manifold is lifted by the dipole-dipole interactions. The target states are then reached by energy resolution (adjusting the laser frequency) and symmetry (choosing the proper m). d) Scaling of the decay rates of energetically ordered collective states starting from the ground state (state index 1) up to the single- and double-excitation manifolds for 6 particles at a distance of $a = 0.02\,\lambda_0$. The arrows identify the decay rates for the lowest energy states in the single (A) and double (B) excitation manifolds. e) Numerical results of the time evolution of the target state population for $N = 6$ and $a = 0.02\,\lambda_0$ during and after the excitation pulse. Near unity population is achieved for both example states A (where we used $\eta = 0.53\,\Gamma$) and B (for $\eta = 2.44\,\Gamma$) followed by a subradiant evolution after the pulse time T shown in contrast to the independent decay with a rate Γ (dashed line).

state experiences and its lifetime are tightly connected allowing one to identify and address interesting states via energy resolution. As a generic ensemble we particularize to a 1D regular chain of quantum emitters coupled by dipole-dipole interactions with a tunable magnitude (by varying the interparticle separation). Collective coupling to the vacuum leads to the occurrence of subradiant as well as superradiant excitonic states [3.10]. In particular, the subradiant states should prove extremely useful for quantum information as well as metrology applications as they exhibit robust, multipartite quantum correlations. As mentioned above, the atoms' interactions provide a first handle for target state selection as they lead to energy resolved collective states. Furthermore, using a narrow bandwidth laser excitation matched to the target states both in energy and symmetry allows for a selective population transfer from the ground state via an effective Rabi π-pulse.

In many cases, however, the required phase structure of the target state is not compatible with the excitation laser phase so that only a very weak coupling can be achieved. On the other hand, increasing the laser power reduces spectral selectivity by an unwanted addressing of off-resonant but strongly coupled states. Hence, to address a larger range of states of practical interest, we also propose and analytically study new methods of phase imprinting via a weak spatial magnetic field gradient. The small relative phase shifts increase the effective coupling to groups of emitters via a nonuniform phase distribution. With this method any state may acquire a finite laser coupling to the ground state via the magnetically induced level shifts resulting in an efficient population transfer with a minimal compromise on lifetime.

The considered setup is a chain (see Fig. 3.1a) of N identical two-level systems (TLS) with levels $|g\rangle$ and $|e\rangle$ separated by a frequency of ω_0 (transition wavelength λ_0) in a geometry defined by the position vectors $\{\mathbf{r}_i\}$ for $i = 1, ...N$. For each i, operations on the corresponding two-dimensional Hilbert space are written in terms of the Pauli matrices $\sigma_i^{x,y,z}$ and raising/lowering operators $\sigma_i^{\pm}$ connected via $\sigma_i^x = \sigma_i^+ + \sigma_i^-$, $\sigma_i^y = -i(\sigma_i^+ - \sigma_i^-)$ and $\sigma_i^z = \sigma_i^+\sigma_i^- - \sigma_i^-\sigma_i^+$. The complete Hamiltonian describing the coherent dynamics is

$$H = H_0 + H_{dip} = \omega_0 \sum_i \sigma_i^+ \sigma_i^- + \sum_{i \neq j} \Omega_{ij} \sigma_i^+ \sigma_j^- , \tag{3.1}$$

where H_0 is the free Hamiltonian and has degenerate energy levels (degeneracy $C_n^N = N!/(N-n)!n!$ for level n) ranging from 0 for the ground state to $N\omega_0$ for the highest excited state. The second term H_{dip} describes interactions between pairs of TLS which can be induced either by an engineered bath (such as a common, fast evolving optical cavity field) or by the inherent electromagnetic vacuum. We denote the couplings between emitters i and j by Ω_{ij} and particularize to the case of a free-space one dimensional equidistant chain of TLS with small interparticle distances a such that $a \ll \lambda_0$ (as depicted in Fig. 3.1a).

For the sake of simplicity, we use dipole moments perpendicular to the chain for all numerical computations. To a good approximation, in the limit of $k_0 a \ll 1$, the nearest-neighbor (NN) assumption can be used (such that $\Omega_{ij} = \Omega\delta_{ij\pm1}$) and exact solutions in the single-excitation manifold can be found [3.17]. Within this subspace and approximation, the Hamiltonian assumes the form of a tridiagonal symmetric Toeplitz matrix with ω_0 on the diagonal and Ω above and below the diagonal. The solutions are readily available [3.18] with eigenvalues $\omega_0 + \epsilon_m$ for an index m running from 1 to N, where $\epsilon_m = 2\Omega \cos[\pi m/(N+1)]$ are the dipole-induced energy shifts. The corresponding eigenstates of the Hamiltonian are then

$$|m\rangle = \sum_j f_j^m \sigma_j^+ |G\rangle , \text{ with } f_j^m = \sqrt{\frac{2}{N+1}} \sin\left(\frac{\pi m j}{N+1}\right), \tag{3.2}$$

where we used $|G\rangle = |g\rangle^{\otimes N}$.

Spontaneous decay via a coupling to the free radiation modes in the evolution of the system can be included in a generalized Lindblad form [3.8],

$$\mathcal{L}[\rho] = \frac{1}{2} \sum_{i,j} \gamma_{ij} \left(2\sigma_i^- \rho\, \sigma_j^+ - \sigma_i^+ \sigma_j^- \rho - \rho\, \sigma_i^+ \sigma_j^- \right), \tag{3.3}$$

where the γ_{ij} denote collective damping rates arising from the coupling to a common radiation field. These rates also strongly depend on the atomic distances a with two prominent limiting cases of $\gamma_{ij}(a \to \infty) = \Gamma\delta_{ij}$ (independent emitters limit) and $\gamma_{ij}(a \to 0) = \Gamma$ (the Dicke limit [3.19]). In general, one can perform a transformation of the Liouvillian into a new basis by diagonalizing the γ_{ij} matrix. This procedure leads to a decomposition into N independent decay channels with both superradiant ($> \Gamma$) and subradiant (robust) decay rates ($< \Gamma$) [3.16]. Note, however, that the states corresponding to these channels generally do not coincide with energy eigenstates of the Hamiltonian, so that we cannot reduce the system dynamics to simple rate equations.

3.2 Results

3.2.1 Selective state preparation

Tailored coherent excitation. As mentioned above, our dipole coupled systems possess states with a large range of radiative lifetimes and energy shifts. Depending on the desired application particular states can be highly preferable over others. In a first straightforward approach we now illustrate that in principle it is possible to access a desired collective state simply by a selective coherent driving with a properly chosen amplitude and phase for each TLS. This is described by the Hamiltonian

$$H_m = \sum_j \eta_j^m (\sigma_j^+ e^{-i\omega_l t} + \sigma_j^- e^{i\omega_l t}), \tag{3.4}$$

with a suitably chosen set of η_j^m. For a targeted eigenstate in the single-excitation manifold, some analytical insight on how to choose these amplitudes can be gathered from the state's symmetry. For energy eigenstates this can be found quite reliably within the NN approximation [3.20]. In an equidistant finite chain our calculation suggests the following choice of driving fields at laser frequency ω_l,

$$\eta_j^m = \eta \sin\left(\frac{\pi m j}{N+1}\right), \tag{3.5}$$

chosen to fit the symmetry of a target state $|m\rangle$.

The selectivity of the excitation process can be further improved by an *energetically resolved excitation* of a given state $|m\rangle$ by a proper choice of the laser frequency $\omega_l = \omega_0 + \epsilon_m$ and its bandwidth. This is possible due to the interaction induced level splitting from H_{dip} (as depicted in Fig. 3.1c). Indeed, in perturbation theory and in a frame rotating at ω_l the evolution of the system starting from the ground state up to a normalization factor leads to

$$e^{-iH_m t} |G\rangle \simeq |G\rangle - i\eta t |m\rangle . \tag{3.6}$$

The success of the corresponding process is illustrated in the sequence of plots in Fig. 3.1, where the $|m = N\rangle$ state with $n = 1$ is considered (target state A) and accessed via the combination η_j^N of pumps lasting for a duration T.

Numerical simulations were performed on a six-atom chain with driving strength $\eta = 0.53\,\Gamma$ at an interatomic separation of $a = 0.02\,\lambda_0$. The time for which the pumps are switched on is $T = 1.58\,\Gamma^{-1}$ which is considerably shorter than the time scale governed by the decay rate of $0.0009\,\Gamma$ of the target state. The resulting dynamic is an effective π-pulse (efficiency of 99.94%) flipping the population into the state $|m = N\rangle$ followed by an extremely slow decay, indicating the robustness of the target state (as seen in curve A of Fig. 3.1e).

It is, of course, desirable to target higher excitation manifolds as well. In the absence of analytical expressions or good approximations for the target states, we employ phases that yield maximal asymmetry, i.e. $\bar{\eta}_j = \eta(-1)^j$ for any $j = 1, ..., N$. Such a driving can be expected to address collective states, where the fields emitted by any two neighboring particles interfere destructively [3.14] (similar to a previously investigated mechanism [3.15]). Numerical simulations show that the resulting collective states indeed exhibit the lowest energy shifts of the targeted manifold and can be expected to be long lived. The resonance condition for a specific state $|\psi\rangle$ within the manifold n is $n\omega_l = n\omega_0 + \delta\omega_\psi$, where $\delta\omega_\psi = \langle\psi| H_{dip} |\psi\rangle$. As an illustration, the curve B in Fig. 3.1e shows an almost perfect efficiency (98.36%) two-photon π-pulse allowing for a population transfer to the longest-lived collective state in the second excitation manifold of $N = 6$ emitters separated by $a = 0.02\,\lambda_0$. The chain was driven with a strength of $\eta = 2.44\,\Gamma$ for a time $T = 3.44\,\Gamma^{-1}$, which again is significantly shorter than the natural time scale given by the target state decay rate of $0.0402\,\Gamma$.

Let us add a comment on the practical implementation of such an addressing. In typical current experimental configurations for clocks based on 1D magic wavelength lattices [3.21, 3.22] the atoms are very close and hardly allow for an individual direct particle addressing. One is largely limited by a quasi plane wave driving, which typically addresses all particles with equal intensity. If the pump light is applied perpendicularly to the trap, the evolution is governed by a symmetric Hamiltonian H_{sym}, obtained from equation (3.4) with an equal pump amplitude $\eta_j^m = \eta$ for any m and j. A laser excitation from the ground state into the state $|m\rangle$ is connected to the coupling amplitude $\chi_m = \langle m| H_{sym} |G\rangle = \eta \sum_i f_i^m$, which yields

$$\chi_m = \begin{cases} 0 & \text{if } m \text{ is even,} \\ \frac{\sqrt{2}\eta}{\sqrt{N+1}} \cot\left(\frac{m\pi}{2N+2}\right) & \text{if } m \text{ is odd.} \end{cases} \tag{3.7}$$

We will refer to states with even m as *dark states* as they cannot be accessed by the laser excitation and call the remaining ones *bright states* [3.14]. In the limit of large atom numbers $N \gg 1$, it is of interest to investigate the two cases, where $m \ll N$ and $m \sim N$, for states at the top/bottom of the manifold. In the first case, the function for the driving yields $\chi_m \approx \eta\sqrt{8N}/m\pi$, whereas in the other case we have $\chi_m \approx 0$.

Note, that sometimes geometry can change this behavior. For a 1D string of equidistant emitters illumination at a chosen angle of incidence and polarization leads to a designable phase gradient of the excitation amplitudes. The situation becomes even more complex for a 3D cubic lattice, where the phases also differ in the different lattice planes. As a lucky coincidence, a perpendicular plane illumination at the clock frequency in a magic lattice for Strontium (Sr) targets an almost dark state. This leads to subradiance and in principle allows for a spectral resolution better than the natural linewidth [3.23]. In not so favorable cases one could also think of a specific lattice design to facilitate a tailored dark state excitation.

Radiative properties. In order to be useful resources for quantum information applications, target states should exhibit *robustness* with respect to the environmental decoherence. To identify states of minimum decay rate, we scan through the eigenstates $|\psi_k\rangle$ of the Hamiltonian $H = H_0 + H_{dip}$ (for $k = 1, ..., 2^N$) and compute their decay rates Γ_{ψ_k} (see section Methods below). We find that generally, for a given manifold, the energetic ranking of the states closely indicates their robustness to decay (as illustrated by the color-coding in Fig. 3.1c) ranging from blue for subradiant states to red for superradiant states. This is due to the fact that both radiation and energetic shifts are strongly dependent on the symmetry of the states. In Fig. 3.1d, for $N = 6$, we plot the decay rates of the collective states in the first ($n = 1$) and second ($n = 2$) excitation manifold arranged as a function of their increasing energy corresponding to the level structure of Fig. 3.1c. Superradiant states are found at the upper sides of the manifolds while the ideal robust states lie at the bottom. In Fig. 3.1d, the arrows indicate the optimal decay rates in the single- ($0.0009\,\Gamma$) and double-excitation manifolds ($0.0402\,\Gamma$) corresponding to target states A and B whose population evolution is depicted in Fig. 3.1e.

Within the single-excitation manifold, an analytical expression for the decay rate of a state $|m\rangle$ can be found as $\Gamma_m = \sum_{i,j} \gamma_{ij} f_i^m f_j^m$. For small distances the state $m = 1$ (upper state) is superradiant, whereas states at the bottom of the manifold $m \sim N$ exhibit subradiant properties. In the Dicke limit where $a = 0$ we have $\gamma_{ij} = \Gamma$ for any i and j, and we can compute $\Gamma_m = 2\Gamma \cot^2 [m\pi/(2N+2)]/(N+1)$ for m odd and $\Gamma_m = 0$ for m even. Note, that in this particular limit, these are the same conditions as for the darkness and brightness of a state. For large numbers of emitters, we recover the expected superradiant scaling with N for the state with $m = 1$, i.e. $\Gamma_1 \approx 8\Gamma N/\pi^2$. On the other hand, large m yield a decay rate of $\Gamma_m \approx 0$ (perfect subradiance) in the same limit.

There are two important conclusions from these results: i) since in the considered limit the decay rate of the superradiant state $|m = 1\rangle$ scales with $\Gamma_1 \propto N$, whereas its driving is $\chi_1 \propto \sqrt{N}$, driving this state becomes more difficult with increasing atom number due to the reduced time-scale and ii) if the number of atoms is not too large, χ_m will remain finite, while Γ_m already indicates vast subradiance due to its scaling-down with N. Hence, there are robust states that remain bright, i.e. they can be driven directly even though the driving is not matched to their symmetry.

3.2.2 Accessing dark states via magnetic field gradients

The direct symmetric driving with H_{sym} allows access to bright states only. Given that nearby dark states can conceivably be more robust, we now employ a progressive level shifting mechanism that allows for a coupling between bright and dark states.

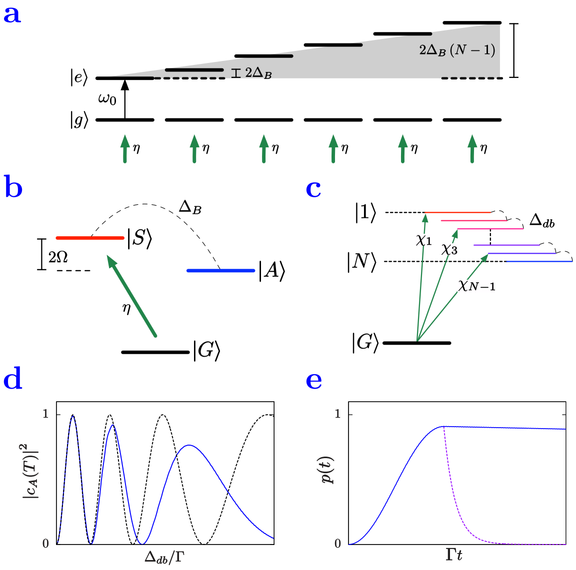

Figure 3.2: *Coupling to dark states via a magnetic field gradient.* a) Linearly increasing level shifts along the chain occuring in the presence of the magnetic field gradient. b) Illustration of the level structure and indirect dark state access for two coupled emitters. While symmetry selects the state $|S\rangle$, off-resonant addressing combined with bright-dark state coupling of strength Δ_B allows for a near-unity population transfer into the state $|A\rangle$. c) Dynamics in the single-excitation manifold of N coupled emitters where symmetric driving reaches the bright states with amplitudes χ_m while the magnetic field couples neighboring dark and bright states. d) Plot of the asymmetric state population for the two-atom case as a function of the increasing magnetic field (solid line) compared to the steady-state approximation (dashed line) at numerically optimized time $T = 16.19\,\Gamma^{-1}$, with parameters $\eta = \Gamma$ and $a = 0.05\,\lambda_0$. e) For a chain of $N = 4$ emitters, a 91%-efficient π-pulse to the most robust state can be achieved as demonstrated in the population evolution plot. The separation is chosen to be $a = 0.025\,\lambda_0$, while $\eta = 40\,\Gamma$ and numerical optimization is employed to find $\Delta_B = 0.98\,\Gamma$.

This is achieved by subjecting the ensemble to a magnetic field with a positive spatial gradient along the chain's direction. The increasing energy shift of the upper atomic levels (as depicted in Fig. 3.2a) plays a role similar to the individual phase imprinting mechanism described previously. For each particle the shift of the excited level induces a time-dependent phase proportional to the value of the magnetic field at its position. We demonstrate the mechanism for a particular two-atom example, where indirect near unity access to the dark subradiant asymmetric collective state is proven and extend it to the single-excitation manifold of N atoms.

Two-atom case. The eigenstates of the Hamiltonian $H_0 + H_{dip}$ are $|E\rangle = |ee\rangle$, $|G\rangle = |gg\rangle$ and in the single-excitation subspace $|S\rangle = (|eg\rangle + |ge\rangle)/\sqrt{2}$ and $|A\rangle = (|eg\rangle - |ge\rangle)/\sqrt{2}$. The symmetric state $|S\rangle$ is superradiant ($\Gamma_S = \Gamma_1 = \Gamma + \gamma_{12}$) and bright, directly accessible via symmetric driving with strength $\chi_1 = \sqrt{2}\eta$. The asymmetric state $|A\rangle$, on the other hand, is subradiant ($\Gamma_A = \Gamma_2 = \Gamma - \gamma_{12}$) and dark. Indirect access can be achieved by shifting the second atom's excited state by $2\Delta_B$ (see schematics in Fig. 3.2b), where Δ_B is tunable and quantifies the per-emitter shift for a given magnetic field amplitude. We first analyze the dynamics in the absence of decay by solving the time-dependent Schrödinger equation governed by the Hamiltonian $H = H_0 + H_{dip} + H_{sym} + H_B$, where $H_B = 2\Delta_B \sigma_2^+ \sigma_2^-$. We reduce the dynamics to three states, and assume a quasi-resonant Raman-like scheme where the population of $|E\rangle$ is at all times negligible. An effective two-level system arises (between the ground state and the asymmetric state; see section Methods below) and the resonance condition can be identified as

$$\Delta^{(2)} = -\Delta_B + \sqrt{\Delta_B^2 + \Omega^2 - 2\eta^2}, \tag{3.8}$$

with an effective Rabi frequency of

$$\nu_R^{(2)} = \frac{\sqrt{2}\eta\Delta_B}{\Omega + \sqrt{\Delta_B^2 + \Omega^2 - 2\eta^2}}. \tag{3.9}$$

To fulfill $|c_S|^2 \ll 1$, we need to restrict the driving to a parameter regime where $\eta, \Delta_B \ll \Omega$. A scan over the magnetic field is performed and the exact numerical results for the asymmetric state population are plotted in Fig. 3.2d against the adiabatic solution showing near unity population transfer for an optimized Δ_B. Further restrictions are imposed when decay is considered. These stem from the fact that the coherent process described by ν_R should be faster than the incoherent one characterized by Γ_A. For close particles, the ability to tune the distance ensures that the scaling down of Γ_A is very fast and the above conditions are readily fulfilled. For the particular example illustrated in Fig. 3.2d we chose $a = 0.05\,\lambda_0$, resulting in $\Omega = 23.08\,\Gamma$, $\Gamma_A = 0.019\,\Gamma$. The 0.994 population is reached at $T = 16.19\,\Gamma^{-1}$, which is very close to the theoretical estimate of $T = \pi/2\nu_R^{(2)} = 16.179\,\Gamma^{-1}$ obtained from the adiabatic solution under the assumption of a π-pulse transferring the population to the target state.

Many-atom case. For a chain of N atoms, we consider the progressive shifting of excited levels along the chain depicted in Fig. 3.2a. This is realized by the application of a magnetic field with a constant gradient and is described by the Hamiltonian $H_B = 2\Delta_B \sum_i (i-1)\sigma_i^+\sigma_i^-$. Let us consider a dark state $|d\rangle$ (d even) and the bright state $|b = d-1\rangle$ immediately above. Their coupling via H_B is quantified by $\Delta_{db} = 2\Delta_B \sum_i (i-1) f_i^d f_i^b$, as shown in Fig. 3.2c.

We develop a protocol where direct off-resonant driving into the bright state (amplitude χ_b) combined with a coupling between the bright and dark states via the magnetic field leads to an almost unity population transfer into the dark state. Given a sufficient energy separation, the problem can be reduced to solving the time-dependent Schrödinger equation for the three coupled state amplitudes c_b, c_d and c_G. Following the same adiabatic approximation as in the two-atom case we reduce the general dynamics to an effective two-level system between the states meant to be connected by an effective

π-pulse, i.e. $|d\rangle$ and $|G\rangle$. The generalized resonance condition (with $\epsilon_{db} = \epsilon_d - \epsilon_b$) reads

$$\Delta^{(N)} = -\Delta_B(N-1) - \frac{\epsilon_d + \epsilon_b}{2} + \sqrt{\frac{\epsilon_{db}^2}{4} + \Delta_{db}^2 - \chi_b^2}, \tag{3.10}$$

and was obtained in the limit where the coupling of the dark state to the other adjacent bright state $|d+1\rangle$ was neglected owing to the relation $\chi_{d-1} \gg \chi_{d+1}$. The effective transition rate between the ground state and the state $|d\rangle$ is

$$\nu_R^{(N)} = \frac{\chi_b |\Delta_{db}|}{\Delta + \epsilon_b + \Delta_B(N-1)}. \tag{3.11}$$

The addition of decay imposes a new constraint on the timescale of the process, i.e. $\nu_R^{(N)} \gg \Gamma_d$, required to ensure near unity population in the dark state. The fulfillment of this condition depends on the individual system under consideration. As an illustration of the procedure, Fig. 3.2e presents the targeting of a robust dark state in the single excitation manifold of four particles. Note, that the numerical results are performed in an exact regime beyond the NN approximation and are in excellent agreement with our conclusions obtained from the NN treatment.

3.3 Discussions

3.3.1 Entanglement properties

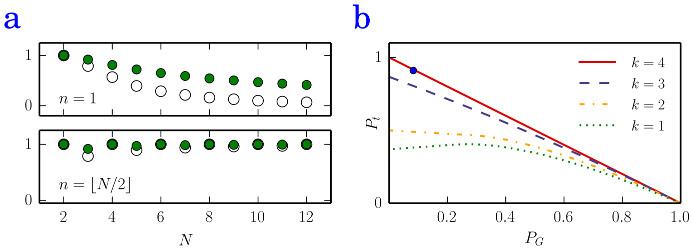

Figure 3.3: *Entanglement properties.* a) Comparison of the numerically computed von Neumann entropy (empty circles) of the reduced density matrix of the chain minimized over the atom index and the analytical expression for the entropy of the Dicke state (green circles), both for excitations $n = 1$ and $n = \lfloor N/2 \rfloor$ as a function of the atom number N at distance $a = 0.1\lambda_0$. b) Depth of entanglement of the subradiant four-atom state (blue dot) prepared by the magnetic field gradient scheme (see Fig. 3.2e). It clearly lies above the $k = 3$ boundary indicating four-atom entanglement. The k-atom entanglement boundaries of the target state population P_t as a function of the ground state population P_G have been computed for the corresponding target state of a four-atom chain at distance $a = 0.025\,\lambda_0$.

To justify the usefulness of collective states for quantum information purposes, we employ the von Neumann entropy to analyze their entanglement properties. More specifically, we compute the von Neumann entropy of the reduced density matrix ρ_s of a single two-level emitter (showing the degree of its bipartite entanglement with the rest of the system) defined by $S(\rho_s) = -\sum_i \lambda_i \log_2 \lambda_i$, where λ_i is the i-th eigenvalue of ρ_s and $0 \log_2 0 \equiv 0$. We furthermore minimize the set of values for all atoms to obtain a lower bound on the entanglement contained in the system. We compare the numerical results to the single-atom entropy of the symmetric Dicke state $|-N/2, -N/2 + n\rangle$ [3.19]. For these particular states the entropy is maximized if the number of excitations in the state is $n = N/2$. It follows that it is highly desirable to drive the system into robust states as close as possible to $n = \lfloor N/2 \rfloor$ excitations (where $\lfloor N/2 \rfloor$ is the largest integer smaller or equal to $N/2$), since this manifold contains the most entangled state. A comparison of the exact numerical data and the analytical expression for the entropy is shown in Fig. 3.3a.

Another way to characterize the entanglement of the prepared state is to investigate their *depth of entanglement* [3.24, 3.25], which does not quantify the entanglement itself but rather shows how many atoms of an ensemble are involved in the present entanglement. This measure has been used in recent experiments [3.25, 3.26] since it is a readily measurable quantity. The depth of entanglement is computed as follows: given an N-atom target state in which an arbitrary number of said N atoms is entangled, we compute the limit of how much population one can drive into this state such that the resulting density matrix ρ remains separable into a subset of density matrices that exhibit no more than k-atom entanglement ($1 \leq k \leq N$). This may be done by numerically maximizing the target state population P_t as a function of the ground state population P_G for different k. The boundaries themselves indicate how many atoms need to be entangled in order to prepare the pure target state, i.e. the boundary where the target state population is maximized to 1 corresponds to the number of atoms entangled in the (pure) target state. If a general prepared state has a target and ground state population such that the corresponding data point lies on or above the k-atom boundary, more than k atoms are entangled.

Obviously, for the pure target states considered in the above computation all atoms contribute to the entanglement, since otherwise the minimal von Neumann entropy as shown in Fig. 3.3a would be zero. For a more interesting result, we can compute the depth of entanglement in order to demonstrate the efficiency of the driving procedure using a magnetic field gradient as in Fig. 3.2e. From Fig. 3.3b, where all boundaries have been plotted for the considered subradiant four-atom state, it is clear that the prepared state shows all-atom entanglement as the corresponding data point lies far above the boundary for three-atom entanglement.

3.3.2 Implementation considerations

The proof-of-principle technique presented above has been particularized on a specific generic system of emitters in an equidistant chain. The choice is natural since the electromagnetic vacuum provides a simple example for both collective dispersive and dissipative dynamics. To exemplify a possible realization we consider a particular system [3.27] where bosonic Sr atoms are trapped in a magic wavelength optical lattice at separations of $a = 206.4$nm. The working transition is at $\lambda_0 = 2.6\mu$m, between the $^3P_0$ and $^3D_1$ electronic states. This amounts to a ratio of $a/\lambda_0 \approx 1/13$ which allows for an operation in the regime targeted by our scheme. The corresponding single atom decay rate is at the order of $\Gamma = 0.3$ MHz and circularly polarized light can allow for transitions between states with a difference of 1 in magnetic quantum number. We have numerically investigated a system of 4 atoms in such a configuration and found a sizeable 73% target state population for $\eta = 2\,\Gamma$ and $\Delta_B = 0.5\,\Gamma$, under the conditions of a relatively small level shift between the dark and bright state around $6\,\Gamma$ which does not allow for large driving powers. For further optimization of the efficiency of the target state preparation one could envision a modified setup where a trapping transition of smaller wavelength can be chosen that would most importantly allow for better state separation (owing to larger dipole shifts). The corresponding magnetic field gradient required to produce the considerable $\Delta_B = 0.5\,\Gamma$ shift on a distance of $a = 206$ nm is around $5.2 \cdot 10^5$ G/m, not far from state-of-the-art values achievable in high magnetic field gradient magneto-optical trap experiments [3.28, 3.29]. Of course, there are many detrimental practical effects that can seriously limit the above technique such as light-assisted collision loss. We envision the extension of the described technique to systems where both the coherent and dissipative particle-particle interactions can be suitably tailored. For example, the same kind of dipole-dipole Hamiltonians can occur in 3D lattices of polar molecules [3.30] or between two different color NV centers in diamonds [3.31].

3.3.3 Conclusions

Direct particle interactions are typically detrimental and limiting in precision measurement applications. Here, we have presented some specific opposite examples, where the *collective* nature of the decoherence combined with the coherent binary dipole-dipole interactions is used as a new resource for the controlled and efficient preparation of specially selected states. The excitation scheme can be tailored to address target states exhibiting both entanglement as well as robustness against decay. As a generic example we studied the case of a one-dimensional system of tightly spaced equidistant quantum emitters. Already the inherent dipole-dipole coupling allows for a targeted state preparation technique via energy selection. The performance of the excitation can be enhanced additionally via the *continuous* application of a spatially increasing magnetic field. The general principle of such a phase imprinting technique is potentially applicable in many specific environments such as optical lattices or atoms and ions localized within one or more common optical cavity modes [3.32, 3.33], NV-centers or superconducting qubits coupled to CPW transmission lines or resonators [3.34, 3.35].

3.4 Methods

3.4.1 Decay rate of the states

In order to arrive at an analytical expression for the decay rate of an eigenstate $|\psi_k\rangle$ of the Hamiltonian in equation (3.1), we consider the homogeneous part of the differential equation of the corresponding density matrix element that arises from the master equation. The solution of this differential equation yields an exponential decay. The rate at which the state population decays may be written as

$$\Gamma_{\psi_k} = -\langle\psi_k| \mathcal{L}\left[|\psi_k\rangle\langle\psi_k|\right] |\psi_k\rangle = \sum_{i,j} \gamma_{ij} \langle\psi_k| \sigma_i^+ \sigma_j^- |\psi_k\rangle \,. \tag{3.12}$$

Note, that this is true only for states that contain one specific number of excitations, i.e. they are eigenstates of the operator $\sum_i \sigma_i^z$. Obviously, this is fulfilled for eigenstates of the considered Hamiltonian. Equation (3.12) was used in order to compute the rates depicted in Fig. 3.1d and throughout the manuscript. For example, we used it in order to compute the decay rate of the eigenstates in the NN approximation Γ_m.

3.4.2 Subradiance and disorder

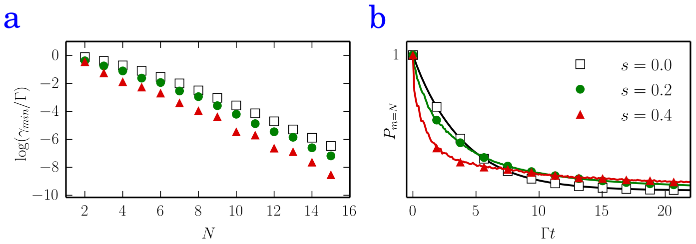

Figure 3.4: *Subradiance and disorder.* a) Plot of the logarithm of the minimal eigenvalue of the decay rate matrix (matrix with entries γ_{ij}) as a function of N at a distance of $a = 0.4\lambda_0$ for increasing levels of disorder ($s = 0, 0.2, 0.4$). b) Decay of the $|m = N\rangle$ state as a function of time. In the presence of disorder ($s = 0.2, 0.4$) the short time and long time behaviors are fundamentally different. At short times, disorder can push the state towards faster decaying channels while decay inhibition due to disorder occurs at larger times.

Let us consider the influence of positioning disorder on subradiant properties of the target states. To mimic disorder we perturb an equidistant chain of N emitters (average separation a) by introducing an uncertainty in each emitter position quantified by a defect parameter s (normal distribution of variance sa). We then write the randomized matrix of decay rates and find the minimum decay channel without as well as in the presence of disorder of $s = 20\%$ and $s = 40\%$. For the $s = 0\%$ case, it has been shown [3.16] that the minimum decay rate scales exponentially with N even for distances up to $0.4\lambda_0$, while the linear scaling with N typical for superradiance is reached for

$a \ll \lambda_0$ only. After averaging over 100 random configurations, we plot the logarithm of the minimal rates as a function of increasing N in Fig. 3.4a.

As a somewhat surprising result, subradiance scales even better with N as the disorder increases. This might be understood as a destructive interference effect brought on by the cancelation of emitted photons stemming from the random positioning. As pointed out in previous investigations [3.16], the states of low symmetry (as, for example, the $m = N$ state) possess decay rates closest to the analytically derived minimal rate. We analyze the respective sensitivity of the state subradiance to disorder by initializing the system of N emitters in the $m = N$ state and allow it to decay. The outcome is plotted in Fig. 3.4b and shows remarkable robustness of the disordered systems on a long time-scale. While on a short time-scale disorder pushes the considered state into faster decaying channels, the long time limit shows that the remaining population accumulates in the disorder-enhanced robust states.

For short time-scales, the state still decays slowly (subradiantly), however, the decay rate increases with growing disorder ($s = 40\%$). More remarkable, though, is the behavior the decaying states show for long time-scales, as the states subject to larger disorder become more robust than the unperturbed system. This is due to the fact that all population in the $m = N$ state that decays through more radiative channels have decayed at that point and only the most subradiant channel (minimal eigenvalue of the decay rate matrix) remains. As seen in Fig. 3.4a, this eigenvalue is even further reduced by disorder which explains the long time-scale behavior in Fig. 3.4b.

3.4.3 Coherent dynamics with a magnetic field gradient

Two-atom case. To find the expressions in equation (3.8) and equation (3.9) we solve three coupled differential equations neglecting the population of the fully inverted state $|E\rangle$ as far off-resonant for all times. In the collective basis, where any state may then be written as $|\psi\rangle = c_S\,|S\rangle + c_A\,|A\rangle + c_G\,|G\rangle$, the equations are

$$i\dot{c}_S = (\Delta + \Delta_B + \Omega)c_S - \Delta_B c_A + \sqrt{2}\eta c_G, \tag{3.13}$$

$$i\dot{c}_A = (\Delta + \Delta_B - \Omega)c_A - \Delta_B c_S, \tag{3.14}$$

$$i\dot{c}_G = \eta c_S, \tag{3.15}$$

where $\Omega = \Omega_{12}$ is the coherent interaction between the atoms and Δ is the detuning between the atomic resonance frequency and the driving laser. For an efficient driving of $|A\rangle$ the population of the state $|S\rangle$ needs to be negligible which allows us to set a steady-state condition, namely $\dot{c}_S = 0$ yielding the desired effective two-level system between $|G\rangle$ and $|A\rangle$.

Many-atom case. The same approach as in the two-atom case may be used to describe the dynamics in the single-excitation manifold for an arbitrary number of atoms in a chain. Given sufficient energy separation we may neglect all states but the ones we aim to address. We can indirectly address a dark state $|d\rangle$ by driving the bright state $|b\rangle$ immediately above, which is coupled to the dark state by a magnetic field gradient. Neglecting all populations but c_b, c_d, and c_G and their respective couplings via the magnetic field gradient, the investigation reduces to the equations

$$i\dot{c}_b = [\Delta + \epsilon_b + \Delta_B(N-1)]\, c_b + \Delta_{db} c_d + \chi_b c_G, \tag{3.16}$$

$$i\dot{c}_d = [\Delta + \epsilon_d + \Delta_B(N-1)]\, c_d + \Delta_{db} c_b, \tag{3.17}$$

$$i\dot{c}_G = \chi_b c_b. \tag{3.18}$$

For an efficient driving of the dark state we may again invoke a steady-state condition on the bright state population $\dot{c}_b = 0$. This, again, yields an effective two-level system between the ground and the dark state with resonance condition and Rabi frequency as displayed in equation (3.10) and equation (3.11), respectively.

3.4.4 Von Neumann entropy

For a Dicke state an analytical expression for the von Neumann entropy of the reduced density matrix can be obtained. First, note that, since Dicke states are invariant under a permutation of the atoms, all reduced density matrices are identical. Hence, they all share the same von Neumann entropy for a given number of excitations n. We may choose to reduce the full density operator ρ to the density matrix of the first atom in the ensemble, i.e. $\rho_s^1 \equiv \rho_s = \mathrm{tr}_{2,\ldots,N}(\rho)$ which yields a von Neumann entropy of

$$S(\rho_s) = \frac{n}{N}\log_2\left(\frac{N}{n}\right) - \left(1-\frac{n}{N}\right)\log_2\left(1-\frac{n}{N}\right). \tag{3.19}$$

For the actual eigenstates of the Hamiltonian in equation (3.1) this computation needs to be done numerically. Furthermore, these states are not invariant under permutation of atoms and hence it is required to minimize the entropy with respect to the atomic chain index in order to find the lower bound.

3.4.5 Depth of entanglement

The boundaries depicted in Fig. 3.3b were found by maximizing the target state population with the condition on the density matrix of the prepared state to contain no more than k-atom entanglement, i.e. $\rho = \bigotimes_i \rho_i^{k_i}$ with $k_i \leq k$ and at least one $k_i = k$. To compute the boundaries we generalized the algorithm that was previously used solely for the W-state [3.25] to arbitrary states in the single-excitation manifold. For the computation of all boundaries we need to distinguish the two cases where $P_G = 0$ and $P_G > 0$. Considering a separable state ($k = 1$), the boundary for $P_G > 0$ is found to be

$$\max(P_t) = P_G \max_{\prod_i \alpha_i = \sqrt{P_G}} \left| \sum_i |c_i| \frac{\sqrt{1-\alpha_i^2}}{\alpha_i} \right|^2, \tag{3.20}$$

where $\alpha_i \in [0,1]$ and c_i are the coefficients of the target state. For $P_G = 0$ the maximization is much simpler, i.e. $\max(P_t) = \max |c_i|^2$, which is found by setting one $\alpha_i = 0$ and the remaining coefficients $\alpha_{j\neq i} = 1$. Note, that for both these and all following computations we neglect the symmetry of the state, i.e. the phases of the coefficients c_i by using $|c_i|$. This is valid due to the invariance of entanglement under local unitary operations and necessary if we restrict the coefficients α_i in the way we did.

For multiple-atom entanglement ($k > 1$) the matter of finding the corresponding boundary is no longer so simple. In order to find the maximum population, we assume maximally allowed entanglement in the prepared state. We split the prepared state into $M = \lceil N/k \rceil$ sets, where $M - 1$ sets are k-atom entangled and the remaining one is $k' = N - k(M-1)$-atom entangled. To find the maximum, one has to consider all possible positions of the k'-entangled state. If, for example, the k'-entangled state is at the last position, the population of the target state $|t\rangle$ in the prepared state reads

$$P_t = \left| \langle t| \left[\left(\bigotimes_{i=1}^{M-1} |\varphi_i^k\rangle \right) \otimes |\varphi_M^{k'}\rangle \right] \right|^2 , \tag{3.21}$$

where

$$|\varphi_i^k\rangle = \alpha_i \, |G_k\rangle + \sqrt{1-\alpha_i^2} \sum_{r=1}^{k} \lambda_r^i \sigma_r^+ \, |G_k\rangle \tag{3.22}$$

is a general non-separable state of k atoms in the single-excitation manifold. The state $|G_k\rangle$ is the k-atom ground state and the coefficients $\lambda_r^i \in [0,1]$ have to be normalized, i.e. $\sum_r (\lambda_r^i)^2 = 1 \; \forall \; i$. One then has to maximize the target state population with respect to the coefficients $\alpha_i \in [0,1]$ and λ_r^i with the condition $\prod_j \alpha_j = \sqrt{P_G}$. The number of these coefficients, however, grows vastly with the number of atoms, hence numerical computations are limited. For $P_G = 0$ one can again choose one $\alpha_i = 0$ and all $\alpha_{j \neq i} = 1$.

Note, that all boundaries computed via this maximization only hold for pure states. In order to find the boundaries for mixed states we need to compute the convex hulls of the respective boundaries [3.25]. The $k = N$ boundary is found when a perfect superposition between the ground and target state is reached.

In this work we considered the specific case of an exciton state of a four-atom chain. In that case, when investigating two-atom entanglement the permutation of the k'-entangled state is rendered unnecessary since $k' = k = 2$. Unfortunately, this is no longer true for $k = 3$, where we did have to account for all permutations.

We acknowledge financial support from the SFB through the FoQus project (D. P.), DARPA through the QUASAR project (L. O. and H. R.) and from the Austrian Science Fund (FWF) via project P24968-N27 (C. G.). Furthermore, we acknowledge the use of the QuTip open-source software [3.36]. H.R. thanks Vladan Vuletic for helpful discussions. C. G. thanks M. W. Mitchell for the suggestion of energetic addressing of collective states.

Author contributions statement

C. G. conceived the ideas and supervised the work. D. P. developed the concepts, conducted analytical calculations, took the main role in writing the manuscript and wrote numerical simulations, with support from L. O. especially in generalizing the depth of entanglement. H. R. provided guidance and expertise. The manuscript has been reviewed and edited by all authors.

Additional information

No competing financial interests arise in the funding of this work.

4 Publication

Journal of Physics B: Atomic, Molecular and Optical Physics **49**, 245501 (2016)

Laser noise imposed limitations of ensemble quantum metrology[†]

D. Plankensteiner[1], J. Schachenmayer[2], H. Ritsch[1] and C. Genes[1,3]

[1] *Institut für Theoretische Physik, Universität Innsbruck,*
Technikerstraße 21a, A-6020 Innsbruck, Austria
[2] *JILA, NIST, Department of Physics, University of Colorado,*
440 UCB, Boulder, CO 80309, USA
[3] *Vienna Center for Quantum Science and Technology,*
TU Wien-Atominstitut, Stadionallee 2, 1020 Vienna, Austria

Laser noise is a decisive limiting factor in high precision spectroscopy of narrow lines using atomic ensembles. In an idealized Doppler and differential light shift free magic wavelength lattice configuration, it remains as one distinct principal limitation beyond collective atomic decay. In this work we study the limitations originating from laser phase and amplitude noise in an idealized Ramsey pulse interrogation scheme with uncorrelated atoms. Phase noise leads to a saturation of the frequency sensitivity with increasing atom number while amplitude noise implies a scaling $1/\sqrt{\tau}$ with τ being the interrogation time. We employ a technique using decoherence free subspaces first introduced in New J. Phys. **14**, 043011 (2012) which can restore the scaling with the square root of the inverse particle number $1/\sqrt{N}$. Similar results and improvements are obtained numerically for a Rabi spectroscopy setup.

doi: 10.1088/0953-4075/49/24/245501

[†] In this publication, all analytical and numerical calculations were conducted by the author of this thesis. J. Schachenmayer provided vital advice for deriving the Liouvillian operator for the noise, as well as providing ideas on how to substantially speed up numerical calculations.

4.1 Introduction

Ultracold atoms in optical lattices [4.1, 4.2] can nowadays be almost perfectly controlled on the quantum level of motion and internal degrees of freedom. Using special magic wavelength configurations for alkaline earth atoms, the lattice introduces only minimal perturbations of the transition frequency [4.3]. Such systems are perfectly suited candidates for state-of-the-art precision measurements. Optical lattice atomic clocks as cutting edge time standards are the most famous example of such exceedingly high resolution experiments [4.4]. Recent endeavors have found what is yet the most accurate determination of time with a fractional uncertainty of 2×10^{-18} [4.5]. To achieve such a small total measurement error known noise sources (e.g. atomic collisions) had to be eliminated or corrected for by proper calibration. One remaining class of imprecisions is tied to the fairly high density of the atomic ensemble, which leads to radiative long range atom-atom interactions like collective decay (super-radiance [4.6]) and dipole-dipole shifts [4.7]. As they cannot be totally avoided, recent calculations targeted the suppression of atomic interactions [4.8–4.10] via optimized lattice geometries and symmetries.

A different but important uncertainty contribution for the clock is the finite linewidth of the reference laser used to interrogate the atomic ensemble. Despite tremendous efforts to construct ultra-stable reference cavities resulting in sub-Hertz oscillators, the randomly fluctuating phase of the laser still contributes significantly to the uncertainty budget in experiments [4.5]. This phase noise acts identically on all atoms and hence adds to the collective atomic dipole. Therefore the effect cannot be canceled by increasing the size of the ensemble. Mathematically, the effect of a noisy laser addressing the atomic ensemble leads to an exponential dephasing of the collective atomic dipole reducing the amount of information about the phase state of the atoms. Over the course of multiple measurements the phase noise aliases (Dick effect [4.11]) and degrades the stability of the clock.

First studies of the effects of laser noise on spectroscopy have been put forward already decades ago almost in parallel with the successful development of high resolution laser spectroscopy [4.12]. Fluctuations in the laser phase and intensity lead to atomic population fluctuations limiting the spectroscopic resolution [4.13, 4.14]. With the fast improvements in laser technology the linewidth of lasers soon became so small, that this effect could be largely ignored in typical setups. Only in the ultimate limit of clock transitions the linewidth is significantly smaller than available lasers. In this case the remaining fast fluctuations can be traced to thermal fluctuations in the mirror coatings while slow changes in the cavity length lead to a drift of the average oscillation frequency [4.4].

Numerous studies have analytically and numerically treated the effect of both phase and amplitude noise. These studies have been mostly focused on deriving spectroscopic precision limits for the case of multipartite entangled input states [4.15–4.21]. Most of these approaches aimed to compute bounds for noisy metrology beyond the standard quantum limit. While it has generally been assumed that laser noise is especially detrimental to the typically fragile multipartite entangled states, significant limitations may occur already for 'classical' product input states.

In this paper we restrict our calculations to such product states in order to address current limitations of standard setups used in high-precision frequency detection. We derive scaling laws for the frequency sensitivity of both Ramsey and Rabi spectroscopy in the presence of collective laser noise. We map the stochastic laser-induced dynamics into an atomic master equation and show that amplitude noise has little impact on the precision. However, collective laser phase noise can lead to a complete saturation of the frequency sensitivity with the atom number (as shown for entangled states in Ref. [4.21]). We apply the proposal from Ref. [4.21], which uses decoherence free subspaces for the efficient suppression of phase noise. This is also reminiscent of the mechanism of quantum noise cancelation in atomic or optomechanical systems [4.22–4.30]. Our scheme is analogous to the negative mass oscillator employed in the aforementioned optomechenical investigations. The suppression can be achieved by splitting the atomic ensemble into two sub-ensembles: the incident laser beam is also split and manipulated such that one sub-ensemble experiences the exact negative detuning (between the laser and the atomic transition frequency) of the other.

4.2 Master equation for atomic dynamics in a noisy laser

We consider an ensemble of identical two-level atoms with a transition frequency ω_0. In a frame rotating with the laser frequency ω_l the ensemble is following free dynamics under the Hamiltonian ($\hbar = 1$)

$$H_0 = \Omega S_z, \tag{4.1}$$

where $S_z = \sum_j \sigma_j^z/2$, σ_j^z is the z Pauli operator of the j-th atom and $\Omega = \omega_0 - \omega_l$ is the detuning between the atomic transition and the laser frequency. The Hamiltonian describing optical excitation of this ensemble reads

$$H_l = 2\eta S_x, \tag{4.2}$$

where η is the coherent pump strength and $S_x = \sum_j \sigma_j^x/2$. We assume that all atoms instantaneously feel any change of the laser phase, which is justified given that typical setups are of much smaller length than the coherence length of a standard laser [4.31]. Furthermore, assuming white noise (i.e. no correlations in time) we may describe the phase noise of a laser as collective dephasing of the atoms via the Lindblad term

$$\mathcal{L}_d[\rho] = \frac{\gamma_d}{2}\left(2S_z\rho S_z - S_z^2\rho - \rho S_z^2\right). \tag{4.3}$$

Here, γ_d is the strength of the dephasing at which the off-diagonal density matrix elements are damped out. The time dynamics for the atomic density matrix ρ including laser phase noise are then described by the master equation

$$\dot{\rho} = i\left[\rho, H\right] + \mathcal{L}_d[\rho], \tag{4.4}$$

where $H = H_0 + H_l$. For details of the derivation of this master equation see Ref. [4.21] or Appendix A.

Analogously, if the laser has a noisy amplitude given by another white noise process and any change of amplitude instantly affects all atoms, we may describe the dynamics of the atomic ensemble by replacing the Lindblad term in the above master equation with (see also Appendix A)

$$\mathcal{L}_a[\rho] = 2\gamma_a \left(2S_x\rho S_x - S_x^2\rho - \rho S_x^2\right), \tag{4.5}$$

where γ_a governs the magnitude of the noise. Hence, amplitude noise can be interpreted as collective energy redistribution within the atomic ensemble.

Note, that one key point of this model is that all noise processes are of collective nature. This allows for simplified analytical and numerical treatment since the evolution described by the master equation takes place on the surface of the collective Bloch sphere, in a Hilbert space of dimension $N + 1$.

4.3 Effects of laser noise in Ramsey spectroscopy

Ramsey spectroscopy [4.32] consists of two consecutive $\pi/2$-pulses applied to an atomic ensemble initially in the ground state. In between the two pulses the atoms are subjected to a period of free time evolution for a time τ. After the second pulse the total population inversion of the atomic ensemble, which is proportional to the expectation value $\langle S_z\rangle$, is measured. This process is repeated for different laser frequencies (detunings) to retrieve the excitation as a function of the delay time and the detuning, $\langle S_z\rangle(\Omega, \tau)$. The $\pi/2$-pulses are assumed to be much faster than characteristic dephasing times and are therefore well approximated by rotations of the collective Bloch vector of the atoms about the y-axis of the Bloch sphere by an angle of $\pi/2$ (at exact resonance).

A figure of merit for the total frequency measurement precision is the so-called signal sensitivity $\delta\Omega$ [4.33],

$$\delta\Omega = \min_{\Omega} \left[\frac{\Delta S_z(\Omega, \tau)}{|\partial_\Omega \langle S_z\rangle(\Omega, \tau)|}\right]. \tag{4.6}$$

This quantity characterizes the minimal distinguishable frequency shift in the setup and thus gives the fundamental limit of accuracy with which one can match the laser frequency to the atomic transition frequency. The optimal operation points are those where the signal is most sensitive to changes in the detuning Ω while the signal quantum standard deviation $\Delta S_z = \sqrt{\langle S_z^2\rangle - \langle S_z\rangle^2}$ is minimized.

4.3.1 Phase noise

Let us first estimate the effect of the collective phase noise on the signal sensitivity obtained by interrogating an ensemble of N atoms with a laser exhibiting phase noise. As previously mentioned, due to the collective nature of the Hamiltonian and the

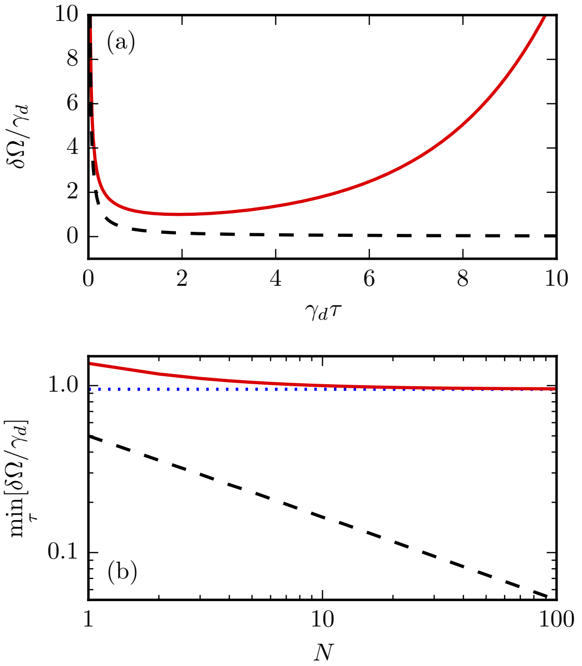

Figure 4.1: *Effects of phase noise.* (a) The phase noise limited (red line) signal sensitivity is compared to the quantum projection limit (black dashed line) of a Ramsey measurement on $N = 10$ atoms as a function of the interrogation time. The optimal time is $\tau_{opt} \approx 2/\gamma_d$. (b) The optimal signal sensitivity in the presence of phase noise saturates quickly with increasing N approaching the lower bound (blue dots). This is compared to the projection noise limited curve scaling with $1/\sqrt{N}$ (for a fixed interrogation time τ_{opt}) on a double-logarithmic scale.

Liouvillian, all system dynamics take place in the symmetric subspace, i.e. the Dicke basis. The density matrix in this basis is

$$\rho(t) = \sum_{M,M'} \rho_{M,M'}(t) \left|S, M\right\rangle \left\langle S, M'\right| , \tag{4.7}$$

where $S = N/2$ and $M, M' = -S, -S+1, ..., S$. Substituting Eq. (4.7) into the master equation, i.e. Eq. (4.4), we find differential equations for all density matrix elements of the form

$$\dot{\rho}_{M,M'} = \left[i\Omega(M' - M) - \frac{\gamma_d}{2}(M' - M)^2 \right] \rho_{M,M'}. \tag{4.8}$$

Since the derivative of each density matrix element is proportional to the matrix element itself, an integration of the equation above is straightforward. The initial state for the free time evolution (the state after the first $\pi/2$-pulse) is described by the density matrix with the elements

$$\rho_{M,M'}(0) = \frac{1}{2^N}\left[\binom{N}{M}\binom{N}{M'}\right]^{\frac{1}{2}}. \tag{4.9}$$

Using the resulting solutions, we find that the expectation value $\langle S_z \rangle$ after the second $\pi/2$-pulse is

$$\langle S_z \rangle = \frac{N}{2} e^{-\gamma_d \tau/2} \cos(\Omega\tau). \tag{4.10}$$

A somewhat more involved but nevertheless straightforward computation delivers the expression of the variance, which is proportional to the expectation value of the squared signal operator (for details see Appendix B),

$$\langle S_z^2 \rangle = \frac{N}{4} e^{-\gamma_d \tau}\left[N \sinh(\gamma_d \tau) + \cosh(\gamma_d \tau)\right]. \tag{4.11}$$

Now the minimization with respect to Ω in Eq. (4.6) can be carried out. The minimum is found where the derivative of the signal $\partial_\Omega \langle S_z \rangle$ is extremal, i.e. $|\sin(\Omega\tau)| = 1$. The final expression of the signal sensitivity for a standard Ramsey experiment is

$$\delta\Omega = \frac{\sqrt{N \sinh(\gamma_d \tau) + \cosh(\gamma_d \tau)}}{\tau\sqrt{N}}. \tag{4.12}$$

An illustration of the temporal behavior of the sensitivity for 10 atoms is given in Fig. 4.1(a). In the absence of phase noise ($\gamma_d = 0$) we recover the quantum projection noise limit. The most prominent characteristic is that already for a small number of atoms the sensitivity saturates, i.e. it omits its scaling with the atom number. The value which it saturates to is found by taking the limit $N \gg 1$:

$$\delta\Omega \approx \frac{\sqrt{\sinh(\gamma_d \tau)}}{\tau}. \tag{4.13}$$

The optimization over τ leads to a transcendental equation $\tanh(\gamma_d\tau/2) = \gamma_d\tau/2$ which can be numerically solved to indicate that the optimal sensitivity is simply limited by the bandwidth of the noise,

$$\min_\tau[\delta\Omega] \approx 0.951\gamma_d. \tag{4.14}$$

This behavior is depicted in Fig. 4.1(b), where the signal sensitivity optimized with respect to the interrogation time asymptotically approaches this lower bound. A similar bound that shows a saturation with the atom number N was derived for GHZ-states in Ref. [4.21].

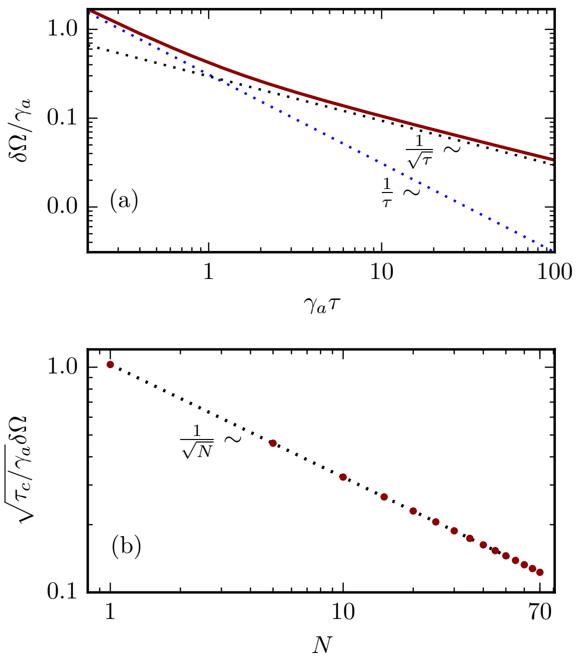

Figure 4.2: *Effects of amplitude noise.* (a) In order to illustrate the scaling with the interrogation time we have numerically computed the signal sensitivity in a standard Ramsey measurement performed on $N = 10$ atoms. As can be seen in the double-logarithmic plot, the sensitivity scales like the quantum projection noise $1/\tau$ at short times and it transitions to a scaling with $1/\sqrt{\tau}$ for larger time scales. (b) The amplitude noise limit exhibits a scaling law of $1/\sqrt{N}$ with the atom number.

4.3.2 Amplitude noise

We now analyze the dynamics described by Eq. (4.5) which includes the effects of amplitude noise. Using standard numerical methods, we can immediately uncover a particular limitation introduced by amplitude noise. The scaling of the sensitivity is modified from the typical $1/\tau$ to $1/\sqrt{\tau}$. This is illustrated in Fig. 4.2(a) where the sensitivities obtained in both the degradation-free regime ($\gamma_a = 0$) and for $\gamma_a > 0$ are compared. The crossover between the two scaling regimes is reached at around the inverse of the amplitude noise bandwidth $\tau \sim 1/\gamma_a$.

We now fix a duration of the free time evolution $\tau_c \gg \gamma_a^{-1}$ deep inside the $1/\sqrt{\tau}$ scaling regime and investigate the scaling of the sensitivity with increasing N. Numerical simulations [see Fig. 4.2(b)] carried up to a fairly large number of atoms $N = 70$ suggest that amplitude noise does not modify the scaling of the sensitivity with N,

$$\delta\Omega\Big|_{\tau\gg\gamma_a^{-1}} \propto \frac{1}{\sqrt{\tau N}}. \tag{4.15}$$

Under typical experimental conditions amplitude noise is orders of magnitude smaller

than the phase noise, i.e. $\gamma_a \ll \gamma_d$. Therefore, as suggested by the analysis above, the first signature of laser noise is the saturation of the sensitivity with an increasing atom number occurring at times much smaller than the times where amplitude noise becomes important.
Let us note that this result agrees with the conclusion of Ref. [4.17] where uncorrelated perpendicular noise (equivalent to independent amplitude noise) is shown to be far less detrimental than parallel noise (phase noise) for the spectroscopic resolution with entangled initial states.

4.4 Circumventing the phase noise induced saturation via twin beam interrogation

To overcome the saturation effect introduced by the noise associated with laser phase and frequency fluctuations, we employ a twin interrogation technique as in Ref. [4.21]. This assumes the division of the N-atom ensemble into two separately addressable sub-ensembles of $N/2$ atoms each (with N even and $S_z^{(1,2)}$ the corresponding population difference operators). Moreover, we set the detunings of the two ensembles opposite to each other leading to the Hamiltonian

$$H_0^- = \Omega S_z^{(1)} - \Omega S_z^{(2)}, \tag{4.16}$$

as a replacement of the free evolution Hamiltonian in the standard Ramsey method. This constitutes an effective time-reversal operation as the sub-ensembles' associated dipoles rotate opposite to each other in time under the action of the same Hamiltonian. This cannot be simply realized by shifting the frequency of each ensemble upwards and downwards compared to the laser frequency but rather involves changing the sign of the laser frequency.

The key point of this mechanism is that, while the systems evolve freely with $S_z^{(1)} - S_z^{(2)}$, the noise retains its collective nature $S_z^{(1)} + S_z^{(2)}$ according to Eq. (4.3). In a first step we notice that the difference in detunings in Eq. (4.16) breaks the symmetry such that the complete Hilbert space can no longer be described by a Dicke basis. Each sub-ensemble in itself though is restricted to its symmetric subspace, such that we can describe each ensemble with a Dicke basis. The complete basis is then just the product basis of the subspaces. We may write the total atomic density matrix as

$$\rho(t) = \sum_{\substack{m_1,m_2 \\ m_1',m_2'}} \rho_{m_1,m_2}^{m_1',m_2'}(t) \left| s, m_1, m_2 \right\rangle \left\langle s, m_1', m_2' \right| , \tag{4.17}$$

where $s = N/4$ and each sum runs from $-s$ to s. The differential equations for the

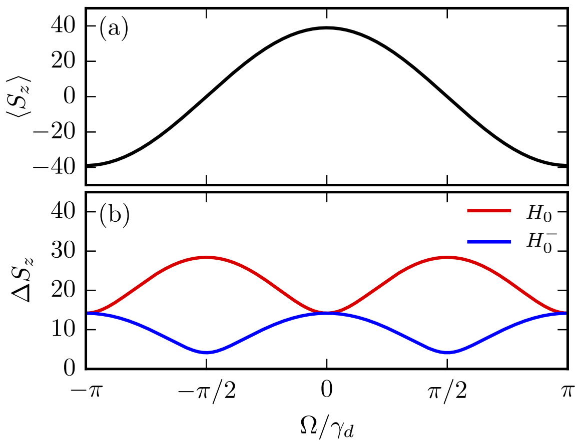

Figure 4.3: *The signal and its quantum standard deviation as a function of the detuning.* The central Ramsey fringe (a) and its standard deviation (b), for $N = 100$ and interrogation time $\tau = 0.5/\gamma_d$. The deviation is significantly reduced at the steepest parts of the signal when using opposite detunings which allows for a more precise measurement of frequency.

density matrix elements we obtain from the master equation now read

$$\dot{\rho}_{m_1,m_2}^{m_1',m_2'} = \left[i\Omega\left(m_1' - m_1\right) - i\Omega\left(m_2' - m_2\right) - \frac{\gamma_d}{2}\left(m_1' + m_2' - (m_1 + m_2)\right)^2 \right] \rho_{m_1,m_2}^{m_1',m_2'}. \tag{4.18}$$

Their integration is straightforward and the density matrix at time τ can be derived (for details see Appendix B) for the initial conditions

$$\rho_{m_1,m_2}^{m_1',m_2'}(0) = \frac{1}{2^N}\left[\binom{2s}{m_1}\binom{2s}{m_2}\binom{2s}{m_1'}\binom{2s}{m_2'}\right]^{\frac{1}{2}}. \tag{4.19}$$

As a first result we find that the signal $\langle S_z \rangle$ is identical to the one in Eq. (4.10). On the other hand, the standard deviation of the signal is drastically changed: at the point where the signal vanishes (optimal detection point) the variance is

$$\langle S_z^2 \rangle = \frac{N}{4} e^{-\gamma_d \tau} \cosh(\gamma_d \tau). \tag{4.20}$$

The significant reduction in the detection quantum noise is immediately apparent by comparing the result's scaling with N to the one in Eq. (4.11). Furthermore, Fig. 4.3(b) clearly shows how the noise cancelation mechanism leads to an extremely reduced quantum noise exactly at the points of maximum signal slope where previously the noise was maximized. The frequency detection sensitivity is subsequently enhanced

$$\delta\Omega = \frac{\sqrt{\cosh(\gamma_d \tau)}}{\tau\sqrt{N}}. \tag{4.21}$$

The optimal interrogation time is as before around $\tau_{opt} \approx 2/\gamma_d$. However, the result is remarkable in that the optimal sensitivity recovers the $1/\sqrt{N}$ scaling as in the case of the noise-free Ramsey procedure. After numerical minimization with respect to τ, the optimal sensitivity is

$$\min_{\tau}[\delta\Omega] \approx \frac{0.969}{\sqrt{N}}\gamma_d. \tag{4.22}$$

Note, that the result obtained above can be exactly reproduced by inverting the sign of the phase instead of the detuning in one of the arms of the twin beam interrogation scheme (see Appendix B). This leaves the free Hamiltonian unchanged but yields a modified dissipator describing collective dephasing with the operator $S_z^{(1)} - S_z^{(2)}$, which is the approach used in Ref. [4.21].

4.5 Noise induced limits in Rabi spectroscopy

Another method routinely used in quantum metrology is Rabi spectroscopy where the population excited during an attempted π-pulse is monitored against the atom-laser detuning. To model this procedure we introduce a coherent driving laser described by the Hamiltonian from Eq. (4.2). The reversible dynamics of the system are then subject to both the free Hamiltonian H_0 and H_l. The condition for a perfect population inversion pulse on resonance is that the pulse area equals π which requires a pulse duration of $\tau = \pi/2\eta$. The frequency sensitivity is then extracted from the detected population signal at the points of the steepest signal to the left and to the right of the resonance.

We proceed with numerical investigations focused on describing and overcoming the effect of phase noise during the Rabi procedure. The system Hamiltonian for standard Rabi spectroscopy reads

$$H_0 + H_l = \Omega S_z + 2\eta S_x, \tag{4.23}$$

while for the suppression of noise we will employ the asymmetric free Hamiltonian H_0^- defined in Eq. (4.16). Similarly to the case of Ramsey spectroscopy, we have illustrated an example of the signal and its standard deviation in Fig. 4.4; the effect of noise reduction occurs again at the optimal operation point where the change of the signal with the detuning is maximal. We quantify the enhancement by using the definition of the signal sensitivity from Eq. (4.6) as a figure of merit for the frequency detection sensitivity. The red dots in Fig. 4.5 convey the message that phase noise again leads to a saturation effect when the atom number is increased. The blue dots instead approximately show the recovery of the $1/\sqrt{N}$ scaling.

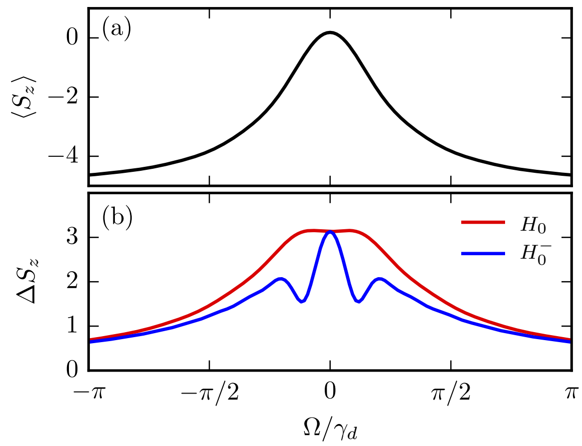

Figure 4.4: *Rabi signal and its quantum standard deviation.* (a) The resonance curve (signal) and (b) the standard deviation which is again exhibiting a significant reduction at the steepest parts to the left and to the right of the resonance when addressing a split ensemble with opposite detunings. The ensemble size is $N = 10$ and we chose a sufficiently small driving of $\eta = 0.2\gamma_d$ in order to minimize power broadening effects.

4.6 Conclusions

We have investigated the effects of both laser phase and amplitude noise on the sensitive detection of frequencies via the Ramsey and Rabi technique. For Ramsey spectroscopy we have found analytical expressions showing a saturation of the minimum sensitivity with the increasing atom number under the action of phase noise. To counteract this effect, we have used an approach which involves the separate interrogation of two sub-ensembles leading to the recovery of the typical standard quantum limited scaling with $1/\sqrt{N}$. This setup is closely related to the one illustrated in Ref. [4.21], but is also reminiscent of techniques used in recent proposals for counteracting the effect of noise [4.23–4.28, 4.30] in quantum force detection setups: we describe an 'anti-noise' path obtained via the inclusion of a negatively detuned sub-ensemble playing the role of a negative mass oscillator. For amplitude noise, we have also numerically uncovered a particular scaling of the Ramsey sensitivity with $1/\sqrt{\tau}$ at times larger than the inverse of the amplitude noise characteristic rate γ_a^{-1}. Numerical investigations suggest that similar results hold for Rabi spectroscopy.

Acknowledgements

We acknowledge very informative and helpful discussions with Laurin Ostermann on theoretical aspects of this work. Also, we thank Aurélien Dantan for input on experimental details of laser noise sources. We acknowledge financial support by the Austrian Science Fund (FWF) within the DK-ALM: W1259-N27 (D. P.) and a stand-

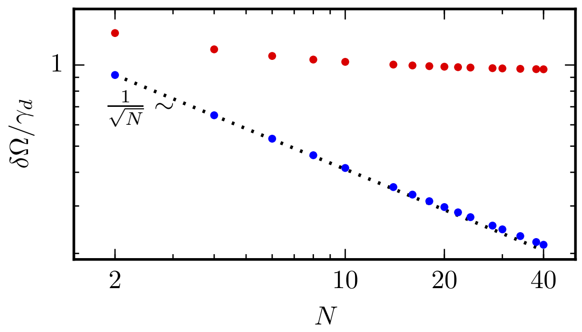

Figure 4.5: *Scaling of the Rabi signal sensitivity with N.* While for standard addressing the sensitivity begins to saturate already for $N \sim 20$, when employing opposite detunings the signal sensitivity approximately scales with $1/\sqrt{N}$. An exact fit returns a scaling with $N^{-0.483}$. The driving strength is fixed to $\eta = \gamma_d$.

alone project with number P24968-N27 (C. G.), by DARPA through the QUASAR project (H. R.), and through JILA under grants JILA-NSF-PFC-1125844 and NSF-PIF-1211914 (J. S.). Furthermore, we acknowledge the use of the open-source software QuTiP [4.34].

4.7 Appendix

Derivation of the master equation

Von Neumann equation with a noisy laser

The Hamiltonian of a perfectly coherent laser source in a frame at rest is

$$H_l = \eta \sum_j \left(\sigma_j^+ e^{-i\omega_l t} + \sigma_j^- e^{i\omega_l t} \right), \tag{4.24}$$

where $\sigma_j^{\pm}$ is the raising and lowering operator of the j-th atom, respectively, and $\sigma_j^x = \sigma_j^+ + \sigma_j^-$. We may now include a noisy phase $\phi(t)$ modelled via the standard phase diffusion theory [4.35] and amplitude noise $\epsilon(t)$ by replacing

$$\omega_l t \;\to\; \omega_l t + \phi(t), \tag{4.25}$$

$$\eta \;\to\; \eta + \epsilon(t), \tag{4.26}$$

respectively. Going into the frame rotating with ω_l, we see that the noisy phase $\phi(t)$ is equivalent to a noisy frequency $\dot{\phi}(t)$, since then the substitution in Eq. (4.25) becomes

$$\Omega \;\to\; \Omega + \dot{\phi}(t), \tag{4.27}$$

while the noise term in the amplitude remains unchanged. We assume both $\dot{\phi}(t)$ and $\epsilon(t)$ to be white noise processes, i.e.

$$\langle \dot{\phi}(t)\dot{\phi}(t') \rangle = \gamma_d \delta(t-t'), \tag{4.28}$$

$$\langle \epsilon(t)\epsilon(t') \rangle = \gamma_a \delta(t-t'). \tag{4.29}$$

Hence, when writing the respective von Neumann equations for the density matrix ρ,

$$\dot{\rho} = -i[H,\rho] + i\dot{\phi}(t)[S_z,\rho], \tag{4.30}$$

$$\dot{\rho} = -i[H,\rho] + 2\epsilon(t)[S_x,\rho], \tag{4.31}$$

we can interpret each of them as a Stratonovich multiplicative stochastic differential equation [4.21, 4.36].

Transformation between Stratonovich and Itô stochastic differential equations

Let us now more generally consider a differential equation for a stochastic process in one variable,

$$\frac{d}{dt}x(t) = a(x(t),t) + b(x(t),t)\xi(t), \tag{4.32}$$

where $\xi(t)$ is a white noise process. Interpreting this equation as a Stratonovich (S) differential equation, it can be transformed into Itô (I) form, where it follows different rules of calculus. The transformation relation between the two formalisms is [4.36]

$$\text{(S) } dx(t) = a(x(t),t)dt + b(x(t),t)dW(t) \tag{4.33}$$

$$\text{(I) } dx(t) = \left[a(x(t),t) + \frac{1}{2}b(x(t),t)\partial_x b(x(t),t)\right]dt + b(x(t),t)dW(t), \tag{4.34}$$

where $dW(t) = \xi(t)dt$ is the Wiener increment of the stochastic variable $\xi(t)$.

For the specific form of a multiplicative stochastic differential equation in the Stratonovich formalism,

$$\text{(S) } dx(t) = a_0 x(t)dt + b_0 x(t)dW(t), \tag{4.35}$$

where a_0 and b_0 are constants, the transformation into the Itô form yields

$$\text{(I) } dx(t) = \left[a_0 x(t) + \frac{1}{2}b_0^2 x(t)\right]dt + b_0 x(t)dW(t). \tag{4.36}$$

If $x(t)$ is a Markov process it is non-anticipating, so it holds that the average $\langle x dW \rangle = 0$. Hence, when performing the average over the above equation, we find

$$d\langle x(t) \rangle = \left(a_0 + \frac{b_0^2}{2}\right)\langle x(t) \rangle\, dt. \tag{4.37}$$

This relation is all we need to derive our master equation.

Master equation

Writing the von Neumann equation for our density matrix subject to an arbitrary multiplicative white noise $\xi(t)$, we have

$$\dot{\rho}(t) = \left(\boldsymbol{L}_0 + \alpha\xi(t)\boldsymbol{L}_1\right)\rho(t), \tag{4.38}$$

where the linear operator $\boldsymbol{L}_0$ corresponds to the deterministic part of the process, while $\boldsymbol{L}_1$ describes the action of the noise process on the density matrix. We interpret the differential equation as a Stratonovich stochastic differential equation. Using the identity for multiplicative linear white noise in Eq. (4.37) we have

$$d\rho(t) = \left(\boldsymbol{L}_0 dt + \frac{1}{2}\alpha^2\boldsymbol{L}_1^2 dt\right)\rho(t), \tag{4.39}$$

where we used the fact that $\rho(t)$ is Markovian and remains approximately unchanged when averaging over the noise time scale. Therefore Eq. (4.39) yields our respective master equations by identifying the terms from the von Neumann equations

$$\boldsymbol{L}_0\rho := -i[H,\rho], \tag{4.40}$$

and, for phase noise

$$\begin{aligned}\boldsymbol{L}_1\rho &:= i[S_z,\rho],\\ \alpha &:= \sqrt{\gamma_d}.\end{aligned} \tag{4.41}$$

For amplitude noise, on the other hand, we have

$$\begin{aligned}\boldsymbol{L}_1\rho &:= i[S_x,\rho],\\ \alpha &:= 2\sqrt{\gamma_a}.\end{aligned} \tag{4.42}$$

Sensitivity of Ramsey spectroscopy subjected to phase noise

The details of the calculations performed for Ramsey spectroscopy when only considering phase noise will be illustrated here. To this end we will perform a general calculation for a split ensemble addressed with two different detunings Ω_1 and Ω_2, respectively. We then recover the standard case by setting $\Omega \equiv \Omega_1 = \Omega_2$ or the enhanced case by setting $\Omega \equiv \Omega_1 = -\Omega_2$. As we have shown in the paper, the derivative of each density matrix element is only proportional to the density matrix element, such that we find the general solutions

$$\rho_{m_1,m_2}^{m_1',m_2'}(t) = \rho_{m_1,m_2}^{m_1',m_2'}(0)e^{i\Omega_1 t(m_1'-m_1)}e^{i\Omega_2 t(m_2'-m_2)}e^{-\gamma_d t/2\left(m_1'+m_2'-(m_1+m_2)\right)^2}. \tag{4.43}$$

In order to compute the signals, we will first consider the following: the prefect $\pi/2$-pulses can be modeled as rotations of the collective Bloch vector about the y-axis. The Pauli spin operators are generators of such rotations such that we can write them as

$$R_y = e^{iS_y \pi/2}, \tag{4.44}$$

where $S_y = \sum_i \sigma_i^y/2$. The final state after the second $\pi/2$-pulse after a free time evolution for a period τ is then described by the density operator $\rho_f = R_y \rho(\tau) R_y^\dagger$. The expectation value of the population inversion at this point is

$$\langle S_z \rangle_f = \operatorname{tr}\left(S_z \rho_f\right) = \operatorname{tr}\left(R_y^\dagger S_z R_y \rho(\tau)\right) = \langle S_x \rangle_\tau \,, \tag{4.45}$$

where we used the invariance of the trace under cyclic permutations. The signal after the second $\pi/2$-pulse is hence equal to the expectation value of the operator S_x after the free time evolution. The same holds for the operator squared, i.e. $\langle S_z^2 \rangle_f = \langle S_x^2 \rangle_\tau$. We can write the S_x operator as

$$S_x = \frac{1}{2}\left(S^+ + S^-\right) = \frac{1}{2}\left(S_1^+ + S_2^+ + S_1^- + S_2^-\right), \tag{4.46}$$

where $S^\pm = \sum_j \sigma_j^\pm$ are the collective atomic raising and lowering operators. The action of the raising and lowering operators for each of the atomic ensembles on a state is

$$S_1^\pm \left| s, m_1, m_2 \right\rangle = \sqrt{s(s+1) - m_1(m_1 \pm 1)} \left| s, m_1 \pm 1, m_2 \right\rangle, \tag{4.47}$$

and analogously for $S_2^\pm$. Using these matrix elements of the raising and lowering operators, we can compute the expectation values $\langle S_x \rangle_\tau$ and $\langle S_x^2 \rangle_\tau$. In order to solve the arising sums we also need to use the initial conditions of these expectation values $\langle S_x \rangle (0) = N/2$, and $\langle S_x^2 \rangle (0) = N^2/4$, respectively. We then acquire the expression for the signal

$$\langle S_z \rangle_f = \frac{N}{4} e^{-\gamma_d \tau} \left(\cos(\Omega_1 \tau) + \cos(\Omega_2 \tau)\right) = \frac{N}{2} e^{-\gamma_d \tau} \cos(\Omega \tau), \tag{4.48}$$

where in the second line we used the fact that the signal is identical for both cases. The expectation value of the operator squared reads

$$\begin{aligned} \langle S_z^2 \rangle_f = \frac{N}{8} \Bigg[& \frac{e^{-2\gamma_d \tau}}{2} \left(\left(\frac{N}{2} - 1 \right) \left(\cos(2\Omega_1 \tau) + \cos(2\Omega_2 \tau)\right) + N \cos((\Omega_1 + \Omega_2)\tau) \right) \\ & + \frac{N}{2} \left(\cos((\Omega_1 - \Omega_2)\tau) + 1\right) + 1 \Bigg]. \end{aligned} \tag{4.49}$$

At this point we will make the distinction between the two cases of identical and opposite detunings. For simplicity, we will already use the fact that the signal sensitivity is minimal where the signal vanishes but its derivative

$$\partial_\Omega \left\langle S_z \right\rangle_f = -\tau \frac{N}{2} e^{-\gamma_d \tau/2} \sin(\Omega\tau) \tag{4.50}$$

is extremal, i.e. where

$$\Omega\tau = (2n+1)\frac{\pi}{2}, \ n \in \mathbb{Z}. \tag{4.51}$$

When setting $\Omega_1 = \Omega_2 = \Omega$ and using the minimization condition from Eq. (4.51), the variance becomes

$$\langle S_z^2 \rangle_f = \frac{N}{8}\left(e^{-2\gamma_d\tau}(-N+1) + N + 1\right) = \frac{N}{4} e^{-\gamma_d\tau}\left(N\sinh(\gamma_d\tau) + \cosh(\gamma_d\tau)\right). \tag{4.52}$$

Substituting this and the derivative of the signal into the definition of the signal sensitivity, we find our expression

$$\delta\Omega = \frac{\sqrt{N\sinh(\gamma_d\tau) + \cosh(\gamma_d\tau)}}{\tau\sqrt{N}}. \tag{4.53}$$

On the other hand, when we set $\Omega_1 = -\Omega_2 = \Omega$, Eq. (4.49) becomes

$$\langle S_z^2 \rangle_f = \frac{N}{8}\left(e^{-2\gamma_d\tau} + 1\right) = \frac{N}{4} e^{-\gamma_d\tau}\cosh(\gamma_d\tau), \tag{4.54}$$

which of course yields the expression for the significantly reduced signal sensitivity,

$$\delta\Omega = \frac{\sqrt{\cosh(\gamma_d\tau)}}{\tau\sqrt{N}}, \tag{4.55}$$

which scales down more favorably with the number of atoms.

Equivalence to phase conjugation

The process used to achieve the gain in measurement precision in Ref. [4.21] was phase conjugation on one of the sub-ensembles. Conjugating the phase changes the sign of the noise in one of the sub-ensembles, such that we find a Lindblad operator

$$\mathcal{L}^-[\rho] = \frac{\gamma_d}{2}\left(S_z^- \rho S_z^- - (S_z^-)^2\rho - \rho(S_z^-)^2\right), \tag{4.56}$$

where $S_z^- = S_z^{(1)} - S_z^{(2)}$. The Hamiltonian, on the other hand, remains unchanged. Following the above calculation with this model yields the slightly different general solutions for the density matrix elements,

$$\rho_{m_1,m_2}^{m_1',m_2'} = \rho_{m_1,m_2}^{m_1',m_2'}(0) e^{i\Omega t(m_1'+m_1+m_2'+m_2)} e^{-\gamma_d t/2\left(m_1'-m_2'-(m_1-m_2)\right)^2}. \tag{4.57}$$

With these solutions one can show that we find the same signal as before and the increased sensitivity from Eq. (4.55).

5 Publication

Physical Review Letters **119**, 093601 (2017)

Cavity antiresonance spectroscopy of dipole coupled subradiant arrays[†]

D. Plankensteiner[1], C. Sommer[2], H. Ritsch[1] and C. Genes[2]

[1]*Institut für Theoretische Physik, Universität Innsbruck,*
Technikerstraße 21a, A-6020 Innsbruck, Austria
[2]*Max Planck Institute for the Science of Light,*
Staudtstraße 2, D-91058 Erlangen, Germany

An array of N closely spaced dipole coupled quantum emitters exhibits super- and subradiance with characteristic tailorable spatial radiation patterns. Optimizing the emitter geometry and distance with respect to the spatial profile of a near resonant optical cavity mode allows us to increase the ratio between light scattering into the cavity mode and free space emission by several orders of magnitude. This leads to distinct scaling of the collective coherent emitter-field coupling versus the free space decay as a function of the emitter number. In particular, for subradiant states, the effective cooperativity increases much faster than the typical linear $\propto N$ scaling for independent emitters. This extraordinary collective enhancement is manifested both in the amplitude and the phase profile of narrow collective antiresonances appearing at the cavity output port in transmission spectroscopy.

doi: 10.1103/PhysRevLett.119.093601

[†] The author of the present thesis performed all analytical and numerical calculations. C. Sommer provided essential insights leading to the investigations of the phase of the transmitted field, which constitutes a crucial part of the paper.

The confinement of atoms and photons in small volumes with very low loss has been a renowned success [5.1–5.3] as it allows for tests of light-matter interactions where the quantum nature of both comes into play. In a cavity quantum electrodynamics setup, the photon-emitter interaction strength $g_1 \propto \mu\mathcal{E}$ for an emitter with a dipole moment μ is strongly enhanced by decreasing the field mode volume and, thus, increasing the local field per photon $\mathcal{E}$. In a standard Fabry-Pérot cavity geometry, this is achieved by closely surrounding the emitter with two high-reflectivity mirrors. The atom-photon interaction time is then enhanced by a factor roughly proportional to the cavity finesse characterizing the number of round trips a photon can make before escaping to the environment at a rate κ. At the single quantum emitter level, this has facilitated experimental progress towards strong coupling allowing the study of single photon nonlinear effects, such as the photon blockade regime [5.4], of vacuum Rabi splittings and other tests of fundamental quantum optics effects [5.5, 5.6].

The single emitter cooperativity $C_1 = g_1^2/(\kappa\gamma)$ (where γ is the rate of spontaneous decay into free space) is a well established measure for strong light-matter interaction when $C_1 \gg 1$. Since, for a single two-level emitter, the dipole matrix element μ appears both in $g_1 \propto \mu$ and $\gamma \propto \mu^2$, the cooperativity C_1 is merely a geometric factor independent of μ [5.7]. This means that cavity design (increasing the finesse and decreasing the transverse mode area) is the central aspect for reaching high single emitter cooperativity. In the parameter regime of large κ, one often targets a large effective cooperativity by coupling N emitters simultaneously to the same cavity mode. For distant fully independent emitters, the effective cooperativity then scales like $C_{\text{eff}} = C_1 N$, as the emitter-cavity coupling $g_N = g_1\sqrt{N}$ increases proportionally to $\sqrt{N}$, while the free space emission rate γ stays constant. However, especially for small emitter-emitter separations, their coupling to the vacuum modes is inherently *collective* generating states with superradiant and subradiant decay [5.8], which invalidates the above simple scaling law. Such decay processes have recently attracted interest in 1D and 2D subwavelength spaced atomic arrays used in topological quantum optics, high extinction media or photon storage [5.9–5.14].

We introduce an alternative, improved path, towards reaching a high cooperativity based on collective dissipative effects. The mechanism involves the separate optimization of the coherent coupling of the emitters to the cavity mode and of the incoherent emitter-vacuum coupling. For a configuration of N closely spaced emitters (separation less than the transition wavelength λ_{e}), the coupling to free space vacuum modes can be strongly suppressed [5.8, 5.15, 5.16]. At the same time, a periodic arrangement of emitters in a rigid geometry (for example implanted inside a solid-state matrix), transversely placed inside a single cavity mode can lead to optimized collective coupling [5.17]. The upshot is that C_{eff} scales strongly in a nonlinear fashion with N, as the effective collective free space decay rate γ_{eff} can be dramatically suppressed. We propose an example for the implementation of phase imprinting using higher order transverse cavity modes leading to the preferential excitation of subradiant collective states. The effect is directly observable by homodyne detection of the cavity output, displayed both in amplitude and phase antiresonant behavior [5.18, 5.19]. As opposed to the strong coupling regime exploited in [5.18], this paper considers the bad cavity regime $\kappa \gg g_1\sqrt{N}$ where one

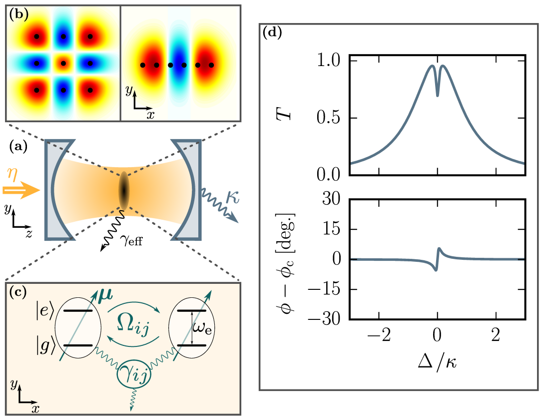

Figure 5.1: *System setup.* (a) Optical cavity supporting (b) different transverse modes coupled to (c) a rigid array of dipole-dipole interacting quantum emitters. (d) Light-matter interaction creates an antiresonance dip and a fast phase switch around the emitter resonance in the cavity transmission spectrum as shown on the right for a single emitter with $g_1 = \kappa/10 = 2\gamma$.

typically expects modest antiresonance phase shifts. Because of the collectively increased effective cooperativity, very narrow antiresonances occur accompanied by extremely fast and large phase shift switches rendering such a system perfect for high resolution spectroscopy.

5.1 Model

Let us consider an ordered ensemble of quantum emitters modeled as two-level systems with ground state $|g\rangle_i$ and an excited state $|e\rangle_i$ (split by frequency ω_e) located at $\mathbf{r}_i$ (for $i = 1, ..., N$) (see Fig. 5.1). The levels are connected by individual Pauli raising and lowering operators $\sigma_i^\pm$ with $\sigma_i^x = \sigma_i^+ + \sigma_i^-$, $\sigma_i^y = -i(\sigma_i^+ - \sigma_i^-)$, and $\sigma_i^z = \sigma_i^+\sigma_i^- - \sigma_i^-\sigma_i^+$. The emitters are embedded in a static 2D support, transversely placed in the center plane of a single higher order transverse electromagnetic (TEM) mode at frequency ω_c (see Fig. 5.1). At position $(\mathbf{r}, z)$ along the cavity axis z, the electric field operator is proportional to $a\cos(kz)f(\mathbf{r})\boldsymbol{\epsilon}_y$, where a is the annihilation operator of the cavity mode, $k = \omega_\mathrm{c}/c$, $f(\mathbf{r})$ is the transverse spatial mode profile, and $\boldsymbol{\epsilon}_y$ denotes linear polarization in the y direction. The cavity is laser driven at frequency ω_l with power P through one mirror. In a frame rotating at ω_l, the dynamics of the mode of interest is described by

$$H_\mathrm{c} = \hbar\Delta_\mathrm{c} a^\dagger a + i\hbar\eta\left(a^\dagger - a\right), \tag{5.1}$$

where $\Delta_\mathrm{c} = \omega_\mathrm{c} - \omega_\mathrm{l}$ and $\eta = \sqrt{2P\kappa/(\hbar\omega_\mathrm{l})}$. Cavity damping with decay rate κ occurs via the collapse operator a.

At dense spacing ($|\mathbf{r}_i - \mathbf{r}_{i+1}| < \lambda_\mathrm{e}$), one has to account for the direct emitter-emitter interactions via the transition dipole moments $\boldsymbol{\mu}_i$. The collective dynamics is governed by the free Hamiltonian H_e and the collective part H_dip,

$$H_\mathrm{e} + H_\mathrm{dip} = \hbar\Delta_\mathrm{e}\sum_i \sigma_i^+\sigma_i^- + \hbar\sum_{i,j:i\neq j}\Omega_{ij}\sigma_i^+\sigma_j^-, \tag{5.2}$$

where $\Delta_\mathrm{e} = \omega_\mathrm{e} - \omega_\mathrm{l}$, and Ω_{ij} is the strength of the coherent dipole-dipole interaction between emitters i and j (see Appendix). Moreover, the incoherent collective dynamics leads to mutual decay rates γ_{ij} that can be accounted for with the Lindblad superoperator [5.20]

$$\mathcal{L}_\mathrm{e}[\rho] = \sum_{i,j}\gamma_{ij}\left(2\sigma_i^-\rho\sigma_j^+ - \sigma_i^+\sigma_j^-\rho - \rho\sigma_i^+\sigma_j^-\right). \tag{5.3}$$

In the single cavity mode limit, the interaction is described by the Tavis-Cummings Hamiltonian

$$H_\mathrm{int} = \hbar\sum_i g_i\left(a^\dagger\sigma_i^- + a\sigma_i^+\right), \tag{5.4}$$

where the coupling strength g_i of an emitter at position $(\mathbf{r}_i, z_i)$ is proportional to $\cos(kz_i)f(x_i, y_i)\boldsymbol{\epsilon}_y\cdot\boldsymbol{\mu}_i$.

The complete dynamics of the system with density matrix ρ are then described by the master equation

$$\dot\rho = \frac{i}{\hbar}[\rho, H] + \mathcal{L}_\mathrm{c}[\rho] + \mathcal{L}_\mathrm{e}[\rho], \tag{5.5}$$

where $H = H_\mathrm{c} + H_\mathrm{e} + H_\mathrm{dip} + H_\mathrm{int}$ and $\mathcal{L}_\mathrm{c}[\rho] = \kappa\left(2a\rho a^\dagger - a^\dagger a\rho - \rho a^\dagger a\right)$. Equivalently, the dynamics can be described via quantum Langevin equations (QLE) [5.21] (see Appendix).

5.2 Single emitter antiresonance

We consider a reference system with a single emitter in the low excitation limit $\langle\sigma_i^z\rangle \approx -1$ where a linear coupled set of QLEs can be derived. For a resonant interaction (i.e. $\Delta \equiv \Delta_\mathrm{c} = \Delta_\mathrm{e}$), this leads to the following mean field equations:

$$\langle\dot a\rangle = -(\kappa + i\Delta)\langle a\rangle + \eta - ig\langle\sigma^-\rangle, \tag{5.6}$$
$$\langle\dot\sigma^-\rangle = -(\gamma + i\Delta)\langle\sigma^-\rangle - ig\langle a\rangle. \tag{5.7}$$

These equations exhibit the phenomenon of atomic antiresonances [5.18, 5.22], where the resonantly driven atomic dipole oscillates in a way to counteract the cavity drive and leads to a minimum of transmission [5.23]. We analyze its dependence on γ by studying the steady-state amplitude transmission t, which is proportional to the output field amplitude $t = \kappa \langle a \rangle / \eta$. It reads

$$t = \frac{\kappa}{i\Delta + \kappa + g^2/(i\Delta + \gamma)}. \tag{5.8}$$

The transmitted intensity is $T = |t|^2$ and the relative phase shift caused by the emitter is $\phi - \phi_{\rm c}$, where $\phi = \operatorname{Arg}(t) = \arctan\left(\Im\{t\}/\Re\{t\}\right)$ and $\phi_{\rm c} = -\arctan\left(\Delta_{\rm c}/\kappa\right)$ is the phase shift of the bare cavity. The detection of the relative phase shift can be done by homodyne detection and analysis of the output field quadratures. Scanning the laser frequency (Δ), we find that the coherent transmitted intensity through the cavity contains an antiresonance dip around $\Delta = 0$ with a corresponding jump in the phase shift (see Fig. 5.1). Fitting the antiresonance with a Lorentzian (see Appendix), we find a depth of $1 - T(\Delta = 0) = C_1(C_1 + 2)/(C_1 + 1)^2$, and a width that can be approximated by $\gamma(C_1 + 1) = g_1^2/\kappa + \gamma$ (for a regime where both $g_1, \gamma \ll \kappa$). An almost vanishing transmission is, then, a signature of reaching a regime of strong cooperativity ($C_1 \gg 1$).

5.3 Collective antiresonance of emitter arrays

As C_1 is independent of μ, an emitter with a larger dipole moment will only broaden the antiresonance. For coupled emitter arrays, this is, however, no longer valid, and one can design the radiative properties of the ensemble. For *collective* subradiant resonances of an array the free space emission is suppressed, while we still can optimize the coupling to the cavity mode. This generates extremely sharp and deep antiresonances accompanied by a fast and large phase change within a narrow frequency range. The immediate upshot of this regime is a dramatically enhanced effective cooperativity, which renders it an ideal configuration for high resolution spectroscopy.

The set of coupled QLEs for many emitters can be cast in vector form

$$\dot{\langle a \rangle} = -i\Delta_{\rm c} \langle a \rangle + \eta - i\mathbf{G}^{\intercal} \langle \boldsymbol{\sigma} \rangle - \kappa \langle a \rangle, \tag{5.9}$$

$$\dot{\langle \boldsymbol{\sigma} \rangle} = -i\Delta_{\rm e} \langle \boldsymbol{\sigma} \rangle - i\boldsymbol{\Omega} \langle \boldsymbol{\sigma} \rangle - i\mathbf{G} \langle a \rangle - \boldsymbol{\Gamma} \langle \boldsymbol{\sigma} \rangle, \tag{5.10}$$

where, now, $\boldsymbol{\sigma}$ and $\mathbf{G}$ are column vectors with entries σ_i^- and g_i. The matrices $\boldsymbol{\Omega}$ and $\boldsymbol{\Gamma}$ have the elements Ω_{ij} and γ_{ij}. In steady state the transmission coefficient for the cavity amplitude reads

$$t = \frac{\kappa}{i\Delta_{\rm c} + \kappa + \mathbf{G}^{\intercal}\mathbf{G}/[i\Delta_{\rm eff}(\Delta_{\rm e}) + \gamma_{\rm eff}(\Delta_{\rm e})]}, \tag{5.11}$$

where the effective $\Delta_{\rm e}$-dependent collective energy shifts and linewidths are derived from the matrix

$$\mathbf{M}(\Delta_{\rm e}) = i\Delta_{\rm e}\mathbb{1} + i\boldsymbol{\Omega} + \boldsymbol{\Gamma} \tag{5.12}$$

as real and imaginary parts

$$\Delta_{\text{eff}}(\Delta_{\text{e}}) = \Im\left\{\frac{\mathbf{G}^{\intercal}\mathbf{G}}{\mathbf{G}^{\intercal}\mathbf{M}^{-1}(\Delta_{\text{e}})\mathbf{G}}\right\}, \tag{5.13}$$

$$\gamma_{\text{eff}}(\Delta_{\text{e}}) = \Re\left\{\frac{\mathbf{G}^{\intercal}\mathbf{G}}{\mathbf{G}^{\intercal}\mathbf{M}^{-1}(\Delta_{\text{e}})\mathbf{G}}\right\}. \tag{5.14}$$

In analogy to the single emitter case, we can define an effective N-emitter cooperativity by

$$C_{\text{eff}}(\Delta_{\text{e}}) = \frac{\mathbf{G}^{\intercal}\mathbf{G}}{\kappa\gamma_{\text{eff}}(\Delta_{\text{e}})}. \tag{5.15}$$

This equation provides a main message of the paper, as it shows that the numerator and denominator no longer share the same dependency on μ. As γ_{eff} is not a natural constant of the ensemble, but strongly dependent on the relative positioning and phase of individual emitters, one can reach subradiant states with $\gamma_{\text{eff}} \ll \gamma$. By proper design of the cavity transverse field amplitude profile, the numerator can, at the same time, be maximized, resulting in a scaling up of C_{eff} well above the independent emitter case $Ng_1^2/(\kappa\gamma)$.

5.4 Two emitters

Let us elucidate the mechanism in the two emitter case, with adjustable separation $d = |\mathbf{r}_1 - \mathbf{r}_2|$. We distinguish two fundamentally different cases: (i) uniform coupling $\mathbf{G} = (g,\ g)^{\intercal}$ and (ii) opposite coupling $\mathbf{G} = (g, -g)^{\intercal}$, resulting in $\mathbf{G}^{\intercal}\mathbf{G} = 2g^2$ for both cases. The matrix of interactions can be diagonalized with eigenvalues $i(\Delta_{\text{e}} \pm \Omega_{12}) + (\gamma \pm \gamma_{12})$, signaling the presence of collective super- and subradiant states $(\gamma \pm \gamma_{12})$ shifted by $\pm\Omega_{12}$ from the emitter resonance ω_{e} (the positive sign corresponds to uniform coupling).

In the extreme case, where $d \ll \lambda_{\text{e}}$, the mutual decay approaches $\gamma_{12} \to \gamma$, and the effective cooperativity reaches (i) $C_{\text{eff}} \to g^2/(\kappa\gamma)$ and (ii) $C_{\text{eff}} \to \infty$, respectively. To account for dipole-dipole energy shifts, we impose $\Delta_{\text{eff}}(\delta) = 0$ and, subsequently, tune the cavity such that $\omega_{\text{c}} = \omega_{\text{e}} - \delta$; i.e. we match the cavity to the shifted collective emitter resonance. For two emitters, the imposed resonance condition yields $\delta = \pm\Omega_{12}$. The resulting depth and width of each antiresonance is $C_{\text{eff}}(C_{\text{eff}}+2)/(C_{\text{eff}}+1)^2$ and $\gamma_{\text{eff}}(C_{\text{eff}}+1)$, respectively. Hence, for $d \to 0$, we have (i) an antiresonance depth as for the single emitter but twice the width (superradiance), and (ii) an antiresonance that has a depth of 1 and a width of $2g^2/\kappa$ (subradiance). While the width of the antiresonance is still limited by g, the phase switch bandwidth is independent of g. This is a direct measure of the subradiance as the slope of the phase switch in this limit is $1/\gamma_{\text{eff}}$ (see Appendix). The result is reminiscent of the one in [5.18], however, in a very different and less stringent regime, where only weak coupling is required and where usually moderate phase shifts are expected; in contrast, for $\gamma_{\text{eff}} \to 0$, the phase even exhibits a π phase change within an extremely narrow frequency range, since in this

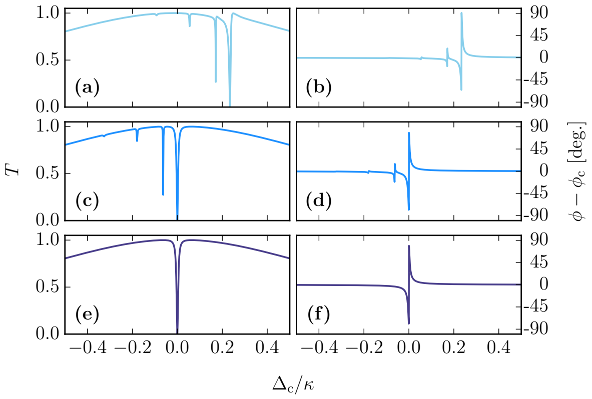

Figure 5.2: *Targeting antiresonances.* (a), (c), and (e) show the cavity intensity transmission and (b), (d), and (f) the corresponding phase for a scan of the laser frequency. The upper row corresponds to $\omega_c = \omega_e$ and asymmetric coupling $g_i = (-1)^i g$; the middle row illustrates frequency selection as $\omega_c \simeq \omega_{m=N}$. Finally, we also match the symmetry to the state corresponding to the subradiant antiresonance (see Appendix). The parameters are $N = 10$, $g = \kappa/50$, $\gamma = \kappa/40$ with a chain separation of $d = 0.08\lambda_e$.

regime, $\lim_{\Delta\to 0^\pm}(\phi - \phi_c) = \pm\pi/2$.

5.5 Addressing collective subradiant states

The above results can be generalized to N emitters in an equidistant chain configuration ($d = |r_{i+1} - r_i|$). Analytical considerations can be made under a nearest neighbor approximation for H_{dip} in the single-excitation regime, very well justified at small interemitter distances and weak driving. Diagonalization of H_{dip} gives rise to an N-band problem with energies $\omega_m = \omega_e + 2\Omega_{12}\cos[m\pi/(N+1)]$ for m running from 1 to N. The Lindblad term then shows a ranking of levels from superradiant ($m = 1$) to very subradiant ($m = N$) for $d \ll \lambda_e/2$ [5.8]. Moreover, the eigenvectors $|m\rangle = \sqrt{2/(N+1)}\sum_j \sin[mj\pi/(N+1)]\sigma_j^+ |g\rangle^{\otimes N}$ have a specific geometry with almost full symmetry ($m = 1$) to almost full asymmetry ($m = N$). The two distinct cases involving uniform $\mathbf{G} = (g,\ g, \ldots)^\intercal$ and opposite couplings $\mathbf{G} = (g, -g, \ldots)^\intercal$ then almost perfectly address these fully symmetric $|m = 1\rangle$ and asymmetric $|m = N\rangle$ states.

Illustrated in Figs. 5.2(a) and 5.2(b) is a scan of the collective resonances of a ten-emitter chain with $g_i = (-1)^i g$ and $\omega_c = \omega_e$. Both the dip and phase show an off-resonant selection of collective subradiant states. We then selectively target a given state by fitting the cavity resonance to its energy as shown in Figs. 5.2(c) and 5.2(d). To achieve this, we focus around the state $|m = N\rangle$ with energy $\omega_{m=N}$ and we recalculate the state's energy by imposing $\Delta_{\text{eff}}(\delta) = 0$ after which we set $\omega_c = \omega_e - \delta$. We note that, as opposed to the two-emitter case, we cannot find an analytical value for δ but solve for it numerically. It corresponds to a value close to $\omega_{m=N} - \omega_e$. Finally, we compare

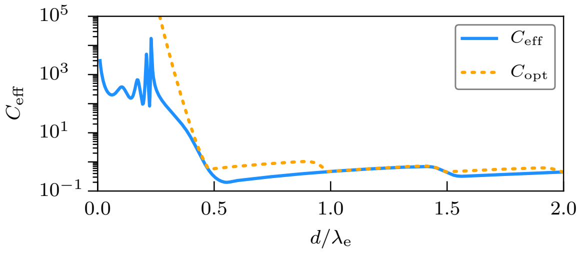

Figure 5.3: *Scaling of effective cooperativity.* $C_{\rm eff}$ for $N = 10$ as a function of $d/\lambda_{\rm e}$. The effective cooperativity (blue, solid curve) is compared to an idealized case of perfect subradiance (yellow, dashed curve). We used $\Delta_{\rm c} = \Delta_{\rm eff} = 0$, $g = \kappa/30$, and $\gamma = \kappa/40$.

the results to an ideal procedure where the components of $\mathbf{G}$ are chosen such that they match the geometry of the target state [Figs. 5.2(e) and 5.2(f)].

The characteristics of the antiresonances can be quantified by $C_{\rm eff}$ (see Fig. 5.3). As above, we assume the asymmetric cavity field profile with $\mathbf{G} = (g, -g, ...)^{\intercal}$ and make a reference plot $C_{\rm opt}$ as a function of d. The optimal cooperativity $C_{\rm opt}$ is obtained from Eq. (5.15) by substituting the decay rate with the minimal eigenvalue of $\boldsymbol{\Gamma}$ [5.24]. In reality, owing to imperfect phase matching to the most subradiant state as well as to the inherent level shifts brought on by the dipole-dipole interactions, the effective gain is more modest. Nevertheless, as suggested by the blue (solid) curve in Fig. 5.3, for $d < 0.5\lambda_{\rm e}$ the enhancement is considerably larger than in the noninteracting quantum emitters case.

5.6 Subradiance using transverse phase gradients

While, in practice, individual phase imprinting on the subwavelength scale is not a trivial task, we present a theoretical illustration using 1D or 2D ensembles transversely placed in the center of a cavity, in the focal point of a higher order TEM mode. In the plane of the emitters, the field profile of a Gaussian-Hermite mode of order m, n is $f(x, y) = A_{mn} H_m\left(\sqrt{2}x/w\right) H_n\left(\sqrt{2}y/w\right) e^{-(x^2+y^2)/w^2}$. Here, $H_n(x)$ is the nth Hermite polynomial, w is the waist of the beam in the center of the cavity assuming a perfectly symmetric cavity and $A_{mn} = \sqrt{2/(\pi 2^{(m+n)} m! n!)}$. Higher order TEM modes exhibit multiple extrema of opposite signs in the transverse profile. For a sufficiently small w (of the order of $\lambda_{\rm e}$), adjacent extrema can be closely spaced (for a $\text{TEM}_{\rm m0}$ mode around $w/\sqrt{m}$) resulting in the desired coupling asymmetry. Note that, in reality, owing to the diffraction limit, optical cavities might not be stable under high transverse mode operation, in which case, an alternative stability regime has to be found.

We illustrate the phase imprinting mechanism for a chain illuminated by a $\text{TEM}_{\rm m0}$ mode with increasing m in Fig. 5.4(a), where now g is the coupling strength in the center of the TEM_{00} mode. While, for small m, the effective cooperativity decreases (owing

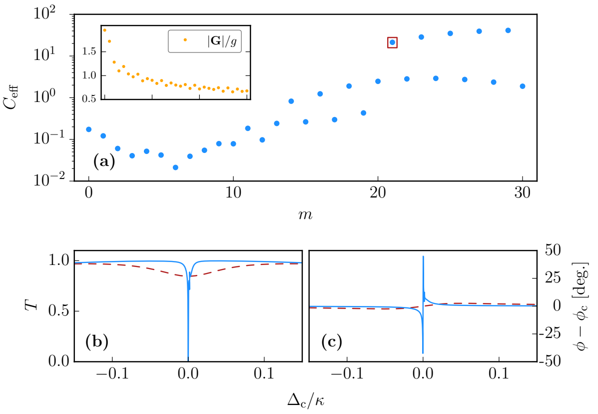

Figure 5.4: *Targeting subradiance via transverse mode driving.* (a) Effective cooperativity as a function of m for $N = 10$ and under illumination with $\mathrm{TEM}_{\mathrm{m}0}$ mode. The inset shows a decrease in cavity coupling $|\mathbf{G}|$. (b),(c) Comparison of antiresonance signatures for TEM_{00} addressing (red, dashed line) vs TEM_{m0} addressing (blue, solid line) with $m = 21$, corresponding to the point enclosed in the red box in (a). The parameters are $d = 0.2\lambda_{\mathrm{e}}$, $w = \lambda_{\mathrm{e}}$, $g = \kappa/30$, $\gamma = \kappa/40$, and $\Delta_{\mathrm{eff}} = 0$ at $\Delta_{\mathrm{c}} = 0$.

to a decrease in $|\mathbf{G}|$), at higher m the alternating field phases are partially addressing asymmetric collective states of high robustness resulting in a considerably enhanced effective cooperativity. The very sharp cavity response for a fixed mode $m = 21$ is shown in Figs. 5.4(b) and 5.4(c) in comparison to the modest results expected for a TEM_{00} illumination. Moreover, we have numerically investigated 2D geometries as well and found, for example, in the case of a 3×3 square array with $d = 0.2\lambda_{\mathrm{e}} = w$ and $g = \kappa/20 = 2\gamma$ (as depicted in Fig. 5.1), an enhancement of effective cooperativity from the bare value $Ng^2/(\kappa\gamma) = 0.9$ to $C_{\mathrm{eff}} \approx 80.1$.

5.7 Conclusions

Tailoring the *collective* dissipative dynamics of N dipole coupled emitters can lead to high effective cooperativity even in the regime $Ng^2/(\kappa\gamma) \ll 1$. The immediate consequence is the occurrence of a narrow antiresonance dip with fast spectral phase switching without the need of strong individual coupling as in Ref. [5.18]. As it applies to narrow atomic transitions, it hints towards applications for precision spectroscopy and quantum network characterization. As opposed to using a lossy cavity field as an engineered bath leading to superradiance as in Ref. [5.25], we only considered the naturally occurring environment provided by the free space radiation modes. The regime treated here is perturbative; i.e. the emitters do not modify the bare mode functions of the cavity mode. Increasing the collective scattering rate close to unity [5.9–5.12, 5.26, 5.27] should result in an interesting regime of cavity QED where the cavity mode functions are strongly modified by a relatively modest number of emitters. A dynamical regime can occur and be exploited for hybrid optomechanical applications [5.28, 5.29] with emitters implanted on vibrating membranes. Stronger phonon-photon interactions could be designed that benefit from narrow collective resonances [5.29]. Similar considerations can be used to analyze metamaterial arrays, where classical analogues of subradiant states are also experimentally seen [5.30].

Acknowledgements

We acknowledge financial support by the Austrian Science Fund (FWF) within the Innsbruck Doctoral School DK-ALM with Grant No. W1259-N27 (D. P.) and Project No. P29318-N27 (H. R) as well as from the Aarhus Universitets Forskningsfond and the Max Planck Society (C. G). We also acknowledge useful discussions with Robert Bettles. The graphs were done with the open source library MATPLOTLIB [5.31].

5.8 Appendix

Vacuum mediated coherent and incoherent dynamics

For a collection of emitters at positions $\mathbf{r}_i$ the collective spontaneous emission rates and the coherent dipole-dipole interaction strengths are [5.20]

$$\gamma_{ij} = \frac{3\gamma}{2} F(\mathbf{k}_\mathrm{e} \cdot \mathbf{r}_{ij}), \tag{5.16}$$

$$\Omega_{ij} = -\frac{3\gamma}{4} G(\mathbf{k}_\mathrm{e} \cdot \mathbf{r}_{ij}), \tag{5.17}$$

respectively. Here, γ is the single emitter free space decay rate, $\mathbf{k}_\mathrm{e}$ is the transition wave vector and $\mathbf{r}_{ij} := \mathbf{r}_i - \mathbf{r}_j$. The functions F and G are defined as

$$F(x) = \left(1 - \cos^2\theta\right) \frac{\sin x}{x} + \left(1 - 3\cos^2\theta\right) \left(\frac{\cos x}{x^2} - \frac{\sin x}{x^3}\right), \tag{5.18}$$

$$G(x) = -\left(1 - \cos^2\theta\right) \frac{\cos x}{x} + \left(1 - 3\cos^2\theta\right) \left(\frac{\sin x}{x^2} + \frac{\sin x}{x^3}\right), \tag{5.19}$$

where θ is the angle drawn by the dipole moment $\boldsymbol{\mu}$ and the separation vector $\mathbf{r}_{ij}$. Note, that for all computations in the paper we assumed the dipoles to be oriented along the y-direction.

Cavity input-output relations

Consider a cavity with two mirrors A and B. We drive the cavity through the mirror B and measure the output at the opposite mirror A. Furthermore, we assume that both mirrors have identical losses of $\kappa/2$. The input-output relations of the total input and output operators (i.e. the input white noise on top of the classical input) for both mirrors are

$$B_{\text{in}} + B_{\text{out}} = \sqrt{\kappa} a, \tag{5.20}$$
$$A_{\text{in}} + A_{\text{out}} = \sqrt{\kappa} a. \tag{5.21}$$

Taking the classical average of the above equations, and assuming the drive through B at amplitude $\langle B_{\text{in}} \rangle = \eta/\sqrt{\kappa}$,

$$\frac{\eta}{\sqrt{\kappa}} + \langle B_{\text{out}} \rangle = \sqrt{\kappa} \langle a \rangle, \tag{5.22}$$
$$\langle A_{\text{out}} \rangle = \sqrt{\kappa} \langle a \rangle. \tag{5.23}$$

Hence, we find that the output at port A reflects the cavity field according to (5.23).

Emitter input noise in the QLE

Writing the input noise in the QLEs for the emitter ensemble is not straightforward as the decay is not diagonal. We first note that for a diagonal Lindblad term describing the damping of a system via multiple damping channels with operators c_j and rates ν_j, the QLE [5.21] of an arbitrary system operator A is

$$\dot{A} = i[H, A] - \sum_j [A, c_j^\dagger] \left(\frac{\nu_j}{2} c + \sqrt{\nu_j} c_{\text{in}} \right) + \sum_j \left(\frac{\nu_j}{2} c^\dagger + \sqrt{\nu_j} c_{\text{in}}^\dagger \right) [A, c], \tag{5.24}$$

where c_{in} is the uncorrelated white input noise $\langle c_{\text{in}}(t) c_{\text{in}}^\dagger(t') \rangle = \delta(t - t')$.

For correlated emitters, it is possible to diagonalize the Lindblad term such that each decay channel is described by a damping operator which is a linear combination of all σ_j^-. We may perform the transformation back to the original non-diagonal form in order to find the input noise terms. To this end, let $\mathbf{T}$ be the real and orthogonal ($\mathbf{T}^{-1} = \mathbf{T}^{\mathrm{T}}$) matrix which diagonalizes the matrix $\mathbf{\Gamma}$ as

$$\operatorname{diag}(\lambda_1, ..., \lambda_N) = \mathbf{T}^{-1} \mathbf{\Gamma} \mathbf{T}, \tag{5.25}$$

where λ_j is the jth eigenvalue of the decay matrix. Defining a set of damping operators

$$\Pi_j^\pm := \sum_k \left(\mathbf{T}^{-1} \right)_{jk} \sigma_k^\pm, \tag{5.26}$$

we may write [5.24]

$$\mathcal{L}_{\text{e}}[\rho] = \sum_i \frac{\lambda_i}{2} \left(2\Pi_i^- \rho \Pi_i^+ - \Pi_i^+ \Pi_i^- \rho - \rho \Pi_i^+ \Pi_i^- \right). \tag{5.27}$$

Obviously, this Lindblad term is diagonal and hence the QLE may be cast into the form given by Eq. (5.24). The input noise terms of the emitter operators $\sigma_{i,\text{in}}^\pm$ follow the transformation rules given by Eq. (5.26). Transforming the QLE for any emitter operator A back into the non-diagonal form gives the usual terms for the deterministic parts. For the noise terms, however, we have

$$\sum_j [A, \Pi_j^+] \sqrt{\lambda_j} \Pi_{j,\mathrm{in}}^- = \sum_j [A, \sigma_j^+] \xi_j(t), \tag{5.28}$$

$$\sum_j [A, \Pi_j^-] \sqrt{\lambda_j} \Pi_{j,\mathrm{in}}^+ = \sum_j [A, \sigma_j^-] \xi_j^\dagger(t), \tag{5.29}$$

where we have implicitly defined our correlated emitter noise terms ξ_j as

$$\xi_j(t) := \sum_{k,l} \mathbf{T}_{jk} \sqrt{\lambda_k} (\mathbf{T}^{-1})_{kl} \sigma_{l,\mathrm{in}}^-. \tag{5.30}$$

Hence, the QLE for any emitter operator A is

$$\dot{A} = i[H, A] - \sum_{ij} [A, \sigma_i^+] \left(\frac{\gamma_{ij}}{2} \sigma_j^- + \xi_i(t) \right) + \sum_{ij} \left(\frac{\gamma_{ij}}{2} \sigma_j^+ + \xi_i^\dagger(t) \right) [A, \sigma_i^-], \tag{5.31}$$

with the spatially correlated white noise ξ_i. From the definition of the noise it is straightforward to show that

$$\langle \xi_i(t) \xi_j^\dagger(t') \rangle = \gamma_{ij} \delta(t - t'). \tag{5.32}$$

Lorentzian shape of the antiresonance

We verify the Lorentzian profile of the antiresonance for a single emitter interacting with a single cavity mode by fitting

$$B(\Delta) = \left| \frac{\kappa}{i\Delta + \kappa} \right|^2 - \left| \frac{\kappa}{i\Delta + \kappa + g^2/(i\Delta + \gamma)} \right|^2, \tag{5.33}$$

with a Lorentzian

$$\left| \frac{\beta s}{i\Delta + \beta} \right|^2, \tag{5.34}$$

where β gives the linewidth while s gives the height. We compute immediately

$$s = 1 - \frac{1}{(1 + C)^2}, \tag{5.35}$$

and from

$$\beta = \sqrt{\frac{2B(0)}{\frac{\partial^2 B}{\partial \Delta^2}(0)}} \tag{5.36}$$

we obtain

$$\beta = \sqrt{\frac{\kappa^2(g^2+\kappa\gamma)^2(g^2+2\kappa\gamma)}{g^6+4g^4\kappa\gamma+2\kappa^3\gamma(\kappa^2+\kappa\gamma+2\gamma^2)+g^2(\kappa^4+6\kappa^2\gamma^2)}}. \tag{5.37}$$

In the limit that both $\gamma, g \ll \kappa$ when only keeping terms of $\mathcal{O}(\kappa^4)$ and higher, this reduces to $\beta \approx \gamma(1+C)$.

The results obtained above are valid for two emitters with the replacements $\gamma \to \gamma_{\text{eff}}$, $C \to C_{\text{eff}}$ and the detuning $\Delta_{\text{c}} = \Delta_{\text{eff}} = \Delta$.

Characterizing the phase of the field

In order to describe the phase analytically, consider that for the single emitter transmission coefficient with $\Delta_{\text{c}} = \Delta_{\text{e}} = \Delta$, we have

$$\frac{\Im\{t\}}{\Re\{t\}} = \frac{\Delta\left(g^2-\Delta^2-\gamma^2\right)}{\kappa\left(\gamma^2+\Delta^2\right)+\gamma g^2}. \tag{5.38}$$

The phase of the field is then given by the arctangent of the above expression. For sufficiently small phase shifts ($C \ll 1$), the phase is well approximated by the argument of the arctangent, such that

$$\frac{\partial}{\partial\Delta}\left(\phi-\phi_{\text{c}}\right) \approx \frac{C\gamma\left(\kappa+\gamma\right)\left(\gamma^2\left(1+C\right)-\Delta^2\right)}{\kappa\left(\gamma^2\left(1+C\right)+\Delta^2\right)^2}. \tag{5.39}$$

Finding the roots of this expression yields the detuning at which the phase shift of the emitter is maximal (positive Δ) or minimal (negative Δ), respectively,

$$\Delta = \pm\gamma\sqrt{1+C}. \tag{5.40}$$

We note, that for large cooperativity the approximation of the phase does no longer hold, however, given that $g, \gamma \ll \kappa$ the position of the maximum and minimum are well approximated by the above detuning even if $C \gg 1$, such that

$$\max_{\Delta}\left[\phi-\phi_{\text{c}}\right] \approx \max_{\Delta}\left[\phi\right] \approx \arctan\left(\frac{C}{2\sqrt{1+C}}\right). \tag{5.41}$$

Here we wrote down the maximum of the phase and note that the minimum only differs from this expression with a negative sign. Now, depending on the sign of Δ, taking the limit of $\gamma \to 0$, the phase either goes to $\pi/2$ or $-\pi/2$, while $\Delta \to 0$, i.e.

$$\lim_{\Delta\to 0^{\pm}} \phi = \pm\frac{\pi}{2}. \tag{5.42}$$

This means that the phase exhibits a jump of magnitude π when crossing the resonance, which can also be seen when computing the slope. To this end, consider the fact that close to the resonance where $|\Delta| \ll \kappa$, the phase is small such that the approximation

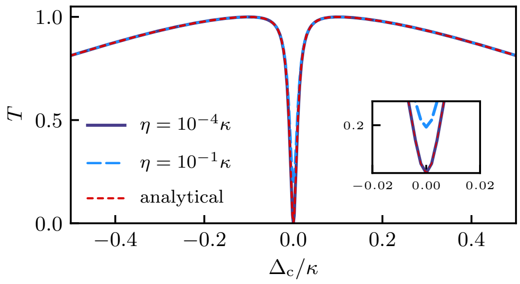

Figure 5.5: *Comparison of analytics with exact numerics.* We compare the full numerics, i.e. without using $\langle\sigma_i^z\rangle \approx -1$, to the analytical result in an extremely subradiant regime for a 4 emitter chain with opposite coupling and without dipole-dipole shifts ($\Omega_{ij} = 0$). The inset is zoomed in on the antiresonance to emphasize the agreement. The parameters are $d = 0.02\lambda_e$, $g = \kappa/20 = 2\gamma$ and $\Delta_e = 0$.

in Eq. (5.39) is valid again. In the limit of $|\Delta| \ll \gamma, g \ll \kappa$ but large cooperativity $g^2 \gg \kappa\gamma$ and hence $g \gg \gamma$, this expression becomes

$$\phi - \phi_c \approx \phi \approx \frac{\Delta}{\gamma}. \tag{5.43}$$

We conclude that the slope at the resonance (where the phase changes sign) is proportional to $1/\gamma$ and hence diverges for $\gamma \to 0$, which is in agreement with the previous result where the phase shift is maximal or minimal at $\Delta \to 0$ depending on whether one takes the left-sided or right-sided limit.

Finally, we note that the above discussion is also applicable to two emitters when replacing $\gamma \to \gamma_{\text{eff}}$, $C \to C_{\text{eff}}$, and setting $\Delta_c = \Delta_{\text{eff}} = \Delta$.

Matching frequency and symmetry of antiresonances

For Fig. 5.2(e),(f) we set

$$\mathbf{G} \approx (0.72, -1.44, 2.03, -2.46, 2.68, -2.68, 2.46, -2.03, 1.44, -0.72)^\intercal \times 10^{-2}\kappa, \tag{5.44}$$

which corresponds to the coefficients of the eigenvector of $\mathbf{\Omega}$ that had the largest overlap with the eigenvector of $\mathbf{\Gamma}$ corresponding to the smallest eigenvalue and therefore the smallest decay rate [5.24]. The frequency was matched by numerically solving $\Delta_{\text{eff}}(\delta) = 0$, which lead to $\delta \approx 0.234\kappa$, and setting $\Delta_c = \Delta_e - \delta$.

Comparison to exact numerics

Let us now comment on the accuracy of the linearization used to obtain the form of eqs. (5.6),(5.7) and (5.9),(5.10). From Fig. 5.5, it is clear that as long as we keep the driving strength η weak enough, the requirements for the low-excitation limit are fulfilled rendering the analytics exact (cf. red dots and dark blue line in Fig. 5.5). If the driving becomes too strong, the excitation of the emitters is no longer negligible resulting in a discrepancy between the full numerics and the analytics (cf. dashed, light blue line in Fig. 5.5). Nevertheless, this does not change the results qualitatively, i.e. there still is a subradiant antiresonance.

6 Publication

Physical Review A, **99**, 043843 (2019)

Enhanced collective Purcell effect of coupled quantum emitter systems[†]

D. Plankensteiner[1], C. Sommer[2], M. Reitz[2], H. Ritsch[1] and C. Genes[2]

[1]*Institut für Theoretische Physik, Universität Innsbruck,*
Technikerstraße 21a, A-6020 Innsbruck, Austria
[2]*Max Planck Institute for the Science of Light,*
Staudtstraße 2, D-91058 Erlangen, Germany

Cavity-embedded quantum emitters show strong modifications of free space radiation properties such as an enhanced decay known as the Purcell effect. The central parameter is the cooperativity C, the ratio of the square of the coherent cavity coupling strength over the product of cavity and emitter decay rates. For a single emitter, C is independent of the transition dipole moment and dictated by geometric cavity properties such as finesse and mode waist. In a recent work [Phys. Rev. Lett. 119, 093601 (2017)] we have shown that collective excitations in ensembles of dipole-dipole coupled quantum emitters show a disentanglement between the coherent coupling to the cavity mode and spontaneous free space decay. This leads to a strong enhancement of the cavity cooperativity around certain collective subradiant antiresonances. Here, we present a quantum Langevin equations approach aimed at providing results beyond the classical coupled dipoles model. We show that the subradiantly enhanced cooperativity imprints its effects onto the cavity output field quantum correlations while also strongly increasing the cavity-emitter system's collective Kerr nonlinear effect.

10.1103/PhysRevA.99.043843

[†] The author of the present thesis performed most analytical and numerical calculations in this paper, with support and vital input from all other authors. The calculations concerning the nonlinear behavior of the system were conducted by C. Sommer. M. Reitz focused on the single-emitter antiresonance and investigated the strong-coupling regime.

6.1 Introduction

The decay rate of a quantum emitter placed in an optical resonator can be strongly modified from its bare free space value. The effect stems from the cavity-induced modification of the optical density of states around the emitter's transition frequency. This was predicted by Purcell in 1946 [6.1] and measured in various systems employing Fabry-Perot optical cavities, plasmonic modes, microwave cavities, etc. [6.2–6.4]. This indicates the possibility of modifying other properties of materials by dressing them with strongly confined resonant optical fields. For example, at the level of single molecules, the Purcell effect has been employed to controllably tailor the ratio of radiative decay rates from excited zero-phonon electronic states to different ground-state vibrational sublevels, thus enhancing the quantum efficiency [6.5]. Experimental and theoretical efforts on the collective strong coupling with organic molecules have shown strong modifications of energy and charge transport [6.6–6.10], Förster resonance energy transfer [6.11, 6.12], chemical reaction rates [6.13, 6.14], etc.

It has been recently predicted [6.15] that the collective dynamics of N interacting quantum emitters in the bad cavity regime exhibits a scaling of the cooperativity with the emitter number N beyond the expected linear one. Such a behavior can be tested by scanning a probe laser around the common resonance of the cavity mode and a single collective state of the coupled emitters. A "hole-burning" effect occurs around the common resonance with a frequency window characterized by the collective Purcell-modified emitter decay rate; i.e., the emitters shut off transmission around this frequency. At the single-particle level, such an antiresonance behavior has been experimentally and theoretically discussed [6.16–6.18]. At the many-particle level, the key point is that closely spaced quantum emitters are subject to intense dipole-dipole interactions leading to collective scattering, as observed experimentally [6.19] and theoretically discussed mostly in one- and two-dimensional geometries [6.19–6.24]. Assuming uniform illumination of the dense ensemble (characterized by particle separations smaller than the wavelength of incoming light), carefully chosen lattice constants can ensure that collective subradiant states are addressed that can efficiently reflect light. Theoretical proposals have been directed towards engineering metamaterials with controlled transparency [6.25], the study of collective motion of atomically thin metamaterials and their interactions with light (optonanomechanics) [6.26–6.28], or the enhancement of nonlinear effects [6.29, 6.30]. Engineered interactions via common coupling of emitters to guided modes of a two-dimensional photonic crystal allowed for the theoretical study of topological quantum optics [6.24]. In one and two dimensions, collective subradiant states have also been studied for the possibility of robust light-storage devices [6.31, 6.32].

One of the widely used theoretical approaches (including in Ref. [6.15]) to describe the response of the quantum emitter ensemble to a driving light field is based on a mapping to a classical problem of coupled dipoles. The simplifying assumption is that in the weak excitation regime the emitters behave as classical oscillators. Collective effects such as superradiance and subradiance are indeed recovered in such an approach. For the treatment in Ref. [6.15], this approach sufficed to give rise to a semianalytical expression of the transmission of light through a cavity containing a collection of interacting emitters; the results indicated a strong modification of the cavity cooperativity around collective antiresonances associated with collective subradiant states. However, questions regarding the quantum effect of subradiance imprinted on the cavity outgoing light were left open. This paper provides an extension to the quantum problem: We focus here on describing the quantum properties of the output cavity fields (transmitted and reflected) as well as of the detected signal. Linearizing the quantum fluctuations around the classical problem allows us to identify regimes of cooperative enhancement of quadrature squeezing and strongly modified signatures in the second-order correlation functions. The treatment of the classical problem beyond the weak excitation regime also allows an analysis of the collective Kerr effect: Around subradiant antiresonances, the third-order nonlinear response of the system is greatly enhanced even for limited numbers of emitters.

The paper is organized as follows: In Sec. 6.2, we introduce the full model of N quantum emitters interacting with a cavity field both within the master equation formalism as well as quantum Langevin equations (QLEs). We proceed by justifying the linear approximation and deriving coupled equations of motion for classical averages as well as fluctuation operators. In Sec. 6.3, we quickly review fundamentals of cavity quantum electrodynamics (cavity QED) with a single emitter such as occurrence of strong coupling, the Purcell effect, and antiresonances. We then derive the classical response in reflection and transmission for two-sided cavities. We introduce operators for the detected signal and provide a formalism for computing variances and correlations for intracavity, outgoing, and detected fields. In Sec. 6.4, we describe some fundamental aspects of vacuum-coupled quantum emitter ensembles exhibiting subradiance and superradiance and investigate some of their entanglement properties. Finally, in Sec. 6.5, we present the dynamics of coupled emitter ensembles inside a common cavity mode, exhibiting a modified collective Purcell effect, and analytically derive cavity transmission properties, equations of motion for the fluctuation operators, and the modification of the collective third-order nonlinearity.

6.2 Cavity dynamics of coupled quantum emitters

We consider an ensemble of N quantum emitters each with a ground state $|g\rangle_j$ and an excited state $|e\rangle_j$ (resonance frequency ω_e) located at $\mathbf{r}_j$. The corresponding raising and lowering operators are denoted by $\hat{S}_j^\dagger$ and $\hat{S}_j$, respectively. The emitters are placed within a plane orthogonal to the cavity axis and inside the waist of a cavity mode at frequency ω_c (see Fig. 6.1). The cavity is laser driven at frequency ω_ℓ with power $\mathcal{P}$ through the left mirror. The coherent cavity mode dynamics are described by the Hamiltonian (in a frame rotating at ω_ℓ),

$$H_\mathrm{cav} = -\hbar\Delta_\mathrm{c}\hat{A}^\dagger\hat{A} + i\hbar\eta\left(\hat{A}^\dagger - \hat{A}\right), \tag{6.1}$$

where $\Delta_\mathrm{c} = \omega_\ell - \omega_\mathrm{c}$ and $\eta = \sqrt{2\mathcal{P}\kappa_\mathrm{A}/(\hbar\omega_\ell)}$. The cavity damping rate is $\kappa = (\kappa_\mathrm{B} + \kappa_\mathrm{A})/2$ (encompassing losses via both left and right mirrors) and occurs via the collapse operator

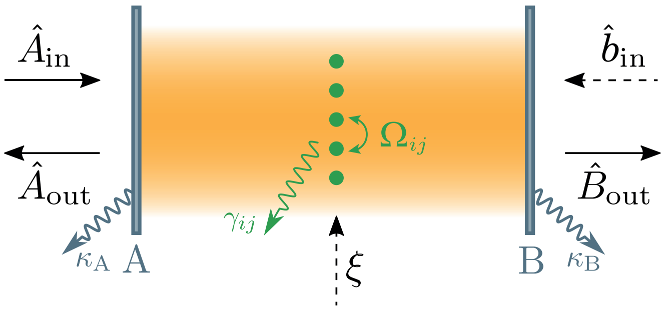

Figure 6.1: *Model schematic.* Optical cavity containing N coupled, closely spaced quantum emitters. The vacuum modes (not supported by the cavity) mediate dipole-dipole interactions with strength Ω_{ij} and induce collective decay with γ_{ij}. Losses through the mirrors occur at rates κ_{A} (left mirror) and κ_{B} (right mirror). The cavity is pumped through the left mirror with nonzero amplitude $\hat{A}_{\text{in}}$ while zero-average noise is entering via the right mirror as $\hat{b}_{\text{in}}$. Transmission and reflection are measured by detecting outgoing nonzero-average operators $\hat{A}_{\text{out}}$ and $\hat{B}_{\text{out}}$.

$\hat{A}$ contained in the Lindblad term, $\mathcal{L}_{\text{c}}[\rho] = \kappa\left(2\hat{A}\rho\hat{A}^\dagger - \hat{A}^\dagger\hat{A}\rho - \rho\hat{A}^\dagger\hat{A}\right)$.

In the single-mode limit, the emitter-cavity interaction is described by the Tavis-Cummings Hamiltonian

$$H_{\text{int}} = \hbar\sum_j g_j\left(\hat{A}^\dagger\hat{S}_j + \hat{A}\hat{S}_j^\dagger\right), \tag{6.2}$$

where each of the emitters couples to the cavity mode with a distinct rate g_j which depends on the emitter positions as well as the cavity mode profile. At dense spacing ($d := |\mathbf{r}_j - \mathbf{r}_{j+1}| < \lambda_{\text{e}}$), one has to account for the vacuum-mediated emitter-emitter interactions via the fields they emit due to their transition dipole moments $\boldsymbol{\mu}$ (assuming all dipole moments to be identical). The total emitter Hamiltonian includes a free part plus the collective coherent dipole-dipole interactions

$$H_{\text{e}} = -\hbar\sum_j \Delta_{\text{e}}\hat{S}_j^\dagger\hat{S}_j + \hbar\sum_{j\neq k}\Omega_{jk}\hat{S}_j\hat{S}_k^\dagger, \tag{6.3}$$

where $\Delta_{\text{e}} = \omega_\ell - \omega_{\text{e}}$. The dipole-dipole interactions governed by the frequencies Ω_{ij} are derived by eliminating the degrees of freedom for the surrounding vacuum modes excluding the single mode supported by the cavity (see Appendix 6.7). Doing so additionally leads to dissipation of the emitters in the form of collective decay with rates $\gamma_{ij} = \gamma h_{ij}$ (where h_{ij} is maximally unity for $i = j$) that are described by the Lindblad term [6.33]

$$\mathcal{L}_{\text{e}}[\rho] = \sum_{j,k}\gamma h_{jk}\left(2\hat{S}_j\rho\hat{S}_k^\dagger - \hat{S}_j^\dagger\hat{S}_k\rho - \rho\hat{S}_j^\dagger\hat{S}_k\right). \tag{6.4}$$

While full numerical simulations for moderate numbers of quantum emitters can be carried out based on the master equation description, $\partial_t \rho(t) = i[\rho(t), H]/\hbar + \mathcal{L}[\rho(t)]$, we move to an equivalent quantum Langevin approach (see Appendix 6.7), which allows for the derivation of analytical results,

$$\dot{\hat{A}} = -(\kappa - i\Delta_{\mathrm{c}})\hat{A} - i\sum_j g_j \hat{S}_j + \eta + \sqrt{\kappa_{\mathrm{A}}}\hat{a}_{\mathrm{in}} + \sqrt{\kappa_{\mathrm{B}}}\hat{b}_{\mathrm{in}}, \tag{6.5a}$$

$$\dot{\hat{S}}_j = -(\gamma - i\Delta_{\mathrm{e}})\hat{S}_j + ig_j\hat{A}\hat{S}^z_j + \sum_{k\neq j}\left(i\Omega_{jk} + \gamma_{jk}\right)\hat{S}^z_j\hat{S}_k - \sqrt{2\gamma}\bar{\xi}_j(t), \tag{6.5b}$$

$$\dot{\hat{S}}^z_j = -2\gamma(\hat{S}^z_j + 1) + 2ig_j\left(\hat{A}^\dagger\hat{S}_j - \hat{S}^\dagger_j\hat{A}\right) - \sum_{k\neq j} 2\gamma_{jk}\left(\hat{S}^\dagger_j\hat{S}_k + \hat{S}^\dagger_k\hat{S}_j\right) + \sqrt{2\gamma}\bar{\xi}^z_j(t). \tag{6.5c}$$

The convention in this paper is that nonzero-average operators are denoted by capital letters while lowercase letters denote fluctuation operators. The left mirror allows for a nonzero-average input $\hat{A}_{\mathrm{in}} = \eta/\sqrt{\kappa_{\mathrm{A}}} + \hat{a}_{\mathrm{in}}$ with the zero-average white-noise term fulfilling $\langle \hat{a}_{\mathrm{in}}(t)\hat{a}^\dagger_{\mathrm{in}}(t')\rangle = \delta(t - t')$ (while all other correlations vanish). The right mirror allows for white noise only with all correlations vanishing except for $\langle \hat{b}_{\mathrm{in}}(t)\hat{b}^\dagger_{\mathrm{in}}(t')\rangle = \delta(t - t')$. One can also define an effective input operator,

$$\hat{C}_{\mathrm{in}} = \sqrt{\frac{\kappa_{\mathrm{A}}}{\kappa_{\mathrm{A}} + \kappa_{\mathrm{B}}}}\hat{A}_{\mathrm{in}} + \sqrt{\frac{\kappa_{\mathrm{B}}}{\kappa_{\mathrm{A}} + \kappa_{\mathrm{B}}}}\hat{b}_{\mathrm{in}}, \tag{6.6}$$

in terms of which the QLE for the cavity field shows a single compound input noise added as $\hat{c}_{\mathrm{in}}$ with $\langle \hat{c}_{\mathrm{in}}(t)\hat{c}^\dagger_{\mathrm{in}}(t')\rangle = \delta(t - t')$ and $\hat{c}_{\mathrm{in}} = \hat{C}_{\mathrm{in}} - \eta/\sqrt{2\kappa}$. On the quantum emitter side, we have defined effective noise operators affecting the emitters (see Appendix 6.7 for more details) $\bar{\xi}_j(t) = \hat{S}^z_j\xi_j(t)$ and $\bar{\xi}^z_j(t) = 2\left(\hat{S}^\dagger_j\xi_j(t) + \xi^\dagger_j(t)\hat{S}_j\right)$. In the absence of classical drive terms for the quantum emitters, the noises are zero-average and δ correlated in time; however, as the emitters are placed in the near field of their neighbors, spatial correlations are included in the pairwise decay terms, i.e., $\langle \xi_i(t)\xi^\dagger_j(t')\rangle = h_{ij}\delta(t - t')$. A linearization procedure can be applied around the average values ($\alpha = \langle \hat{A}\rangle$, $\beta_j = \langle \hat{S}_j\rangle$ and $z_j = \langle \hat{S}^z_j\rangle$), introducing zero-average fluctuation operators $\hat{a} = \hat{A} - \alpha$, $\hat{\sigma}_j = \hat{S}_j - \beta_j$, and $\hat{\sigma}^z_j = \hat{S}^z_j - z_j$, respectively. We then proceed by neglecting products of fluctuation operators. This allows us to derive two distinct sets of equations, one for the classical averages (which still includes nonlinear behavior as long as we keep the equation for the population inversion) and one set for the fluctuation operators (linearized). For the classical averages, we find

$$\dot{\alpha} = -(\kappa - i\Delta_{\mathrm{c}})\alpha - i\sum_j g_j\beta_j + \eta, \tag{6.7a}$$

$$\dot{\beta}_j = -(\gamma - i\Delta_{\mathrm{e}})\beta_j + ig_j\alpha z_j + \sum_{k\neq j}\left(i\Omega_{jk} + \gamma_{jk}\right) z_j\beta_k, \tag{6.7b}$$

$$\dot{z}_j = -2\gamma\left(z_j + 1\right) + 2ig_j\left(\alpha^*\beta_j - \beta_j^*\alpha\right) - 4\sum_{k\neq j}\gamma_{jk}\Re\left\{\beta_j^*\beta_k\right\}. \tag{6.7c}$$

Note that, in this limit, we can express the inversion average as $z_j = \langle 2\hat{S}_j^\dagger\hat{S}_j - 1\rangle \approx 2|\beta_j|^2 - 1$ as a second-order perturbation in η. Next-order terms, stemming from two fluctuation operators averages such as $\langle\hat{\sigma}_j^\dagger\hat{\sigma}_j\rangle$, are already fourth-order corrections in η. We can then write QLEs for the quantum fluctuations of all operators,

$$\dot{\hat{a}} = -\left(\kappa - i\Delta_{\mathrm{c}}\right)\hat{a} - i\sum_j g_j\hat{\sigma}_j + \sqrt{\kappa_{\mathrm{A}}}\hat{a}_{\mathrm{in}} + \sqrt{\kappa_{\mathrm{B}}}\hat{b}_{\mathrm{in}}, \tag{6.8a}$$

$$\dot{\hat{\sigma}}_j = -\left(\gamma - i\Delta_{\mathrm{e}}\right)\hat{\sigma}_j + ig_j\left(z_j\hat{a} + \alpha\hat{\sigma}_j^z\right) + \sum_{k\neq j}\left(i\Omega_{jk} + \gamma_{jk}\right)\left(z_j\hat{\sigma}_k + \beta_k\hat{\sigma}_j^z\right) - \sqrt{2\gamma}\bar{\xi}_j(t), \tag{6.8b}$$

$$\begin{aligned}\dot{\hat{\sigma}}_j^z = {}& -2\gamma\hat{\sigma}_j^z + 2ig_j\left(\alpha^*\hat{\sigma}_j + \beta_j\hat{a}^\dagger - \alpha\hat{\sigma}_j^\dagger - \beta_j^*\hat{a}\right) - 2\sum_{k\neq j}\gamma_{jk}\left(\beta_j^*\hat{\sigma}_k + \beta_k\hat{\sigma}_j^\dagger + \text{H.c.}\right) + \\ & + \sqrt{2\gamma}\bar{\xi}_j^z(t).\end{aligned} \tag{6.8c}$$

Let us now discuss the correlations of the emitter noise terms. Assuming the environment for the emitter input noise to be in a vacuum state, the effective noise terms are also of zero average. However, they have the following nonvanishing correlations,

$$\langle\bar{\xi}_j(t)\bar{\xi}_k^\dagger(t')\rangle = \begin{cases}\delta(t-t'), & \text{if } j = k\\ h_{jk}z_jz_k\delta(t-t'), & \text{if } j \neq k\end{cases} \tag{6.9a}$$

$$\langle\bar{\xi}_j^z(t)\bar{\xi}_k^z(t')\rangle = \begin{cases}2\left(z_j + 1\right)\delta(t-t'), & \text{if } j = k\\ 4h_{jk}\beta_j^*\beta_k\delta(t-t'), & \text{if } j \neq k\end{cases} \tag{6.9b}$$

$$\langle\bar{\xi}_j^z(t)\bar{\xi}_k^\dagger(t')\rangle = \begin{cases}-2\beta_j^*\delta(t-t'), & \text{if } j = k\\ 2h_{jk}z_k\beta_j^*\delta(t-t'), & \text{if } j \neq k\end{cases} \tag{6.9c}$$

and $\langle\bar{\xi}_j(t)\bar{\xi}_k^z(t')\rangle = \langle\bar{\xi}_k^z(t')\bar{\xi}_j^\dagger(t)\rangle^*$.

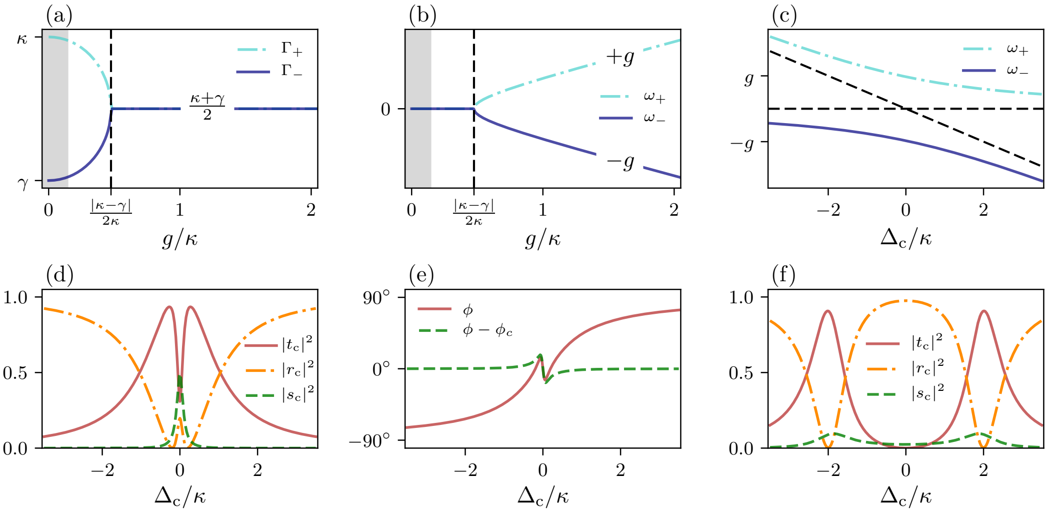

Figure 6.2: *Single emitter cavity mode hybridization.* Plot of hybrid cavity-emitter decay rates (a) and frequencies (b) when sweeping the coupling g past the strong coupling onset point of $g = |(\kappa - \gamma)/2|$ (in the resonant case). The grey region shows the weak coupling but strong cooperativity regime where the Purcell effect shows up as a modification of the emitter's radiative rate. (c) Standard picture of avoided resonances in the strong-coupling regime when the cavity detuning is scanned. (d) Intensity of transmitted, reflected, and scattered fields of an emitter-cavity system in the Purcell regime (antiresonance regime) for a laser scan around the resonance. The parameters are $g = \kappa/5$, $\gamma = \kappa/20$. (e) Cavity phase shift and emitter-only induced phase shift in the same regime. (f) Cavity response in transmission and reflection as well as scattered field showing the signature of polaritons in the strong coupling regime ($g = 2\kappa$).

6.3 Single-emitter antiresonance spectroscopy

Let us first fully analyze the emitter-cavity mode hybridization by solving Eqs. (6.5) for a single emitter. Steady-state solutions for the operator averages already suffice to provide an overview of effects such as cavity strong coupling (occurrence of polaritons), antiresonances, and the Purcell modification of the emitter's decay rate. We then make the connection between the intra-cavity dynamics and the amplitude and phase transmission/reflection for asymmetric two-sided cavities. In the next step, we describe the quantum properties of the field inside the cavity and of the output fields (in transmission/reflection). By assuming a particular detection scheme which allows us to define nondimensional operators for the detected field, we analyze the connection between the detected signal and the continuous output fields. Finally, we compute the next-order correction to the steady-state solution to derive the scaling of the system's Kerr nonlinearity.

6.3.1 Regimes of interaction

The classical equations of motion for the cavity field amplitude and the dipole of the quantum emitter are sufficient to characterize the different regimes of interaction inside the optical cavity,

$$\dot{\alpha} = -\left(\kappa - i\Delta_{\mathrm{c}}\right)\alpha - ig\beta + \eta, \tag{6.10a}$$

$$\dot{\beta} = -(\gamma - i\Delta_{\mathrm{e}})\beta - ig\alpha. \tag{6.10b}$$

We denoted by κ the effective decay rate via both mirrors $\kappa = (\kappa_A + \kappa_B)/2$. The diagonalization of the above equations (under resonance conditions, i.e., fixed $\Delta_{\mathrm{c}} = \Delta_{\mathrm{e}} = 0$) leads to the hybridized decay rates and frequencies,

$$\Gamma_{\pm} = \frac{\kappa+\gamma}{2} \pm \Re\left\{\sqrt{\left(\frac{\kappa-\gamma}{2}\right)^2 - g^2}\right\}, \tag{6.11a}$$

$$\omega_{\pm} = \pm\Im\left\{\sqrt{\left(\frac{\kappa-\gamma}{2}\right)^2 - g^2}\right\}. \tag{6.11b}$$

The threshold $g > |(\kappa-\gamma)/2|$ indicates the onset of the strong coupling regime where the two frequencies combine into distinct polariton branches. Far above this threshold the polaritons are symmetrically displaced by $\pm g$ from the original energies [see Fig. 6.2(b)]. The decay rates show a different behavior as they already hybridize before the onset of strong coupling and ultimately reach the algebraic average $(\kappa+\gamma)/2$. We will be mostly interested in the weak coupling regime, highlighted in grey in Figs. 6.2(a) and 7.2(b), where for $\gamma \ll \kappa$, a strong modification of the emitter bare decay rate by a factor $1 + C$ occurs [where C is the cooperativity defined as $C = g^2/(\kappa\gamma)$]. This is the Purcell effect and one can cast the Purcell factor [6.1] given by $F_{\mathrm{p}} = 6\pi c^3 Q/(\omega_{\mathrm{e}}^3 V)$ in terms of the cooperativity parameter. Using the definition of the quality factor $Q = \omega_{\mathrm{c}}/\kappa$, the dipole coupling strength $g = \mu\sqrt{\omega_{\mathrm{c}}/(2\epsilon_0\hbar V)}$ and the free space decay rate $\gamma = \omega_{\mathrm{e}}^3\mu^2/(3\pi\hbar c^3\epsilon_0)$, we can express the Purcell factor as $F_{\mathrm{p}} = 4C$.

6.3.2 Antiresonance: Transmission, reflection, and absorption

Assuming steady state, we set the derivatives to zero in Eqs. (6.10) and obtain

$$\alpha = \frac{-ig\beta + \eta}{\kappa - i\Delta_{\mathrm{c}}}, \tag{6.12a}$$

$$\beta = \frac{-ig\alpha}{\gamma - i\Delta_{\mathrm{e}}}. \tag{6.12b}$$

Under the considered approximations, the dipole responds linearly to the intracavity field; the cavity field in turn is the result of interference between the pump signal and the dipole re-radiated amplitude. Solving the above equations, we find

$$\alpha = \frac{\eta\,(\gamma - i\Delta_{\mathrm{e}})}{(\kappa - i\Delta_{\mathrm{c}})\,(\gamma - i\Delta_{\mathrm{e}}) + g^2}, \tag{6.13a}$$

$$\beta = \frac{-ig\eta}{(\kappa - i\Delta_{\mathrm{c}})\,(\gamma - i\Delta_{\mathrm{e}}) + g^2}. \tag{6.13b}$$

The cavity output signal consists of three parts: The reflected (r_{c}), transmitted (t_{c}), and scattered (s_{c}) field. The latter is the field leaking out of the sides of the cavity due to spontaneous decay of the emitter. In order to investigate these three parts, we make use of the input-output relations written separately at both left and right mirrors,

$$\hat{A}_{\mathrm{in}} + \hat{A}_{\mathrm{out}} = \sqrt{\kappa_{\mathrm{A}}}\hat{A}, \tag{6.14a}$$

$$\hat{b}_{\mathrm{in}} + \hat{B}_{\mathrm{out}} = \sqrt{\kappa_{\mathrm{B}}}\hat{A}. \tag{6.14b}$$

As specified above, driving is done through the left mirror such that $\langle \hat{A}_{\mathrm{in}} \rangle = \eta/\sqrt{\kappa_{\mathrm{A}}}$. Averaging of the equations above thus leads to

$$\langle \hat{B}_{\mathrm{out}} \rangle = \sqrt{\kappa_{\mathrm{B}}}\alpha, \tag{6.15a}$$

$$\eta/\sqrt{\kappa_{\mathrm{A}}} + \langle \hat{A}_{\mathrm{out}} \rangle = \sqrt{\kappa_{\mathrm{A}}}\alpha. \tag{6.15b}$$

The amplitude transmission coefficient t_{c} and the reflection coefficient r_{c}, respectively, are then given by

$$t_{\mathrm{c}} = \frac{\langle \hat{B}_{\mathrm{out}} \rangle}{\langle \hat{A}_{\mathrm{in}} \rangle} = \frac{\sqrt{\kappa_{\mathrm{A}}\kappa_{\mathrm{B}}}}{\eta}\alpha, \tag{6.16a}$$

$$r_{\mathrm{c}} = \frac{\langle \hat{A}_{\mathrm{out}} \rangle}{\langle \hat{A}_{\mathrm{in}} \rangle} = \frac{\kappa_{\mathrm{A}}}{\eta}\alpha - 1 = t_{\mathrm{c}}\sqrt{\frac{\kappa_{\mathrm{A}}}{\kappa_{\mathrm{B}}}} - 1. \tag{6.16b}$$

While generally the cavity properties strongly depend on the mirror asymmetry, let us focus on a perfectly balanced cavity where $\kappa = \kappa_{\mathrm{A}} = \kappa_{\mathrm{B}}$ and express the complex transmission amplitude as

$$t_{\mathrm{c}} = \frac{\kappa}{\kappa - i\Delta_{\mathrm{c}} + g^2/(\gamma - i\Delta_{\mathrm{e}})}, \tag{6.17}$$

while the reflectivity is immediately derived as $r = -1 + t$. This expression already contains the phenomenon of emitter antiresonances [6.15, 6.17, 6.34], where the resonantly driven dipole oscillates in a way to counteract the cavity drive leading to a local minimum of transmission [6.35].

The respective intensities are given by the absolute squares of the complex coefficients. We note, that it is possible to write down a similar input-output relation for the scattered field in the linearized regime. However, for more general purposes, one can use the fact that the sum of all the intensities has to be conserved, namely $|r_{\mathrm{c}}|^2 + |t_{\mathrm{c}}|^2 + |s_{\mathrm{c}}|^2 = 1$.

This gives the scattered intensity $|s_\mathrm{c}|^2 = 1 - |t_\mathrm{c} - 1|^2 - |t_\mathrm{c}|^2 = 2\left(\Re\{t_\mathrm{c}\} - |t_\mathrm{c}|^2\right)$. At resonance ($\Delta_\mathrm{c} = \Delta_\mathrm{e} = 0$), we can express all the intensities in terms of the cooperativity,

$$|t_\mathrm{c}|^2 = \frac{1}{(1+C)^2}, \tag{6.18a}$$

$$|r_\mathrm{c}|^2 = \frac{C^2}{(1+C)^2}, \tag{6.18b}$$

$$|s_\mathrm{c}|^2 = \frac{2C}{(1+C)^2}. \tag{6.18c}$$

An interesting point here is the scaling of the scattered field with the cooperativity. Namely, not only does it vanish for small cooperativity (where the emitter is simply never excited and thus cannot scatter), but also for $C \gg 1$ the radiation to the side is suppressed. Since the transmission vanishes as well in this regime, the entire input field is reflected [see Fig. 6.2(f)].

The phase shift of the field that passes through the cavity is given by the transmission coefficient as

$$\phi = \mathrm{Arg}(t_\mathrm{c}) = \arctan\left(\frac{\Im\{t_\mathrm{c}\}}{\Re\{t_\mathrm{c}\}}\right). \tag{6.19}$$

While this corresponds to the phase shift caused by the hybrid system, in the resonant case one can approximate the phase shift caused only by the emitter by subtracting the empty-cavity response $\phi_\mathrm{c} = \arctan\left(\Delta_\mathrm{c}/\kappa\right)$ [see Fig. 6.2(e)].

6.3.3 Intracavity steady state

In a first step, we will write the QLEs in the single emitter case and solve for the intra-cavity fluctuation operators in steady state. For $N = 1$, Eqs. (6.8) reduce to

$$\dot{\hat{a}} = -\left(\kappa - i\Delta_\mathrm{c}\right)\hat{a} - ig\hat{\sigma} + \sqrt{\kappa}\hat{a}_\mathrm{in}(t) + \sqrt{\kappa}\hat{b}_\mathrm{in}(t), \tag{6.20a}$$

$$\dot{\hat{\sigma}} = -\left(\gamma - i\Delta_\mathrm{e}\right)\hat{\sigma} + ig\left(\alpha\hat{\sigma}^z + z\hat{a}\right) - \sqrt{2\gamma}\bar{\xi}(t), \tag{6.20b}$$

$$\dot{\hat{\sigma}}^z = -2\gamma\hat{\sigma}^z + 2ig\left(\alpha^*\hat{\sigma} + \beta\hat{a}^\dagger - \alpha\hat{\sigma}^\dagger - \beta^*\hat{a}\right) + \sqrt{2\gamma}\bar{\xi}^z(t).$$

The correlation functions for the single-emitter input noise are derived from Eqs. (6.9a)–(6.9c) for $N = 1$. We proceed by casting the above set of equations in a more convenient matrix form with the following definitions:

$$\mathbf{v} := \begin{pmatrix} \hat{a} \\ \hat{a}^\dagger \\ \hat{\sigma} \\ \hat{\sigma}^\dagger \\ \hat{\sigma}^z \end{pmatrix}, \quad \mathbf{v}_{\text{in}} := \begin{pmatrix} \hat{a}_{\text{in}} \\ \hat{a}_{\text{in}}^\dagger \\ \hat{b}_{\text{in}} \\ \hat{b}_{\text{in}}^\dagger \\ \bar{\xi} \\ \bar{\xi}^\dagger \\ \bar{\xi}^z \end{pmatrix}. \tag{6.21}$$

The system dynamics can then be written as a matrix-vector differential equation,

$$\dot{\mathbf{v}} = \mathbf{M}\mathbf{v} + \mathbf{N}\mathbf{v}_{\text{in}}(t). \tag{6.22}$$

The matrix $\mathbf{M}$ is a drift matrix that is completely determined by steady-state expectation values,

$$\mathbf{M} = \begin{pmatrix} -(\kappa - i\Delta_{\text{c}}) & 0 & -ig & 0 & 0 \\ 0 & -(\kappa + i\Delta_{\text{c}}) & 0 & ig & 0 \\ igz & 0 & -(\gamma - i\Delta_{\text{e}}) & 0 & ig\alpha \\ 0 & -igz & 0 & -(\gamma + i\Delta_{\text{e}}) & -ig\alpha^* \\ -2ig\beta^* & 2ig\beta & 2ig\alpha^* & -2ig\alpha & -2\gamma \end{pmatrix}. \tag{6.23}$$

The input noise terms are multiplied with the matrix $\mathbf{N}$, which is given by the decay rates for each dissipation channel,

$$\mathbf{N} = \begin{pmatrix} \sqrt{\kappa} & 0 & \sqrt{\kappa} & 0 & 0 & 0 & 0 \\ 0 & \sqrt{\kappa} & 0 & \sqrt{\kappa} & 0 & 0 & 0 \\ 0 & 0 & 0 & 0 & -\sqrt{2\gamma} & 0 & 0 \\ 0 & 0 & 0 & 0 & 0 & -\sqrt{2\gamma} & 0 \\ 0 & 0 & 0 & 0 & 0 & 0 & \sqrt{2\gamma} \end{pmatrix}. \tag{6.24}$$

Formal integration of the fluctuation operators' QLEs, Eq. (6.22), leads to

$$\mathbf{v}(t) = e^{\mathbf{M}t}\mathbf{v}(0) + \int_0^t dt' e^{\mathbf{M}(t-t')}\mathbf{N}\mathbf{v}_{\text{in}}(t'), \tag{6.25}$$

where the first term is the transient solution. Assuming that the system is stable, i.e., all the eigenvalues of the drift matrix have negative real parts, this solution vanishes at large times and the system reaches a unique steady state independent of the initial conditions. One can then fully analyze the properties of the system in steady state by looking at the fluctuation correlation matrix $\mathbf{V} = \langle \mathbf{v}(t)\mathbf{v}^\top(t) \rangle$. The correlations of all input noises can be jointly written as $\langle \mathbf{v}_{\text{in}}(t)\mathbf{v}_{\text{in}}^\top(t') \rangle = \delta(t - t')\mathbf{C}$, where the noise correlation matrix is

$$\mathbf{C} = \begin{pmatrix} 0 & 1 & 0 & 0 & 0 & 0 & 0 \\ 0 & 0 & 0 & 0 & 0 & 0 & 0 \\ 0 & 0 & 0 & 1 & 0 & 0 & 0 \\ 0 & 0 & 0 & 0 & 0 & 0 & 0 \\ 0 & 0 & 0 & 0 & 0 & 1 & -2\beta \\ 0 & 0 & 0 & 0 & 0 & 0 & 0 \\ 0 & 0 & 0 & 0 & 0 & -2\beta^* & 2\left(1+z\right) \end{pmatrix}. \tag{6.26}$$

A diffusion matrix can afterwards be constructed $\mathbf{D} = \mathbf{N}\mathbf{C}\mathbf{N}^\top$ and a simplified equation involving only the correlation and the diffusion matrix can be obtained (see details in Appendix 6.7),

$$\mathbf{M}\mathbf{V} + \mathbf{V}\mathbf{M}^\top = -\mathbf{D}. \tag{6.27}$$

This is known as the Lyapunov equation and it allows one to derive all two-point operator correlations for the system in the long-time limit (steady-state condition).

6.3.4 Output fields

To derive quantum properties of the field exiting the cavity, we use the input-output relations such as the ones in Eq. (6.14). All input-output relations combined into a convenient vector form read

$$\mathbf{v}_{\text{out}}(t) = \mathbf{N}^\top \mathbf{v}(t) - \mathbf{v}_{\text{in}}(t). \tag{6.28}$$

In the time domain, the output field is not δ correlated, which makes calculations more cumbersome. However, a transformation to the Fourier domain provides an immediate simplification as the output is obtained as a matrix multiplication of the input, ensuring that the δ correlations in the frequency domain are still valid. First, we express the output Fourier components in terms of input noise,

$$\mathbf{v}_{\text{out}}(\omega) = \mathbf{F}(\omega)\mathbf{v}_{\text{in}}(\omega), \tag{6.29}$$

where $\mathbf{F}(\omega) := [\mathbf{N}^\top \left(i\omega\mathbb{1} - \mathbf{M}\right)^{-1} \mathbf{N} - \mathbb{1}]$. This allows one to compute any correlations

$$\langle \mathbf{v}_{\text{out}}(\omega)\mathbf{v}_{\text{out}}^\top(\omega')\rangle = \boldsymbol{\mathcal{S}}_{\text{out}}(\omega)\delta(\omega+\omega'), \tag{6.30}$$

contained in the frequency spectrum matrix $\boldsymbol{\mathcal{S}}_{\text{out}}$ compactly expressed as

$$\boldsymbol{\mathcal{S}}_{\text{out}}(\omega) = \mathbf{F}(\omega)\mathbf{C}\mathbf{F}^\top(-\omega). \tag{6.31}$$

As we will see in the following, the output spectrum matrix contains all the information required to compute quantum properties such as squeezing of the output field, or of the detected field, or the variance of the detected photon number.

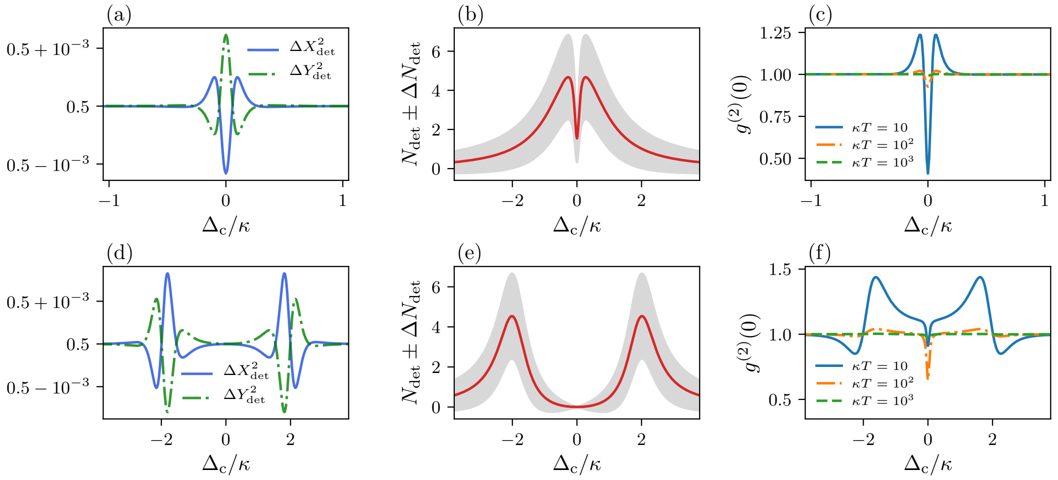

Figure 6.3: *Detected signal with a single emitter.* Plots of quadrature squeezing [(a),(d)], average photon number and variance (shaded area) [(b),(e)], and the photon correlation function $g^{(2)}(0)$ [(c),(f)] for a laser scan around the resonance (a)–(c) in the Purcell regime ($g = 0.2\kappa$) and (d)–(f) in the strong-coupling regime ($g = 2\kappa$), respectively. The remaining parameters here are $\gamma = \kappa/20$, $\eta = \kappa/20$, and $T = 10^3\kappa^{-1}$. In (c) and (f), the effect of increasing integration time on bunching and antibunching is illustrated.

6.3.5 Time-integrated signal detection

We define detected field operators at some time t (chosen already after reaching steady state) by integrating over the continuous output fields during the detection window $t - T$ to $t + T$. While in Ref. [6.15] we have analyzed the antiresonance behavior in terms of the classical average of the intracavity field amplitude, we can here compute expectation values of the detected field photon number operator and its variance. We provide analytical expressions for these quantities as well as for the quadrature variances and the second-order correlation function at zero time $g^{(2)}(0)$.

Classical signal

The classical detected signal is defined as the time integral (over the detection window $2T$) of the continuous output field amplitude expectation value. The reflected signal is

$$\langle \hat{A}_{\mathrm{det}}(t)\rangle = \frac{1}{\sqrt{2T}}\int_{t-T}^{t+T} dt'\ \langle \hat{A}_{\mathrm{out}}(t')\rangle = \sqrt{\frac{2T\eta^2}{\kappa}}r_{\mathrm{c}}, \tag{6.32}$$

while in transmission one detects

$$\langle \hat{B}_{\mathrm{det}}(t)\rangle = \frac{1}{\sqrt{2T}}\int_{t-T}^{t+T} dt'\ \langle \hat{B}_{\mathrm{out}}(t')\rangle = \sqrt{\frac{2T\eta^2}{\kappa}}t_{\mathrm{c}}. \tag{6.33}$$

The definition of the operators above fulfills the canonical commutation relations $[\hat{A}_{\text{det}}, \hat{A}^\dagger_{\text{det}}] = 1$ and $[\hat{B}_{\text{det}}, \hat{B}^\dagger_{\text{det}}] = 1$. The transmission of the cavity shows the signature of the antiresonance (both in amplitude as a dip and in phase as a rapid phase switch when the laser is swept across the common emitter-field resonance) as it is simply proportional to the cavity transmission function derived in Ref. [6.15]. Notice that for weak pumping, especially around the resonance dip, the integration time has to be large in order to distinguish the classical signal from shot noise.

Fluctuation correlation matrix of the detected field

According to the approach we employed to obtain higher order correlations of the output, let us define a vector of detected zero-average operators,

$$\mathbf{v}_{\text{det}}(t) = \frac{1}{\sqrt{2T}} \int_{t-T}^{t+T} dt' \; \mathbf{v}_{\text{out}}(t'). \tag{6.34}$$

Note, that the component $v^1_{\text{det}}(t) = \hat{a}_{\text{det}}(t)$ is the detected signal fluctuation operator in reflection, and similarly $v^3_{\text{det}}(t) = \hat{b}_{\text{det}}(t)$ is the detected signal fluctuation operator in transmission. Two-point correlations are needed in order to find the expectation value of the photon number. Therefore, one has to relate the correlation matrix of the output fields with the intra-cavity correlations. As a general formulation, we write the whole correlation matrix of the detected quantities as

$$\mathbf{V}_{\text{det}}(t) = \frac{1}{2T} \int_{t-T}^{t+T} dt' \int_{t-T}^{t+T} dt'' \left\langle \mathbf{v}_{\text{out}}(t')\mathbf{v}_{\text{out}}(t'')^\top \right\rangle . \tag{6.35}$$

We now use the Fourier transformation of the output operators (see Appendix 6.7) to relate the detected correlation matrix to the spectrum matrix of output operators,

$$\mathbf{V}_{\text{det}} = \frac{1}{\pi T} \int_{-\infty}^{\infty} d\omega \left[\frac{\sin^2 \omega T}{\omega^2} \right] \boldsymbol{\mathcal{S}}_{\text{out}}(\omega). \tag{6.36}$$

In general, one can already compute the correlation matrix from this expression. However, for long integration times (longer than the inverse of the characteristic linewidth of the spectrum), the sinc function inside the integral picks out only frequencies close to zero (around the laser frequency). This allows one to replace the sinc function with a δ function and the detected correlation matrix is given by the simple expression

$$\mathbf{V}_{\text{det}} = \boldsymbol{\mathcal{S}}_{\text{out}}(0). \tag{6.37}$$

We will use this result in the following subsections to derive expressions in terms of matrix elements of $\boldsymbol{\mathcal{S}}_{\text{out}}(0)$ for the variance in quadratures, photon number expectation value and variance, and the second-order correlation function. The detected time-integrated quadratures in transmission are

$$\hat{X}_{\mathrm{det}} = \frac{1}{\sqrt{2}}\left(\hat{B}_{\mathrm{det}} + \hat{B}^{\dagger}_{\mathrm{det}}\right), \tag{6.38a}$$

$$\hat{Y}_{\mathrm{det}} = \frac{-i}{\sqrt{2}}\left(\hat{B}_{\mathrm{det}} - \hat{B}^{\dagger}_{\mathrm{det}}\right), \tag{6.38b}$$

with similar expressions for the reflected field. With the help of the above expressions for the correlation matrix one can compute their respective variances as

$$\Delta X^2_{\mathrm{det}} = \frac{1}{2} + \mathcal{S}^{43}_{\mathrm{out}}(0) + \Re\left[\mathcal{S}^{33}_{\mathrm{out}}(0)\right], \tag{6.39a}$$

$$\Delta Y^2_{\mathrm{det}} = \frac{1}{2} + \mathcal{S}^{43}_{\mathrm{out}}(0) - \Re\left[\mathcal{S}^{33}_{\mathrm{out}}(0)\right]. \tag{6.39b}$$

In Fig. 6.3(a) the detected quadrature variances are shown around the cavity resonance (by scanning the laser frequency around it) exhibiting small squeezing properties around the antiresonance dip. While the squeezing in the strong coupling regime depicted in Fig. 6.3(d) is approximately of the same magnitude, it is shifted by $\pm g$ from the cavity and emitter resonance, i.e., the squeezing occurs at the polariton resonances.

Photon number and its variance.

The detected photon number operator for the transmission is

$$\hat{N}_{\mathrm{det}}(t) = \frac{1}{2T}\int_{t-T}^{t+T} dt' \int_{t-T}^{t+T} dt''\; \hat{B}^{\dagger}_{\mathrm{out}}(t')\hat{B}_{\mathrm{out}}(t''), \tag{6.40}$$

with an expectation value

$$N_{\mathrm{det}} = \langle \hat{N}_{\mathrm{det}}(t)\rangle = |\langle \hat{B}_{\mathrm{det}}(t)\rangle|^2 + \langle \hat{b}^{\dagger}_{\mathrm{det}}\hat{b}_{\mathrm{det}}\rangle. \tag{6.41}$$

Notice that in the absence of any nonlinear terms in the evolution, the detected photon number would be simply given by the absolute square of the classical amplitude as is characteristic for coherent states. However, the second term in Eq. (6.41) is nonzero and can again be expressed in terms of the output as $\langle \hat{b}^{\dagger}_{\mathrm{det}}\hat{b}_{\mathrm{det}}\rangle = \mathcal{S}^{43}_{\mathrm{out}}(0)$. We can then analyze the behavior of the photon number at the detector which is plotted for variable laser drive frequency (around the antiresonance) in Fig. 6.3(b) and for the strong coupling regime in Fig. 6.3(e). The behavior, as expected, mimics the cavity transmission profile. More interesting aspects emerge when one analyzes the variance of the photon number around the average; to this end, we explicitly write the expression for the variance,

$$\begin{aligned}[\Delta N_{\mathrm{det}}(t)]^2 = {} & \langle \hat{b}^{\dagger}_{\mathrm{det}}\hat{b}_{\mathrm{det}}\hat{b}^{\dagger}_{\mathrm{det}}\hat{b}_{\mathrm{det}}\rangle - \langle \hat{b}^{\dagger}_{\mathrm{det}}\hat{b}_{\mathrm{det}}\rangle^2 + |\langle \hat{B}_{\mathrm{det}}\rangle|^2\left[1 + 2\langle \hat{b}^{\dagger}_{\mathrm{det}}\hat{b}_{\mathrm{det}}\rangle\right] \\ & + \langle \hat{B}_{\mathrm{det}}\rangle^{*2}\langle \hat{b}^2_{\mathrm{det}}\rangle + \langle \hat{B}_{\mathrm{det}}\rangle^2\langle (\hat{b}^{\dagger}_{\mathrm{det}})^2\rangle.\end{aligned} \tag{6.42}$$

The two-operator averages emerge immediately from the spectrum matrix as $\langle \hat{b}_{\mathrm{det}}^2 \rangle = \mathcal{S}_{\mathrm{out}}^{33}(0)$ and $\langle (\hat{b}_{\mathrm{det}}^\dagger)^2 \rangle = \mathcal{S}_{\mathrm{out}}^{44}(0)$. The task of evaluating four-point correlations is a bit more cumbersome. However, we can apply Isserlis' theorem to the output (see Appendix 6.7) to express any four-operator correlations as sums over all permutations of two operator correlations. After time integration, one derives an according expansion for four detected operator correlations. This allows one to compute quantities such as

$$\langle \hat{b}_{\mathrm{det}}^\dagger \hat{b}_{\mathrm{det}} \hat{b}_{\mathrm{det}}^\dagger \hat{b}_{\mathrm{det}} \rangle = \mathcal{S}_{\mathrm{out}}^{43}(0)\mathcal{S}_{\mathrm{out}}^{43}(0) + \mathcal{S}_{\mathrm{out}}^{44}(0)\mathcal{S}_{\mathrm{out}}^{33}(0) + \mathcal{S}_{\mathrm{out}}^{43}(0)\mathcal{S}_{\mathrm{out}}^{34}(0). \tag{6.43}$$

Finally, the expression for the detected photon number variance after replacement of two- and four-operator correlations in Eq. (6.42) becomes

$$\begin{aligned}[\Delta N_{\mathrm{det}}(t)]^2 = {} & \left|\mathcal{S}_{\mathrm{out}}^{44}(0)\right|^2 + |\langle \hat{B}_{\mathrm{det}} \rangle|^2 [1 + 2\mathcal{S}_{\mathrm{out}}^{43}(0)] \\ & + 2\Re\left\{ \langle \hat{B}_{\mathrm{det}} \rangle^2 \mathcal{S}_{\mathrm{out}}^{44}(0) \right\} + \mathcal{S}_{\mathrm{out}}^{43}(0)\mathcal{S}_{\mathrm{out}}^{34}(0). \end{aligned} \tag{6.44}$$

The result is illustrated in Fig. 6.3(b) (in the antiresonance regime) and in Fig. 6.3(e) (in the strong coupling regime). The variance is included as a shaded region around the mean photon number. Owing to the weak coupling and large integration time, the result corresponds to the standard shot noise of a detected coherent state. The contribution from the two-photon terms $\mathcal{S}^{33}$ and $\mathcal{S}^{44}$, while showing up as quadrature squeezing, have little effect on the photon number variance.

Second-order correlation function of the photon number

In order to understand the photon statistics of the transmitted light from the cavity, we calculate the second-order correlation function [6.36] at zero delay $g^{(2)}(0)$ defined by

$$g^{(2)}(0) = \frac{\langle \hat{B}_{\mathrm{det}}^\dagger \hat{B}_{\mathrm{det}}^\dagger \hat{B}_{\mathrm{det}} \hat{B}_{\mathrm{det}} \rangle}{\langle \hat{B}_{\mathrm{det}}^\dagger \hat{B}_{\mathrm{det}} \rangle^2}. \tag{6.45}$$

Note, that for a coherent state $g^{(2)}(0) = 1$, which is characteristic for Poissonian light. However, terms in the output spectrum such as $\mathcal{S}_{\mathrm{out}}^{44}(0)$ denote the presence of photon-photon correlations coming from non-vanishing expectation values of $\langle \hat{b}_{\mathrm{det}}^\dagger \hat{b}_{\mathrm{det}}^\dagger \rangle$. After evaluating the different terms in the expression above and rewriting all occurring four-point correlations as before (see Appendix 6.7), one finds

$$\begin{aligned} & g^{(2)}(0) = \\ & \frac{|\langle \hat{B}_{\mathrm{det}} \rangle|^4 + 4|\langle \hat{B}_{\mathrm{det}} \rangle|^2 \mathcal{S}_{\mathrm{out}}^{43}(0) + 2\Re\left\{ \langle \hat{B}_{\mathrm{det}} \rangle^2 \mathcal{S}_{\mathrm{out}}^{44}(0) \right\} + |\mathcal{S}_{\mathrm{out}}^{44}(0)|^2 + 2\mathcal{S}_{\mathrm{out}}^{43}(0)\mathcal{S}_{\mathrm{out}}^{43}(0)}{|\langle \hat{B}_{\mathrm{det}} \rangle|^4 + 2|\langle \hat{B}_{\mathrm{det}} \rangle|^2 \mathcal{S}_{\mathrm{out}}^{43}(0) + \mathcal{S}_{\mathrm{out}}^{43}(0)\mathcal{S}_{\mathrm{out}}^{43}(0)}. \end{aligned} \tag{6.46}$$

For different detection time windows, the behavior of the second-order correlation function is shown in Fig. 6.3(c) (for the antiresonance regime) and in Fig. 6.3(f) (for the strong coupling regime). Longer detection times have the tendency of washing out

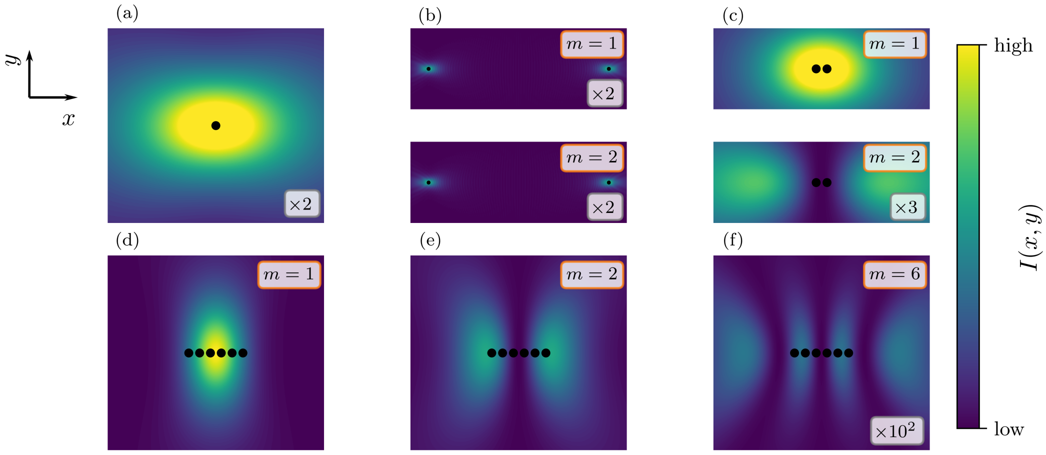

Figure 6.4: *Free space radiation patterns of exciton states.* The spatial intensity profile of the emitted field is plotted in arbitrary units but to scale. (a) For a single emitter, we observe the standard dipole radiation. (b) For two emitters placed far apart ($d \gg \lambda_{\mathrm{e}}$), they hardly interact and the chosen state therefore has little effect on the emitted field. (c) When the two emitters are placed much closer ($d = 0.3\lambda_{\mathrm{e}}$) than a single wavelength, the interactions become very strong, leading to superradiant loss ($m = 1$) and subradiance ($m = 2$), where the emitted field is predominantly radiated into the axis along which the emitters are placed. (d)–(f) The same effect is even more distinct for a closely spaced ($d = 0.3\lambda_{\mathrm{e}}$) equidistant chain of emitters (here $N = 6$). With increasing phase asymmetry (increasing m) there are more and more field nodes. Note that some of the shown field intensities had to be scaled since they are orders of magnitude smaller than the superradiant field of the chain. This is indicated (where needed) by the scaling factor in the bottom right. The dipole moments have been chosen along the y axis and the profile in the x-y plane is observed at a transverse distance $z = 2\lambda_{\mathrm{e}}$.

the photon bunching and antibunching effects.

6.3.6 Nonlinear effects

A single quantum emitter is a nonlinear object as its response (the amplitude of the stimulated transition dipole moment) is not only proportional to the driving field amplitude. In the next order of approximation, a small component emerges from the AC Stark shift of the excited state level proportional to the field intensity, the so-called Kerr effect. At the macroscopic level, this effect is seen as a modification of the index of refraction with increasing light field intensities. For the hybrid cavity-emitter system, we analyze the response of the transition dipole moment to the driving laser amplitude η. As opposed to the bare free space nonlinearity expected from a two-level system, the cavity can lead to a modified ”vacuum-dressed emitter” nonlinearity. Inside the cavity, we analytically derive this small correction by assuming that $z = (2|\beta|^2 - 1)$ and obtaining the new steady-state solution from

$$0 = -(\kappa - i\Delta_{\mathrm{c}})\alpha + \eta - ig\beta, \tag{6.47a}$$

$$0 = -(\gamma - i\Delta_{\mathrm{e}})\beta + ig\alpha(2|\beta|^2 - 1). \tag{6.47b}$$

We can find a solution for $\beta = \beta^{(1)} + \beta^{(3)}$ where the linear term $\beta^{(1)}$ is the previously derived response of the emitter's dipole in Eq. (6.13b) proportional to η. The next order correction is

$$\beta^{(3)} = -2\beta^{(1)}|\beta^{(1)}|^2 \left(1 - \frac{ig}{\eta}\beta^{(1)}\right). \tag{6.48}$$

The Kerr nonlinearity is proportional to the field intensity η^2 (we considered the field amplitude real) and leads to a modification of the cavity transmission function from the computed $t^{(1)}$ expression in Eq. (6.17),

$$t_{\mathrm{c}} = t_{\mathrm{c}}^{(1)} \left(1 + \frac{2g^2 \left|\beta^{(1)}\right|^2 \left[1 - i(g/\eta)\beta^{(1)}\right]}{(\gamma - i\Delta_{\mathrm{e}})(\kappa - i\Delta_{\mathrm{c}})}\right). \tag{6.49}$$

Notice that the nonlinearity matches the behavior of the linear response in that it is largest around the antiresonance. Maximal nonlinear response occurs when the linear one is maximal as well. We can then find a simple and instructive expression $\beta^{(1)}(\Delta = 0) = -iC/(1 + C)\eta/g$, which shows that an increase in the cooperativity (by, for example, suppressing the radiative rate while keeping g constant) brings the nonlinearity to a saturation value.

6.4 Free space collective dynamics: super- and subradiant states

Before analyzing the physics of a cavity mode interacting with an ensemble of coupled quantum emitters, let us briefly review some properties of the bare coupled emitter ensemble (in free space). In general, it is not possible to diagonalize the Hamiltonian including dipole-dipole interactions. However, a common approach is to truncate the Hilbert space at small or even single excitations [6.31, 6.37]. Then, at extremely small distances, one can use the fact that $|\Omega_{ii+1}| \gg |\Omega_{ii+2}|$ to make the nearest-neighbor (NN) approximation. The full Hamiltonian then becomes a tridiagonal symmetric Töplitz matrix, which can be analytically diagonalized. The resulting set of eigenstates $\{|m\rangle\}_{m=1}^{N}$ is given by

$$|m\rangle = \sqrt{\frac{2}{N+1}} \sum_j \sin\left(\frac{\pi m j}{N+1}\right) \hat{\sigma}_j^{+} |g\rangle^{\otimes N}. \tag{6.50}$$

They correspond to collective excitations of different symmetries with corresponding energies

$$\omega_m = \omega_{\mathrm{e}} + 2\Omega_{12}\cos\left(\frac{\pi m}{N+1}\right), \tag{6.51}$$

ranging from $-2\Omega_{12}$ to $2\Omega_{12}$ around the bare noninteracting energy ω_{e}. These expressions illustrate what is required to faithfully excite a specific collective state: One needs to match both the local phases given by the coefficients of the states as well as the shifted resonance energies. While the latter is quite straightforward, addressing an ensemble of emitters with large local phase differences within a small volume can be challenging. A number of proposals on how this could be achieved have been brought forward in recent studies. The suggested schemes involve among others a magnetic field gradient [6.31] or light that imprints the phases due to a polarization gradient [6.15, 6.38].

The reason for these extensive studies of preparation schemes is that large phase differences cause the emitter dipole fields to interfere destructively [see Fig. 6.4(f)], thus yielding an extremely small total field. Thereby, the lifetime of states with large phase differences (subradiant states) is vastly enhanced, making them ideal candidates for precision spectroscopy or quantum memories. This gain in lifetime becomes even more significant when considering the fact that symmetric excitation in dense emitter ensembles leads to superradiance [6.39], which in the limit of vanishing separation leads to a factor N enhancement in spontaneous emission.

This behavior due to phase (a-)symmetry can be investigated by computing the field radiated by the dipoles of the emitters taking into account the fact that they interfere with one another. Namely, the free electric field is just

$$\hat{\mathbf{E}}(\mathbf{r},t) = \hat{\mathbf{E}}^{(+)}(\mathbf{r},t) + \text{H.c.}, \tag{6.52}$$

where

$$\hat{\mathbf{E}}^{(+)}(\mathbf{r},t) = \sum_{\mathbf{k},\lambda}\sqrt{\frac{\hbar\omega_k}{2\epsilon_0 V}}\mathbf{e}_{\mathbf{k},\lambda}\hat{A}_{\mathbf{k},\lambda}(t)e^{i\mathbf{k}\cdot\mathbf{r}}. \tag{6.53}$$

Because of the dipole coupling of all emitters to the field, the photon annihilation operators simply follow the emitter coherence operators,

$$\dot{\hat{A}}_{\mathbf{k},\lambda}(t) = -ig_{\mathbf{k},\lambda}\sum_j \hat{S}_j(t)e^{-i\mathbf{k}\cdot\mathbf{r}_j}e^{i(\omega_k-\omega_{\mathrm{e}})t}, \tag{6.54}$$

Resolving the sum over wave vectors as an integral (due to the density of modes) and in addition making the Markov approximation allows one to find an expression for the electric field containing only emitter operators and geometric factors (see Appendix 6.7 for details).

The intensity of the resulting field is illustrated in Fig. 6.4 for a single emitter, two emitters, and a chain of emitters. While for a single emitter we observe dipole radiation

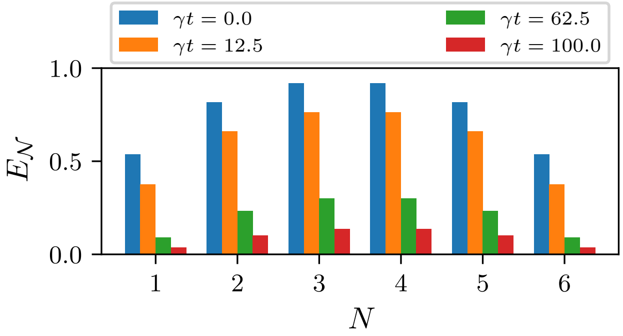

Figure 6.5: *Entanglement of emitters in a free space chain in a subradiant state.* A six-emitter equidistant chain with a separation of $d = 0.1\lambda_\mathrm{e}$ is initialized in the state $|m = N\rangle$ and left to evolve freely. We plot the logarithmic negativity of each emitter with respect to the $N - 1$ remaining emitters in the chain at different point in times (the left-most bar for each site corresponds to $\gamma t = 0$).

[see Fig. 6.4(a)], interference occurs when more than one emitter is present. If the separation between emitters is large, there are no substantial interactions enhancing or suppressing radiation. As illustrated in Fig. 6.4(b), the radiated field is then independent of the chosen state. As soon as the emitters are close (separation smaller than half a wavelength), the state in which they are prepared has a significant effect on the field. The radiated intensity is either enhanced due to constructive interference (superradiance) or suppressed due to destructive interference (subradiance).

These phenomena are even more dominant for more emitters. In Figs. 6.4(d)–6.4(f), we see the radiated intensity for different choices of m for an equidistant chain of $N = 6$ emitters. While the field is quite large in the symmetric case ($m = 1$), we can see that for other choices of m, destructive interference occurs. Namely, for the smallest asymmetric choice of states, $m = 2$, there is only one change in sign of the phase which occurs in the middle of the chain. It is clear that at this point the fields radiated by each half of the chain cancel each other. For $m = N$ this effect culminates in maximal destructive interference, which widely inhibits spontaneous emission from the chain.

Another property of these collective states (both super- and subradiant ones) is that they commonly feature high degrees of entanglement [6.31, 6.40]. As such, they form an interesting resource for quantum information processing, where highly subradiant states are even more useful due to the increased lifetime of correlations.

Even though subradiant systems show only moderate two-pair correlations, the overall entanglement is large. Specifically, each of the emitters is highly entangled with all the other emitters. In order to illustrate this point, we plot the logarithmic negativity [6.41], which is an entanglement monotone. For a bipartite system consisting of the subsystems A and B, it is defined as

$$E_{\mathcal{N}}(\rho) = \log_2 \left(|\rho^{T_A}| \right) , \tag{6.55}$$

where ρ^{T_A} denotes the partial transpose with respect to the subsystem A and $|\cdot|$ is the trace norm. In Fig. 6.5, we initialize a chain of emitters in the state with the highest phase difference ($m = N$) and let it evolve freely over time. At distinct time points, we compute the logarithmic negativity for each emitter (i.e., we choose our bipartite system to consist of the ith emitter and the rest of the chain). One can see that the amount of entanglement is even in the initial state significantly larger in the center of the chain. Over time, this behavior is retained, and correlation is only slowly lost due to excitation loss of the chain. Even at $t = 100\gamma^{-1}$, there still is considerable entanglement in the system.

6.5 Spectroscopy of the collective Purcell effect

We now generalize the formalism developed for the single quantum emitter case to many coupled quantum emitters with special focus on addressing collective subradiant states. In a first step, we derive the cavity transmission function in the linear regime showing the occurrence of collective resonances of different radiative natures (subradiant and superradiant) and the scaling of the cooperativity when proper illumination techniques (matching phase and energy of the collective subradiant resonances) are employed. We then look at collective cooperative effects on output field squeezing, photon-photon correlations, and the enhancement of the overall ensemble Kerr nonlinearity. We find that in all these investigations, enhancement is always reached in the *cooperative collective* regime (where the interacting ensemble shows a much higher cooperativity than a noninteracting ensemble).

6.5.1 Subradiant enhancement of cavity-emitter cooperativity

In order to perform a classical analysis of the response of a cavity weakly coupled to N interacting quantum emitters (deriving the amplitude transmission), it suffices to solve the coupled equations of motion for classical averages. In a compact matrix form, this is written as the following equations of motions [6.15],

$$\dot{\alpha} = -\left(\kappa - i\Delta_{\mathrm{c}}\right)\alpha + \eta - i\mathbf{G}\cdot\boldsymbol{\beta}, \tag{6.56a}$$

$$\dot{\boldsymbol{\beta}} = i\Delta_{\mathrm{e}}\boldsymbol{\beta} - i\boldsymbol{\Omega}\boldsymbol{\beta} - i\mathbf{G}\alpha - \boldsymbol{\Gamma}\boldsymbol{\beta}, \tag{6.56b}$$

where now $\boldsymbol{\beta}$ and $\mathbf{G}$ are column vectors with entries β_i and g_i. The matrices $\boldsymbol{\Omega}$ and $\boldsymbol{\Gamma}$ have the elements Ω_{ij} and γ_{ij}, respectively. In steady state, the transmission coefficient for the cavity amplitude reads

$$t_{\mathrm{c}} = \frac{\kappa}{-i\Delta_{\mathrm{c}} + \kappa + \mathbf{G}^{\top}\mathbf{G}/[-i\Delta_{\mathrm{eff}}(\Delta_{\mathrm{e}}) + \gamma_{\mathrm{eff}}(\Delta_{\mathrm{e}})]}, \tag{6.57}$$

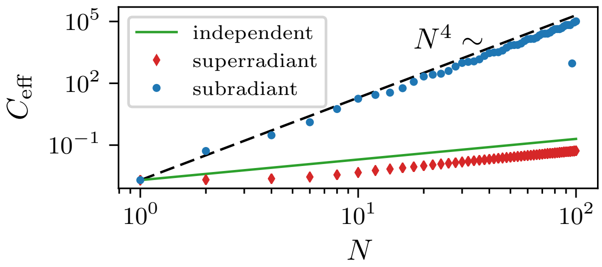

Figure 6.6: *Scaling of the effective cooperativity with the number of emitters in an equidistant chain.* Strong collective effects are present when the emitters are closely spaced at $d = 0.1\lambda_{\rm e}$, leading to distinct scalings of the cooperativity. As a reference, we plot the cooperativity for independent emitters, which scales linearly with the number of emitters. The dashed line indicates the scaling of the subradiant case with N^4 (note that a simple polynomial fit returns a scaling of approximately $N^{3.81\pm0.01}$). The super- and subradiance is caused by symmetric ($g_i = g$) and asymmetric [$g_i = (-1)^i g$] coupling, respectively. We chose the parameters $\gamma = \kappa/20 = 5g$ such that for all N we are in the regime where $NC \ll 1$.

where the effective $\Delta_{\rm e}$-dependent collective energy shifts and linewidths are given by

$$\Delta_{\rm eff}(\Delta_{\rm e}) = \Im\left\{\frac{\mathbf{G}^\top\mathbf{G}}{\mathbf{G}^\top\left(-i\Delta_{\rm e}\mathbb{1} + i\mathbf{\Omega} + \mathbf{\Gamma}\right)^{-1}\mathbf{G}}\right\}, \tag{6.58a}$$

$$\gamma_{\rm eff}(\Delta_{\rm e}) = \Re\left\{\frac{\mathbf{G}^\top\mathbf{G}}{\mathbf{G}^\top\left(-i\Delta_{\rm e}\mathbb{1} + i\mathbf{\Omega} + \mathbf{\Gamma}\right)^{-1}\mathbf{G}}\right\}. \tag{6.58b}$$

In analogy to the single-emitter case, we can define an effective N-emitter cooperativity by

$$C_{\rm eff}(\Delta_{\rm e}) = \frac{\mathbf{G}^\top\mathbf{G}}{\kappa\gamma_{\rm eff}(\Delta_{\rm e})}. \tag{6.59}$$

The message of the above equation is that the numerator and denominator no longer share the same dependency on the individual emitter properties (such as the dipole moment). Thus, a much larger effective cooperativity can be reached if one manages to excite a subradiant collective state for which the effective decay rate is small.

Note that, as mentioned before, in addition to matching the symmetry of the collective state one wants to address, one also has to match the state's energy. The cavity has to be tuned to fulfill the condition $\Delta_{\rm eff}(\omega_{\rm c} - \omega_{\rm e}) = 0$, such that at the point of resonance where $\omega_{\rm c} = \omega_\ell$ the collective state is also resonant. This is straightforward to do numerically. The distinct scaling of the cooperativity is shown in Fig. 6.6. It can be seen that the subradiant enhancement of the effective cooperativity shows a beneficial scaling with the number of emitters with approximately N^4. It has been shown that the lowest decay rate theoretically possible reduces exponentially with the number of emitters [6.42].

The most robust states that can be reached in reality, though, scale with N^{-3} [6.43]. This, combined with the collective enhancement of the coupling to the cavity mode with N, yields the scaling observed in Fig. 6.6. Deviations from the N^4 scaling are due to imperfect addressing of subradiant states as well as to finite-size effects.

On the other hand, the superradiant decay almost compensates the enhancement of the coupling with N for small numbers of emitters, since in that case also the decay rate scales approximately linear. This keeps the effective cooperativity constant at the value for a single emitter. Again, due to imperfect resonance matching and finite-size effects, the decay rate does not show perfect linear scaling and saturates at some point. The enhanced coupling is therefore no longer perfectly compensated for larger N and we again observe a linear enhancement of the cooperativity. However, the effective cooperativity affected by superradiance can never surpass the cooperativity of the same number of independent emitters.

Besides the number of quantum emitters, another parameter on which the collective modification of the cooperativity strongly depends is the distance between the emitters. It governs the strength of the dipole-dipole interactions and subsequently any enhancement or reduction of the light-emitter interactions. Systematic investigations of the dependence of super- and subradiance on the emitter separation have been performed [6.42, 6.43]. At sufficiently small distances – which is the regime we consider here – the collective decay has been shown to be a monotonous function of the particle-particle separation [6.42]; i.e., collective effects increase as the distance between emitters decreases. Furthermore, disorder in the emitter positions only marginally affects subradiance and can even lead to more long-lived states [6.31].

6.5.2 Nonclassical collective effects in detected fields

We can follow the same procedure as for a single emitter to investigate the squeezing at the output port. From Eq. (6.22), we obtain the vector equations for the quantum fluctuations in the form

$$\dot{\hat{a}} = -\left(\kappa - i\Delta_{\mathrm{c}}\right)\hat{a} - i\mathbf{G}\cdot\hat{\boldsymbol{\sigma}} + \sqrt{\kappa}\hat{a}_{\mathrm{in}} + \sqrt{\kappa}\hat{b}_{\mathrm{in}}, \tag{6.60a}$$

$$\dot{\hat{\boldsymbol{\sigma}}} = \mathbf{A}\hat{\boldsymbol{\sigma}} + \mathbf{B}\hat{\boldsymbol{\sigma}}^{z} + i\mathbf{G}_{z}\hat{a} - \bar{\boldsymbol{\xi}}, \tag{6.60b}$$

$$\dot{\hat{\boldsymbol{\sigma}}}^{z} = -2\gamma\hat{\boldsymbol{\sigma}}^{z} + \mathbf{K}\hat{\boldsymbol{\sigma}} + \mathbf{K}^{*}\hat{\boldsymbol{\sigma}}^{\dagger} + 2i\mathbf{G}_{\beta}\hat{a}^{\dagger} - 2i\mathbf{G}_{\beta}^{*}\hat{a} + 2\bar{\boldsymbol{\xi}}^{z}. \tag{6.60c}$$

We have defined the modified coupling vectors $\mathbf{G}_{z} = (z_1 g_1, ..., z_N g_N)^{\top}$ and $\mathbf{G}_{\beta} = (\beta_1 g_1, ..., \beta_N g_N)^{\top}$. The coupling matrices are given by

$$\mathbf{A}_{jk} = -\left(\gamma - i\Delta_{\mathrm{e}}\right)\delta_{jk} + \left(1 - \delta_{jk}\right)\left(i\Omega_{jk} + \gamma_{jk}\right)z_{j}, \tag{6.61a}$$

$$\mathbf{B}_{jk} = \delta_{jk}\big(ig_{j}\alpha + \sum_{l\neq j}\left(i\Omega_{jl} + \gamma_{jl}\right)\beta_{l}\big), \tag{6.61b}$$

$$\mathbf{K}_{jk} = \big(2ig_{j}\alpha^{*} - 2\sum_{l\neq j}\gamma_{jk}\beta_{l}^{*}\big)\delta_{jk} - 2\left(1 - \delta_{jk}\right)\gamma_{jk}\beta_{j}^{*}. \tag{6.61c}$$

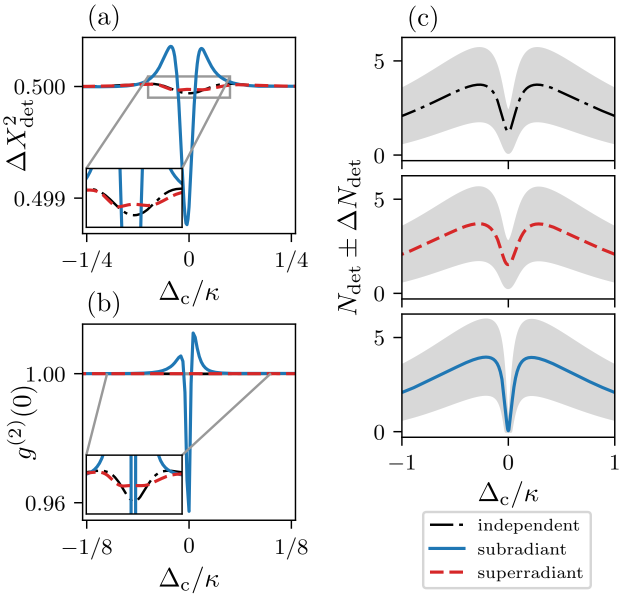

Figure 6.7: *Cooperative effects of four coupled emitters.* Plots of (a) the variance of the detected x-quadrature, (b) the $g^{(2)}(0)$ function, and (c) the photon number with its variance for four coupled emitters around the antiresonance for subradiant/superradiant and independent cases. The parameters are $g = 2\gamma = \kappa/10$, $\eta = \kappa/100$, and $T = 2 \times 10^4 \kappa^{-1}$, with the emitter dipoles oriented perpendicular to the cavity axis and a separation of the emitters of $0.3\lambda_{\mathrm{e}}$.

We can now express Eqs. (6.60) in vector form, $\dot{\mathbf{v}} = \mathbf{M}\mathbf{v} + \mathbf{N}\mathbf{v}_{\mathrm{in}}$, in analogy with the single-emitter case, with the proper matrix definitions. The drift matrix is given by

$$\mathbf{M} = \begin{pmatrix} -(\kappa - i\Delta_{\mathrm{c}}) & 0 & -i\mathbf{G}^{\top} & \mathbf{0}^{\top} & \mathbf{0}^{\top} \\ 0 & -\kappa - i\Delta_{\mathrm{c}} & \mathbf{0}^{\top} & i\mathbf{G}^{\top} & \mathbf{0}^{\top} \\ i\mathbf{G}_z & \mathbf{0} & \mathbf{A} & \underline{\mathbf{0}} & \mathbf{B} \\ \mathbf{0} & -i\mathbf{G}_z & \underline{\mathbf{0}} & \mathbf{A}^* & \mathbf{B}^* \\ -2i\mathbf{G}^*_{\beta} & 2i\mathbf{G}_{\beta} & \mathbf{K} & \mathbf{K}^* & -2\gamma\mathbb{1} \end{pmatrix}, \tag{6.62}$$

where $\mathbf{0}$ is a vector containing N zeros and $\underline{\mathbf{0}}$ is a $N \times N$ matrix with only zero elements. The matrix multiplying the input noise operators is

$$\mathbf{N} = \begin{pmatrix} \sqrt{\kappa} & 0 & \sqrt{\kappa} & 0 & \mathbf{0}^{\top} & \mathbf{0}^{\top} & \mathbf{0}^{\top} \\ 0 & \sqrt{\kappa} & 0 & \sqrt{\kappa} & \mathbf{0}^{\top} & \mathbf{0}^{\top} & \mathbf{0}^{\top} \\ \mathbf{0} & \mathbf{0} & \mathbf{0} & \mathbf{0} & -\sqrt{2\gamma}\mathbb{1} & \underline{\mathbf{0}} & \underline{\mathbf{0}} \\ \mathbf{0} & \mathbf{0} & \mathbf{0} & \mathbf{0} & \underline{\mathbf{0}} & -\sqrt{2\gamma}\mathbb{1} & \underline{\mathbf{0}} \\ \mathbf{0} & \mathbf{0} & \mathbf{0} & \mathbf{0} & \underline{\mathbf{0}} & \underline{\mathbf{0}} & \sqrt{2\gamma}\mathbb{1} \end{pmatrix}. \tag{6.63}$$

Finally, the input noise correlation matrix in the many emitter case is

$$\mathbf{C} = \begin{pmatrix} 0 & 1 & 0 & 0 & \mathbf{0}^\top & \mathbf{0}^\top & \mathbf{0}^\top \\ 0 & 0 & 0 & 0 & \mathbf{0}^\top & \mathbf{0}^\top & \mathbf{0}^\top \\ 0 & 0 & 0 & 1 & \mathbf{0}^\top & \mathbf{0}^\top & \mathbf{0}^\top \\ 0 & 0 & 0 & 0 & \mathbf{0}^\top & \mathbf{0}^\top & \mathbf{0}^\top \\ \mathbf{0} & \mathbf{0} & \mathbf{0} & \mathbf{0} & \underline{\mathbf{0}} & \mathbf{C}_{\beta\beta} & \mathbf{C}_{\beta z} \\ \mathbf{0} & \mathbf{0} & \mathbf{0} & \mathbf{0} & \underline{\mathbf{0}} & \underline{\mathbf{0}} & \underline{\mathbf{0}} \\ \mathbf{0} & \mathbf{0} & \mathbf{0} & \mathbf{0} & \underline{\mathbf{0}} & \mathbf{C}^\dagger_{\beta z} & \mathbf{C}_{zz} \end{pmatrix}, \tag{6.64}$$

where $\mathbf{C}_{\beta\beta}$ is the correlation matrix whose elements are given by Eq. (6.9a), and analogous for the other indexed $\mathbf{C}$ matrices (see Appendix 6.7). Note that $\mathbf{C}_{\beta z} = \mathbf{C}^\dagger_{z\beta}$.

With the help of these matrix definitions, it is straightforward to compute all figures of interest. All expressions for the field operators and variances are the same as for the single-emitter case; we merely have to insert the corresponding output spectrum matrix elements obtained for the many emitter case. The output spectrum matrix can be computed with the matrices above using Eq. (6.31).

The resulting higher order averages are shown in Fig. 6.7. There, we compare four independent, subradiant [asymmetric coupling, $g_i = (-1)^i g$] and superradiant (symmetric coupling, $g_i = g$) emitters. Note that, as in the discussion of the effective cooperativity, we match the cavity to the addressed collective state by choosing the cavity resonance such that $\Delta_{\text{eff}}(\omega_\text{c} - \omega_\text{e}) = 0$.

The detected photon number and its standard deviation is depicted in Fig. 6.7(c) and, as in the single-emitter case, it exhibits the same behavior as the transmission obtained from the average amplitude [6.15]. The superradiance broadens and lessens the antiresonance, while the subradiant emitters lead to a very deep but narrow antiresonance.

As for the quadrature variance and second-order coherence function shown in Figs. 6.7(a) and 6.7(b), the clear overall point here is this: Compared to independent emitters, superradiance (slightly) diminishes all nonlinear effects (see insets), while subradiance offers enhancements by orders of magnitude. Squeezing and antibunching both occur around the resonance (as for the single emitter in the weak coupling regime). However, both effects are distinctly larger in a frequency range much smaller than the cavity linewidth when the emitters are in a subradiant state. This enhancement is a signature of the counterintuitive effect that subradiant systems exhibit stronger classical dipoles: The stationary excited state population and thus the stationary magnitude of the induced dipole moment are inversely proportional to the spontaneous decay rate of the considered state. Therefore, as we see in Fig. 6.7, nonlinear effects such as squeezing and antibunching increase in consequence of the inhibited decay of a subradiant state. In contrast to this, superradiant states exhibit smaller stationary values for their collective dipole moments. However, the broadening of the effective linewidth due to superradiance is less prominent compared to the suppression of the decay in subradiant states. Going from the independent emitter to the superradiant case, there

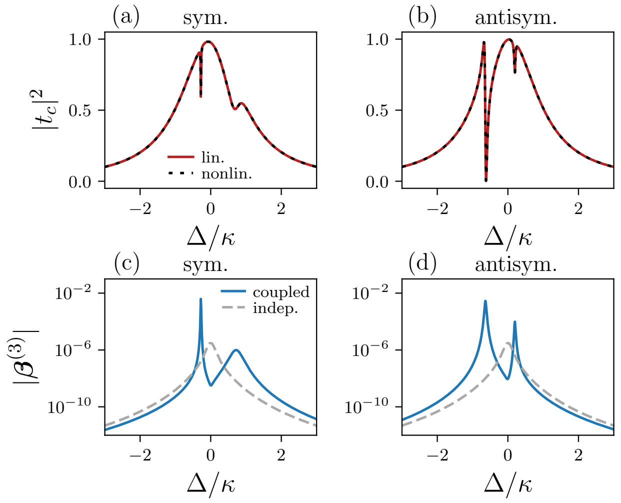

Figure 6.8: *Kerr nonlinearity for coupled quantum emitters.* Plot of transmission functions in the linear and nonlinear approximations for (a) symmetric and (b) asymmetric excitation of four equally spaced emitters at distance $d = 0.07\lambda_\mathrm{e}$. The corresponding nonlinearity is plotted in (c) for symmetric and (d) for asymmetric addressing compared to the independent emitter case (dashed line obtained setting $d \gg \lambda_\mathrm{e}$). The remaining parameters here are $g = \kappa/10$, $\gamma = \kappa/20$, and $\eta = \kappa/100$. Note that no frequency matching was assumed, such that $\omega_\mathrm{e} = \omega_\mathrm{c}$ and a scan of the laser frequency will consequently hit all the collective states ($\Delta_\mathrm{c} = \Delta_\mathrm{e} = \Delta$), producing a set of four antiresonances.

is thus a decrease in these quantum effects. Compared to the large enhancement due to subradiance, however, this reduction is somewhat less significant.

6.5.3 Collective nonlinear effects

The vector of individual classical dipoles can be expressed in steady state as

$$\boldsymbol{\beta}^{(1)} = -i\eta[(\kappa - i\Delta_\mathrm{c})(i\boldsymbol{\Omega} + \boldsymbol{\Gamma} - i\Delta_\mathrm{e}\mathbb{1}) + \mathbf{G}\mathbf{G}^\top]^{-1}\mathbf{G}. \tag{6.65}$$

We then find the next order correction, similarly to the single-emitter case, by writing $\boldsymbol{\beta} \approx \boldsymbol{\beta}^{(1)} + \boldsymbol{\beta}^{(3)}$ (see Appendix 6.7 for details) and obtain a compact expression

$$\begin{aligned}\boldsymbol{\beta}^{(3)} =& \frac{2i\eta \sum_{j=1}^{N} \mathbf{P}_j \boldsymbol{\beta}^{(1)} {\boldsymbol{\beta}^{(1)}}^\dagger \mathbf{P}_j}{(\kappa - i\Delta_\mathrm{c})(i\boldsymbol{\Omega} + \boldsymbol{\Gamma} - i\Delta_\mathrm{e}\mathbb{1}) + \mathbf{G}\mathbf{G}^\top} \\ & \times \left(\mathbf{G} - \frac{i}{\eta}\left[(\kappa - i\Delta_\mathrm{c})(i\boldsymbol{\Omega} + \tilde{\boldsymbol{\Gamma}}) + \mathbf{G}\mathbf{G}^\top\right]\boldsymbol{\beta}^{(1)}\right),\end{aligned} \tag{6.66}$$

where $\tilde{\boldsymbol{\Gamma}} = \boldsymbol{\Gamma} - \gamma\mathbb{1}$ and $\mathbf{P}_j$ is the projector on the jth unit vector. This describes the collective cooperative Kerr effect where the induced nonlinear polarization of each emitter in the ensemble depends on the collective response of all the other emitters.

As a basis for comparison, we estimate that for independent emitters, illuminated symmetrically, the maximum linear response per emitter (they all respond equally to the excitation) is $\beta_j^{(1)}(\Delta = 0) = iC_{\text{eff}}/(1 + C_{\text{eff}})\eta/(Ng)$. In particular, for $N = 1$, one would have $\beta^{(1)}(\Delta = 0) = iC/(1 + C)\eta/g$. Notice that an increase in N leads to an increase in the cooperativity such that the factor $C_{\text{eff}}/(1 + C_{\text{eff}})$ increases but eventually saturates at unity. The other factor decreases with N such that, in the many-emitter limit, the per-emitter nonlinearity decreases. Emitter-emitter coupling, on the other hand, can strongly modify the width of the antiresonance and consequently strongly enhance the overall nonlinearity.

This is illustrated in Fig. 6.8. We consider a system of four coupled emitters exhibiting four collective states with energies approximately given by Eq. (6.51). Three of these states are subradiant while the superradiant state is energetically located at the frequency $\omega_e + 2\Omega_{12}\cos(\pi/5)$ on the right of the cavity resonance. We drive the system either symmetrically with $\mathbf{G} = (g, g, g, g)^\top$ or asymmetrically with $\mathbf{G} = (g, -g, g, -g)^\top$. On the left side, in Figs. 6.8(a) and 6.8(c), the symmetric addressing partially overlaps with one subradiant state and one superradiant state. The coupling to the other two states is negligible. At the point where the laser fits the displaced collective states, the collective nonlinearity (shown as the norm of the $\boldsymbol{\beta}^{(3)}$ vector) exhibits a large enhancement. The superradiant antiresonance, on the other hand, shows a decrease from the independent emitter's maximum nonlinearity (dashed line evaluated at the origin). Notice that in the independent case the four collective states have the same degenerate energy equal to ω_{e}. For asymmetric driving, the laser encounters two subradiant collective states and shows the corresponding enhancement in the nonlinearity.

In order to further investigate the physics here, we can look at two special cases. First, consider an ensemble of independent emitters all of which couple equally to the cavity mode. At resonance, we find that the magnitude of the Kerr nonlinearity is

$$|\boldsymbol{\beta}^{(3)}(\Delta = 0)| = \frac{2\eta^3}{N}\sqrt{\frac{(NC)^3}{\gamma^3\,(1 + NC)^8\,\kappa^3}}. \tag{6.67}$$

In the limit of many emitters, $N \gg 1$, one can see that the nonlinearity at resonance scales as $1/\sqrt{N^7}$. This is expected as in this limit the ensemble of emitters more and more closely resembles a harmonic oscillator making the entire system linear. The situation is much less trivial for coupled emitters. The scaling of the collective Kerr nonlinearity with the number of emitters is shown in Fig. 6.9(a). There, it can be seen that depending on the symmetry of the coupling to the cavity mode, the scaling down with N is drastically different. Namely, we find that even under symmetric addressing which leads to superradiance, the nonlinearity is larger than for uncoupled emitters. As shown below, this is due to the presence of collective shifts. Eventually, though, the nonlinearity attains a scaling close to the independent case in the limit of many emitters. Asymmetric addressing, on the other hand, leads to a completely different behavior. Since not only collective shifts are present, but also the linewidth is reduced due to subradiance, the resulting Kerr nonlinearity is much more robust; i.e., it scales

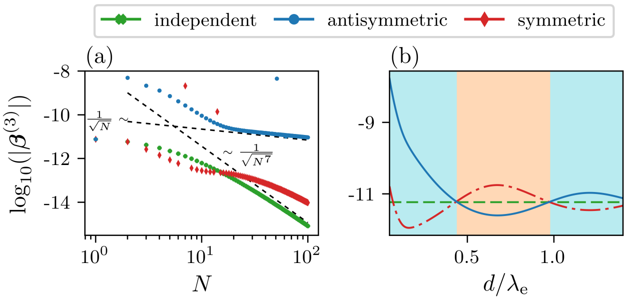

Figure 6.9: *Behavior of the Kerr nonlinearity.* (a) The nonlinearity as a function of N for a chain with separation $d = 0.07\lambda_\mathrm{e}$. We observe different scaling laws in the limit where $N \gg 1$. While for independent emitters the nonlinearity attains the scaling with $1/\sqrt{N^7}$, in the case of asymmetric driving (subradiance) a much more robust scaling with $1/\sqrt{N}$ is found. Even for symmetrically coupled emitters (superradiance) the nonlinearity remains larger due to the presence of collective shifts. (b) The two-emitter nonlinearity as a function of the inter-particle distance d. The light blue area highlights where the nonlinearity for asymmetric addressing (blue, solid line) is larger than for symmetric addressing (red, dash-dotted line). The orange region highlights the opposite case. The regions coincide with $\gamma_{12} > 0$ (blue) and $\gamma_{12} < 0$ (orange, $0.5\lambda_\mathrm{e} \leq d \leq \lambda_\mathrm{e}$). Note that at extremely small distances the energetic shift Ω_{12} is so dominant that even under symmetric addressing the nonlinearity surpasses the independent one, despite the emitters being almost perfectly superradiant. Note, that we chose a small driving strength, $\eta = 10^{-4}\kappa$, in order to ensure that the excited state population remains sufficiently small. This is why at a first glance the nonlinearity appears to be a lot smaller than the one shown in Fig. 6.8. The remaining parameters were $\gamma = \kappa/20$, $g = \kappa/10$.

down with $1/\sqrt{N}$.

The second special case we want to look at is the smallest collective system, which consists of two emitters only. If we consider symmetric $(+)$ and asymmetric $(-)$ addressing, i.e., $\mathbf{G} = (g, \pm g)^T$, the collective shifts amount to $\pm\Omega_{12}$. Matching the cavity frequency to this collective resonance, we find the Kerr nonlinearity at resonance ($\Delta = \Delta_\mathrm{c} = \Delta_\mathrm{e} \mp \Omega_{12}$)

$$|\boldsymbol{\beta}^{(3)}(\Delta = 0)| = \sqrt{\frac{C_\mathrm{eff}^3}{(1 + C_\mathrm{eff})^3}} \frac{\eta^3 \sqrt{(\gamma^2 + \Omega_{12}^2)}}{\sqrt{\left[\gamma_\mathrm{eff}\,(1 + C_\mathrm{eff})\right]^5 \kappa^3}}. \tag{6.68}$$

The first term above is the same as in $\beta^{(1)}$. The second term, on the other hand, exhibits some peculiarities. Specifically, while it is inversely proportional to the width of the antiresonance $\gamma_\mathrm{eff}(1 + C_\mathrm{eff})$, it also depends on the collective shifts Ω_{12}. Making use of subradiance can significantly decrease the antiresonance width. However, it is eventually limited by the decay channel constituted by the cavity with the rate Ng^2/κ. The shifts, though, can still compensate the broadening by the cavity and increase the nonlinearity above the one exhibited by decoupled emitters. At extremely small distances, where the shifts start to diverge, this effect is so predominant that it can even compensate for an additional broadening of the antiresonance due to superradiance. This can be seen in Fig. 6.9(b), where the behavior of the two-emitter nonlinearity as a function of the inter-particle distance is depicted. Since the shifts also increase with the number of emitters, the same argument applies to the fact that the symmetric nonlinearity surpasses the independent one in Fig. 6.9(a). At moderate particle-particle separation, the shifts are not too large, such that the nonlinearity is essentially governed by the collective decay [see Fig. 6.9(b)]. As the mutual decay rate γ_{12} changes sign, symmetric addressing and asymmetric addressing switch roles, such that the system becomes subradiant under symmetric addressing and subsequently is more nonlinear.

6.6 Conclusions

We have followed a quantum Langevin equations approach to the input-output problem of an optical cavity containing an ensemble of N coupled quantum emitters. Linearization of operators around steady-state values in the weak excitation regime allows one to compactly write the evolution of quantum fluctuations and derive expectation values not only for two-operator products but products of any number of operators. In particular, we focused on describing the properties of the reflected and transmitted output field as well as of the detected fields (assuming a flat-window time integration). We have developed the formalism first for the case of a single quantum emitter coupled to an optical cavity applicable both in the Purcell and strong coupling regimes. We have then extended this formalism to the case of many emitters where numerical simulations become difficult and found the signature of collective cooperative behavior: N emitters do not only imprint an N times larger effect on the cavity field but far beyond this linear scaling. The results originally shown in Ref. [6.15] were extended. There, the cooperativity was shown to increase drastically with N when asymmetric, energetically matched excitation schemes were employed to prepare collective subradiant states. The formalism developed allows one to go beyond the classical problem and describe quantum properties of the output field. Moreover, the same *cooperative collective* effects, stemming from the coupling among emitters, lead to a strong enhancement of the nonlinear response of the cavity-embedded ensemble around specific antiresonances. A more detailed study of such effects (which are promising for nonlinear quantum optics applications) will be tackled in a future publication aiming at deriving precise conditions for the antiresonance points where the effect could be optimized even for distances achievable by optical lattice trapping techniques.

Acknowledgments

We acknowledge financial support from the Austrian Science Fund (FWF) within the Innsbruck Doctoral School DK-ALM: W1259-N27 (D. P.) and Project No. P29318-N27 (H. R.), from the Max Planck Society (M. R., C. S., and C. G.) and from the German Federal Ministry of Education and Research, cofunded by the European Commission (Project RouTe), Project No. 13N14839 within the research program ”Photonik Forschung Deutschland” (C. S. and C. G.).

The graphs were produced with the open-source plotting library MATPLOTLIB [6.44] and some numerical calculations were carried out with the QUANTUMOPTICS.JL toolbox [6.45].

6.7 Appendix

Collective noise in quantum Langevin equations

For a system operator $\hat{O}$, for each individual Lindblad collapse operator $\hat{c}$ acting at rate γ_c and with associated input noise $\hat{c}_\mathrm{in}$, one can derive the QLE including the noise terms as [6.46]

$$\dot{\hat{O}} = \frac{i}{\hbar}[H, \hat{O}] - [\hat{O}, \hat{c}^\dagger]\left\{\gamma_\mathrm{c}\hat{c} + \sqrt{2\gamma_\mathrm{c}}\hat{c}_\mathrm{in}\right\} + \left\{\gamma_\mathrm{c}\hat{c}^\dagger + \sqrt{2\gamma_\mathrm{c}}\hat{c}_\mathrm{in}^\dagger\right\}[\hat{O}, \hat{c}] \tag{6.69}$$

However, collective incoherent dynamics represented by nondiagonal Liouvillian terms cannot be directly cast into Langevin equations. One instead has to first write the total decay term as a sum of independent decay channels. This is achieved by a basis transformation with the matrix $\mathbf{T}$ (such that $\mathbf{T}^{-1} = \mathbf{T}^\top$) that diagonalizes the decay rate matrix $\mathbf{\Gamma}$,

$$\mathrm{diag}\left(\lambda_1, ..., \lambda_N\right) = \mathbf{T}^\top \mathbf{\Gamma} \mathbf{T}, \tag{6.70}$$

where λ_j is the jth eigenvalue of the decay matrix. Defining a set of damping operators

$$\hat{\Pi}_j := \sum_k \left(\mathbf{T}^\top\right)_{jk} \hat{S}_k, \tag{6.71}$$

we may write [6.42]

$$\mathcal{L}_\mathrm{e}[\rho] = \sum_i \lambda_i \left(2\hat{\Pi}_i \rho \hat{\Pi}_i^\dagger - \hat{\Pi}_i^\dagger \hat{\Pi}_i \rho - \rho \hat{\Pi}_i^\dagger \hat{\Pi}_i\right). \tag{6.72}$$

Obviously, this Lindblad term is diagonal and hence the QLE may be cast into the form given by Eq. (6.69). The input noise terms of the emitter operators $\hat{\sigma}_{i,\mathrm{in}}$ follow the transformation rules given by Eq. (6.71). Transforming the QLE for any emitter operator $\hat{O}$ back into the non-diagonal form gives the usual terms for the deterministic parts. For the noise terms, however, we have

$$\sum_j [\hat{O}, \hat{\Pi}_j^\dagger] \sqrt{\lambda_j} \hat{\Pi}_{j,\mathrm{in}} = \sqrt{\gamma} \sum_j [\hat{O}, \hat{S}_j^\dagger] \xi_j(t), \tag{6.73}$$

$$\sum_j [\hat{O}, \hat{\Pi}_j] \sqrt{\lambda_j} \hat{\Pi}_{j,\mathrm{in}}^\dagger = \sqrt{\gamma} \sum_j [\hat{O}, \hat{S}_j] \xi_j^\dagger(t), \tag{6.74}$$

where we have implicitly defined our correlated emitter noise terms ξ_j as

$$\xi_j(t) := \sum_{k,l} \sqrt{\frac{\lambda_k}{\gamma}} \mathbf{T}_{jk}(\mathbf{T}^{-1})_{kl}\hat{\sigma}^-_{l,\mathrm{in}}. \tag{6.75}$$

Hence, the QLE for any emitter operator $\hat{O}$ is

$$\dot{\hat{O}} = i[H,\hat{O}] - \sum_{ij}[\hat{O},\hat{S}_i^\dagger]\left(\gamma_{ij}\hat{S}_j + \delta_{ij}\sqrt{2\gamma}\xi_i(t)\right) + \sum_{ij}\left(\gamma_{ij}\hat{S}_j^\dagger + \delta_{ij}\sqrt{2\gamma}\xi_i^\dagger(t)\right)[\hat{O},\hat{S}_i], \tag{6.76}$$

with the spatially correlated white noise ξ_i. From the definition of the noise it is straightforward to show that

$$[\xi_i(t),\xi_j^\dagger(t')] = h_{ij}\delta(t-t'). \tag{6.77}$$

In order to evaluate the correlation functions of the modified collective input noise terms,

$$\bar{\xi}_j = \hat{S}_j^z(t)\xi_j(t), \tag{6.78a}$$

$$\bar{\xi}_j^z(t) = 2\left(\hat{S}_j^\dagger(t)\xi_j(t) + \xi_j^\dagger(t)\hat{S}_j(t)\right), \tag{6.78b}$$

we need to consider the commutation relations of the system operators with the input noise terms $\xi_j(t)$. To this end, we write the collective input-output relation [6.46] which is straightforward from the diagonal form of the QLEs,

$$\hat{\Pi}_{j,\mathrm{in}}(t) + \hat{\Pi}_{j,\mathrm{out}}(t) = \sqrt{2\lambda_j}\hat{\Pi}_j(t). \tag{6.79}$$

Because of causality, it is clear that for any system operator $\hat{O}$,

$$[\hat{O}(t),\hat{\Pi}_{j,\mathrm{in}}(t')] = 0, \quad t' > t; \tag{6.80}$$

i.e., the system does not depend on future input noise. For the output, we can invert this reasoning such that $\hat{\Pi}_{j,\mathrm{out}}(t')$ commutes with $\hat{O}(t)$ if $t' < t$. Using these findings in combination with the input-output relation from Eq. (6.79), we obtain [6.46]

$$[\hat{O}(t),\hat{\Pi}_{j,\mathrm{in}}(t')] = \Theta(t-t')\sqrt{2\lambda_j}[\hat{O}(t),\hat{\Pi}_j(t')], \tag{6.81}$$

where we defined Θ as the step function with the half-maximum convention, i.e., $\Theta(0) = 1/2$. Using the transformation between the diagonal operators and the correlated noise operators, $\xi_k(t) = \sum_j \sqrt{\lambda_j/\gamma}\mathbf{T}_{kj}\hat{\Pi}_{j,\mathrm{in}}(t)$, we find the commutation relations of a system operator with the correlated input noise,

$$[\hat{O}(t), \xi_k(t')] = \Theta(t-t')\sqrt{2\gamma}\sum_l h_{kl}[\hat{O}(t), \hat{S}_l(t')]. \tag{6.82}$$

Using this, we can compute the correlation functions of the modified input noise operators,

$$\langle \bar{\xi}_j(t)\bar{\xi}_k^\dagger(t')\rangle = h_{jk}\delta(t-t')\,\langle \hat{S}_j^z(t)\hat{S}_k^z(t')\rangle + \langle \hat{S}_j^z(t)\xi_k^\dagger(t')\xi_j(t)\hat{S}_k^z(t')\rangle\,, \tag{6.83}$$

where we used the commutation relation from Eq. (6.77). Using the commutation rules from Eq. (6.82), one can show that the second term is proportional to $\Theta(t-t')\Theta(t'-t)$. Thus, it is only finite if $t = t'$ and does not contribute as a distribution. In other words, an integral over any time interval (such as our detection window) of this term vanishes. We can therefore neglect this term and arrive at

$$\langle \bar{\xi}_j(t)\bar{\xi}_k^\dagger(t')\rangle = h_{jk}\delta(t-t')\,\langle \hat{S}_j^z(t)\hat{S}_k^z(t')\rangle\,, \tag{6.84}$$

which in the linearized regime yields Eq. (6.9a).

Proceeding, we have

$$\langle \bar{\xi}_j^z(t)\bar{\xi}_k^z(t')\rangle = 4\Big[h_{jk}\delta(t-t')\,\langle \hat{S}_j^\dagger(t)\hat{S}_k(t')\rangle + \langle \hat{S}_j^\dagger(t)\xi_k^\dagger(t')\xi_j(t)\hat{S}_k(t')\rangle\Big]. \tag{6.85}$$

Since $\xi_j(t)$ and $\hat{S}_k(t')$ commute if $t \geq t'$ and $\xi_j(t)$ applied to the right vanishes, the second term in the above expression is zero for $t \geq t'$. The same reasoning applies to $\xi_k^\dagger(t')$ and $\hat{S}_j^\dagger(t)$ for $t \leq t'$, such that we have

$$\langle \bar{\xi}_j^z(t)\bar{\xi}_k^z(t')\rangle = 4h_{jk}\delta(t-t')\,\langle \hat{S}_j^\dagger(t)\hat{S}_k(t')\rangle\,, \tag{6.86}$$

which after linearizing gives the expression in Eq. (6.9b). Finally, we can use the same line of argument to derive the correlation function $\langle \bar{\xi}_j(t)\bar{\xi}_k^z(t')\rangle$ in Eq. (6.9c).

Steady-state Lyapunov equation

The general solution for a system of N linearly coupled QLEs with constant coefficients reads

$$\mathbf{v}(t) = e^{\mathbf{M}t}\mathbf{v}(0) + \int_0^t dt' e^{\mathbf{M}(t-t')}\mathbf{N}\mathbf{v}_{\text{in}}(t'). \tag{6.87}$$

When the real part of all eigenvalues of the drift matrix $\mathbf{M}$ are negative, the system is stable and goes towards a steady state where $e^{\mathbf{M}t}$ vanishes and the transient solution (containing information about the initial state) plays no role. In such a case, for times t large enough such that steady state is already reached, one can define (a time-independent) correlation matrix $\mathbf{V} = \langle \mathbf{v}(t)\mathbf{v}^\top(t)\rangle$ that is easily constructed with the steady-state solution only,

$$\mathbf{V} = \int_0^t dt' e^{\mathbf{M}(t-t')} \mathbf{D} e^{\mathbf{M}^T(t-t')}, \tag{6.88}$$

where we have use $\langle \mathbf{v}_{\text{in}}(t')\mathbf{v}_{\text{in}}(t'')^\top \rangle = \mathbf{C}\delta(t'-t'')$ and defined the diffusion matrix as $\mathbf{D} = \mathbf{N}\mathbf{C}\mathbf{N}^T$. The expression for $\mathbf{C}$ can be computed from the input correlations and the results is listed in the main text as Eq. (6.26). We can then derive a Lyuapunov equation for the covariance matrix using integration by parts

$$\begin{aligned} \mathbf{M}\mathbf{V} + \mathbf{V}\mathbf{M}^\top &= \int_0^t dt' \mathbf{M} e^{\mathbf{M}(t-t')} \mathbf{D} e^{\mathbf{M}^T(t-t')} + V\mathbf{M}^\top = \\ &= e^{\mathbf{M}(t-t')} \mathbf{D} e^{\mathbf{M}^\top(t-t')} \Big|_{t'=0}^{t} - \mathbf{V}\mathbf{M}^\top + \mathbf{V}\mathbf{M}^\top = -\mathbf{D} \end{aligned} \tag{6.89}$$

Notice that one can write a similar equation for the symmetrized covariance matrix defined as $V_{ij} = \left(\langle v_i v_j \rangle + \langle v_j v_i \rangle\right)/2$, by a simple replacement of the diffusion matrix with the symmetrized one $\mathbf{D} = \mathbf{N}\left(\mathbf{C} + \mathbf{C}^\top\right)\mathbf{N}^\top/2$.

Fourier analysis of the output and the detected signal

Output spectrum

We define the Fourier transform for an arbitrary operator $\hat{O}(t)$ as

$$\hat{O}(t) = \frac{1}{\sqrt{2\pi}} \int_{-\infty}^{\infty} d\omega e^{i\omega t} \hat{O}(\omega), \tag{6.90}$$

which we employ to transform the linear set of differential equations to a set of coupled equations,

$$i\omega \mathbf{v}(\omega) = \mathbf{M}\mathbf{v}(\omega) + \mathbf{N}\mathbf{v}_{\text{in}}(\omega). \tag{6.91}$$

This allows us to express the intra-cavity quantum fluctuations in terms of the input noise as

$$\mathbf{v}(\omega) = \left(i\omega \mathbb{1} - \mathbf{M}\right)^{-1} \mathbf{N}\mathbf{v}_{\text{in}}(\omega), \tag{6.92}$$

Furthermore, using input-output relations in the time domain

$$\mathbf{v}_{\text{out}}(t) = \mathbf{N}^\top \mathbf{v}(t) - \mathbf{v}_{\text{in}}(t). \tag{6.93}$$

allows us to connect the output to the input as a simple matrix multiplication,

$$\mathbf{v}_{\text{out}}(\omega) = \mathbf{F}(\omega)\mathbf{v}_{\text{in}}(\omega), \tag{6.94}$$

where $\mathbf{F}(\omega) = [\mathbf{N}^\top (i\omega\mathbb{1} - \mathbf{M})^{-1} \mathbf{N} - \mathbb{1}]$. In the frequency space, the response of the system ensures the preservation of δ correlations,

$$\langle \mathbf{v}_{\text{out}}(\omega)\mathbf{v}_{\text{out}}^\top(\omega')\rangle = \boldsymbol{\mathcal{S}}_{\text{out}}(\omega)\delta(\omega+\omega'). \tag{6.95}$$

The system response for two-operator correlations is completely encoded in the spectrum matrix given by

$$\boldsymbol{\mathcal{S}}_{\text{out}}(\omega) = \mathbf{F}(\omega)\mathbf{C}\mathbf{F}^\top(-\omega). \tag{6.96}$$

Time-integrated correlations

The output can be used directly to compute correlations for time-integrated operators at equal times,

$$\mathbf{V}_{\text{det}}(t) = \frac{1}{2T}\int_{t-T}^{t+T} dt' \int_{t-T}^{t+T} dt'' \left\langle \mathbf{v}_{\text{out}}(t')\mathbf{v}_{\text{out}}(t'')^\top \right\rangle. \tag{6.97}$$

We then expand operators in terms of their Fourier components and use the δ correlations in the frequency space. This leads to the evaluation of the following integral:

$$\int_{t-T}^{t+T} dt' \int_{t-T}^{t+T} dt'' e^{i\omega t'} e^{-i\omega t''} = \left[\frac{2\sin\omega T}{\omega}\right]^2. \tag{6.98}$$

For sufficiently long detection times (much longer than the characteristic bandwidth of the spectrum matrix), the sinc function picks only the zero-frequency component (since we are in a rotating frame, this corresponds to the laser frequency),

$$\mathbf{V}_{\text{det}} = \frac{1}{\pi T}\int_{-\infty}^{\infty} d\omega \left[\frac{\sin^2\omega T}{\omega^2}\right] \boldsymbol{\mathcal{S}}_{\text{out}}(\omega) \approx \boldsymbol{\mathcal{S}}_{\text{out}}(0). \tag{6.99}$$

Resolving four-point correlations

Let us generally write expectation values for any combinations of detected operators as $\mathcal{R}_{i_1 i_2 i_3 i_4} = \langle v_{\text{det}}^{i_1} v_{\text{det}}^{i_2} v_{\text{det}}^{i_3} v_{\text{det}}^{i_4}\rangle$. We then connect these expectations values to the output operators combinations for which Isserlis' theorem applies, allowing one to express any product of operators in sums of all different products of two-point correlations as

$$\begin{aligned}\langle v_{\text{out}}^{i_1}(\omega_1)v_{\text{out}}^{i_2}(\omega_2)v_{\text{out}}^{i_3}(\omega_3)v_{\text{out}}^{i_4}(\omega_4)\rangle = \; & \mathcal{S}_{\text{out}}^{i_1 i_2}(\omega_1)\mathcal{S}_{\text{out}}^{i_3 i_4}(\omega_3)\delta(\omega_1+\omega_2)\delta(\omega_3+\omega_4) \\ & + \mathcal{S}_{\text{out}}^{i_1 i_3}(\omega_1)\mathcal{S}_{\text{out}}^{i_2 i_4}(\omega_2)\delta(\omega_1+\omega_3)\delta(\omega_2+\omega_4) \\ & + \mathcal{S}_{\text{out}}^{i_1 i_4}(\omega_1)\mathcal{S}_{\text{out}}^{i_2 i_3}(\omega_2)\delta(\omega_1+\omega_4)\delta(\omega_2+\omega_3).\end{aligned} \tag{6.100}$$

The integration over the detection time window will, of course, again give rise to the sinc functions in the integrand; in the long detection time limit, we then write the general expression

$$\mathcal{R}_{i_1 i_2 i_3 i_4} = \mathcal{S}^{i_1 i_2}_{\text{out}}(0)\mathcal{S}^{i_3 i_4}_{\text{out}}(0) + \mathcal{S}^{i_1 i_3}_{\text{out}}(0)\mathcal{S}^{i_2 i_4}_{\text{out}}(0) + \mathcal{S}^{i_1 i_4}_{\text{out}}(0)\mathcal{S}^{i_2 i_3}_{\text{out}}(0), \tag{6.101}$$

which we can make use of to evaluate any four-point operator correlations. For example, we can evaluate the first term in the left-hand side of Eq. (6.42) as

$$\langle b^\dagger_{\text{det}} b_{\text{det}} b^\dagger_{\text{det}} b_{\text{det}} \rangle = \mathcal{S}^{43}_{\text{out}}(0)\mathcal{S}^{43}_{\text{out}}(0) + \mathcal{S}^{44}_{\text{out}}(0)\mathcal{S}^{33}_{\text{out}}(0) + \mathcal{S}^{43}_{\text{out}}(0)\mathcal{S}^{34}_{\text{out}}(0). \tag{6.102}$$

Free space spatial field distribution

In order to express the electric field amplitude as function of the emitter operators $\hat{S}_i$, we follow an approach along the lines of Ref. [6.33]. Recall that the Heisenberg equation for the photon annihilation operator of a mode with wave vector $\mathbf{k}$ and polarization λ coupled to N identical quantum emitters is

$$\dot{\hat{A}}_{\mathbf{k},\lambda}(t) = -i g_{\mathbf{k},\lambda} \sum_j \hat{S}_j(t) e^{-i\mathbf{k}\cdot\mathbf{r}_j} e^{i(\omega_k - \omega_\text{e})t}. \tag{6.103}$$

Here, $g_{\mathbf{k},\lambda} = \sqrt{\omega_k/(2\hbar\epsilon_0 V}\mathbf{e}_{\mathbf{k},\lambda}\cdot\boldsymbol{\mu}$ is the dipole interaction between the mode and the emitter with dipole moment $\boldsymbol{\mu}$. Note that the equation above is already written in a frame rotating at $\omega_k - \omega_\text{e}$. The formal solution of the above equation is

$$\hat{A}_{\mathbf{k},\lambda}(t) = \hat{A}_{\mathbf{k},\lambda}(0) - i g_{\mathbf{k},\lambda} \sum_j \int_0^t dt' \hat{S}_j(t') e^{-i\mathbf{k}\cdot\mathbf{r}_j} e^{i(\omega_k - \omega_\text{e})t'}.$$

The initial value above corresponds to the input of the mode. Assuming that the modes surrounding the emitters are in vacuum, this term does not contribute to any averages. We therefore drop it in the following calculation.

Performing the Markov approximation, we can already see that it is possible to express the field annihilation operators at any time directly by the emitter operator at equal time.

Inserting the expression obtained for $\hat{A}_{\mathbf{k},\lambda}$ results in the electric field amplitude

$$\hat{\mathbf{E}}^+(\mathbf{r},t) = -i \sum_j \hat{S}_j(t) \sum_{\mathbf{k}} \mathbf{f}(\mathbf{k}) \int_0^t dt' e^{-i(\omega_k - \omega_\text{e})(t-t')}, \tag{6.104}$$

where

$$\mathbf{f}(\mathbf{k}) = \sum_\lambda \sqrt{\frac{\hbar\omega_k}{2\epsilon_0 V}} g_{\mathbf{k},\lambda}\mathbf{e}_{\mathbf{k},\lambda} e^{i\mathbf{k}\cdot(\mathbf{r}-\mathbf{r}_j)} = \frac{\omega_k}{2\epsilon_0 V}\left(\boldsymbol{\mu} - \frac{\boldsymbol{\mu}\cdot\mathbf{k}}{k^2}\mathbf{k}\right) e^{i\mathbf{k}\cdot(\mathbf{r}-\mathbf{r}_j)}. \tag{6.105}$$

In the last step, we exploited the liberty of choosing $\boldsymbol{\mu}$ to lie in the plane spanned by $\mathbf{k}$ and $\mathbf{e}_{\mathbf{k}1}$ to resolve the sum over the polarization $\lambda = 1, 2$.

Since the set of free space modes is continuous, we can replace the sum over wave vectors by an integral

$$\sum_{\mathbf{k}} \to \frac{V}{(2\pi c)^3} \int d\omega_k \omega_k^2 \int d\Omega_k, \tag{6.106}$$

where we have already written the integral in spherical coordinates in **k** space. The part of the expression that has an angular dependence can be separated and the solid angle integral can be solved (for arbitrary **r** and **k**),

$$\int d\Omega_k \left(\boldsymbol{\mu} - \frac{\boldsymbol{\mu}\cdot\mathbf{k}}{k^2}\mathbf{k}\right) e^{i\mathbf{k}\cdot\mathbf{r}} = 2\pi \left(\boldsymbol{\mu} + \frac{(\boldsymbol{\mu}\cdot\nabla_{\mathbf{r}})}{k^2}\nabla_{\mathbf{r}}\right) \int_0^\pi d\theta \sin\theta e^{ikr\cos\theta}. \tag{6.107}$$

Here, we already solved the polar angle integral obtaining 2π and written the products with **k** as derivatives of the exponential function. The remaining integral is straightforward to solve and the problem of solving the solid angle integral surmounts to applying the Nabla operator.

Inserting the result back into the electric field, we obtain

$$\begin{aligned}\hat{\mathbf{E}}^+(\mathbf{r},t) = \frac{-i\mu}{\epsilon_0(2\pi)^2c^3} \sum_j \hat{S}_j(t) \int d\omega_k \omega_k^3 \times \\ \int_0^t dt' e^{-i(\omega_k-\omega_\mathrm{e})(t-t')} \sum_{i\in\{x,y,z\}} F_i(k|\mathbf{r}-\mathbf{r}_j|)\mathbf{e}_i,\end{aligned} \tag{6.108}$$

where $\mathbf{e}_{x,y,z}$ is the respective unit vector in Cartesian coordinates and

$$F_x(kr) = -\cos\theta\sin\theta\cos\phi\left(\frac{\sin(kr)}{kr} + 3\frac{\cos(kr)}{(kr)^2} - 3\frac{\sin(kr)}{(kr)^3}\right), \tag{6.109a}$$

$$F_y(kr) = -\cos\theta\sin\theta\sin\phi\left(\frac{\sin(kr)}{kr} + 3\frac{\cos(kr)}{(kr)^2} - 3\frac{\sin(kr)}{(kr)^3}\right), \tag{6.109b}$$

$$F_z(kr) = \sin^2\theta\frac{\sin(kr)}{kr} + \left(1 - 3\cos^2\theta\right)\left(\frac{\cos(kr)}{(kr)^2} - \frac{\sin(kr)}{(kr)^3}\right). \tag{6.109c}$$

In order to solve the time integral, we make use of the Sokhotski formula,

$$\begin{aligned}&\int d\omega_k \omega_k^3 \int_0^t dt' e^{-i(\omega_k-\omega_\mathrm{e})(t-t')} F_i(kr) = \\ &= \int d\omega_k \omega_k^3 \left(-i\mathcal{P}\frac{1}{\omega_k-\omega_\mathrm{e}} + \pi\delta(\omega_k-\omega_\mathrm{e})\right) F_i(kr),\end{aligned} \tag{6.110}$$

where $\mathcal{P}$ denotes the principal value. The integral proportional to the δ distribution is straightforward to solve, while the principal value integrals require some more elaborate (yet standard) methods of complex contour integration.

Finally, the resulting electric field is given by

$$\hat{\mathbf{E}}^{+}(\mathbf{r},t) = -i\frac{3\gamma}{4\mu}\sum_{j} S_j(t) \sum_{m\in\{x,y,z\}} \left(F_m(k_{\mathrm{e}}|\mathbf{r}-\mathbf{r}_j|) - iG_m(k_{\mathrm{e}}|\mathbf{r}-\mathbf{r}_j|)\right), \tag{6.111}$$

with

$$G_x(kr) = -\cos\theta\sin\theta\cos\phi\left(\frac{\cos(kr)}{kr} - 3\frac{\sin(kr)}{(kr)^2} - 3\frac{\cos(kr)}{(kr)^3}\right), \tag{6.112a}$$

$$G_y(kr) = -\cos\theta\sin\theta\sin\phi\left(\frac{\cos(kr)}{kr} - 3\frac{\sin(kr)}{(kr)^2} - 3\frac{\cos(kr)}{(kr)^3}\right), \tag{6.112b}$$

$$G_z(kr) = \sin^2\theta\frac{\cos(kr)}{kr} - \left(1-3\cos^2\theta\right)\left(\frac{\sin(kr)}{(kr)^2} + \frac{\cos(kr)}{(kr)^3}\right). \tag{6.112c}$$

Note, that one can easily calculate the dipole interaction with the field given by Eq. (6.111). This selects the component parallel to the dipole moment $\boldsymbol{\mu}$ (the z component) and we obtain the effective emitter dipole-dipole interactions [6.33],

$$\Omega_{ij} = -\frac{3\gamma}{4}G_z\left(k_{\mathrm{e}}|\mathbf{r}_i-\mathbf{r}_j|\right), \tag{6.113a}$$

$$\gamma_{ij} = \gamma h_{ij} = \frac{3\gamma}{2}F_z\left(k_{\mathrm{e}}|\mathbf{r}_i-\mathbf{r}_j|\right). \tag{6.113b}$$

The intensity shown in Fig. 6.4 is the average intensity at $t=0$ given by

$$I(\mathbf{r}) = \langle\hat{\mathbf{E}}(\mathbf{r})\cdot\hat{\mathbf{E}}(\mathbf{r})\rangle = \langle\hat{\mathbf{E}}^{-}(\mathbf{r})\cdot\hat{\mathbf{E}}^{+}(\mathbf{r})\rangle. \tag{6.114}$$

Correlation matrix for many emitters

The definition of the many-emitter autocorrelation matrix as given in Eq. (6.64) is rather condensed. Hence, here we specify once again what the matrix elements required to write this matrix down are. In essence, it boils down to the noise correlation functions given in Eqs. (6.9). In particular, the $N\times N$ matrices used to define the overall autocorrelation matrix $\mathbf{C}$ have the matrix elements

$$\langle\bar{\xi}_j(t)\bar{\xi}_k^{\dagger}(t')\rangle = \mathbf{C}_{\beta\beta}^{jk}\delta(t-t'), \tag{6.115a}$$

$$\langle\bar{\xi}_j^{z}(t)\bar{\xi}_k^{z}(t')\rangle = \mathbf{C}_{zz}^{jk}\delta(t-t'), \tag{6.115b}$$

$$\langle\bar{\xi}_j^{z}(t)\bar{\xi}_k^{\dagger}(t')\rangle = \mathbf{C}_{z\beta}^{jk}\delta(t-t'), \tag{6.115c}$$

$$\langle\bar{\xi}_j(t)\bar{\xi}_k^{z}(t')\rangle = \mathbf{C}_{\beta z}^{jk}\delta(t-t'). \tag{6.115d}$$

Nonlinear correction

Starting from the QLEs for N emitters which are given by

$$\dot{\alpha} = -\left(\kappa - i\Delta_{\mathrm{c}}\right)\alpha + \eta - i\mathbf{G}^{\top}\boldsymbol{\beta}, \tag{6.116}$$

$$\dot{\boldsymbol{\beta}} = \Big((i\Delta_{\mathrm{e}} - \gamma)\mathbb{1} + \mathbf{z}(i\boldsymbol{\Omega} + \tilde{\boldsymbol{\Gamma}})\Big)\boldsymbol{\beta} + i\mathbf{z}\mathbf{G}\alpha, \tag{6.117}$$

where we define $\tilde{\boldsymbol{\Gamma}} = \boldsymbol{\Gamma} - \gamma\mathbb{1}$, $\mathbf{z} = \sum_{j=1}^{N} z_j \mathbf{P}_j$, and $\mathbf{P}_j = \mathbf{e}_j\mathbf{e}_j^{\top}$ ($\mathbf{e}_j$ being a Cartesian basis vector). By employing the relation $z_j \approx 2|\beta_j|^2 - 1$, we obtain the equations

$$\dot{\alpha} = -\left(\kappa - i\Delta_{\mathrm{c}}\right)\alpha + \eta - i\mathbf{G}^{\top}\boldsymbol{\beta}, \tag{6.118}$$

$$\dot{\boldsymbol{\beta}} = -\left(i\boldsymbol{\Omega} + \boldsymbol{\Gamma} - i\Delta_{\mathrm{e}}\right)\boldsymbol{\beta} - i\mathbf{G}\alpha + 2|\boldsymbol{\beta}|^2(i\boldsymbol{\Omega} + \tilde{\boldsymbol{\Gamma}})\boldsymbol{\beta} + i2|\boldsymbol{\beta}|^2\mathbf{G}\alpha, \tag{6.119}$$

with the matrix $|\boldsymbol{\beta}|^2 = \sum_{j=1}^{N} \mathbf{P}_j\boldsymbol{\beta}\boldsymbol{\beta}^{\dagger}\mathbf{P}_j$. For the steady-state scenario with $\dot{\alpha} = 0$, we obtain $\alpha = (\eta - i\mathbf{G}^{\top}\boldsymbol{\beta})/(\kappa - i\Delta_c)$. Substituting this into the steady-state equation ($\dot{\boldsymbol{\beta}} = 0$) of Eq. (6.119) results in

$$\begin{aligned} 0 = &-\Big[(-i\Delta_{\mathrm{c}} + \kappa)(-i\Delta_{\mathrm{e}}\mathbb{1} + i\boldsymbol{\Omega} + \boldsymbol{\Gamma}) + \mathbf{G}\mathbf{G}^{\top}\Big]\boldsymbol{\beta} - i\mathbf{G}\eta \\ &+ i2|\boldsymbol{\beta}|^2\mathbf{G}\eta + 2|\boldsymbol{\beta}|^2\Big[(i\Delta_{\mathrm{c}} + \kappa)(i\boldsymbol{\Omega} + \tilde{\boldsymbol{\Gamma}}) + \mathbf{G}\mathbf{G}^{\top}\Big]\boldsymbol{\beta}. \end{aligned} \tag{6.120}$$

With the linear solution being

$$\boldsymbol{\beta}^{(1)} = -i\eta\Big[(\kappa - i\Delta_{\mathrm{c}})(i\boldsymbol{\Omega} + \boldsymbol{\Gamma} - i\Delta_{\mathrm{e}}\mathbb{1}) + \mathbf{G}\mathbf{G}^{\top}\Big]^{-1}\mathbf{G}, \tag{6.121}$$

the next order of correction can be found by introducing the perturbative ansatz $\boldsymbol{\beta} \approx \boldsymbol{\beta}^{(1)} + \boldsymbol{\beta}^{(3)}$ into Eq. (6.120) which leads to

$$\begin{aligned} \boldsymbol{\beta}^{(3)} =& 2\Big[(\kappa - i\Delta_{\mathrm{c}})(i\boldsymbol{\Omega} + \boldsymbol{\Gamma} - i\Delta_{\mathrm{e}}) + \mathbf{G}\mathbf{G}^{\top}\Big]^{-1}\left(\sum_{j=1}^{N}\mathbf{P}_j\boldsymbol{\beta}^{(1)}\boldsymbol{\beta}^{(1)\dagger}\mathbf{P}_j\right) \\ &\times\Big(i\eta\mathbf{G} + [(\kappa - i\Delta_{\mathrm{c}})(i\boldsymbol{\Omega} + \tilde{\boldsymbol{\Gamma}}) + \mathbf{G}\mathbf{G}^{\top}]\boldsymbol{\beta}^{(1)}\Big). \end{aligned} \tag{6.122}$$

Here, we have ignored all terms with $O(\eta^4)$. The term $\boldsymbol{\beta}^{(3)}$ describes the collective Kerr nonlinearity of the N-emitter system. For $N = 1$, this simplifies to $\beta^{(3)} = -2\beta^{(1)}|\beta^{(1)}|^2\left(1 - i(g/\eta)\beta^{(1)}\right)$.

The modified transmission amplitude can be obtained from the relation $t = (\kappa - i(\kappa/\eta)\mathbf{G}^{\top}(\boldsymbol{\beta}^{(1)} + \boldsymbol{\beta}^{(3)}))/(\kappa - i\Delta_c)$. For a single emitter, we have

$$t_{\mathrm{c}} = t_{\mathrm{c}}^{(1)}\left(1 + \frac{2g^4\eta^2}{((\gamma - i\Delta_{\mathrm{e}})(\kappa - i\Delta_{\mathrm{c}}) + g^2)|(\gamma - i\Delta_{\mathrm{e}})(\kappa - i\Delta_{\mathrm{c}}) + g^2|^2}\right), \tag{6.123}$$

where $t_{\mathrm{c}}^{(1)} = \kappa/[(\kappa - i\Delta_{\mathrm{c}}) + g^2/(\gamma - i\Delta_{\mathrm{e}})]$ is the result for the transmission in the linear case.

7 Preprint

arXiv:1901.10598

Extraordinary subradiance with lossless excitation transfer in dipole-coupled nano-rings of quantum emitters†

M. Moreno-Cardoner[1,2], D. Plankensteiner[3], L. Ostermann[3], D. Chang[1,4] and H. Ritsch[3]

[1]*ICFO-Institut de Ciencies Fotoniques, The Barcelona Institute of Science and Technology, 08860 Castelldefels (Barcelona), Spain*
[2]*Física Teòrica: Informació i Fenòmens Quàntics. Departament de Física, Universitat Autònoma de Barcelona, 08193 Bellaterra, Spain*
[3]*Institut für Theoretische Physik, Universität Innsbruck, Technikerstraße 21a, A-6020 Innsbruck, Austria*
[4]*ICREA-Institució Catalana de Recerca i Estudis Avancats, 08015 Barcelona, Spain*

A ring of sub-wavelength spaced dipole-coupled quantum emitters possesses only few radiant but many extraordinarily subradiant collective modes. These exhibit a 3D-confined spatial radiation field pattern forming a nano-scale high-Q optical resonator. We show that tailoring the geometry, orientation and distance between two such rings allows for increasing the ratio of coherent ring-to-ring coupling versus free-space emission by several orders of magnitude. In particular we find that subradiant excitations, when delocalized over several ring sites, are effectively transported between the rings with a high fidelity.

arXiv:1901.10598

[†] The effort behind this work was lead by M. Moreno-Cardoner in close collaboration with the author of this thesis. M. Moreno-Cardoner performed most analytical and numerical calculations in the first part of the paper and the author offered valuable input in these calculations. The main contribution of the author, however, lies in the development of the final part of the paper, in which a key result, namely the transport fidelity between two rings is investigated. L. Ostermann offered helpful discussions and input. D. Chang acted as supervisor and provided vital ideas.

7.1 Introduction

An efficient and controllable energy transfer is significant for a wide variety of applications, ranging from solar energy conversion, near-field communication protocols, and photosynthetic processes, to quantum communication, just to name a few. In all these processes it is crucial to find mechanisms that allow for a minimization of the energy loss. A concrete example is the coupling between two or more conventional optical ring resonators, which can be used for the realization of switches, high-order optical filters or mechanical sensors. This coupling relies on the evanescent field extending outside the waveguide modes, and it can be enhanced by reducing the distance between them, increasing the coupling length or modifying their refractive indices. In a very different context, in light-harvesting complexes such as LHC-II, an intriguing question is whether nature chooses a particular configuration to minimize the energy loss in the transport of the absorbed photon.

In this work, we will focus on excitation transport between two independent chains formed by regularly arranged atom-like emitters and show how subradiance can aid this process. In particular, we will show that chains of atoms forming two rings can reduce the energy loss and enhance the fidelity in the excitation transport between them.

Spontaneous photon emission from a single excited atom in free space is strongly modified by identical emitters in the ground state nearby. Dipole-dipole coupling leads to the appearance of fast decay via superradiant states as well as long-lived subradiant behavior [7.1–7.5]. Energy shifts originating from coherent dipole-dipole coupling [7.6] lead to a broadening of the collective energy spectrum strongly growing with smaller atomic distances [7.7]. The properties of these collective states strongly depend on the geometry of the dipole arrays [7.1, 7.8, 7.9]. While superradiance is a well-known experimental phenomenon, subradiance is much more elusive [7.10].

As shown before, excitons become perfectly dark in an infinite chain of sub-wavelength spaced dipoles [7.11] when their wave-vector surpasses the free-space photon wave-vector. For a finite chain of emitters the maximal excited state lifetime grows with the third power of the atom number N as photon emission only occurs at its ends [7.4, 7.7]. As excitations are efficiently guided without dissipation as in a thin optical fiber [7.12, 7.13] this should have useful applications for efficient optical photon storage [7.4]. Low loss guiding studies have also been performed for chains of gold nano-particles [7.14].

As a central new phenomenon, we study the excitation transfer between two separate dipole arrays. Although the strong transverse field confinement of subradiant states leads to an exponential suppression with distance between two parallel chains, energy eventually is still transferred between them with an almost negligible loss [7.12]. Here, we focus on chains folded into rings, which as shown and discussed in Ref. [7.4] exhibit extraordinarily long exciton lifetimes with very special radiative properties. A ring of dipoles at small distances in this sense implements a minimalist form of an optical ring resonator as depicted in Fig. 7.1, which, in principle, can exchange energy with a second nearby ring.

As with conventional fiber-optical ring resonators we study how two such rings can be coupled via their mode overlap at a minimal free-space radiation loss. Efficient

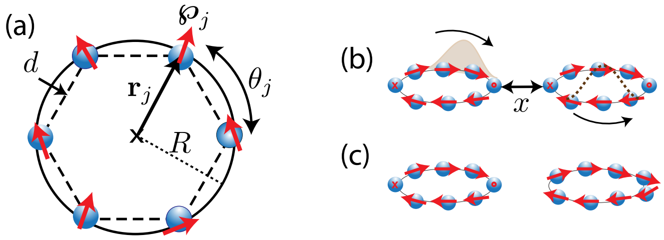

Figure 7.1: *Schematics of the system setup.* **(a)** A single ring with inter-particle distance d and radius R. The red arrows denote arbitrary dipole orientations. **(b)** and **(c)** A single excitation is transferred between two in-plane rings separated by the distance x. **(b)** and **(c)** correspond to the site-site and site-edge configurations, respectively.

coherent coupling between two long-lived states is one of the central ingredients needed in distributed quantum computing [7.15]. Surprisingly, the subradiant states of individual rings feature a slower but much more efficient ring-to-ring energy transfer than superradiant states.

Note, that many light-harvesting complexes such as LHC-II in biological systems exhibit a structure made out of coupled dipole rings [7.16–7.18]. While modeling them realistically certainly requires a much more detailed and sophisticated description, a corresponding simplistic model of eight outer rings commonly coupled to an inner ring [7.19] shows a wealth of complex and nontrivial dynamics with evidence of coherent excitation propagation already [7.19, 7.20]. In our toy model inspired by this geometry, dark states play an essential role in the coupled dynamics and energy transfer between the rings.

7.2 System

Let us consider N identical two-level quantum emitters with given dipole orientations (denoted by $\hat{\wp}_i$, $i = 1, \dots, N$) positioned in a regular ring with inter-particle distance d [see Fig. 7.1(a)]. The emitters can be excited by an external field, and we assume that they have a significant optical response in a narrow bandwidth around their resonance frequency ω_0 only. Integrating out the photonic degrees of freedom, and in the Born-Markov approximation, the internal dynamics of the atoms are governed by the master equation $\dot{\rho} = -i[H, \rho] + \mathcal{L}[\rho]$. The Hamiltonian in a frame rotating at the atomic transition frequency ω_0 reads

$$H = \sum_{ij;i\neq j} \Omega_{ij} \sigma_i^{ge} \sigma_j^{eg}, \tag{7.1}$$

and the Lindblad operator is

$$\mathcal{L}[\rho] = \frac{1}{2} \sum_{i,j} \Gamma_{ij} \left(2\sigma_i^{ge} \rho \sigma_j^{eg} - \sigma_i^{eg} \sigma_j^{ge} \rho - \rho \sigma_i^{eg} \sigma_j^{ge} \right). \tag{7.2}$$

The dipole interaction and collective decay matrices with elements Ω_{ij} and Γ_{ij}, respectively, are given by

$$\Omega_{ij} = -\frac{3\pi\Gamma_0}{k_0} \operatorname{Re}\left\{\hat{\wp}_i^* \cdot \boldsymbol{G}(\vec{r}_i - \vec{r}_j, \omega_0) \cdot \hat{\wp}_j\right\}, \tag{7.3}$$

$$\Gamma_{ij} = \frac{6\pi\Gamma_0}{k_0} \operatorname{Im}\left\{\hat{\wp}_i^* \cdot \boldsymbol{G}(\vec{r}_i - \vec{r}_j, \omega_0) \cdot \hat{\wp}_j\right\}, \tag{7.4}$$

where $\boldsymbol{G}(\vec{r}, \omega_0)$ is Green's tensor in free space, which acts on an oscillating unit dipole according to

$$\begin{aligned}\boldsymbol{G}(\vec{r}, \omega_0) \cdot \hat{\wp} = \frac{e^{ik_0 r}}{4\pi r}\big[&(\hat{\mathbf{r}} \times \hat{\wp}) \times \hat{\mathbf{r}} + \\ &+ \left(\frac{1}{k_0^2 r^2} - \frac{i}{k_0 r}\right)(3\hat{\mathbf{r}}(\hat{\mathbf{r}} \cdot \hat{\wp}) - \hat{\wp})\big].\end{aligned} \tag{7.5}$$

Here, $\hat{\mathbf{r}} = \vec{r}/|\vec{r}|$ is the position unit-vector, $k_0 = \omega_0/c$ is the wavenumber associated with the atomic transition, and $\Gamma_0 = |\wp|^2 k_0^3/3\pi\hbar\epsilon_0$ is the spontaneous emission rate of a single emitter with dipole moment strength $\wp$.

After solving for the atomic density matrix the quantum fields can be obtained from a generalized input-output relation [7.4, 7.21], which in absence of an external field reads:

$$\boldsymbol{E}^+(\vec{r}) = \frac{|\wp| k_0^2}{\epsilon_0} \sum_i \boldsymbol{G}(\vec{r} - \vec{r}_i, \omega_0) \cdot \hat{\wp}_i \sigma_i^{ge}. \tag{7.6}$$

In the following, we will consider the single-excitation manifold to be significantly occupied only. In this case, for the observables of interest (such as the fields generated by the ring or the excited state population) we can neglect the recycling term (first term in the Lindblad expression). This term accounts for the change in the ground state population, which does not modify said observables. Then, the system can be fully understood from the properties of the eigenstates of an effective Hamiltonian (containing the other two terms of the Lindblad expression only). It reads

$$H_{\text{eff}} = \sum_{ij} \left(\Omega_{ij} - i\frac{\Gamma_{ij}}{2}\right) \sigma_i^{eg} \sigma_j^{ge} \tag{7.7}$$

with $\Omega_{ii} = 0$, as all the emitters are identical and a finite value would represent a global energy shift in the Hamiltonian only.

7.3 Collective excitations and radiative properties of a single ring

We start by analyzing a single ring of N dipole-coupled quantum emitters. The eigenstates of H_{eff} define a set of collective modes with associated complex eigenvalues, whose real and imaginary parts correspond to the collective frequency shifts and decay

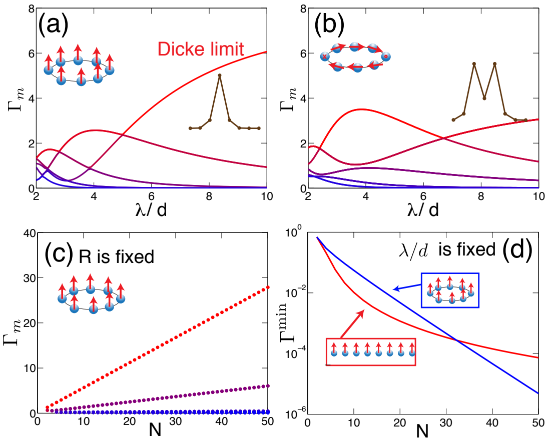

Figure 7.2: *Single ring properties.* **(a)** Collective decay rates Γ_m (in units of Γ_0) as a function of λ/d, for a ring of $N = 8$ emitters with transverse polarization and a single excitation. In the Dicke limit, $\lambda/d \to \infty$, only a single bright mode with a decay rate on the order of $N\Gamma_0$ is present, and $N-1$ modes are dark. **(b)** Identical setup as in (a) but for tangential polarization. Two bright modes arise in the Dicke limit at $m = \pm 1$. **(c)** Γ_m (in units of Γ_0) for a ring of fixed radius with transverse polarization when increasing the density of emitters. For the bright mode, $\Gamma \sim N\Gamma_0$. **(d)** Decay rate (log scale) of the most subradiant eigenmode versus the atom number, for a ring (blue circles) and an open linear chain (red circles), both with $\lambda = 3d$. The lifetime of the most subradiant mode increases exponentially with the atom number.

rates, respectively.

For a symmetric ring, where the dipole orientations preserve the rotational symmetry (e.g. if the dipoles are oriented perpendicularly to the plane of the ring, or tangentially to the ring), the collective modes in the single-excitation manifold are perfect spin waves given by $|\psi_m\rangle = \tilde{\sigma}_m^{eg}\,|g\rangle$, with

$$\tilde{\sigma}_m^{eg} = N^{-1/2} \sum_{j=1}^{N} e^{im\theta_j} \sigma_j^{eg}. \tag{7.8}$$

This is contrary to the case of a finite one-dimensional open chain, where the spin wave approximates the exact solution only [7.4]. Here, $\theta_j = 2\pi(j-1)/N$ is the angle associated with position j ($j = 1, \cdots, N$, see Fig. 7.1), and $m = 0, \pm 1, \pm 2, \cdots, \lceil \pm(N-1)/2 \rceil$ corresponds to the angular momentum of the mode. In these states the single excitation is completely delocalized over all sites, and its angular momentum is well defined. The corresponding eigenvalues are

$$\lambda_m = -\frac{3\pi\Gamma_0}{Nk_0} \sum_{j\ell} e^{im(\theta_\ell - \theta_j)} G_{j\ell}. \tag{7.9}$$

Here, $G_{j\ell} \equiv \hat{\wp}_j^* \cdot \boldsymbol{G}(\vec{r}_j - \vec{r}_\ell, \omega_0) \cdot \hat{\wp}_\ell$ includes the dispersive as well as the dissipative coupling of sites j and ℓ. Note that, due to the rotational symmetry, the coupling is invariant under a translation along the ring, *i.e.*, $G_{j\ell} = G_{j+1\ell+1}$. The real and imaginary parts of these eigenvalues define the collective frequency shifts and emission rates of the mode $J_m = \text{Re}\{\lambda_m\}$ and $\Gamma_m = -2\text{Im}\{\lambda_m\}$, respectively. It is easy to see that the spectrum will be symmetric under $m \leftrightarrow -m$, that is, $\lambda_m = \lambda_{-m}$. We note that the mode $m = 0$ is always non-degenerate, whereas the eigenstates with a maximum value of m will be doubly-degenerate if N is odd.

Intuitively, as we decrease the inter-particle distance d with respect to the light wavelength $\lambda = 2\pi/k_0$, we expect to approach the Dicke limit [7.22]. In this limit the emitters are so close that the range of the interaction is effectively infinite, yielding a single bright mode decaying at rate $\Gamma = N\Gamma_0$, and $N - 1$ perfectly dark modes. This is indeed the case if the polarization is transverse, as it is shown in Fig. 7.2(a), where we have plotted the collective decay rates as a function of the decreasing particle separation. For tangential polarization, on the other hand, there are two bright modes corresponding to $m = \pm 1$ with a decay rate $\Gamma = N\Gamma_0/2$, while $m = 0$ is dark by symmetry [see Fig. 7.2(b)].

We can observe this linear scaling of the decay of the most radiant mode with the number of emitters by gradually increasing the density of a ring of constant size. This is shown in Fig. 7.2(c) for transverse polarization. In addition, the covered frequency spectrum becomes increasingly larger as the ring gets denser. The polarization orientation will determine whether the dark or bright modes are lower or higher in energy. For instance, for transverse polarization, bright modes are lower in energy, whereas for tangential polarization (closer to a head-tail configuration of the dipoles) bright modes are higher in energy.

Moreover, the modes of the ring feature extraordinary radiative properties in contrast to an open linear chain. In particular, for a large enough number of emitters there exist subradiant modes whose emission is strongly suppressed. Indeed, if we increase the number of emitters while keeping λ/d constant, the system will start to locally resemble an infinite chain. The radiative properties of the infinite chain have been studied in detail in [7.4]. Interestingly, dark modes in an infinite chain correspond to spin waves characterized by a wavevector along the chain which is larger than k_0. In this case the eigenmode generates an evanescent field transversally to the chain and therefore the emitters can guide light perfectly, as if they were a real fiber. For the finite chain, these modes retain a small decay rate since a photon can still scatter off the ends of the chain. However, by bending and closing the chain to form a ring, an increased lifetime of the excitation can be achieved. As observed in Ref. [7.4], for a large enough ring, there is an exponential suppression of the decay rate with the number of emitters, in contrast to the polynomial suppression ($\sim N^{-3}$) observed for the open linear chain. A comparison of how the smallest decay rate scales with the atom number in the two cases is shown in Fig. 7.2(d).

Next, we show that the electromagnetic fields generated by a superradiant or a subradiant eigenmode can be radically different. Using Eq. (7.6) we evaluate the fields in Fig. 7.3 in real space for a ring with tangential polarization. The fields of the most subradiant (left column) and a radiant eigenmode (right column) are depicted. In

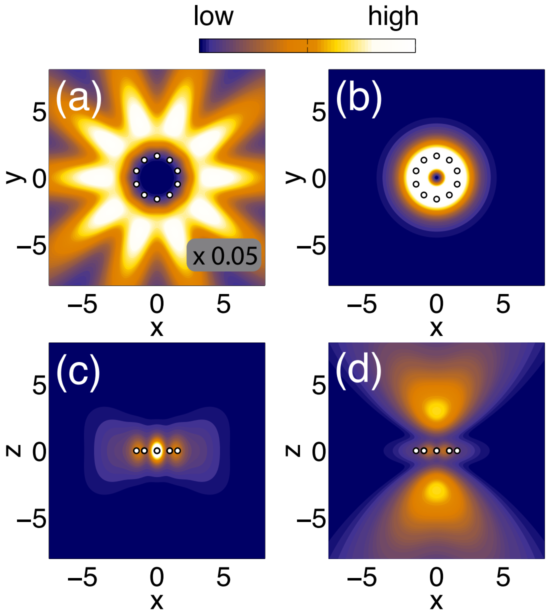

Figure 7.3: *Ring radiation patterns.* The field intensity generated by a single ring with a single excitation and tangential polarization, in the most subradiant mode with $m = \lfloor N/2 \rfloor$ [(a), (c)] and in the radiant mode with $m = 0$ [(b), (d)]. The top panels [(a), (b)] show the field in the xy-plane at fixed $z = 1.5R$. The bottom panels [(c), (d)] show the field in the xz-plane at fixed $y = 1.5R$. The white circles denote the position of the emitters. The field pattern is remarkably different in the two cases: for the subradiant mode it is evanescent transversally to the ring, and it vanishes at the center of the ring. ($N = 10$, $d/\lambda = 0.4$).

addition to the difference in the magnitude of the fields, we find a remarkably distinct radiation pattern. In the case of a subradiant mode, the field is evanescent transversally to the plane that contains the ring, and moreover, it vanishes at the center of the ring. The radiant state, on the other hand, causes strong emission in the transverse direction, and shows an interference maximum at the center of the ring.

7.4 Tailored collective coupling of two rings

As previously discussed in Ref. [7.4] and presented in more detail above, single rings have very intriguing radiative properties. We will, however, now continue with the study of two coupled rings which lie in the same plane and are separated by a distance x [see Fig. 7.1(b),(c)]. In particular, we study how excitations are transferred from one ring to another with minimal loss. While superradiant states possess the strongest dipole moments and thus couple strongly to neighboring dipoles, they also feature a much faster decay. The effective Hamiltonian, Eq. (7.7), can be rewritten as the sum of

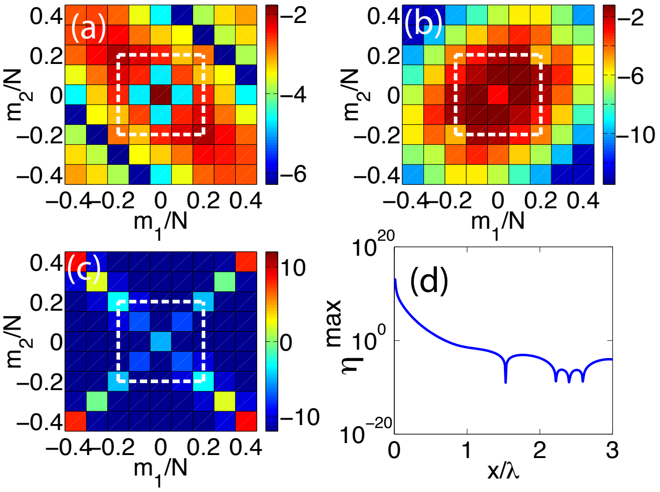

Figure 7.4: *Ring-to-ring coupling.* (a) Absolute values of the dispersive J_{m_1,m_2}, (b) dissipative Γ_{m_1,m_2} couplings and (c) the ratio η_{m_1,m_2} on a logarithmic scale. We consider two rings in spin-wave states with well-defined angular momenta m_1 and m_2. The rings are contained in the same plane and separated by the distance $x = 0.15\lambda$, in the configuration shown in Fig. 7.1(b). The dashed white line denotes the light line, beyond which the modes are mainly subradiant. Subradiant states primarily couple dispersively to subradiant states. Moreover, η is maximal for subradiant states with an opposite value of angular momentum. (d) The maximum value of η_{m_1,m_2} obtained with $m_1 = m_2 = N/2$, as a function of the ring separation x. ($N = 10$, $d/\lambda = 0.1$).

intra-ring and ring-ring coupling terms,

$$H_{\text{eff}} = \sum_{i,j\in\mathcal{R}_1} \hat{h}_{i,j} + \sum_{i,j\in\mathcal{R}_2} \hat{h}_{i,j} + \sum_{\substack{i\in\mathcal{R}_1,\\ j\in\mathcal{R}_2}} \hat{h}_{i,j}, \tag{7.10}$$

with $\hat{h}_{i,j} = h_{i,j}\sigma_i^{eg}\sigma_j^{ge}$ and $h_{i,j} \equiv -(3\pi\Gamma_0/k_0)G_{ij}$. As a shorthand notation, we defined two sets of indices, one for the sites in the first ring, $\mathcal{R}_1 = \{1, 2, ..., N\}$, and one for the sites in the second ring, $\mathcal{R}_2 = \{N+1, ..., 2N\}$, respectively. The last term describes the coupling between the two rings, and it can be written in the angular momentum basis,

$$\sum_{\substack{i\in\mathcal{R}_1,\\ j\in\mathcal{R}_2}} \hat{h}_{i,j} = \sum_{m_1,m_2} \left(J_{m_1,m_2} - i\frac{\Gamma_{m_1,m_2}}{2} \right) \sigma_{m_1,1}^{eg}\sigma_{m_2,2}^{ge},$$

where $J_{m_1,m_2} = \text{Re}\{\lambda_{m_1,m_2}\}$ is the dispersive and $\Gamma_{m_1,m_2} = -2\text{Im}\{\lambda_{m_1,m_2}\}$ the dissipative coupling, and

$$\lambda_{m_1,m_2} = \frac{1}{N} \sum_{\substack{i\in\mathcal{R}_1,\\ j\in\mathcal{R}_2}} h_{i,j} e^{i(m_1\theta_i - m_2\theta_j)}. \tag{7.11}$$

In Fig. 7.4(a),(b), we show the dispersive and dissipative couplings as a function of the angular momentum of the two rings m_1 and m_2. We use the configuration shown in Fig. 7.1(b) with a fixed separation between the two rings $x = \lambda/2$ and tangential polarization. The white dashed line in Fig. 7.4(a)-(c) represents the light line beyond which the states are predominantly subradiant. We observe that subradiant states mainly couple dispersively to other subradiant states, whereas radiant states couple to other radiant states with large dissipation. Furthermore in Fig. 7.4(c) we show the ratio $\eta_{m_1,m_2} \equiv J^2_{m_1,m_2}/[4\Delta^2_{m_1,m_2} + \max\{\Gamma^2_{m_1}, \Gamma^2_{m_2}\}]$, with $\Delta_{m_1,m_2} = |J_{m_1} - J_{m_2}|$. This is a figure of merit that quantifies how efficiently two modes in the two rings are coupled, and thus, how efficiently an excitation can be transferred between them. Remarkably, we find that in the subradiant sector, η is non-negligible for states where $m_1 = \pm m_2$ only. Moreover, it is several orders of magnitude larger for $m_1 = -m_2$, that is, for two guided modes that propagate in opposite directions in the two rings. This result indicates that in the subradiant regime the physics is well captured by a two-mode model consisting of the two states with m and $-m$.

We also note that the efficiency in the coupling strongly depends on the particular configuration of the dipoles. As the separation between the rings increases, the maximum value of η displays oscillations with an overall decay. This is shown in Fig. 7.4(d), where we have evaluated $\eta^{\max} = \eta_{m_1=N/2,m_2=N/2}$ for $N = 10$ as a function of the rings' separation x. Interestingly, a different configuration such as the site-edge arrangement illustrated in Fig. 7.1(c) can yield a dramatically different result. In this case, it is easy to see that due to symmetry, the fields created by the two rings in the $m = N/2$ mode completely destructively interfere yielding a coupling which is exactly zero.

7.5 Efficient excitation transfer between two rings

According to the previous results for the couplings, we might expect that if one of the rings is initially prepared in a very subradiant state, the excitation oscillates between the two rings for a very long time before it finally decays.

Up to now we have considered eigenstates of the system which are fully delocalized in space. This gives more insight into the native behavior of the system than investigating single excited sites. However, excitations in reality will often be partially (de-)localized only. This leads to the natural question whether it is still possible to achieve an efficient excitation transport between the two rings for a multi-mode wave packet. In the following, we investigate the dynamics of a wave function initially prepared in the form

$$|\Psi^m_{i,k}\rangle = \frac{1}{\sqrt{n}} \sum_{j\in\mathcal{R}_i} e^{i\theta_j m} e^{-\frac{|\vec{r}_j-\vec{r}_k|^2}{2R^2\Delta\theta^2}} \sigma_j^{eg} |g\rangle . \tag{7.12}$$

This corresponds to a wave packet with a Gaussian population distribution centered at site k in the ith ring with an angular spread $\Delta\theta$ (wave packet width $R \cdot \Delta\theta$) and central momentum m. The constant n accounts for the normalization. An infinitely wide wave packet of this form represents the eigenstate given by m. On the other hand, if the wave packet is of zero spread, only the atom at the site given by the index k is excited.

For a mode guided by the first ring with momentum m, it is only natural that it will invert its direction upon being transported to the second ring. This is a more intuitive picture of the previous result that the coupling is optimal between modes with opposite m. Thus, for a finite width wave packet, we expect that it is transferred into a wave packet with the same shape but central momentum $-m$. Therefore, we evaluate the fidelity $\mathcal{F}(t)$ of creating this wave packet in the second ring as

$$\mathcal{F}(t) = \max_k \left\{ \langle \Psi_{2,k}^{-m} | \Psi(t) \rangle \right\}, \tag{7.13}$$

where we maximize over the site index k in the second ring since we do not know the (center) position of the wave packet created there at all times. The wave function $|\Psi(t)\rangle$ is given by the time evolution with H_{eff} with the initial condition $|\Psi(0)\rangle = |\Psi_{1,k}^{m}\rangle$.

In Fig. 7.5(a) we show the maximal fidelity during time evolution as a function of the ring separation as well as of the width of the initial wave packet for two rings with $N = 20$. We start out with a wave packet centered at the site that is farthest from the second ring. The momentum is chosen to be $m = \lfloor N/4 \rfloor$ such that all modes the packet is made up of have momenta of the same sign. As one can see, the fidelity is rather low as long as the width is small, *i.e.,* the excitation is localized at one site almost perfectly. However, for a comparably small width in real space already, the wave packet is sufficiently localized in momentum space to exhibit coherent transport. The fidelity grows to values larger than 90% quickly as the width increases, indicating a reliable transport of a subradiant wave packet from the first ring to the next. Moreover, the transport is best if the separation between the rings is comparable to the inter-particle distance. This is due to the change of the energetic shifts of neighboring atoms with their separation: if the atoms at the points where the rings are closest are too far (or too close) to one another, the shifts vary greatly, effectively detuning these atoms far from the rest. Excitations can then no longer propagate.

In Fig. 7.5(b) we plot the fidelity of the same wave packet being transported as a function of time. The wave packet oscillates between the two rings with the same period for both finite and infinite width. The amplitude, however, damps out considerably faster for the case of a finite width. Nevertheless, a large fidelity is achieved even when the initial state is not a perfect eigenstate of the system.

7.6 Conclusions

We started off by showing that a single ring of dipole-dipole coupled emitters exhibits peculiar radiative properties. Specifically, the lifetime of subradiant states prepared in such a ring increases exponentially with a growing number of atoms. Accordingly, the intensity emitted from a ring when a subradiant state is prepared is largely diminished compared to a superradiant state.

We then showed that if another ring is present, optimal coupling occurs between

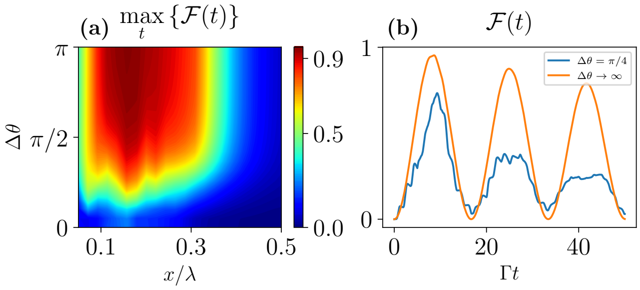

Figure 7.5: *Fidelity of wave packet transport between two rings.* **(a)** A scan of the maximal fidelity (over time) as a function of the ring separation and the wave packet width for two rings consisting of $N = 20$ atoms. For a sufficiently large width and a separation comparable to the inter-particle distance $d = 0.1\lambda$, the fidelity is almost unity. **(b)** The larger the width in real space, the more the wave packet is localized in momentum space thus showing better transport behavior. The separation between the rings was $x = 0.15\lambda$. For both (a) and (b) the dipoles were oriented tangentially.

subradiant states of each ring. An excitation that is sufficiently delocalized and moving with a velocity along one ring that closely corresponds to the momentum of an eigenstate that is subradiant can be transported to another ring with a large fidelity. This reliable coherent transport takes place for a comparably small delocalization already and culminates in damped Rabi-like oscillations between the rings once the excitation is spread over the entire first ring.

Note that beyond the two-level approximation analogous bright and dark states also appear in more complex level structures with several decay channels [7.23]. Hence much of the physics discussed here should also hold in rings of particles with a more complex internal structure.

Acknowledgements

We acknowledge financial support by the Austrian Science Fund (FWF) through projects P29318-N27 (H. R. and L. O.) and the DK-ALM W1259-N27 (D. P.) as well as from ERC Starting Grant FOQAL, MINECO Plan Nacional Grant CANS, MINECO Severo Ochoa Grant No. SEV 2015-0522, CERCA Programme/Generalitat de Catalunya, AGAUR Grant 2017 SGR 1334, and Fundacio Privada Cellex (D.C.). We thank N. van Hulst and C. Genes for helpful discussions and comments. Part of the numerical simulations were performed with the open-source framework QuantumOptics.jl [7.24]. After completion we became aware of related work on coupling between two planar arrays using collective dark states [7.25].

8 Publication

Computer Physics Communications **227**, 109 (2018)

QuantumOptics.jl: A Julia framework for simulating open quantum systems[†]

S. Krämer[1], D. Plankensteiner[1], L. Ostermann[1] and H. Ritsch[1]

[1]*Institut für Theoretische Physik, Universität Innsbruck,*
Technikerstraße 21, A-6020 Innsbruck, Austria

We present an open source computational framework geared towards the efficient numerical investigation of open quantum systems written in the Julia programming language. Built exclusively in Julia and based on standard quantum optics notation, the toolbox offers speed comparable to low-level statically typed languages, without compromising on the accessibility and code readability found in dynamic languages. After introducing the framework, we highlight its features and showcase implementations of generic quantum models. Finally, we compare its usability and performance to two well-established and widely used numerical quantum libraries.

doi: 10.1016/j.cpc.2018.02.004

[†] This publication presents the QuantumOptics.jl framework which was developed by S. Krämer. The author of this thesis contributed to this work mainly by writing some of the brief examples shown in the publication, as well as contributing to the code behind the benchmarks. L. Ostermann provided helpful discussions and composed Fig. 1. Additionally, he designed and still maintains the website for the project. After completion of the publication, the author of this thesis took over the responsibility for development and maintenance of the QuantumOptics.jl framework.

8.1 Introduction

Numerical simulations of open quantum systems are essential to research fields like quantum optics or quantum information as the number of analytically solvable systems is quite limited. Due to the usefulness of such numerical calculations to study systems and phenomena otherwise only accessible through elaborate experimental tests, it is of interest to make said numerical calculations as approachable as possible to a wide audience without compromising too much on their efficiency. In this form they can also be a useful tool in teaching. An early, greatly successful attempt in this direction has been the Quantum Optics (QO) Toolbox in Matlab [8.1], which dates back almost two decades. Other approaches [8.2, 8.3] have mostly focused on efficiency, thus sacrificing accessibility by employing lower level languages like C++ and template metaprogramming. None of these, however, have managed to gain a popularity comparable to the QO Toolbox.

It was not until recent years, that a toolbox similar to the one in Matlab called QuTiP (Quantum Toolbox in Python) has been developed [8.4, 8.5], which in some sense superseded the QO Toolbox. QuTiP's wide adaptation can be traced back to a couple of advantageous properties: QuTiP as well as its underlying language, Python, are both open source, a fact that is greatly appreciated in the scientific community. When compared to the QO Toolbox, which runs on the proprietary Matlab, QuTiP is equally convenient to use and switching to it requires very little effort. Additionally, due to its open development approach the project has acquired many active contributors since its debut and as a consequence it contains many features that go beyond QO Toolbox's capabilities. Another outstanding feature is QuTiP's extensive documentation and the considerable amount of available examples. One downside, however, is the fact, that any time-critical calculations need to be outsourced via Cython [8.6] or performed by external libraries written in e.g. C, C++ or Fortran. This not only applies to the framework itself, but is also a concern for any user. If some code provided by the user happens to be time-critical, he or she then has to port it to a low-level programming language.

The programming language Julia [8.7, 8.8] avoids this problem by offering a clean and convenient syntax typically associated with dynamic languages while at the same time providing speed comparable to compiled languages due to its just in time (JIT) compilation. For this reason, it has been gaining a lot of momentum in the community of scientific programming already, even though it is still under active development. While Python packages like PyPy [8.9] or Numba [8.10] will also allow for JIT compilation in the same fashion as Julia, with the later even relying on the same LLVM compiler, Python was designed to be an interpreted language and thus only a subset of functions will benefit from the JIT functionality. In contrast, Julia was created with the JIT paradigm in mind and no extra effort by the user is required.

Taking full advantage of its easy-to-read syntax and its efficiency, we built a new open source framework, *QuantumOptics.jl*, written entirely in Julia. It is specifically geared towards the efficient and easy numerical simulation of open quantum systems. In this paper, we demonstrate the capabilities of our toolbox in its current version v0.4.1. We show that it offers speed in numerical calculations, while at the same time the source code remains intuitive and easily accessible.

Our framework can be installed very straight-forwardly: after having setup Julia itself, where detailed instructions can be found on the Julia website [8.11], one can make use of Julias's package manager and simply execute the following command:

```
Pkg.add("QuantumOptics")
```

To obtain a first impression of QuantumOptics.jl consider code sample 8.2, which simulates the well-known Jaynes-Cummings model. A two-level atom with a transition frequency ω_a, modeled as a spin-1/2 particle, coherently couples to a cavity mode of frequency ω_c. Initially, the particle is in the ground state and the field mode is prepared in a coherent state $|\alpha\rangle$. The time evolution of the system is governed by the Schrödinger equation

$$i\frac{\partial\psi}{\partial t} = H_\mathrm{JC}\psi, \tag{8.1}$$

where the Hamiltonian, given in a suitable reference frame reads ($\hbar = 1$)

$$H_\mathrm{JC} = \Delta a^\dagger a + g\left(a^\dagger\sigma^- + a\sigma^+\right). \tag{8.2}$$

Here, $\Delta = \omega_\mathrm{c} - \omega_\mathrm{a}$ and g is the coupling strength between the atom and the cavity. Furthermore, a ($a^\dagger$) is the photon annihilation (creation) operator of the cavity and σ^- (σ^+) denotes the atomic dipole's lowering (raising) operator. As one can see from code sample 8.2, the framework predefines all the necessary operators, which enables one to implement the above model in a few simple lines of code.

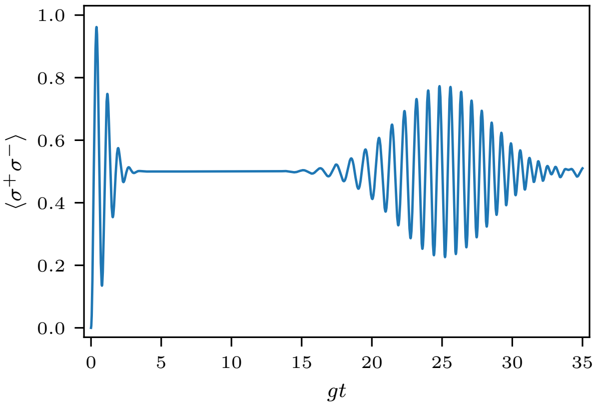

Figure 8.1: *Jaynes-Cummings model: atomic population dynamics.* The plot was created with the results from code sample 8.2.

```
using QuantumOptics

# Define required parameters
```

```julia
g = 1.0
Δ = -0.1
α = 4.0

# Define bases for cavity (Fock) and atom (Spin-1/2)
bc = FockBasis(40)
ba = SpinBasis(1//2)

# Construct operators
a = destroy(bc) ⊗ one(ba)
σ⁻ = one(bc) ⊗ sigmam(ba)

# Construct Hamiltonian
H = Δ*dagger(a)*a + g*(dagger(a)*σ⁻ + a*dagger(σ⁻))

# Define initial state
ψ₀ = coherentstate(bc, α) ⊗ spindown(ba)

# Define list of time steps
T = [0:0.01:35;]

# Evolve in time according to Schrödinger's equation
tout, ψₜ = timeevolution.schroedinger(T, ψ₀, H)

# Calculate atomic excitation
excitation = expect(dagger(σ⁻)*σ⁻, ψₜ)
```

Code sample 8.2: *Jaynes-Cummings model.*

The resulting atomic dynamics is depicted in Fig. 8.1, where we show the energy stored in the atom as function of time. We clearly see the well-known collapse and revival of coherent oscillations of the energy between atom and the cavity [8.12]. This is a well studied and numerically nontrivial phenomenon for which no simple analytic solution exists.

8.2 Framework design

QuantumOptics.jl's design, and especially its interface, closely resembles QuTiP's successful architecture and shows a lot of similarities to the QO Toolbox, yet features a few fundamental differences. First and foremost, QuantumOptics.jl distinguishes itself in the way it treats quantum objects, such as states, operators and super-operators. In QuTiP, quantum objects are more or less equal to their numerical coefficients with regards to a chosen basis. This is a practical and reasonable approach, as, in the end, the aim is to perform numerical calculations with these objects. However, in order to faithfully represent an abstract state in a Hilbert space, one has to keep track of the choice of basis that was made as well. Thus, in QuantumOptics.jl we explicitly track the basis for every quantum object (see Fig. 8.2a). From the relation

$$|\Psi\rangle = \sum_i \langle u_i|\Psi\rangle\, |u_i\rangle = \sum_i \Psi_i\, |u_i\rangle \tag{8.3}$$

it is evident that a state is defined completely by specifying the coefficients Ψ_i and a basis $\{|u_i\rangle\}$. For operators, however, it makes sense to allow for more than one basis, since an operator is, in general, a mapping from one Hilbert space into another. Therefore, it is associated with two bases – one for the domain and another one for the co-domain. The following equation formalizes this idea as

$$A = \sum_{ij} \langle u_i|\, A\, |v_j\rangle\, |u_i\rangle\, \langle v_j| = \sum_{ij} A_{ij}\, |u_i\rangle\, \langle v_j|\,, \tag{8.4}$$

where we call $\{|u_i\rangle\}$ the left basis and $\{|v_j\rangle\}$ the right basis. The generalization to superoperators is straightforward and culminates in storing four different bases.

Introducing this notion of bases has several advantages. On one hand, it adds an additional layer of safety, as for any operation (e.g. for a multiplication) we check whether or not the bases of the two objects involved are compatible. Without this information about the basis the only thing that can be checked is if the Hilbert space dimensions match. On the other hand, the use of bases arguably improves the code's readability. This is of course a subjective assessment but using a basis as a parameter when creating operators, instead of specifying the Hilbert space's dimension only, leads to more understandable code. Additionally, the possibility of dispatching a function like e.g. `momentum()` on a `PositionBasis` as well as on a `MomentumBasis` and obtaining the correct result in both cases, allows for very elegant coding.

Besides the conceptional differences in the understanding of quantum objects, a more tangible distinction to QuTiP and the QO Toolbox is QuantumOptics.jl's choice of the internal representation of their numerical data. While QuTiP and the QO Toolbox both use sparse matrices as their underlying data structure, QuantumOptics.jl takes a more general approach. It defines an abstract operator interface which is implemented by specialized operator types. At this point, primarily dense and sparse matrices are used but there are additional possibilities, as depicted in Fig. 8.2b. The existence of different data types for operators is mostly transparent to the user as suitable choices are made automatically. Nevertheless, it is always possible to specify the desired operator type explicitly. Admittedly, the increased complexity that comes from this approach can be an additional burden on the user. However, in our opinion, this disadvantage is far outweighed by the improved versatility (see for example Sec. 8.4.3) and a huge boost in speed in many cases. A more detailed discussion of this claim is provided in Sec. 8.5.

8.3 Development philosophy

To ensure the quality as well as the usability of our code we adhere to a certain set of self imposed rules:

Open source - Access to the underlying code is a fundamental necessity in any scientific

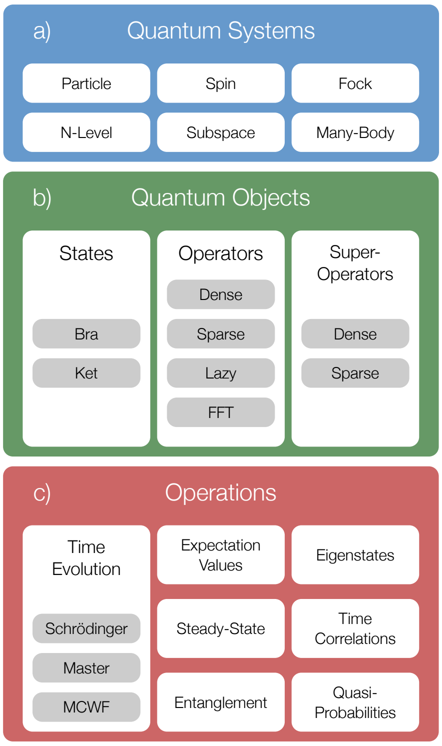

Figure 8.2: *Illustration of the framework's design.* a) Quantum systems provide functions that allow for an effortless construction of typical quantum objects. b) Quantum objects, i.e. states, operators and superoperators, constitute the fundamental building blocks of QuantumOptics.jl. They are defined as abstract interfaces which are then realized by several specialized types. This makes it possible to choose an implementation that is most favorable for the investigated problem. c) Finally, these quantum objects can be used as an input for various time evolutions as well as other operations.

endeavor. This is why our code is open source. Additionally, it can be modified since it is published under the MIT license.

Open development model - Framework development takes place transparently using the convenient GitHub platform [8.13]. Anybody who is interested and motivated can join discussions effortlessly and submit patches. Every single patch is reviewed by at least one person besides its author to ensure high code quality.

Extensive testing - Rigorous testing is a core requirement for our code. It enables us to perform restructuring and redesigning while being confident that our code will remain functional. Every function that is part of the public interface is unit-tested. The test suite is run against every single change before it is incorporated into the framework ensuring that even the newest features can be used reliably. Additional high-level tests compare the numerical results against known analytical solutions.

Documentation - From a user's point of view undocumented code is equal to nonexisting code. Thus, every function of the public interface is documented directly in the code via docstrings, which can be accessed easily from the command line. High-level documentation [8.14] can be found on our website [8.15], which not only references these docstrings but also provides various examples that cover a wide variety of quantum mechanical systems and can be used as a convenient starting point for more specialized investigations. Every single code snippet in the documentation is executed during the build process to guarantee that it is functional and always up to date.

Benchmarking - An extensive benchmark suite allows us to detect and therefore avoid any speed regressions [8.16]. It also includes benchmarks for other quantum simulation frameworks, at the moment for QuTiP and the QO Toolbox, which can be used to identify areas that should be optimized in our own code. A few selected examples are presented in Sec. 8.5.

8.4 Examples

In this section we demonstrate the versatility of our framework by simulating a few well-known quantum systems using models and techniques of increasing complexity. As is already discernible from code sample 8.2, each script roughly follows a simple scheme:

1. Define the required physical parameters (frequencies, decay rates, etc.) as numerical constants.
2. Specify the bases of the respective Hilbert spaces (Fig. 8.2a).
3. Construct the corresponding operators, the Hamiltonian, jump operators and states (Fig. 8.2b).
4. Use operations such as a time evolution, expectation values, etc. to obtain physical results (Fig. 8.2c).

8.4.1 Lossy Jaynes-Cummings model

First, let us extend the example of the Jaynes-Cummings model from code sample 8.2 to an open system. When the cavity mode is coupled to a thermal bath with a mean photon number n_{th}, photons can leak out of the cavity at a rate $(n_{\mathrm{th}}+1)\kappa$ and enter the cavity at a rate $n_{\mathrm{th}}\kappa$. Similarly, the atom can lose energy via spontaneous emission at a rate γ as it interacts with the electromagnetic vacuum field. These dynamics are modeled by a master equation for the system density operator ρ [8.17],

$$\dot{\rho} = i\left[\rho, H_{\mathrm{JC}}\right] + \mathcal{L}\rho. \tag{8.5}$$

Here, $\mathcal{L}$ is the Liouvillian which includes the various dissipation channels,

$$\mathcal{L}\rho = \left(n_{\mathrm{th}}+1\right)\kappa\mathcal{D}[a]\rho + n_{\mathrm{th}}\kappa\mathcal{D}\left[a^{\dagger}\right]\rho + \gamma\mathcal{D}\left[\sigma^{-}\right]\rho, \tag{8.6}$$

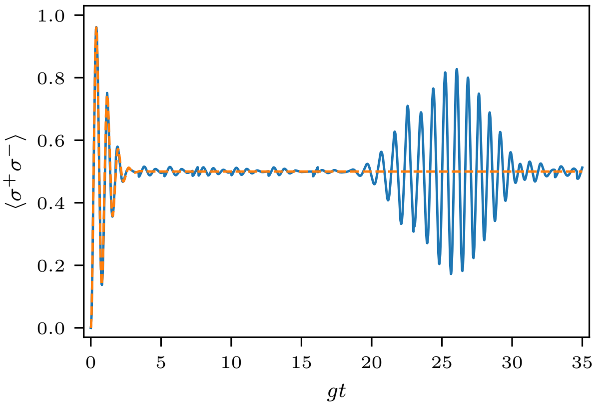

Figure 8.3: *Jaynes-Cummings model with damping: comparison of full master equation dynamics (orange, dashed) and a single noisy MCWF trajectory (blue, solid).* The plot was created with the results from code sample 8.3 and code sample 8.4.

where

$$\mathcal{D}[A]\rho = A\rho A^\dagger - \frac{1}{2}\left(A^\dagger A\rho + \rho A^\dagger A\right). \tag{8.7}$$

The framework is built in such a way that one can easily extend the code from the unitary evolution in code sample 8.2 to dissipative dynamics. This is shown in code sample 8.3, where instead of a Schrödinger equation for a pure quantum state we solve the master equation, which inherently requires the use of a density matrix to represent the resulting mixed state.

```
# Decay rates
κ = 0.01
γ = 0.01
n_th = 0.75
R = [(n_th + 1)*κ, n_th*κ, γ]

# Jump operators
J = [a, dagger(a), σ⁻]

# Time evolution according to master equation
tout, ρₜ = timeevolution.master(T, ψ₀, H, J; rates=R)

# Caclulate atomic excitation
excitation = expect(dagger(σ⁻)*σ⁻, ρₜ)
```

Code sample 8.3: *Jaynes-Cummings model including decay (requires code sample 8.2).*

As one can see in Fig. 8.3, even though we chose small damping rates, $\kappa, \gamma \ll g$, they already suppress the revival of the atomic excitation.

As an alternative to the master equation one can resort to a stochastic time evolution via the Monte Carlo wave-function (MCWF) method [8.18]. Since for a single trajectory the state of the system is defined completely by a ket $|\psi\rangle$ rather than a density operator ρ it is easier to simulate. However, this gain comes at the expense of requiring time consuming stochastic averaging. Essentially, the MCWF method evolves the state according to a Schrödinger equation with a non-Hermitian Hamiltonian

$$H_{\mathrm{JC}}^{(\mathrm{nh})} = H_{\mathrm{JC}} - \frac{i}{2}\sum_i r_i J_i^\dagger J_i, \tag{8.8}$$

with randomly occurring quantum jumps connected to the jump operators $J_i \in \{a, a^\dagger, \sigma^-\}$ and the corresponding rates $r_i \in \{(n_{\mathrm{th}}+1)\kappa, n_{\mathrm{th}}\kappa, \gamma\}$.

Once again, it is straightforward to implement this time evolution with our framework. To this end, let us extend the Jaynes-Cummings model from code sample 8.2 and code sample 8.3 further. In code sample 8.4 we show how to calculate a single MCWF trajectory.

```
# Calculate single MCWF trajectory
tout, ψₜ = timeevolution.mcwf(T, ψ₀, H, J; rates=R, seed=2)

excitation = expect(dagger(σ⁻)*σ⁻, ψₜ)
```

Code sample 8.4: *Monte Carlo wave-function method for the lossy Jaynes-Cummings model (requires code sample 8.2 and code sample 8.3).*

In contrast to the average over infinitely many trajectories (result from the master equation approach), single MCWF trajectories still exhibit a revival in the atomic excitation (see Fig. 8.3) but with different phase and timing.

8.4.2 Time-dependent Jaynes-Cummings model

Very often the Hamiltonian of a problem contains an explicit time-dependent term, modeling e.g. a controlled change of operating parameters or a pulsed excitation. Let us thus demonstrate how to solve such a time-dependent problem in our framework. Consider the Hamiltonian of the Jaynes-Cummings model. In Eq. (8.2) it is written in a frame rotating at the atomic frequency ω_{a}, resulting in the term $\Delta a^\dagger a$. To eliminate this term as well we change into a frame rotating at the detuning Δ. The Hamiltonian then becomes time-dependent,

$$\tilde{H}_{\mathrm{JC}} = g\left(a^\dagger\sigma^- e^{i\Delta t} + a\sigma^+ e^{-i\Delta t}\right). \tag{8.9}$$

In order to solve the time evolution with a time-dependent Hamiltonian, we need to write a small function that updates the Hamiltonian at every time step and returns the result. In addition, let us also include the decay processes as used in the master equation (see code sample 8.3). The code required to solve this problem is shown in code sample 8.5 and we obtain the same results as in code sample 8.3.

```
# Separate time-dependent terms of H
H₁ = g*dagger(a)*σ⁻
```

```
H₂ = dagger(H₁)

# Calculate the Hermitian conjugate for the jump operators
Jdagger = dagger.(J)

function Hₜ(t, ρ) # time-dependent Hamiltonian
  H = exp(1im*Δ*t)*H₁ + exp(-1im*Δ*t)*H₂
  return H, J, Jdagger
end

tout, ρₜ = timeevolution.master_dynamic(T, ψ₀, Hₜ; rates=R)
excitation = expect(dagger(σ⁻)*σ⁻, ρₜ)
```

Code sample 8.5: *Time evolution of the Jaynes-Cummings model with a time-dependent Hamiltonian (requires code sample 8.2 and code sample 8.3).*

8.4.3 Gross-Pitaevskii equation

In addition to the implementation of time-dependent Hamiltonians, the framework also allows for state-dependent effective Hamiltonians. This enables one to, for example, quite easily simulate the Gross-Pitaevskii equation [8.19]. For a one-dimensional Bose-Einstein condensate (BEC) in free space described by $\psi(x,t)$, the equation reads

$$i\dot{\psi}(x,t) = H_{\text{GPE}}\psi(x,t), \tag{8.10}$$

where the Hamiltonian is

$$H_{\text{GPE}} = \frac{p^2}{2m} + g|\psi(x,t)|^2. \tag{8.11}$$

Here, x and p are the position and momentum operators, respectively, and m is the mass. The parameter g governs whether the interaction is attractive ($g < 0$) or repulsive ($g > 0$). The equation has the form of a Schrödinger equation, but with the state-dependent term $g|\psi|^2$ in the Hamiltonian. The implementation of this equation is shown in code sample 8.6. In our example, the condensate is in a superposition of two counter-propagating wave-packets initially. These collide after some time as depicted in Fig. 8.4, where the probability density of the BEC $|\psi(x,t)|^2$ is plotted as a function of space and time.

```
using QuantumOptics

x_min = -10
x_max = 10
x_steps = 300
dx = (x_max - x_min)/x_steps
m = 1
x₀ = 2π
g = -3.33
```

```
b_x = PositionBasis(x_min, x_max, x_steps)
b_p = MomentumBasis(b_x)

Tpx = transform(b_p, b_x)
Txp = transform(b_x, b_p)

p = momentum(b_p)
Hkin = LazyProduct(Txp, p^2/2m, Tpx)
Hψ = diagonaloperator(b_x, Ket(b_x).data) # ∝ |ψ|^2
H₀ = LazySum(Hkin, Hψ)

function H(t, ψ) # Update state-dependent term in H
  Hψ.data.nzval .= g/dx*abs2.(ψ.data)
  return H₀
end

p₀ = 2
σ = 1.5
ψ₁ = gaussianstate(b_x, -x₀, p₀, σ)
ψ₂ = gaussianstate(b_x, x₀, -p₀, σ)
ψ₀ = normalize(ψ₁ + ψ₂)
T = [0:0.01:6;]
tout, ψₜ = timeevolution.schroedinger_dynamic(T, ψ₀, H)

density = [abs2(ψ.data[j]) for ψ=ψₜ, j=1:x_steps]
```

Code sample 8.6: *Gross-Pitaevskii equation.*

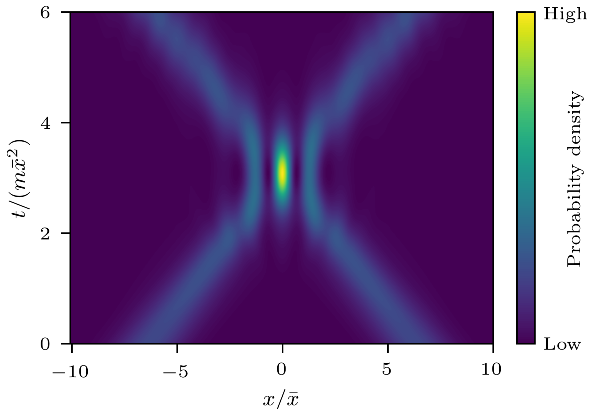

Figure 8.4: *Nonlinear Schroedinger equation: collision of two soliton like wave-packets.* The plot was created with the results from code sample 8.6 and $\bar{x}$ is a characteristic length scale.

Besides the state-dependent Hamiltonian this example showcases a few additional features which are unique to QuantumOptics.jl. For performance reasons it is advantageous to continuously switch between position and momentum space since some operators are sparse in one but not in the other basis. The transformation operators `Txp` and `Tpx` are of a special type, which adheres to the general operator interface, and implicitly performs fast Fourier transformations (FFTs) when multiplied with a state. Since these FFT operators cannot be combined with sparse or dense operators in a meaningful way without losing their advantage, QuantumOptics.jl provides the concept of lazy operators which can be used to delay evaluation until the operator has been applied to a state. For example, instead of adding two operators first and multiplying them with a state afterwards, lazy operators make it possible to first separately multiply the two operators with the state and then sum up the two results.

8.4.4 Semi-classical model of cavity cooling

When a physical system has too many degrees of freedom for an efficient full quantum solution, it is often convenient to approximate a part of the dynamics classically, while other quantum degrees of freedom are kept. Our framework easily allows for implementations of simulating such *semi-classical* dynamics.

Let us demonstrate this at the example of a two-level atom moving in the field of a coherently driven cavity mode along the cavity axis. The cavity has a mode function $\cos(kx)$, where k is the cavity mode wave number and x represents the position of the atom. The full quantum system can be described by the Hamiltonian [8.20]

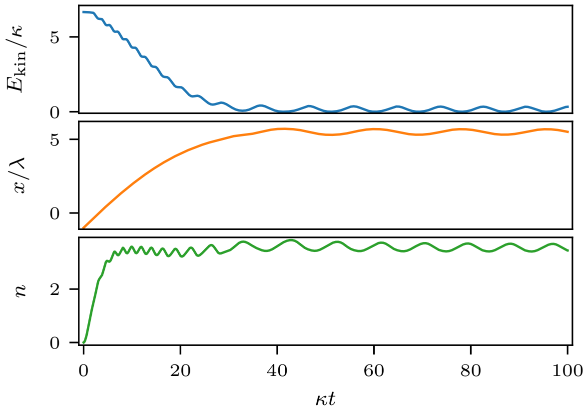

Figure 8.5: *Cavity cooling of a two-level atom.* The plot was created from the results in code sample 8.7. One can see the cooling process in terms of the decrease of the kinetic energy $E_{\mathrm{kin}} = p^2/2m$ and the localization in x (where $\lambda = 2\pi/k$ is the cavity wavelength). Additionally, the cavity photon number n saturates.

$$H_{\mathrm{cooling}} = -\Delta_{\mathrm{c}} a^\dagger a - \Delta_{\mathrm{a}} \sigma^+ \sigma^- + \eta \left(a^\dagger + a\right) + g\cos(kx)\left(a^\dagger \sigma^- + a\sigma^+\right) + \frac{p^2}{2m}. \quad (8.12)$$

Here, $\Delta_i = \omega_{\mathrm{p}} - \omega_i$ is the detuning from the pump laser with frequency ω_{p} and amplitude η. The coupling strength between the atom and the cavity is g and p is the momentum of the atom. The atom is subject to spontaneous emission with a rate γ and the cavity is damped with a rate κ, which we include by the Liouvillian

$$\mathcal{L}[\rho] = \kappa\mathcal{D}[a]\rho + \gamma\mathcal{D}\left[\sigma^{-}\right]\rho. \tag{8.13}$$

Describing the field, atomic motion and internal atomic dynamics quantum mechanically creates a very large Hilbert space for realistic photon numbers and velocities. However, if the atom has a kinetic energy that is far above the recoil limit, it is well justified to approximate the atomic motion by classical Newtonian mechanics and variables, i.e. x and p are merely numbers instead of operators. This is the case for cavity cooling. The force exerted on the atom is then

$$\dot{p} = -\partial_x \langle H_{\text{cooling}}\rangle = 2gk\sin(kx)\mathrm{Re}\left\{\langle a^{\dagger}\sigma^{-}\rangle\right\}, \tag{8.14}$$

and the velocity is given by $\dot{x} = p/m$. Tuning the cavity to a frequency lower than the atomic transition frequency, the atom loses kinetic energy upon absorbing a photon from the cavity. It therefore experiences friction and its motion is cooled.

The above model can be simulated in a straightforward fashion using the implemented semi-classical functions, as demonstrated in code sample 8.7. The resulting cooling process is depicted in Fig. 8.5.

```julia
using QuantumOptics

κ = 1.0
η = 1.0
g = 0.5
γ = 2.0
Δc = 0.0
Δa = -1.0
m = 3.33

bc = FockBasis(16)
ba = SpinBasis(1//2)
a = destroy(bc) ⊗ one(ba)
σ⁻ = one(bc) ⊗ sigmam(ba)

Hc = -Δc*dagger(a)*a + η*(a + dagger(a))
Hat = -Δa*dagger(σ⁻)*σ⁻
H₀ = Hc + Hat # Position-independent part
Hₓ = g*(a*dagger(σ⁻) + dagger(a)*σ⁻) # ∝ cos(x)

rates = [κ, γ]
J = [a, σ⁻]
Jdagger = dagger.(J)

function f_q(t, ψ, u) # Quantum part
  x = real(u[1])
  return H₀ + Hₓ*cos(x), J, Jdagger, rates
end
```

```
atsm = dagger(a)*σ⁻ # Compute a priori for efficiency
function f_cl(t, ψ, u, du) # Classical part
  x, p = real(u)
  du[1] = p/m
  du[2] = 2g*sin(x)*real(expect(atsm, ψ))
end

x₀ = -2π
p₀ = 2m
u₀ = Complex128[x₀, p₀]
ψ₀ = fockstate(bc, 0) ⊗ spindown(ba)
ψsc = semiclassical.State(ψ₀, u₀)

T = [0:0.1:100;]
tout, ρₜ = semiclassical.master_dynamic(T, ψsc, f_q, f_cl)

x = [r.classical[1] for r=ρₜ]
p = [r.classical[2] for r=ρₜ]
n = expect(dagger(a)*a, ρₜ)
```

Code sample 8.7: *Semi-classical model of cavity cooling.*

8.5 Performance

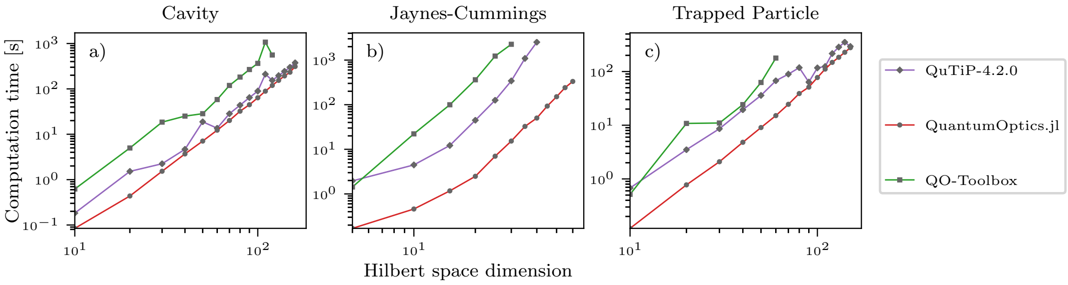

Figure 8.6: *Benchmarks measuring the time elapsed when performing a time-evolution according to a master equation.* Three different systems exhibiting different sparseness properties are investigated: a) a pumped cavity with photon decay (sparse Hamiltonian and dense density operator), b) the Jaynes-Cummings model including particle as well as cavity decay (sparse Hamiltonian and sparse density operator), c) a particle trapped in a harmonic potential (dense Hamiltonian and dense density operator). Depending on the sparseness of the system, QuantumOptics.jl's flexible operator types can lead to considerable speed-ups compared to the purely sparse matrix approach in QuTiP and the QO Toolbox.

Besides the correctness of the numerical results, providing an adequate performance is one of our main goals. An extensive benchmark-suite [8.16] allows us to detect and therefore avoid speed regressions from one version to the next. Additionally, since these

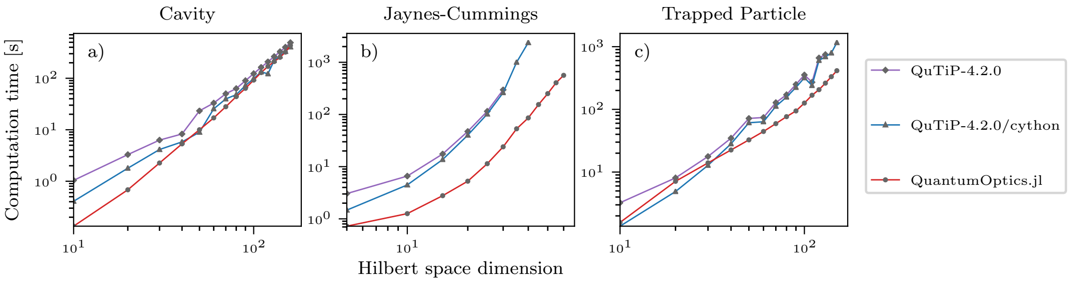

Figure 8.7: *Benchmarks measuring the time elapsed when performing a time-evolution according to a master equation with time-dependent Hamiltonians.* The same systems as in Fig. 8.6 are depicted in the same order. QuTiP provides two different implementations - a Cython and a pure Python based approach. Both, the compilation time of Julia and the Cython approach are not included in the above time measurements. Note, though, that in general the GCC compiler used by Cython gives it a certain advantage over Julia (see Sec. 8.6)

benchmarks contain respective tests for QuTiP and the QO Toolbox as well, it helps us to identify areas in our code that should be optimized further.

In principle, there are two intrinsic aspects that should give us an advantage in terms of speed. The first one is the fact that the internal layout of operators can be chosen according to the investigated problem. This means that one can choose to work with dense or sparse matrices or even more specialized operators. Note, that at the moment the time-evolution methods in our framework require density operators to be represented as dense operators. There is no fundamental reason for this limitation and a future implementation of time evolutions with sparse density operators is part of our roadmap. The positive effect of having a choice between dense and sparse operators can be seen best in the benchmarks in Fig. 8.6 which compare the different frameworks by performing a time-evolution according to a master equation for three different physical examples. Here, the cavity example exhibits a sparse Hamiltonian and a dense density operator, the Jaynes-Cummings model features a sparse Hamiltonian and a relatively sparse density operator, while the particle example demonstrates a completely dense Hamiltonian as well as a dense density operator. The more sparseness the whole system entails the closer the benchmark results are to each other. Contrastingly, for the low sparsity case huge speed improvements are observable.

The second aspect is Julia's natural speed advantage in comparison to Python and Matlab. While code written in Julia can achieve the speed of C or Fortran, in interpreted languages the philosophy is to rewrite speed-critical parts in a fast compiled language. However, this comes at the cost of flexibility, which manifests itself, e.g. when simulating time- or especially state-dependent problems. The simplest way for the user would be to define an arbitrary function directly within Python or Matlab. However, this function is most likely critical for performance, which means it should be compiled. QuTiP uses Cython [8.6] to achieve this and, as can be seen in the time-dependent benchmarks in Fig. 8.7, quite successfully so. This again comes at the cost of accessibility, though.

While in this publication we focus on the speed of performing various time-evolutions, our benchmarks cover a greater variety of calculations. This is especially important when investigating more involved examples, e.g. when treating a system semi-classically as in the example in Sec. 8.4.4, where in every step of the time evolution expectation values have to be calculated.

Finally, let us provide a few more details on how these benchmarks were carried out: the data shown in this paper was obtained on a single core of an Intel(R) Core(TM) i7-5960X CPU running at 3.00GHz under Linux and Julias's compile time is neglected in the results as we focus on the speed of the actual calculations. Furthermore, we tested QuTiP and QuantumOptics.jl on other hardware and different operating systems obtaining qualitatively similar results.

8.6 Disadvantages

While QuantumOptics.jl relies on Julia and embraces many of its modern features, we have to acknowledge the fact that Julia is still a very young language and not yet completely stable. The very same is true for the framework itself, which will continue to grow and future changes to the interface might very well be in its path. This, however, implies that code written for the current release of QuantumOptics.jl, namely v0.4.1, might have to be adopted to its future versions, if they include changes in the interface.

Another consequence of the framework being very young is the fact that QuantumOptics.jl is clearly not as feature-rich as other well-established frameworks such as QuTiP. We are confident, though, that over time the framework will continue to grow and eventually reach a comparable versatility.

A clear disadvantage when comparing Julia to Cython is the compilation time. We want to point out that Julia uses the noticeably slower LLVM compiler, while Cython relies on GCC making it advantageous at short running times. When going to longer times, however, this difference in compilation time becomes a negligible constant offset.

Another noteworthy issue lies with the Julia language itself. As of the writing of this manuscript, Julia has quite a large memory footprint. Hence, so does our framework in its current form. This may be an issue especially for users running many simultaneous instances of Julia (e.g. when performing calculations on a cluster or server). We hope that this issue will be addressed in the future of Julia's development.

8.7 Conclusions & Outlook

We have presented a new computational framework for the efficient numerical investigation of open quantum systems, demonstrated its capabilities and highlighted its performance.

In its current version (v0.4.1), QuantumOptics.jl is a very young framework and, as mentioned above, still under active development. We strongly encourage community contributions in the form of additions to the framework itself or even separate extensions based on QuantumOptics.jl, like our own Correlation Expansion Package [8.21], which allows for simulating larger systems by specifying which quantum correlations should be included or neglected, respectively, or the CollectiveSpins library [8.22], providing more specialized building blocks for the investigation of dipole-dipole coupled two-level systems in various approximations. Planned short term improvements include the addition of stochastic Schrödinger and master equations as well as adopting DifferentialEquations.jl [8.23] for the time evolution functions.

Acknowledgements

We acknowledge financial support by the Austrian Science Fund (FWF) through projects SFB FoQus F4006-N13 (S.K. & H.R), the DK-ALM: W1259-N27 (D.P.) and P29318-N27 (L.O.). Graphs were done with the open source plotting library Matplotlib [8.24].

9 Conclusions & Outlook

At the beginning, we provided a succinct introduction to the theoretical tools and models required to follow the research presented in the subsequent publications. We presented a number of studies on the precise dynamics of interacting quantum emitters.

First, we focused on the usefulness and properties of subradiant states in chains of quantum emitters. Employing a magnetic field gradient we were able to efficiently address subradiant states even if they are otherwise fully decoupled from the environment.

Moving forward, the collective nature of noise, which stemmed from a laser interacting with an ensemble of quantum emitters rather than from the emitters themselves, was modeled. Its effects on metrological applications were discussed followed by a proposal on how to suppress the noise by addressing parts of the ensemble with opposite detunings.

Next, we found that otherwise weak light-matter interactions could greatly profit from coupling an optical cavity mode to a subradiant state of an emitter ensemble. The subradiant lines caused a large inhibition of transmission and were therefore observable in the cavity spectrum. Furthermore, they caused a large phase shift in the transmitted field in an extremely narrow frequency range. While these central results were found already in a classical description of the problem, we proceeded by studying the quantum mechanical aspects of this system in great detail. To this end, we developed and discussed a quantum-Langevin approach for interacting quantum emitters. We showed that the quantum noise in the detection signal is inhibited around subradiant antiresonances as well. The subradiantly enhanced light-matter interactions also lead to a significant increase in the quadrature squeezing of the cavity field. These effects are accompanied by characteristic nonlinear behavior.

Interesting physics also arose in a different system, consisting of nanorings in free space. This model was to some extent inspired by the fundamental biological building blocks responsible for light harvesting in plants. A single such ring already features strongly suppressed spontaneous emission due to subradiance. We were further able to show that, due to this subradiant coupling, highly efficient transport of excitations between two nanorings can occur.

In summary, we showed that, performing clever manipulations of ensembles of quantum emitters, collective interactions can be used to extend the excitation lifetime, reduce collective laser noise, or enhance light-matter interactions. Furthermore, efficient and lossless excitation transport is made possible.

Finally, we presented the QuantumOptics.jl framework and showed how one can efficiently solve problems in quantum optics in a straightforward fashion.

These studies motivate further investigations in many directions. For one, the phenomenon of collective radiation of quantum emitters inside an optical cavity makes for an interesting lasing setup, a so-called superradiant laser. Research focusing on such a laser, which does not require a large intensity to exhibit a narrow linewidth, has been gaining a lot of momentum in recent years.

Treating the motional degree of freedom of quantum emitters that also interact via dipole-dipole interactions could be interesting. One could aim at exotic phenomena in terms of cooling as well as including motional effects in laser models.

The model of dipole-coupled nanorings can also be further developed, such that it eventually resembles the biological counterpart it was originally inspired by.

Considerable effort will go towards the further development of the QuantumOptics.jl framework. It already offers a manifold of essential routines useful in research applications. The aim here is to not only optimize those existing features, but to also add new solution methods and algorithms for the problems encountered during future research. The modular concept of the framework in combination with Julia's inherent ease of use allows us to continuously extend its versatility.

10 Publication

Physical Review Letters **122**, 153603 (2019)

Ion-based quantum sensor for optical cavity photon numbers[†]

M. Lee[1], K. Friebe[1], D. A. Fioretto[1], K. Schüppert[1], F. R. Ong[1] D. Plankensteiner[2], V. Torggler[2], H. Ritsch[2], R. Blatt[1,3] and T. E. Northup[1]

[1]*Institut für Experimentalphysik, Universität Innsbruck,*
Technikerstraße 25, A-6020 Innsbruck, Austria
[2]*Institut für Theoretische Physik, Universität Innsbruck,*
Technikerstraße 21a, A-6020 Innsbruck, Austria
[3]*Institut für Quantenoptik und Quanteninformation,*
Österreichische Akademie der Wissenschaften,
Technikerstraße 21a, 6020 Innsbruck, Austria

We dispersively couple a single trapped ion to an optical cavity to extract information about the cavity photon-number distribution in a nondestructive way. The photon-number-dependent ac Stark shift experienced by the ion is measured via Ramsey spectroscopy. We use these measurements first to obtain the ion-cavity interaction strength. Next, we reconstruct the cavity photon-number distribution for coherent states and for a state with mixed thermal-coherent statistics, finding overlaps above 99% with the calibrated states.

doi: 10.1103/PhysRevLett.122.153603

[†] Together with V. Torggler, the main contribution of the author of this thesis were frequent discussions on the theoretical aspects of the experiment presented in the paper as well as some calculations.

Cavity quantum electrodynamics (cavity QED) provides a conceptually simple and powerful platform for probing the quantized interaction between light and matter [10.1]. Early experiments opened a window into the dynamics of coherent atom–photon interactions, first through observations of collective Rabi oscillations and vacuum Rabi splittings [10.2–10.5] and later at the single-atom level [10.6–10.11]. More recently, building on measurements of the cavity field via the atomic phase [10.12, 10.13], cavity photon statistics have been analyzed in experiments with Rydberg atoms or superconducting qubits in microwave resonators [10.14–10.17], culminating in the generation and stabilization of nonclassical cavity field states [10.18–10.24]. These experiments operate in a dispersive regime, in which information about the cavity field can be extracted via the qubits with minimal disturbance to the field [10.1].

Dispersive experiments often operate in a regime in which one photon induces a significant atomic phase shift, the so-called strong pull regime [10.25]. However, interesting physical phenomena have also been explored with microwave cavities in the weak-pull regime, in which the small phase shift allows partial information about the atomic state to be acquired without collapse onto an eigenstate. Examples include the observation of quantum trajectories [10.26], the stabilization of Rabi oscillations via quantum feedback [10.27], and the entanglement of remote qubits [10.28].

In parallel, it was pointed out that the Jaynes-Cummings Hamiltonian that describes cavity QED also describes the interaction of light and ions in a harmonic trapping potential [10.29]. This interaction underpins the generation of nonclassical states of motion [10.30–10.33] and the implementation of gates between trapped ions [10.34]. In analogy to the phase shifts experienced by qubits due to the cavity field, ions experience quantized ac Stark shifts due to their coupling to the harmonic trap potential [10.35]. These shifts have been characterized using techniques similar to those introduced in Ref. [10.12]. Here, we have transferred the principle of dispersive measurement to an ion qubit coupled to a cavity. In contrast to experiments with flying Rydberg atoms, the ion is strongly confined; in contrast to both Rydberg and superconducting-qubit experiments, our cavity operates in the optical regime.

We employ a single trapped $^{40}\mathrm{Ca}^+$ ion as a quantum sensor [10.36] to extract information about cavity photons without destroying them. Via Ramsey spectroscopy of the ion, we measure the phase shift and dephasing of the ion's state, both of which result from the interaction of the ion with the cavity field. The mean phase shift is proportional to the mean cavity photon occupation number, due to the ac Stark effect, and the dephasing is due to the cavity photon state not being a pure number state. Reconstructing the cavity photon-number distribution from these measurements allows us to determine the mean and the width of the distribution and thus to distinguish between states with coherent photon statistics and mixed thermal-coherent statistics.

The ion is modelled as a three-level system in which two states, $|S\rangle \equiv |4^2\mathrm{S}_{1/2}, m_J = +1/2\rangle$ and $|D\rangle \equiv |3^2\mathrm{D}_{5/2}, m_J = +1/2\rangle$, comprise a qubit (Fig. 1). The cavity is dispersively coupled to the transition between $|D\rangle$ and the third state, $|P\rangle \equiv |4^2\mathrm{P}_{3/2}, m_J = +1/2\rangle$, with a detuning $\Delta = 2\pi \times 125$ MHz. The quantization axis is defined by a magnetic field of 4.06 G in the plane perpendicular to the cavity axis. The relevant ion-cavity parameters are given by $(g, \kappa, \gamma) = 2\pi\times(0.968,\ 0.068,\ 11.5)$ MHz,

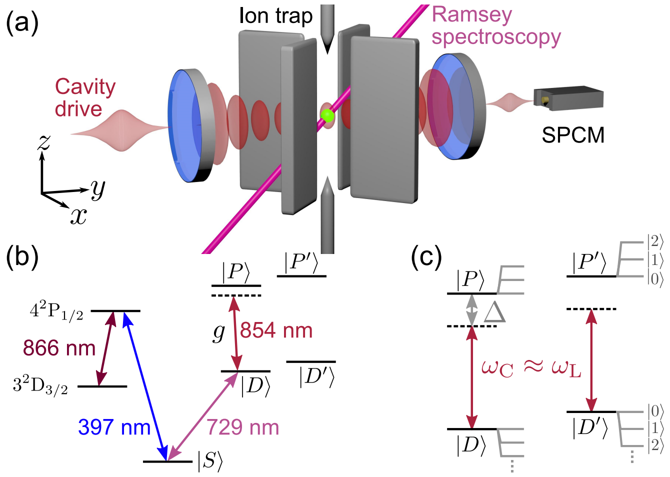

Figure 10.1: (a) Experimental set-up. A single ion is coupled to the cavity, which is driven by a weak laser field (cavity drive). The cavity drive laser (along $\hat{y}$) is polarized parallel to the quantization axis, in the direction $\hat{x} + \hat{z}$. The Ramsey spectroscopy laser propagates along $-(\hat{y}+\hat{z})$. Cavity output photons are detected by a single-photon-counting module (SPCM). (b) Energy level diagram of $^{40}\mathrm{Ca}^+$ with the relevant levels $|S\rangle$, $|D\rangle$, $|P\rangle$, $|D'\rangle \equiv |3^2\mathrm{D}_{5/2}, m_J = +3/2\rangle$ and $|P'\rangle \equiv |4^2\mathrm{P}_{3/2}, m_J = +3/2\rangle$ of the ion. The $4^2\mathrm{P}_{1/2}$ and $3^2\mathrm{D}_{3/2}$ manifolds are used for ion cooling and detection. (c) Levels $|D\rangle$, $|P\rangle$, $|D'\rangle$, and $|P'\rangle$ experience photon-number-dependent ac Stark shifts due to the cavity field, indicated in grey. The frequencies of the bare cavity and the drive laser are ω_C and ω_L, respectively, and Δ is the difference between ω_C and the transition frequency from $|D\rangle$ to $|P\rangle$.

where g is the ion-cavity coupling strength calculated from the cavity properties and the atomic transition, κ is the cavity field decay rate, and γ is the atomic decay rate of state $|P\rangle$. Here, we assume that the ion is positioned at the waist and in an antinode of a TEM_{00} mode of the cavity [10.37, 10.38]. The expected frequency shift of the cavity resonance induced by the dispersively coupled ion is $g^2/\Delta = 2\pi \times 7.50$ kHz, which is much smaller than κ, such that we operate in the weak-pull regime [10.25, 10.26]; see appendix for further discussion of the choice of Δ. In this regime, the drive laser can be considered to be resonant with the cavity, irrespective of the state of the qubit.

In order to probe the cavity field, the ion is first Doppler-cooled and optically pumped to $|S\rangle$. As the first part of a Ramsey measurement, the qubit is then initialized in a superposition of $|S\rangle$ and $|D\rangle$ by a $\pi/2$-pulse of the Ramsey spectroscopy laser at 729 nm. Next, we drive the cavity with a weak laser field with wavelength $\lambda_\mathrm{L} = 854$ nm for $T = 50\ \mu$s. Note that the interaction time T is much larger than the cavity photon lifetime of $\tau_\mathrm{C} = 1/(2\kappa) = 1.2\ \mu$s, such that for a mean intracavity photon number of $\langle n\rangle$, $\langle n\rangle T/\tau_\mathrm{C}$ photons on average successively interact with the ion. Note also that T is much shorter than the coherence time of 950 μs on the $|S\rangle$–$|D\rangle$ transition [10.39]. The independently calibrated mean photon number $\langle n\rangle$ of the cavity field is set to a value between 0 and 1.6(3), and the drive laser frequency $\omega_\mathrm{L} = 2\pi c/\lambda_\mathrm{L}$ is resonant with the cavity frequency $\omega_\mathrm{C} + \langle\sigma_D\rangle g^2/\Delta$, where ω_C is the cavity resonance frequency when

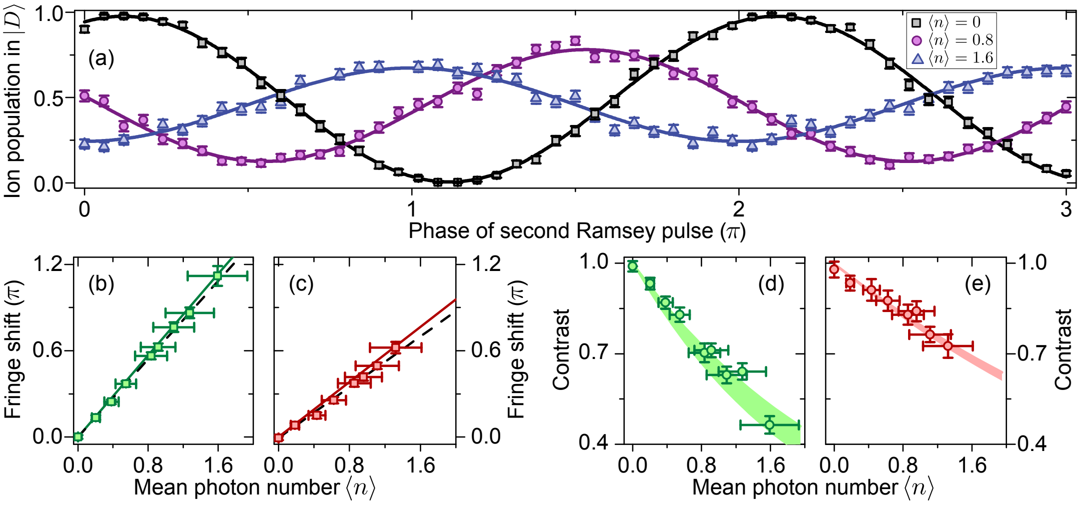

Figure 10.2: (a) Ramsey fringes for mean photon numbers $\langle n\rangle = 0$ (black squares), 0.8(2) (purple circles), and 1.6(3) (blue triangles). The solid lines are sinusoidal fits (see appendix) and error bars denote quantum projection noise. (b) The phase shift of the Ramsey fringes as a function of $\langle n\rangle$ for the transition $|D\rangle - |P\rangle$. Squares are experimental data, while the solid line shows the theoretical model using the calculated coupling strength g. The dashed line is a linear fit to the data, from which g_{exp} is extracted (see main text). (c) Ramsey fringe phase shift as a function of $\langle n\rangle$ for the transition $|D'\rangle - |P'\rangle$ with $g' = 0.82\,g$. (d) Contrast of the Ramsey fringes as a function of $\langle n\rangle$ for the transition $|D\rangle - |P\rangle$. The shaded area shows the contrast expected from the theoretical model with g_{exp} as input, including its uncertainty. (e) Contrast vs. $\langle n\rangle$ for the transition $|D'\rangle - |P'\rangle$. For (b)-(e), the plotted uncertainties in $\langle n\rangle$ are statistical and systematic uncertainties from the calibration of the photon number. Systematic uncertainties in $\langle n\rangle$ are 20%. Error bars of fringe shift and contrast are uncertainties of the fits to the Ramsey fringes.

no ion is coupled to the cavity, and σ_D is the operator for the ion population in $|D\rangle$. Finally, a second $\pi/2$-pulse with variable phase ϕ completes the Ramsey measurement, after which the qubit state is detected using laser fields at 397 nm and 866 nm [10.39]. The measurement is repeated 250 times for each phase to obtain the ion population in $|D\rangle$.

The mean population in $|D\rangle$ as a function of the phase ϕ is plotted in Fig. 10.2(a) for three values of $\langle n\rangle$. As $\langle n\rangle$ is increased, two features emerge: the Ramsey fringe is shifted, and its contrast is reduced. The phase shift is directly proportional to $\langle n\rangle$, as shown in Fig. 10.2(b), with proportionality factor Tg^2/Δ. For $\langle n\rangle = 0.8(2)$ and 1.6(3), the phase of the qubit is shifted by $0.57(3)\pi$ and $1.12(7)\pi$, respectively. A single photon only interacts with the ion during its time in the cavity, which has a mean value τ_{C}, corresponding to a phase shift of the ion by $\tau_{\text{C}}\, g^2/\Delta = 0.018\pi$. The accumulated effect of all successive photons injected into the cavity accounts for the total phase shift of the qubit.

The measured phase shift as a function of $\langle n \rangle$ can be used to determine the ion-cavity coupling strength. This method is independent of the single-atom cooperativity and thus is valid also for systems in intermediate and even weak coupling regimes. In such regimes, observing the vacuum Rabi splitting is not possible, making it difficult to measure the coupling strength directly. As we have independently determined all ion-cavity parameters and calibrated the photo-detection efficiency, we fit a theoretical model to the data with the coupling strength as the only free parameter. In this way, we extract the experimental value of $g_{\mathrm{exp}} = 2\pi \times 0.96(4)$ MHz from the data displayed in Fig. 10.2(b), in agreement with the theoretical value of $g = 2\pi \times 0.968$ MHz. We performed the same set of measurements on another $^{40}\mathrm{Ca}^{+}$ transition, using the states $|S\rangle$, $|D'\rangle \equiv |3^2\mathrm{D}_{5/2}, m_J = +3/2\rangle$, and $|P'\rangle \equiv |4^2\mathrm{P}_{3/2}, m_J = +3/2\rangle$ (Fig. 10.2(c)); the coherence time for the transition $|S\rangle - |D'\rangle$ is 510 μs. For the transition $|D'\rangle - |P'\rangle$, we expect $g' = 2\pi \times 0.790$ MHz and extract $g'_{\mathrm{exp}} = 2\pi \times 0.77(4)$ MHz. From the two independent measurements on two transitions, we thus see that this new method determines the atom-cavity coupling strength in agreement with theory.

In Fig. 10.2(d), the fringe contrast, defined as the peak-to-peak value of the fringe divided by twice the fringe offset, is plotted as a function of $\langle n \rangle$ for the transition $|D\rangle - |P\rangle$ and in Fig. 10.2(e) for the transition $|D'\rangle - |P'\rangle$. This definition of the contrast takes into account that the midpoint of the fringe is not necessarily 0.5, due to spontaneous emission (see appendix). For $|D\rangle - |P\rangle$, the contrast decreases from 0.99(2) to 0.46(3) as $\langle n \rangle$ increases from 0 to 1.6. This reduction reflects the fact that the intracavity photon number is inherently probabilistic, and in this case, for a coherent drive, follows a Poissonian distribution. The corresponding photon-number fluctuations in the cavity field lead to fluctuations of the qubit transition frequency through the photon-number-dependent ac Stark shift. Note that the observed reduction of contrast can, equivalently, be interpreted as a consequence of the qubit state being measured by the cavity field [10.14, 10.25]: Intracavity photons interact dispersively with the qubit before leaking to the environment. The phase of the output photons thus carries information about the qubit state that could be accessed, e.g., with homodyne or heterodyne detection. All such quantum measurements imply some amount of backaction [10.25], which in our case takes the form of qubit decoherence. Note that in the absence of a cavity, photons would also induce an ac Stark shift of the ion's states, but due to the weakness of the free-space interaction, the effect would be too small to be measured at the single-photon level.

Spontaneous emission contributes to decoherence for both the cavity-drive measurement of Fig. 10.2 and free-space measurements. We quantify this effect in a reference measurement using an "ion-drive" configuration: The cavity is translated by a few mm along $\hat{x}$ in order to decouple it from the ion. The ion is driven with a laser beam with frequency $\omega_{\mathrm{L}} = \omega_{\mathrm{C}}$. We perform Ramsey measurements with the cavity interaction replaced by the interaction of the ion with this ion-drive laser. The Ramsey fringe contrast is reduced due to off-resonant excitation of the population from $|D\rangle$ to $|P\rangle$, followed by spontaneous emission. Fig. 10.3 compares the Ramsey fringe contrast as a function of the phase shift for both the ion-drive and cavity-drive measurements. A given phase shift corresponds to the same ac Stark shift at the ion in both measurements.

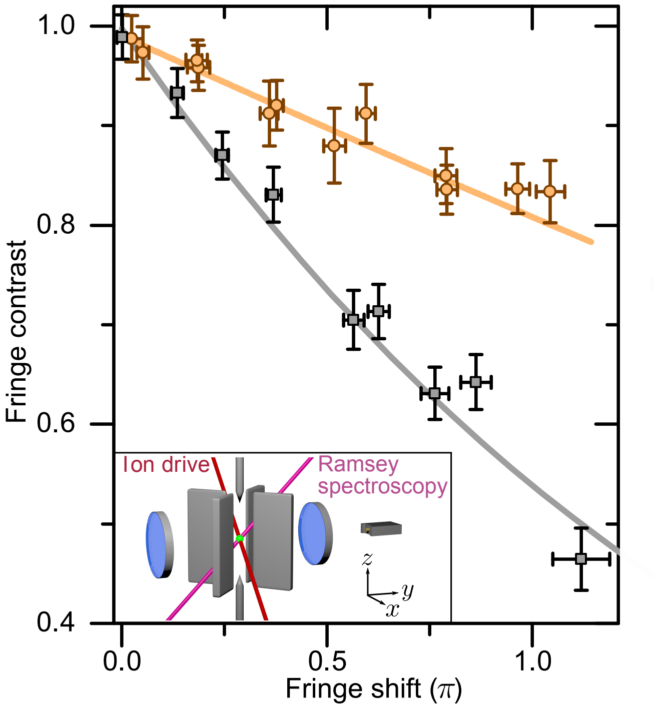

Figure 10.3: Ramsey fringe contrast as a function of phase shift for ion-drive (orange circles) and cavity-drive (black squares; same data as in Fig. 10.2(b) and (d)) measurements on the $|D\rangle$–$|P\rangle$ transition. The lines are theory curves, using g_{exp} for the cavity-drive data. The inset shows the ion-drive beam, which propagates along $\hat{x} - \hat{z}$ and is polarized along $\hat{x} + \hat{z}$, along with the Ramsey spectroscopy beam. The ion is decoupled from the cavity for the ion-drive measurement.

The contrast of the cavity-drive data is smaller than that of the ion-drive data because in the former case, both spontaneous emission and decoherence induced by the cavity photons play a role. We therefore conclude from this reference measurement that decoherence is not just caused by spontaneous emission; rather, a significant contribution to decoherence of the ion qubit stems from interaction with the cavity field via the backaction of the cavity photons on the ion.

Next, we reconstruct the cavity photon number distribution with a maximum likelihood algorithm (see appendix). This algorithm finds the photon number distribution that is most likely to have interacted with the ion. It is based on a model, in which the coherent cavity drive with mean photon number n_{coh} is described by an amplitude $\eta = \kappa\sqrt{n_{\text{coh}}}$, and additional number fluctuations are described by a thermal bath with mean photon number n_{th} corresponding to an incoherent contribution to the driving [10.40]. The photon number distribution of the intracavity field is then determined by the two parameters η and n_{th}. The result of the reconstruction is shown in Fig. 10.4. For the three Ramsey fringes measured on the $|D\rangle - |P\rangle$ transition, displayed in Fig. 10.2(a), the reconstruction yields a squared statistical overlap (SSO) $\left(\sum_n \sqrt{p_{\text{rec}}(n)p_{\text{cal}}(n)}\right)^2$

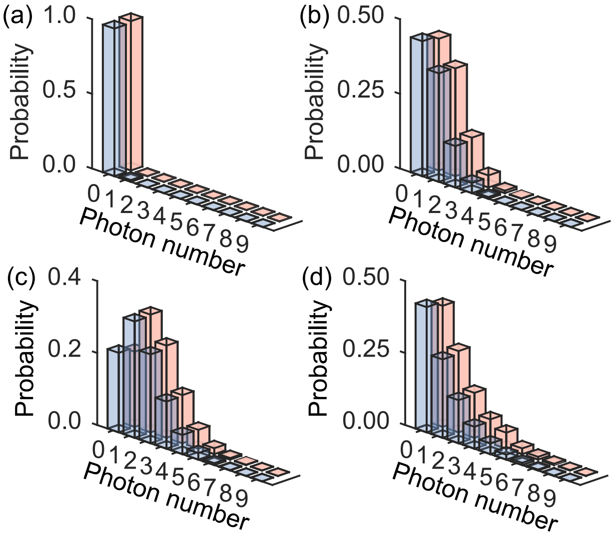

Figure 10.4: Photon number distributions reconstructed from the measured Ramsey fringes for intracavity mean photon numbers of (a) 0, (b) 0.8(2), and (c) 1.6(3) (blue bars), and the expected distributions (pink bars). The reconstructed distributions yield mean photon numbers of $0.01^{+0.05}_{-0.02}$, 0.84(8), and $1.49^{+0.05}_{-0.06}$. (d) Reconstructed distribution when the cavity is driven with light of mixed coherent-thermal statistics with mean photon number $\langle n \rangle = 1.05^{+0.07}_{-0.11}$, yielding a reconstructed mean photon number of $\langle n \rangle = 1.12^{+0.14}_{-0.15}$. The squared statistical overlap between the reconstructed distributions and the expected distributions is higher than 0.99 for (a)-(d).

between the reconstructed distribution $p_{\mathrm{rec}}(n)$ and the independently calibrated input state distribution $p_{\mathrm{cal}}(n)$ above 99% (Figs. 10.4(a)-(c)). The reconstructed state shown in Fig. 10.4(a) corresponds to the vacuum state, and the states in Fig. 10.4(b) and (c) are coherent states, with Mandel Q parameters $Q = \left(\langle n^2 \rangle - \langle n \rangle^2\right) / \langle n \rangle - 1$ of $0.00^{+0.02}_{-0.01}$, $-0.03(7)$, and 0.04(5), respectively [10.41]. The uncertainty of the reconstructed distribution is dominated by quantum projection noise in the Ramsey measurement (see appendix).

This reconstruction method is also applied to a fourth state which is generated by applying amplitude noise to the cavity drive laser via an acousto-optic modulator. The noise has a bandwidth of 10 MHz $\gg 2\kappa$ and can therefore be considered as white noise. The reconstructed state, shown in Fig. 10.4(d), can be described by mixed coherent and thermal statistics: From the calibration of the added noise (see appendix), a value of $Q = 0.64(6)$ is expected, while the reconstruction yields $Q = 0.70^{+0.07}_{-0.10}$. The result thus shows super-Poissonian intracavity photon statistics caused by the added thermal noise and is clearly distinct from the statistics of a coherent state. Note that our sensing technique is nondestructive because the dispersive interaction with the ion does not annihilate the measured intracavity photons.

An extension of this work would be to reconstruct the full density matrix of arbitrary states of the cavity field. For this purpose, we require a displacement operation of the cavity field, as has been demonstrated in microwave cavities [10.18]. With the target field to be measured populating the cavity, a second field as a local oscillator would be sent to the cavity. The total field interacting with the ion would be the sum of the known (local oscillator) and unknown (target) fields, and by varying the known field and measuring the state of the ion, one would be able to extract the full target field density matrix.

We have focused here on measuring the ion's state to extract information about the cavity field. However, the scenario can be reversed: quantum nondemolition measurements of the ion's state become possible in our setup via heterodyne measurement of the cavity output field, allowing single quantum trajectories of the ion's electronic state to be monitored and the qubit state to be stabilized, as demonstrated with superconducting qubits [10.26, 10.27]. Furthermore, the strong-pull regime ($g^2/\Delta > \kappa$) would be accessible with a higher finesse cavity [10.25, 10.26]. In this regime, the qubit spectrum splits into several lines, each corresponding to a different photon-number component [10.15, 10.42], providing a route to engineer nonclassical cavity-field states in the optical domain. Other possible extensions include increasing the sensitivity of the measurement by using several ions via their collective coupling to the cavity [10.43] or via their entanglement [10.44].

In summary, we have implemented an ion-based analyzer for the statistics of optical photons that does not destroy the photons. Information about the intracavity photon number is imprinted onto the state of an ion qubit via a dispersive interaction. Ramsey spectroscopy and the maximum likelihood method are used to reconstruct the intracavity photon statistics, yielding results in excellent agreement with the expected distributions. Our work represents the first such nondestructive probing of cavity photon distributions in the optical domain, providing tools for the generation of nonclassical optical states.

This work has been financially supported by the Austrian Science Fund (FWF) through Projects F4019, V252, M1964, W1259-N27, and F4013-N23; by the Army Research Laboratory's Center for Distributed Quantum Information via the project SciNet: Scalable Ion-Trap Quantum Network, Cooperative Agreement No. W911NF15-2-0060; and by the European Union's Horizon 2020 research program through the Marie Skłodowska-Curie Actions, Grant No. 656195.

M.L. and K.F. contributed equally to this work.

Appendix

Modelling the system

Atomic levels

In order to calculate the theory lines in Fig. 2(b)-(e) in the main text, we consider the following atomic basis states: $|S\rangle = |4^2\mathrm{S}_{1/2}, m_J = +1/2\rangle$, $|D\rangle = |3^2\mathrm{D}_{5/2}, m_J = +1/2\rangle$, $|P\rangle = |4^2\mathrm{P}_{3/2}, m_J = +1/2\rangle$, and $|S'\rangle$ (see Fig. 10.5), where $|S'\rangle$ is a dark state, which collects spontaneous emission from $|P\rangle$ to the second ground state $|4^2\mathrm{S}_{1/2}, m_J = -1/2\rangle$,

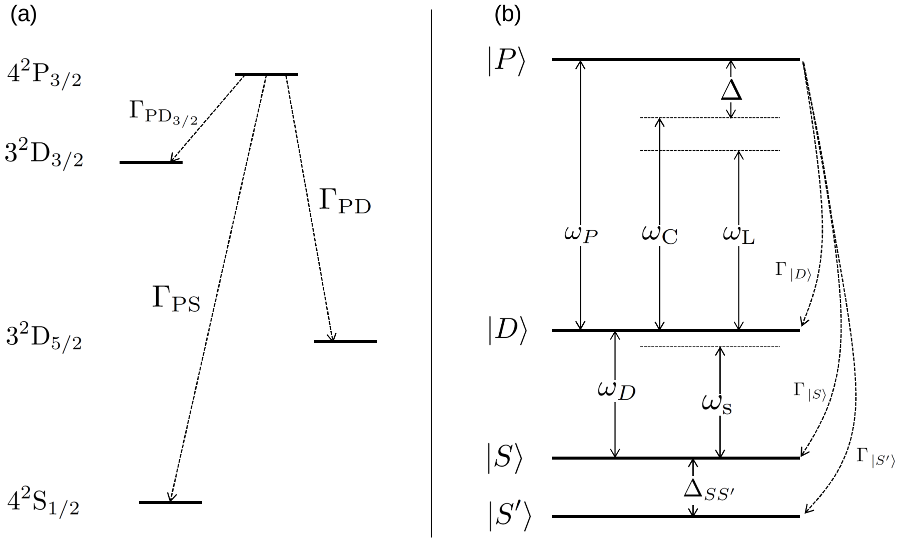

Figure 10.5: Definition of the involved levels and transitions. (a) Levels and decay channels considered in the model. Note that decay to $4^2\mathrm{S}_{1/2}$ from $3^2\mathrm{D}_{5/2}$ is not included, since the lifetime of the latter level of 1 s is much longer than the duration of one experimental cycle. (b) Definition of the levels, energies, detunings and decay constants in the model. Note that the decay from $|P\rangle$ to $|S'\rangle$ combines decay channels ending in $4^2\mathrm{S}_{1/2}$, $3^2\mathrm{D}_{5/2}$, and $3^2\mathrm{D}_{3/2}$.

as well as to the states $|3^2\mathrm{D}_{5/2}, m_J = -1/2\rangle$, $|3^2\mathrm{D}_{5/2}, m_J = +3/2\rangle$, and the states in the $3^2\mathrm{D}_{3/2}$ manifold. $|S'\rangle$ does not participate in the ion-cavity interaction and is not coupled to the Ramsey spectroscopy laser. The manifolds involved in the process are displayed in Fig. 10.5(a). The total decay rate of state $|P\rangle$ is $\Gamma_P = \Gamma_{\mathrm{PS}} + \Gamma_{\mathrm{PD}} + \Gamma_{\mathrm{PD}_{3/2}} = 2\pi \times 23$ MHz, with values $\Gamma_{\mathrm{PS}} = 2\pi \times 21.4$ MHz for decay from $4^2\mathrm{P}_{3/2}$ to $4^2\mathrm{S}_{1/2}$, $\Gamma_{\mathrm{PD}} = 2\pi \times 1.34$ MHz for decay from $4^2\mathrm{P}_{3/2}$ to $3^2\mathrm{D}_{3/2}$, and $\Gamma_{\mathrm{PD}_{3/2}} = 2\pi \times 0.152$ MHz for decay from $4^2\mathrm{P}_{3/2}$ to $3^2\mathrm{D}_{3/2}$. Taking into account the Clebsch-Gordan coefficients, the decay rates are $\Gamma_{|S\rangle} = 2/3\,\Gamma_{\mathrm{PS}} = 2\pi \times 14.3$ MHz from $|P\rangle$ to $|S\rangle$, $\Gamma_{|S'\rangle} = 1/3\,\Gamma_{PS} + 3/5\,\Gamma_{PD} + \Gamma_{PD_{3/2}} = 2\pi \times 8.1$ MHz from $|P\rangle$ to $|S'\rangle$, and $\Gamma_{|D\rangle} = 2/5\,\Gamma_{PD} = 2\pi \times 0.54$ MHz from $|P\rangle$ to $|D\rangle$.

Hamiltonian

The Hamiltonian of the system is given by

$$\begin{aligned}H_S/\hbar =&\omega_D\sigma_D + (\omega_D + \omega_P)\,\sigma_P + \omega_{\mathrm{C}} a^\dagger a + g\,(\sigma_{PD} a + \text{h.c.}) + \\ &+ \left(\eta a^\dagger e^{-i\omega_{\mathrm{L}} t} + \text{h.c.}\right) + \left(\Omega\sigma_{SD} e^{-i\omega_{\mathrm{R}} t} + \text{h.c.}\right).\end{aligned} \tag{10.1}$$

Here, ω_D corresponds to the energy of the level $|D\rangle$, ω_P to that of $|P\rangle$, $\sigma_{D(P)}$ is the projection operator onto the state $|D\rangle$ ($|P\rangle$), ω_{C} is the cavity frequency, a is the annihilation operator of the cavity mode, g is the ion-cavity coupling strength, $\sigma_{PD} = \sigma_{DP}^\dagger$ is the transition operator between states $|P\rangle$ and $|D\rangle$, η is the amplitude of the drive laser in the cavity drive term, ω_{L} is the frequency of the cavity drive laser, Ω is the Rabi frequency of the laser on the $|S\rangle$–$|D\rangle$ qubit transition, $\sigma_{SD} = \sigma_{DS}^\dagger$ is the transition operator between states $|S\rangle$ and $|D\rangle$, and ω_{R} is the frequency of the Ramsey spectroscopy laser. The energy of the ground state $|S\rangle$ is chosen as the energy reference. Fig. 10.5(b) shows the relevant states, frequencies and decay channels. This Hamiltonian is transformed into a rotating frame via

$$H_I = i\hbar\dot{U}U^\dagger + UH_SU^\dagger,$$

with a unitary operator

$$U = \exp\left[i\left(\omega_{\mathrm{R}}\sigma_D + (\omega_s + \omega_P)\sigma_P + \omega_P a^\dagger a\right)t\right].$$

We thus obtain the Hamiltonian in the interaction picture as

$$\begin{aligned}H_I/\hbar =&\Delta_{D\mathrm{R}}\sigma_D + (\Delta_{P\mathrm{L}} + \Delta_{\mathrm{CL}} + \Delta_{D\mathrm{R}})\sigma_P + \Delta_{SS'}\sigma_{S'} + \Delta_{\mathrm{CL}}\, a^\dagger a + \\ &+ g\left(\sigma_{PD}\, a + \sigma_{DP}\, a^\dagger\right) + \eta(a + a^\dagger) + \Omega\,(\sigma_{SD} + \sigma_{DS}).\end{aligned} \tag{10.2}$$

Here, $\Delta_{D\mathrm{R}} = \omega_D - \omega_{\mathrm{R}}$ is the detuning between the Ramsey spectroscopy laser and the $|D\rangle$–$|S\rangle$ transition, $\Delta_{P\mathrm{L}} = \omega_P - \omega_{\mathrm{L}}$ is the detuning between the cavity drive laser and the $|P\rangle$–$|D\rangle$ transition, $\Delta_{\mathrm{CL}} = \omega_{\mathrm{C}} - \omega_{\mathrm{L}}$ is the detuning between the cavity drive laser and the cavity mode, and $\Delta_{SS'}$ is the detuning between state $|S\rangle$ and the dark state $|S'\rangle$. In the cavity drive term, the drive amplitude η for coherent driving on resonance, i.e., for $\Delta_{\mathrm{CL}} = 0$, is given by $\eta = \kappa\sqrt{n_{\mathrm{coh}}}$ with n_{coh} the mean photon number and 2κ the decay rate of the cavity photons. This relation can be derived from the Heisenberg-Langevin equation for the cavity field a in steady state (cf. section I.C). The value of η used in the simulation stems from the calibration of the mean photon number.

In the dispersive regime $\Delta_{P\mathrm{L}} \gg g$, the Hamiltonian can be approximated: Using the transformation

$$U = e^{\frac{g}{\Delta_{P\mathrm{L}}}\left(\sigma_{PD} a - a^\dagger\sigma_{DP}\right)}$$

and the Baker-Campbell-Hausdorff formula, and truncating the series at first order in $g/\Delta_{P\mathrm{L}}$, one finds the transformed Hamiltonian

$$
\begin{aligned}
UHU^\dagger/\hbar \approx & \left(\Delta_{\mathrm{DR}} - 2\frac{g^2}{\Delta_{\mathrm{PL}}} a^\dagger a\right)\sigma_D + \left(\Delta_{PL} + \Delta_{\mathrm{CL}} + \Delta_{DR} + 2\frac{g^2}{\Delta_{\mathrm{PL}}}\left(a^\dagger a + 1\right)\right)\sigma_P + \\
& + \Delta_{\mathrm{CL}} a^\dagger a + \eta\left(a + a^\dagger\right) + \Omega\left(\sigma_{SD} + \sigma_{DS}\right) + \frac{\eta g}{\Delta_{PL}}\left(\sigma_{DP} + \sigma_{PD}\right) + \\
& + \frac{\Omega g}{\Delta_{PL}}\left(a^\dagger \sigma_{SP} + \sigma_{PS} a\right).
\end{aligned}
$$

The first two lines of this equation describe the ac Stark shift of the states $|D\rangle$ and $|P\rangle$, with the magnitude of the shift dependent on the dispersive shift per photon g^2/Δ_{PL} and the photon number operator $a^\dagger a$. The energy shift of the state $|D\rangle$, when time-integrated during the interaction time, leads to the phase shift of the Ramsey fringe. The detuning between cavity and atom Δ_{PL} is denoted by Δ in the main text and the remainder of the appendix.

Master equation

The system evolution is calculated by numerically integrating the following master equation in Python, using QuTiP [10.45, 10.46]. The master equation consists of four terms, describing unitary evolution, atomic decay, cavity decay with rate κ, and incoherent cavity driving, derived from a stochastic drive term [10.40, 10.47]:

$$
\begin{aligned}
\frac{d\rho}{dt} = & -\frac{i}{\hbar}\left[\rho, H_I\right] + \sum_{i=D,S,S'} \frac{\Gamma_i}{2}\left(2\sigma_i^- \rho \sigma_i^+ - \rho\sigma_i^+\sigma_i^- - \sigma_i^+\sigma_i^-\rho\right) + \\
& + \frac{\kappa}{2}\left(2a\rho a^\dagger - \rho a^\dagger a - a^\dagger a \rho\right) + \delta n\left(\left[\left[a, \rho\right], a^\dagger\right] + \left[\left[a^\dagger, \rho\right], a\right]\right)
\end{aligned} \tag{10.3}
$$

The photons are described by a Fock state basis, truncated at $n = 9$. This number is sufficient, since for the measured coherent states the mean photon number is below two, which would correspond to a population of below $2 \cdot 10^{-4}$ for the Fock state $|n = 9\rangle$. In the experiment, the incoherent drive is implemented by adding white amplitude noise to the RF-amplitude for the acousto-optic modulator of the cavity drive beam. The bandwidth of the frequency generator used for generating the noise reaches from DC to 10 MHz. Since the full cavity linewidth is only $2\kappa = 2\pi \times 136$ kHz, this can be considered white noise.

Expanding the last term of Eq. 10.3 and combining it with the cavity-decay term, we get:

$$
\frac{\kappa + \delta n}{2}\left(2a\rho a^\dagger - \rho a^\dagger a - a a^\dagger \rho\right) + \frac{\delta n}{2}\left(2a^\dagger \rho a - \rho a a^\dagger - a a^\dagger \rho\right),
$$

which corresponds to thermal driving of the cavity [10.48] with a thermal bath with mean photon number $n_{\mathrm{th}} = \delta n/\kappa$. Since the coherent and incoherent drive do not interfere, the total mean photon number is given by the sum of the coherent and incoherent contributions as $\langle n\rangle = n_{\mathrm{coh}} + n_{\mathrm{th}}$.

Second transition $|D'\rangle$–$|P'\rangle$

For simulating the second transition, (data in Fig. 2(c) and (e) of the main text), the following parameters need to be changed: g is replaced by g', and due to the different Clebsch-Gordan coefficients, only the following decay channels exist: $\Gamma_{|S'\rangle} = 11/15\,\Gamma_{\mathrm{PD}}$ for decay from $|P'\rangle$ to the dark state $|S'\rangle$, and $\Gamma_{|S\rangle} = \Gamma_{\mathrm{PS}}$ for decay from $|P'\rangle$ to $|S\rangle$. $\Gamma_{|D\rangle}$ is replaced with $\Gamma_{|D'\rangle} = 4/15\,\Gamma_{\mathrm{PD}}$ for decay from $|P'\rangle$ to $|D'\rangle$. Note that for this transition, $|P'\rangle$ has no allowed decay to the second ground state $|4^2\mathrm{S}_{1/2}, m_J = -1/2\rangle$. In Eq. 10.2, D is replaced by D' and P by P'. Note also that the photon polarization is the same for both transitions $|D\rangle$–$|P\rangle$ and $|D'\rangle$–$|P'\rangle$.

Reconstruction algorithm

In order to reconstruct the photon number distribution in the cavity (Fig. 4 in the main text), we first define a likelihood function [10.49] as

$$L(\eta, \delta n) = \prod_{k=1}^{N} \left[P_k(\eta, \delta n)\right]^{f_k} \left[1 - P_k(\eta, \delta n)\right]^{1-f_k} \times \mathrm{const.}$$

In this formula, $N = 51$ is the number of points per Ramsey fringe, f_k is the measured probability to find the ion in $|D\rangle$ for point k in the fringe, P_k is the excitation probability expected from solving the master equation with the cavity drive parameters η and δn as input, and const is a scaling factor. The quantity L describes the likelihood to observe the measured result (given by f_k) for certain parameters $(\eta, \delta n)$, based on the model of the system (given by $P_k(\eta, \delta n)$). The parameters that best describe the data are obtained by maximizing the likelihood or its logarithm

$$\log\left[L(\eta, \delta n)\right] = \sum_{k=1}^{N} \left(f_k \log\left[P_k(\eta, \delta n)\right] + (1 - f_k) \log\left[1 - P_k(\eta, \delta n)\right]\right) + \mathrm{const.} \quad (10.4)$$

In order to obtain P_k for a given set $(\eta, \delta n)$, we numerically integrate the master equation Eq. 10.3. The number N was chosen such that there are a sufficient number of points for the sinusoidal fits to the Ramsey fringes.

The iterative algorithm for maximizing the likelihood function runs as follows:

1. Integrate Eq. 10.3 for given values of η and δn.
2. Calculate the likelihood function using Eq. 10.4.
3. Change η and δn and repeat.

This sequence is iterated until the maximum value of the likelihood has been found in a Nelder-Mead simplex optimization. The corresponding values of η_{opt} and δn_{opt} are the most likely ones to explain the measured data, and the reconstructed photon number distribution is given by the corresponding diagonal elements $p(n)$ of the cavity density matrix obtained from integrating the master equation with η_{opt} and δn_{opt} as input.

Photon number calibration

We independently calibrated the intracavity mean photon number to be able to compare the reconstructed photon number distribution with the expected values. Given the probability for a photon to leave the cavity through the output mirror of $p_{\mathrm{out}} = 11(2)\%$, which corresponds to a total photon detection efficiency $\varepsilon = p_{\mathrm{out}} \times \zeta = 4(1)\%$ (including detector efficiency and optical loss in the path efficiency ζ), we calculate an expected count rate of $2\kappa \times p_{\mathrm{out}} \times \zeta = 38(8)$ kHz for the single-photon counting module (SPCM) at the cavity output for a mean photon number of $\langle n \rangle = 1$ in the cavity. This rate corresponds to an expected number of counts of $C_0 = 475(100)$ during the interaction time of $\tau = 50$ μs. We take the cavity field build-up time into account by including a correction factor $c = 0.922$, extracted from a simulation, and accordingly get a number of counts of $C_1 = C_0/c = 515(108)$ for the calibration. By measuring the output counts C, we are thus able to calibrate the mean photon number in the cavity field for a given input power as $\langle n \rangle = C/C_1$.

Fit model

For analyzing the Ramsey fringes, we use a fit model of the following form:

$$E(\phi) = B + A \cdot \cos\left(\pi\left(\phi - \phi_0\right)\right)$$

Here, $E(\phi)$ stands for the excitation of the ion to the state $|D\rangle$ (or $|D'\rangle$), ϕ for the phase of the second Ramsey pulse with respect to the first one, A is the amplitude of the fringe, ϕ_0 the fringe shift, and B is the offset of the fringe. The contrast is calculated as $2A/(2B)$, with $2A$ the peak-to-peak value of the fringe and $2B$ the maximum possible peak-to-peak value. This definition takes into account that spontaneous emission reduces the fringe offset to $B < 0.5$, leading to a maximum possible peak-to-peak value of the fringe of $2B$, as the minimum value is zero and the midpoint of the fringe is B. We include the spontaneous emission from the excited state $|P\rangle$ by making the offset B dependent on the off-resonant excitation to state $|P\rangle$ (or $|P'\rangle$). B therefore has to be recalculated for each value of $\langle n \rangle$ as

$$B = B_{\langle n \rangle = 0} \cdot \exp\left(-\Gamma_{|S'\rangle} p_{P(')} \langle n \rangle \, \tau\right)$$

Here, $p_{P(')} = 2g^2\langle n \rangle / \left(\Gamma^2_{|D(')\rangle} + \Delta^2\right)$ is the probability to off-resonantly excite the ion from $|D\rangle$ ($|D'\rangle$) to state $|P\rangle$ ($|P'\rangle$), and $B_{\langle n \rangle = 0} = 0.4915$ is the maximum offset achievable for the given coherence time and $\langle n \rangle = 0$. This number is half of the maximum achievable excitation of a single Doppler-cooled ion.

The phase offset of $-0.12(1)\pi$ for $\langle n \rangle = 0$, obtained from the fit, is due to an ac Stark shift of the ion levels, caused by the non-zero spatial overlap of the ion wave packet and a laser field at 783 nm used to actively stabilize the cavity length; this field populates a TEM$_{01}$ cavity mode [10.50].

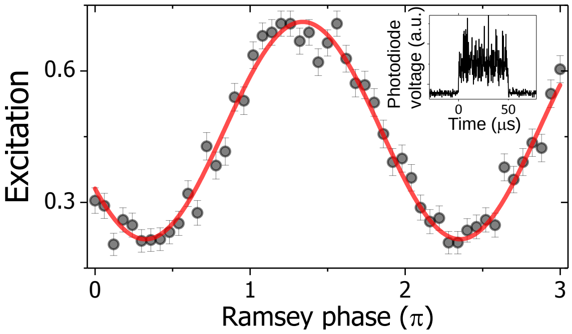

Figure 10.6: Ramsey fringe when the cavity is driven with a coherent field with additional white noise. The black circles are data points and the red line is a sinusoidal fit to the data. From the fit, a phase shift of $0.71(2)\pi$ and a contrast of 0.57(3) are extracted. The error bars are quantum projection noise. (inset) Photodiode measurement of the cavity input field.

Uncertainty analysis of the reconstructed photon statistics

The uncertainties of the reconstructed photon number distributions are determined by quantum projection noise [10.51] in the Ramsey measurement. The following method is used to estimate the uncertainties of the reconstructed states shown in Fig. 4 of the main text.

1. For a given Ramsey fringe, the maximum likelihood method returns the parameter set $(\eta_{\mathrm{opt}},\ \delta n_{\mathrm{opt}})$, which determines the corresponding photon number distribution.

2. A Monte-Carlo simulation is executed to obtain a random Ramsey fringe which takes into account the quantum projection noise: The ion populations of this fringe are based on the measured ion populations with additional noise following a binomial distribution with 250 cycles used in the experiment.

3. We reconstruct $(\eta_i,\ \delta n_i)$ from the Ramsey fringe obtained in Step 2. The index i indicates the iteration number in the Monte Carlo simulation.

4. Steps 2 and 3 are repeated until the standard deviations of all calculated numbers $(\eta_i,\ \delta n_i)$ have converged according to the criterion that the standard deviation as a function of the number of samples varies less than 5%. The uncertainties $(\Delta\eta,\ \Delta\delta n)$ are then set to the values of the standard deviations. The mean of the obtained η_i and δn_i is η_{opt} and δn_{opt}.

5. The upper limit of the reconstructed distribution is given by $(\eta + \Delta\eta,\ \delta n + \Delta\delta n)$, and the lower limit by $(\eta - \Delta\eta,\ \delta n - \Delta\delta n)$. The uncertainties of the mean photon numbers $\langle n\rangle$ and Mandel Q parameters are calculated by propagating these values.

Driving the cavity with additional amplitude noise

We estimate the intracavity field from a calibration measurement of the cavity drive beam (inset of Fig. 10.6) with a photodiode. In the photodiode signal, there is a contribution from the coherent statistics, which is calibrated independently (see Sec. 10), and a noise contribution with thermal statistics. The coherent statistics is determined by the coherent amplitude η, while the thermal part is described via the mean thermal photon number $n_{\text{th}} = \delta n/\kappa$. By dividing the voltage on the photodiode into the offset part (coherent statistics) and oscillations on top (thermal part), we can calibrate δn as a function of the amplitude V_{AC} of the oscillations: we first extract the conversion factor S_{V} between photodiode voltage and SPCM counts, as $C = S_{\text{V}} \cdot V_{\text{DC}}$, where C is the number of measured counts in the SPCM and V_{DC} is the voltage measured on the photodiode for coherent driving. Next, we can calculate the noise contribution via $\delta n = \kappa S_{\text{V}} V_{\text{AC}}/C_1$, using the fact that the number of SPCM counts originating from the thermal part is proportional to V_{AC}. In this way, we calculate the mean coherent and thermal photon numbers of the expected as $n_{\text{coh}} = 0.64(14)$ and $n_{\text{th}} = 0.44(9)$, both of which agree with the reconstructed values $n_{\text{coh, rec}} = 0.68(16)$ and $n_{\text{th,rec}} = 0.47(15)$.

Phase resolution of the Ramsey measurements

The phase resolution $\delta\phi$ of our Ramsey measurement is limited by quantum projection noise [10.51] in the measurement of the ion's state. In order to estimate $\delta\phi$, we start by simulating a single reference fringe for a mean photon number $\langle n \rangle = 1$ with N phase values, by numerically solving the master equation Eq. 10.3. Using the excitation probability Q_k for a given phase ϕ_k in this fringe, we draw a random sample m_k with a probability Π_k given by the binomial distribution

$$\Pi_k(m_k) = \binom{M}{m_k} Q_k^M \left(1 - Q_k\right)^{M-m_k},$$

where $M = 250$ is the number of repetitions for measuring the ion excitation and m_k is the number of times that the ion is found in the excited state $|D\rangle$ out of M trials. The excitation of the ion to state $|D\rangle$ is then calculated as $p_k = m_k/M$ (corresponding to the values f_k in Eq. 10.4). This is repeated for all N phase values ϕ_k used in the real measurement. Next, we extract the phase shift of this simulated fringe, by fitting a sinusoidal function to the simulated data p_k vs. ϕ_k. This procedure is repeated $50,000$ times and we obtain a distribution of extracted phase values with a standard deviation σ_ϕ. We define the phase resolution as $\delta\phi = 2\sigma_\phi$, since this is the minimum distance between two phase distributions that are distinguishable. A value of $\delta\phi = 0.011\,\pi$ is found. Translating this result into a resolution of the mean photon number via

$$\delta\phi = \frac{g^2}{\Delta}\tau\,\delta\bar{n},$$

we find values of $\delta\bar{n}_{PD} = 0.013(5)$ for the $|D\rangle$–$|P\rangle$ transition and $\delta\bar{n}_{P'D'} = 0.020(8)$ for the $|D'\rangle$–$|P'\rangle$ transition. In other words, it is possible to distinguish the phase shift of the qubit Bloch vector for cavity field states, whose mean photon number is different by just $\delta\bar{n}_{PD}$ or $\delta\bar{n}_{P'D'}$, respectively.

Choice of experiment parameters

The detuning Δ and interaction time τ are chosen in the following way:

1. First, τ is fixed. We require τ to be short enough that the measured Ramsey fringe contrast is not significantly reduced due to noise sources that become significant on this time scale, but long enough that we can consider the cavity field to be in steady state, that is, longer than the build-up time of the cavity field. In our case, $\tau = 50\ \mu$s is chosen to be much shorter than the coherence time of 950 μs of the ion qubit (due to magnetic field fluctuations) and much longer than the cavity build-up time of 1.7 μs, extracted from a numerical simulation of our cavity. For this value of τ, we observe a Ramsey fringe contrast of 99(2)% with no photons in the cavity.

2. Next, the maximum intracavity photon number $\langle n\rangle_{\max}$ is chosen for the planned set of measurements. Here, we wanted to observe the contrast reduction and phase shift at the single-photon level up to values beyond $\langle n\rangle = 1$, so we chose $\langle n\rangle_{\max} = 1.5$.

3. Finally, Δ is fixed. For a given value of $\langle n\rangle$, as Δ is reduced, the Ramsey fringe contrast is also reduced due to the increased rates of measurement-induced dephasing and spontaneous emission. If Δ is too small, it will not be possible to distinguish the contrast for $\langle n\rangle_{\max}$ from noise. On the other hand, increasing Δ extends the range of observable photon numbers, but at the cost of reduced sensitivity to changes in contrast and phase as a function of photon number. We chose the detuning $\Delta = 2\pi \cdot 125$ MHz, corresponding to a contrast of 0.5 for $\langle n\rangle_{\max} = 1.5$.

Note that in our experiment, uncertainties in the measured Ramsey fringe contrasts and phase shifts stem from quantum projection noise [10.51]. For each phase in the Ramsey fringe of Fig. 2(a) in the main text, the measurement was repeated 250 times, corresponding to a total data acquisition time of several hours. With these statistics, the signal-to-noise ratio (SNR) of the Ramsey fringe, defined as the ratio of the root-mean-square of the ion excitation data in the fringe to the mean quantum projection noise, decreases from 30 for the fringe with $\langle n\rangle = 0$ to 16 for the fringe with $\langle n\rangle = 1.6$. Our choice of a contrast of 0.5 for the maximum mean photon number was therefore conservative: We could have chosen a lower value for Δ and accepted a lower SNR. Also, acquiring more data to reduce the statistical uncertainty would have given us even more room to reduce Δ. However, this approach becomes more challenging for longer measurement times in view of experimental drifts.

It is also worth noting that the ratio of the spontaneous emission rate $\gamma_{\text{sp}} = \gamma\langle n\rangle g^2/\Delta^2$ and the rate of measurement-induced dephasing in the weak-pull regime [10.25] $\gamma_{\text{m}} \propto \langle n\rangle g^4/(\kappa\Delta^2)$ is independent of Δ and proportional only to the mean photon number and the cooperativity: $\gamma_{\text{m}}/\gamma_{\text{sp}} \propto \langle n\rangle g^2/(\kappa\gamma)$. For this reason, increasing Δ does not enhance the relative strength of the measurement-induced dephasing effect with respect to the contrast reduction due to spontaneous emission.

Strong-pull regime in an optical cavity

We estimate that it would be possible to reach the strong-pull regime ($g^2/\Delta > \kappa$) in the optical domain with state-of-the-art mirrors. Ref. [10.52] reports a measurement of high-reflectivity mirrors with transmission $T = 5 \cdot 10^{-7}$ and scattering and absorption loss of $A = 1.1 \cdot 10^{-6}$ per mirror for wavelengths near 850 nm, corresponding to a finesse of $2 \cdot 10^6$. For a cavity with such mirrors and the length of our cavity of 19.98 mm, a photon lifetime of $\tau_{\text{c}} = 42$ μs is expected, while the one-sided output coupling $T/(2T + 2A) = 16\%$ is comparable to that of our cavity.

In this regime, we would need to modify the procedure of Sec. 10 because our experimental goal would be different. The goal of the measurements presented in the main text is to observe the evolution of the Ramsey fringe contrast and phase shift over a range of intracavity photon numbers. In contrast, the strong pull regime offers a setting in which one could resolve a splitting of the qubit transition corresponding to the different photon number states in the cavity field [10.25]. In this way, it would be possible to project the cavity field onto a particular number state via measurement of the ion state.

The question then becomes: For given values of g and κ corresponding to a particular experimental implementation, what values of Δ satisfy the strong-pull condition while allowing the dispersive frequency shift $\chi = g^2/\Delta$ to be resolved via qubit spectroscopy within the cavity lifetime?

We consider that an ion is initially prepared in $|S\rangle$ and is coupled to the cavity field on the $|P\rangle - |D\rangle$ transition for an interval τ_1. During this interval, the ion is driven by a classical laser field (which we refer to as a spectroscopy laser) on the $|S\rangle - |D\rangle$ transition. Subsequently, for an interval τ_2, state detection with 397 nm and 866 nm laser fields is used to determine whether the ion is in $|S\rangle$ or $|D\rangle$. Performing this measurement for different detunings of the spectroscopy laser would allow one to resolve the photon number-state splitting.

For a projective measurement that collapses the cavity field onto a nonclassical state, the total interval $\tau_1 + \tau_2$ must be shorter than the cavity lifetime. As an initial estimate, we neglect τ_2 and choose the longest possible interval for the ion interaction with the cavity field, that is, by setting $\tau_1 = \tau_{\text{c}} = 42\ \mu s$. The frequency resolution of the spectroscopy laser is then given by $2\pi/\tau_1 = 2\pi \cdot 24$ kHz. This frequency resolution must be narrower than χ, thus constraining our choice of Δ: $\Delta < \frac{g^2\tau_1}{2\pi}$. A second bound corresponds to the strong-pull condition: $\Delta < \frac{g^2}{\kappa}$.

Table 10.1 lists values for g corresponding to both the $^{40}\text{Ca}^+$ transition used in the main text and to the D2 line in neutral ^{133}Cs. In ^{133}Cs, the qubit would be comprised of

Table 10.1: Estimation for the strong-pull regime in atom-cavity systems. For $^{40}\mathrm{Ca}^+$, the $|D\rangle - |P\rangle$ transition from the main text was considered, while for $^{133}\mathrm{Cs}$ we considered the transition $|6^2\mathrm{S}_{1/2}, F = 4, m_F = 4\rangle - |6^2\mathrm{P}_{3/2}, F' = 5, m'_F = 5\rangle$.

Species	$^{40}\mathrm{Ca}^+$	$^{133}\mathrm{Cs}$
Wavelength (nm)	854	852
$g/2\pi$ (MHz)	0.968	2.0
$\gamma/2\pi$ (MHz)	11.5	2.6
$\kappa/2\pi$ (kHz)	1.9	1.9
$\Delta/2\pi$ (MHz)	39	164

the states $|6^2\mathrm{S}_{1/2}, F = 3, m_F = 3\rangle$ and $|6^2\mathrm{S}_{1/2}, F = 4, m_F = 4\rangle$, and a microwave field or an optical Raman transition would be used to probe the qubit transition. Here, we assume that the cavity lifetime is τ_c and that the mirror radii of curvature are identical to those of our current cavity, yielding the same mode volume. We see that the first bound corresponds to $\Delta < 2\pi \cdot 39$ MHz for $^{40}\mathrm{Ca}^+$ and to $\Delta < 2\pi \cdot 164$ MHz for $^{133}\mathrm{Cs}$. The second bound corresponds to $\Delta < 2\pi \cdot 490$ MHz for $^{40}\mathrm{Ca}^+$ and to $\Delta < 2\pi \cdot 2$ GHz for $^{133}\mathrm{Cs}$. In both cases, the first bound is the infimum and thus the relevant bound. This bound also corresponds to an optimum point for experiments, since decreasing Δ further will increase the effective spontaneous emission rate, broadening the spectroscopic signal. Note that g can be further enhanced by taking advantage of collective atom-cavity coupling.

Finally, we return to the question of ion state detection in the interval τ_2. Detecting the state of the ion was achieved with current technology in 10.5 μs with 99% readout fidelity [10.53, 10.54]; the detection time can be made faster or slower depending on the fidelity requirement. We thus see that including realistic values for τ_2 in the estimate above will lower the upper bound on Δ by about 25%.

Bibliography

References for Chapter 1

[1.1] A. Einstein, “Zur Quantentheorie der Strahlung,” *Phys. Z.*, vol. 18, pp. 121–128, 1917.

[1.2] P. A. M. Dirac, “The quantum theory of the emission and absorption of radiation,” *Proc. R. Soc. Lond. A Math. Phys. Sci.*, vol. 114, no. 767, pp. 243–265, 1927.

[1.3] R. H. Dicke, “Coherence in spontaneous radiation processes,” *Phys. Rev.*, vol. 93, pp. 99–110, 1954.

[1.4] M. Gross and S. Haroche, “Superradiance: An essay on the theory of collective spontaneous emission,” *Phys. Rep.*, vol. 93, no. 5, pp. 301–396, 1982.

[1.5] N. Skribanowitz, I. P. Herman, J. C. MacGillivray, and M. S. Feld, “Observation of Dicke superradiance in optically pumped HF gas,” *Phys. Rev. Lett.*, vol. 30, pp. 309–312, 1973.

[1.6] R. Lehmberg, “Radiation from an N-atom system. I. General formalism,” *Phys. Rev. A*, vol. 2, no. 3, p. 883, 1970.

[1.7] A. D. Ludlow, M. M. Boyd, J. Ye, E. Peik, and P. O. Schmidt, “Optical atomic clocks,” *Rev. Mod. Phys.*, vol. 87, no. 2, p. 637, 2015.

[1.8] A. Ekert and R. Jozsa, “Quantum computation and Shor’s factoring algorithm,” *Rev. Mod. Phys.*, vol. 68, pp. 733–753, 1996.

[1.9] C. H. Bennett and D. P. DiVincenzo, “Quantum information and computation,” *nature*, vol. 404, no. 6775, p. 247, 2000.

[1.10] L. M. Duan, M. D. Lukin, J. I. Cirac, and P. Zoller, “Long-distance quantum communication with atomic ensembles and linear optics,” *Nature*, vol. 414, no. 6862, p. 413, 2001.

[1.11] B. M. Garraway, “The Dicke model in quantum optics: Dicke model revisited,” *Philos. Trans. A Math. Phys. Eng. Sci.*, vol. 369, no. 1939, pp. 1137–1155, 2011.

[1.12] E. Vetsch, D. Reitz, G. Sagué, R. Schmidt, S. T. Dawkins, and A. Rauschenbeutel, “Optical Interface Created by Laser-Cooled Atoms Trapped in the Evanescent Field Surrounding an Optical Nanofiber,” *Phys. Rev. Lett.*, vol. 104, p. 203603, 2010.

[1.13] M. Tavis and F. W. Cummings, “Exact Solution for an N-Molecule—Radiation-Field Hamiltonian,” *Phys. Rev.*, vol. 170, pp. 379–384, 1968.

[1.14] W. Guerin, M. O. Araújo, and R. Kaiser, “Subradiance in a large cloud of cold atoms,” *Phys. Rev. Lett.*, vol. 116, p. 083601, 2016.

[1.15] T. L. Nicholson, S. L. Campbell, R. B. Hutson, G. E. Marti, B. J. Bloom, R. L. McNally, W. Zhang, M. D. Barrett, M. S. Safronova, G. F. Strouse, W. L. Tew, and J. Ye, “Systematic evaluation of an atomic clock at 2×10^{-18} total uncertainty,” *Nat. Commun.*, vol. 6, p. 6896, 2015.

[1.16] E. Oelker, R. Hutson, C. Kennedy, L. Sonderhouse, T. Bothwell, A. Goban, D. Kedar, C. Sanner, J. Robinson, G. Marti, *et al.*, “Optical clock intercomparison with 6×10^{-19} precision in one hour,” *arXiv preprint arXiv:1902.02741*, 2019.

[1.17] L. Ostermann, H. Ritsch, and C. Genes, “Protected state enhanced quantum metrology,” *Phys. Rev. Lett.*, vol. 111, p. 123601, 2013.

[1.18] L. Ostermann, D. Plankensteiner, H. Ritsch, and C. Genes, “Protected subspace Ramsey spectroscopy,” *Phys. Rev. A*, vol. 90, p. 053823, 2014.

[1.19] J. Bezanson, A. Edelman, S. Karpinski, and V. B. Shah, “Julia: A fresh approach to numerical computing,” *SIAM Rev.*, vol. 59, no. 1, pp. 65–98, 2017.

References for Chapter 2

[2.1] R. Loudon, *The quantum theory of light.* OUP, 2000.

[2.2] C. Gardiner and P. Zoller, *The Quantum World of Ultra-Cold Atoms and Light Book I: Foundations of Quantum Optics.* ICP, 2014.

[2.3] C. Gerry, P. Knight, and P. L. Knight, *Introductory quantum optics.* CUP, 2005.

[2.4] R. Lehmberg, “Radiation from an N-atom system. I. General formalism,” *Phys. Rev. A*, vol. 2, no. 3, p. 883, 1970.

[2.5] J. D. Jackson, *Classical electrodynamics.* John Wiley & Sons, 2007.

[2.6] Y. W. Sokhotski, “On definite integrals and functions used in series expansions,” *St. Petersburg*, 1873.

[2.7] L. Ostermann, *Collective Radiation of Coupled Atomic Dipoles and the Precise Measurement of Time.* PhD thesis, University of Innsbruck, 2016.

[2.8] R. H. Dicke, “Coherence in spontaneous radiation processes,” *Phys. Rev.*, vol. 93, pp. 99–110, 1954.

[2.9] N. Skribanowitz, I. P. Herman, J. C. MacGillivray, and M. S. Feld, "Observation of Dicke superradiance in optically pumped HF gas," *Phys. Rev. Lett.*, vol. 30, pp. 309–312, 1973.

[2.10] C. Gardiner and P. Zoller, *Quantum noise: a handbook of Markovian and non-Markovian quantum stochastic methods with applications to quantum optics.* SSBM, 2004.

[2.11] Z. Ficek and R. Tanaś, "Entangled states and collective nonclassical effects in two-atom systems," *Phys. Rep.*, vol. 372, no. 5, pp. 369–443, 2002.

[2.12] M. Gross and S. Haroche, "Superradiance: An essay on the theory of collective spontaneous emission," *Phys. Rep.*, vol. 93, no. 5, pp. 301–396, 1982.

[2.13] H. Walther, B. T. H. Varcoe, B. Englert, and T. Becker, "Cavity quantum electrodynamics," *Rep. Prog. Phys.*, vol. 69, no. 5, pp. 1325–1382, 2006.

[2.14] E. T. Jaynes and F. W. Cummings, "Comparison of quantum and semiclassical radiation theories with application to the beam maser," *Proc. IEEE*, vol. 51, no. 1, pp. 89–109, 1963.

[2.15] M. Tavis and F. W. Cummings, "Exact Solution for an N-Molecule—Radiation-Field Hamiltonian," *Phys. Rev.*, vol. 170, pp. 379–384, 1968.

[2.16] A. L. Schawlow and C. H. Townes, "Infrared and Optical Masers," *Phys. Rev.*, vol. 112, pp. 1940–1949, 1958.

[2.17] M. Hamilton, K. Arnett, S. Smith, D. Elliott, M. Dziemballa, and P. Zoller, "Saturation of an optical transition by a phase-diffusing laser field," *Phys. Rev. A*, vol. 36, no. 1, p. 178, 1987.

[2.18] T. Haslwanter, H. Ritsch, J. Cooper, and P. Zoller, "Laser-noise-induced population fluctuations in two-and three-level systems," *Phys. Rev. A*, vol. 38, no. 11, p. 5652, 1988.

[2.19] L. Isserlis, "On a formula for the product-moment coefficient of any order of a normal frequency distribution in any number of variables," *Biometrika*, vol. 12, no. 1/2, pp. 134–139, 1918.

[2.20] S. M. Tan, "A computational toolbox for quantum and atomic optics," *J. Opt. B: Quantum Semiclassical Opt.*, vol. 1, no. 4, p. 424, 1999.

[2.21] A. Vukics and H. Ritsch, "C++ QED: an object-oriented framework for wave-function simulations of cavity QED systems," *Eur. Phys. J. D*, vol. 44, no. 3, p. 585, 2007.

[2.22] J. R. Johansson, P. D. Nation, and F. Nori, "QuTiP: An open-source Python framework for the dynamics of open quantum systems," *Comp. Phys. Comm.*, vol. 183, no. 8, pp. 1760–1772, 2012.

[2.23] J. Bezanson, S. Karpinski, V. B. Shah, and A. Edelman, "Julia: A fast dynamic language for technical computing," *arXiv preprint arXiv:1209.5145*, 2012.

[2.24] J. Bezanson, A. Edelman, S. Karpinski, and V. B. Shah, "Julia: A fresh approach to numerical computing," *SIAM Rev.*, vol. 59, no. 1, pp. 65–98, 2017.

[2.25] R. Dum, P. Zoller, and H. Ritsch, "Monte carlo simulation of the atomic master equation for spontaneous emission," *Physical Review A*, vol. 45, no. 7, p. 4879, 1992.

[2.26] K. Mølmer, Y. Castin, and J. Dalibard, "Monte Carlo wave-function method in quantum optics," *J. Opt. Soc. Am. B*, vol. 10, no. 3, pp. 524–538, 1993.

References for Chapter 3

[3.1] M. Lukin, "Colloquium: Trapping and manipulating photon states in atomic ensembles," *Rev. Mod. Phys.*, vol. 75, no. 2, p. 457, 2003.

[3.2] M. Lukin, M. Fleischhauer, R. Cote, L. Duan, D. Jaksch, J. Cirac, and P. Zoller, "Dipole blockade and quantum information processing in mesoscopic atomic ensembles," *Phys. Rev. Lett.*, vol. 87, no. 3, p. 037901, 2001.

[3.3] K. Hammerer, A. Sørensen, and E. Polzik, "Quantum interface between light and atomic ensembles," *Rev. Mod. Phys.*, vol. 82, no. 2, p. 1041, 2010.

[3.4] D. Wineland, J. Bollinger, W. Itano, F. Moore, and D. Heinzen, "Spin squeezing and reduced quantum noise in spectroscopy," *Phys. Rev. A*, vol. 46, no. 11, p. R6797, 1992.

[3.5] N. Sangouard, C. Simon, H. De Riedmatten, and N. Gisin, "Quantum repeaters based on atomic ensembles and linear optics," *Rev. Mod. Phys.*, vol. 83, no. 1, p. 33, 2011.

[3.6] I. Leroux, M. Schleier-Smith, and V. Vuletić, "Focus: Atomic clock beats the quantum limit," *Phys. Rev. Focus*, vol. 25, p. 24, 2010.

[3.7] E. Davies, *Quantum theory of open systems.* AP, 1976.

[3.8] C. Gardiner and P. Zoller, *Quantum noise: a handbook of Markovian and non-Markovian quantum stochastic methods with applications to quantum optics*, vol. 56. SSBM, 2004.

[3.9] K. Gheri, W. Alge, and P. Grangier, "Quantum analysis of the photonic blockade mechanism," *Phys. Rev. A*, vol. 60, no. 4, p. R2673, 1999.

[3.10] H. Zoubi and H. Ritsch, "Metastability and directional emission characteristics of excitons in 1D optical lattices," *Europhys. Lett.*, vol. 90, no. 2, p. 23001, 2010.

[3.11] R. Lehmberg, “Radiation from an N-atom system. I. General formalism,” *Phys. Rev. A*, vol. 2, no. 3, p. 883, 1970.

[3.12] H. Freedhoff, “Collective atomic effects in resonance fluorescence: Dipole-dipole interaction,” *Phys. Rev. A*, vol. 19, no. 3, p. 1132, 1979.

[3.13] B. Zhu, J. Restrepo, A. Rey, and M. Holland, “Quantum synchronization of ultracold atoms with dipole-dipole interactions in an optical lattice,” *Bull. APS*, vol. 59, 2014.

[3.14] H. Zoubi and H. Ritsch, “Bright and dark excitons in an atom-pair–filled optical lattice within a cavity,” *Europhys. Lett.*, vol. 82, no. 1, p. 14001, 2008.

[3.15] L. Ostermann, H. Ritsch, and C. Genes, “Protected state enhanced quantum metrology,” *Phys. Rev. Lett.*, vol. 111, p. 123601, 2013.

[3.16] L. Ostermann, D. Plankensteiner, H. Ritsch, and C. Genes, “Protected subspace Ramsey spectroscopy,” *Phys. Rev. A*, vol. 90, p. 053823, 2014.

[3.17] H. Zoubi and H. Ritsch, “Optical properties of collective excitations for an atomic chain with vacancies,” *Europhys. Lett. D*, vol. 66, no. 11, p. 292, 2012.

[3.18] A. Böttcher and B. Silbermann, *Introduction to large truncated Toeplitz matrices.* SSBM, 2012.

[3.19] R. Dicke, “Coherence in spontaneous radiation processes,” *Phys. Rev.*, vol. 93, no. 1, p. 99, 1954.

[3.20] H. Zoubi and H. Ritsch, “Excitons and cavity optical lattice ultracold atoms,” *Adv. Aom. Mol. Opt. Phy.*, vol. 62, p. 171, 2013.

[3.21] B. Bloom *et al.*, “An optical lattice clock with accuracy and stability at the 10^{-18} level,” *Nature*, vol. 506, pp. 71–75, 2014.

[3.22] I. Ushijima, M. Takamoto, M. Das, T. Ohkubo, and H. Katori, “Cryogenic optical lattice clocks,” *Nat. Photonics*, vol. 9, no. 3, p. 185, 2015.

[3.23] T. Maier, S. Krämer, L. Ostermann, and H. Ritsch, “A superradiant clock laser on a magic wavelength optical lattice,” *Opt. Express*, vol. 22, pp. 13269–13279, 2014.

[3.24] A. Sørensen and K. Mølmer, “Entanglement and extreme spin squeezing,” *Phys. Rev. Lett.*, vol. 86, no. 20, p. 4431, 2001.

[3.25] F. Haas, J. Volz, *et al.*, “Entangled states of more than 40 atoms in an optical fiber cavity,” *Science*, vol. 344, no. 6180, p. 180, 2014.

[3.26] R. McConnell, H. Zhang, *et al.*, “Entanglement with negative Wigner function of almost 3,000 atoms heralded by one photon,” *Nature*, vol. 519, no. 7544, p. 439, 2015.

[3.27] B. Olmos, D. Yu, Y. Singh, F. Schreck, K. Bongs, and I. Lesanovsky, “Long-range interacting many-body systems with alkaline-earth-metal atoms,” *Phys. Rev. Lett.*, vol. 110, no. 14, p. 143602, 2013.

[3.28] B. Ueberholz, S. Kuhr, D. Frese, V. Gomer, and D. Meschede, “Cold collisions in a high-gradient magneto-optical trap,” *J. Phys. B*, vol. 35, no. 23, p. 4899, 2002.

[3.29] S. Yoon, Y. Choi, S. Park, W. Ji, J. H. Lee, and K. An, “Characteristics of single-atom trapping in a magneto-optical trap with a high magnetic-field gradient,” in *J. Phys. Conf. Ser.*, vol. 80, p. 012046, IOP Publishing, 2007.

[3.30] B. Yan, S. A. Moses, B. Gadway, J. P. Covey, K. R. Hazzard, A. M. Rey, D. S. Jin, and J. Ye, “Observation of dipolar spin-exchange interactions with lattice-confined polar molecules,” *Nature*, vol. 501, no. 7468, pp. 521–525, 2013.

[3.31] P. Neumann, R. Kolesov, B. Naydenov, J. Beck, F. Rempp, M. Steiner, V. Jacques, G. Balasubramanian, M. Markham, D. Twitchen, *et al.*, “Quantum register based on coupled electron spins in a room-temperature solid,” *Nat. Phys.*, vol. 6, no. 4, pp. 249–253, 2010.

[3.32] H. Zoubi and H. Ritsch, “Hybrid quantum system of a nanofiber mode coupled to two chains of optically trapped atoms,” *New J. Phys.*, vol. 12, no. 10, p. 103014, 2010.

[3.33] D. Meiser and M. Holland, “Steady-state superradiance with alkaline-earth-metal atoms,” *Phys. Rev. A*, vol. 81, no. 3, p. 033847, 2010.

[3.34] K. Sandner, H. Ritsch, R. Amsüss, C. Koller, T. Nöbauer, S. Putz, J. Schmiedmayer, and J. Majer, “Strong magnetic coupling of an inhomogeneous nitrogen-vacancy ensemble to a cavity,” *Phys. Rev. A*, vol. 85, p. 053806, 2010.

[3.35] K. Lalumière, B. C. Sanders, A. F. van Loo, A. Fedorov, A. Wallraff, and A. Blais, “Input-output theory for waveguide QED with an ensemble of inhomogeneous atoms,” *Phys. Rev. A*, vol. 88, p. 043806, 2013.

[3.36] J. Johansson, P. Nation, and F. Nori, “Qutip 2: A Python framework for the dynamics of open quantum systems,” *Comput. Phys. Commun.*, vol. 184, no. 4, p. 1234, 2013.

References for Chapter 4

[4.1] I. Bloch, J. Dalibard, and W. Zwerger, “Many-body physics with ultracold gases,” *Rev. Mod. Phys.*, vol. 80, no. 3, p. 885, 2008.

[4.2] M. Lewenstein, A. Sanpera, V. Ahufinger, B. Damski, A. Sen, and U. Sen, “Ultracold atomic gases in optical lattices: mimicking condensed matter physics and beyond,” *Adv. Phys.*, vol. 56, no. 2, pp. 243–379, 2007.

[4.3] H. Katori, "Optical lattice clocks and quantum metrology," *Nat. Phot.*, vol. 5, no. 4, pp. 203–210, 2011.

[4.4] A. D. Ludlow, M. M. Boyd, J. Ye, E. Peik, and P. O. Schmidt, "Optical atomic clocks," *Rev. Mod. Phys.*, vol. 87, no. 2, p. 637, 2015.

[4.5] T. L. Nicholson, S. L. Campbell, R. B. Hutson, G. E. Marti, B. J. Bloom, R. L. McNally, W. Zhang, M. D. Barrett, M. S. Safronova, G. F. Strouse, W. L. Tew, and J. Ye, "Systematic evaluation of an atomic clock at 2×10^{-18} total uncertainty," *Nat. Commun.*, vol. 6, p. 6896, 2015.

[4.6] R. H. Dicke, "Coherence in spontaneous radiation processes," *Phys. Rev.*, vol. 93, pp. 99–110, 1954.

[4.7] Z. Ficek and R. Tanaś, "Entangled states and collective nonclassical effects in two-atom systems," *Phys. Rep.*, vol. 372, no. 5, pp. 369 – 443, 2002.

[4.8] D. E. Chang, J. Ye, and M. D. Lukin, "Controlling dipole-dipole frequency shifts in a lattice-based optical atomic clock," *Phys. Rev. A*, vol. 69, no. 2, p. 023810, 2004.

[4.9] L. Ostermann, H. Ritsch, and C. Genes, "Protected state enhanced quantum metrology with interacting two-level ensembles," *Phys. Rev. Lett.*, vol. 111, p. 123601, 2013.

[4.10] L. Ostermann, D. Plankensteiner, H. Ritsch, and C. Genes, "Protected subspace ramsey spectroscopy," *Phys. Rev. A*, vol. 90, p. 053823, 2014.

[4.11] G. J. Dick, "Local oscillator induced instabilities in trapped ion frequency standards," *Proc. 19th Precise Time and Time Interval Meeting*, 1987.

[4.12] C. Wieman and T. W. Hänsch, "Doppler-free laser polarization spectroscopy," *Phys. Rev. Lett.*, vol. 36, no. 20, p. 1170, 1976.

[4.13] M. W. Hamilton, K. Arnett, S. J. Smith, D. S. Elliott, M. Dziemballa, and P. Zoller, "Saturation of an optical transition by a phase-diffusing laser field," *Phys. Rev. A*, vol. 36, pp. 178–188, 1987.

[4.14] T. Haslwanter, H. Ritsch, J. Cooper, and P. Zoller, "Laser-noise-induced population fluctuations in two-and three-level systems," *Phys. Rev. A*, vol. 38, no. 11, p. 5652, 1988.

[4.15] J. Jeske, J. H. Cole, and S. F. Huelga, "Quantum metrology subject to spatially correlated markovian noise: restoring the heisenberg limit," *New J. Phys.*, vol. 16, no. 7, p. 073039, 2014.

[4.16] K. Macieszczak, M. Fraas, and R. Demkowicz-Dobrzański, "Bayesian quantum frequency estimation in presence of collective dephasing," *New J. Phys.*, vol. 16, no. 11, p. 113002, 2014.

[4.17] R. Chaves, J. Brask, M. Markiewicz, J. Kołodyński, and A. Acín, "Noisy metrology beyond the standard quantum limit," *Phys. Rev. Lett.*, vol. 111, no. 12, p. 120401, 2013.

[4.18] J. B. Brask, R. Chaves, and J. Kołodyński, "Improved quantum magnetometry beyond the standard quantum limit," *Phys. Rev. X*, vol. 5, no. 3, p. 031010, 2015.

[4.19] S. I. Knysh, E. H. Chen, and G. A. Durkin, "True limits to precision via unique quantum probe," *arXiv preprint arXiv:1402.0495*, 2014.

[4.20] P. Szańkowski, M. Trippenbach, and J. Chwedeńczuk, "Parameter estimation in memory-assisted noisy quantum interferometry," *Phys. Rev. A*, vol. 90, no. 6, p. 063619, 2014.

[4.21] U. Dorner, "Quantum frequency estimation with trapped ions and atoms," *New J. Phys.*, vol. 14, no. 4, p. 043011, 2012.

[4.22] K. Hammerer, M. Aspelmeyer, E. S. Polzik, and P. Zoller, "Establishing einstein-poldosky-rosen channels between nanomechanics and atomic ensembles," *Phys. Rev. Lett.*, vol. 102, p. 020501, 2009.

[4.23] M. Tsang and C. M. Caves, "Coherent quantum-noise cancellation for optomechanical sensors," *Phys. Rev. Lett.*, vol. 105, p. 123601, 2010.

[4.24] M. Tsang and C. M. Caves, "Evading quantum mechanics: Engineering a classical subsystem within a quantum environment," *Phys. Rev. X*, vol. 2, p. 031016, 2012.

[4.25] M. H. Wimmer, D. Steinmeyer, K. Hammerer, and M. Heurs, "Coherent cancellation of backaction noise in optomechanical force measurements," *Phys. Rev. A*, vol. 89, p. 053836, 2014.

[4.26] E. S. Polzik and K. Hammerer, "Trajectories without quantum uncertainties," *Ann. Phys.*, vol. 527, pp. A15–A20, 2015.

[4.27] W. Wasilewski, K. Jensen, H. Krauter, J. J. Renema, M. V. Balabas, and E. S. Polzik, "Quantum noise limited and entanglement-assisted magnetometry," *Phys. Rev. Lett.*, vol. 104, p. 133601, 2010.

[4.28] M. J. Woolley and A. A. Clerk, "Two-mode back-action-evading measurements in cavity optomechanics," *Phys. Rev. A*, vol. 87, p. 063846, 2013.

[4.29] K. Zhang, P. Meystre, and W. Zhang, "Back-action-free quantum optomechanics with negative-mass bose-einstein condensates," *Phys. Rev. A*, vol. 88, p. 043632, 2013.

[4.30] A. Motazedifard, F. Bemani, M. H. Naderi, R. Roknizadeh, and D. Vitali, "Force sensing based on coherent quantum noise cancellation in a hybrid optomechanical cavity with squeezed-vacuum injection," *arXiv:1603.09399*, 2016.

[4.31] T. L. Nicholson, M. J. Martin, J. R. Williams, B. J. Bloom, M. Bishof, M. D. Swallows, S. L. Campbell, and J. Ye, "Comparison of two independent sr optical clocks with $1{\times}10^{-17}$ stability at 10^3 s," *Phys. Rev. Lett.*, vol. 109, p. 230801, 2012.

[4.32] N. F. Ramsey, "A molecular beam resonance method with separated oscillating fields," *Phys. Rev.*, vol. 78, pp. 695–699, 1950.

[4.33] D. J. Wineland, J. J. Bollinger, W. M. Itano, and D. J. Heinzen, "Squeezed atomic states and projection noise in spectroscopy," *Phys. Rev. A*, vol. 50, pp. 67–88, 1994.

[4.34] J. Johansson, P. Nation, and F. Nori, "Qutip 2: A Python framework for the dynamics of open quantum systems," *Comput. Phys. Commun.*, vol. 184, no. 4, p. 1234, 2013.

[4.35] R. Graham and H. Haken, "Laserlight—first example of a second-order phase transition far away from thermal equilibrium," *Z. Phys.*, vol. 237, no. 1, pp. 31–46, 1970.

[4.36] C. W. Gardiner, *Handbook of stochastic methods.* Springer Berlin, 1985.

References for Chapter 5

[5.1] S. Haroche and D. Kleppner, "Cavity Quantum Electrodynamics," *Phys. Today*, vol. 42, no. 1, pp. 24–30, 1989.

[5.2] H. Walther, B. T. Varcoe, B. Englert, and T. Becker, "Cavity Quantum Electrodynamics," *Rep. Prog. Phys.*, vol. 69, no. 5, p. 1325, 2006.

[5.3] H. J. Kimble, "Strong interactions of single atoms and photons in cavity QED," *Phys. Scripta*, vol. 1998, no. T76, p. 127, 1998.

[5.4] K. M. Birnbaum *et al.*, "Photon blockade in an optical cavity with one trapped atom," *Nature*, vol. 436, no. 7047, pp. 87–90, 2005.

[5.5] T. Yoshie *et al.*, "Vacuum Rabi splitting with a single quantum dot in a photonic crystal nanocavity," *Nature*, vol. 432, no. 7014, pp. 200–203, 2004.

[5.6] J. Casanova, G. Romero, I. Lizuain, J. J. García-Ripoll, and E. Solano, "Deep strong coupling regime of the jaynes-cummings model," *Phys. Rev. Lett.*, vol. 105, p. 263603, 2010.

[5.7] V. Vuletić, H. W. Chan, and A. T. Black, "Three-dimensional cavity Doppler cooling and cavity sideband cooling by coherent scattering," *Phys. Rev. A*, vol. 64, no. 3, p. 033405, 2001.

[5.8] D. Plankensteiner, L. Ostermann, H. Ritsch, and C. Genes, "Selective protected state preparation of coupled dissipative quantum emitters," *Sci. Rep.*, vol. 5, p. 16231, 2015.

[5.9] R. J. Bettles, S. A. Gardiner, and C. S. Adams, “Cooperative ordering in lattices of interacting two-level dipoles,” *Phys. Rev. A*, vol. 92, p. 063822, 2015.

[5.10] R. J. Bettles, S. A. Gardiner, and C. S. Adams, “Cooperative eigenmodes and scattering in one-dimensional atomic arrays,” *Phys. Rev. A*, vol. 94, p. 043844, 2016.

[5.11] R. J. Bettles, S. A. Gardiner, and C. S. Adams, “Enhanced optical cross section via collective coupling of atomic dipoles in a 2D array,” *Phys. Rev. Lett.*, vol. 116, p. 103602, 2016.

[5.12] E. Shahmoon, D. S. Wild, M. D. Lukin, and S. F. Yelin, “Cooperative resonances in light scattering from two-dimensional atomic arrays,” *arxiv:1610.00138*, 2016.

[5.13] J. Perczel, J. Borregaard, D. Chang, H. Pichler, S. F. Yelin, P. Zoller, and M. D. Lukin, “Topological quantum optics in two-dimensional atomic arrays,” *arXiv:1703.04849*, 2017.

[5.14] A. Asenjo-Garcia, M. Moreno-Cardoner, A. Albrecht, H. J. Kimble, and D. E. Chang, “Exponential improvement in photon storage fidelities using subradiance and ”selective radiance” in atomic arrays,” *arXiv:1703.03382*, 2017.

[5.15] R. H. Dicke, “Coherence in spontaneous radiation processes,” *Phys. Rev.*, vol. 93, pp. 99–110, 1954.

[5.16] M. Gross and S. Haroche, “Superradiance: An essay on the theory of collective spontaneous emission,” *Phys. Rep.*, vol. 93, no. 5, pp. 301 – 396, 1982.

[5.17] H. Zoubi and H. Ritsch, “Bright and dark excitons in an atom-pair–filled optical lattice within a cavity,” *Europhys. Lett.*, vol. 82, no. 1, p. 14001, 2008.

[5.18] C. Sames, H. Chibani, C. Hamsen, P. A. Altin, T. Wilk, and G. Rempe, “Antiresonance phase shift in strongly coupled cavity QED,” *Phys. Rev. Lett.*, vol. 112, p. 043601, 2014.

[5.19] P. R. Rice and R. J. Brecha, “Cavity induced transparency,” *Opt. Commun.*, vol. 126, no. 4–6, pp. 230 – 235, 1996.

[5.20] R. Lehmberg, “Radiation from an N-atom system. I. General formalism,” *Phys. Rev. A*, vol. 2, no. 3, p. 883, 1970.

[5.21] C. Gardiner and P. Zoller, *Quantum noise: a handbook of Markovian and non-Markovian quantum stochastic methods with applications to quantum optics*, vol. 56. SSBM, 2004.

[5.22] P. M. Alsing, D. A. Cardimona, and H. J. Carmichael, “Suppression of fluorescence in a lossless cavity,” *Phys. Rev. A*, vol. 45, pp. 1793–1803, 1992.

[5.23] S. Zippilli, G. Morigi, and H. Ritsch, “Suppression of Bragg scattering by collective interference of spatially ordered atoms with a high-Q cavity mode,” *Phys. Rev. Lett.*, vol. 93, no. 12, p. 123002, 2004.

[5.24] L. Ostermann, D. Plankensteiner, H. Ritsch, and C. Genes, “Protected subspace Ramsey spectroscopy,” *Phys. Rev. A*, vol. 90, p. 053823, 2014.

[5.25] E. Mascarenhas, D. Gerace, M. F. Santos, and A. Auffèves, “Cooperativity of a few quantum emitters in a single-mode cavity,” *Phys. Rev. A*, vol. 88, p. 063825, 2013.

[5.26] S. D. Jenkins and J. Ruostekoski, “Controlled manipulation of light by cooperative response of atoms in an optical lattice,” *Phys. Rev. A*, vol. 86, p. 031602, 2012.

[5.27] S. D. Jenkins and J. Ruostekoski, “Metamaterial transparency induced by cooperative electromagnetic interactions,” *Phys. Rev. Lett.*, vol. 111, p. 147401, 2013.

[5.28] M. L. Juan, G. Molina-Terriza, T. Volz, and O. Romero-Isart, “Near-field levitated quantum optomechanics with nanodiamonds,” *Phys. Rev. A*, vol. 94, p. 023841, 2016.

[5.29] A. Dantan, B. Nair, G. Pupillo, and C. Genes, “Hybrid cavity mechanics with doped systems,” *Phys. Rev. A*, vol. 90, no. 3, p. 033820, 2014.

[5.30] S. D. Jenkins, J. Ruostekoski, N. Papasimakis, S. Savo, and N. I. Zheludev, “Many-body subradiant excitations in metamaterial arrays: Experiment and theory,” *arXiv preprint arXiv:1611.01509*, 2016.

[5.31] J. D. Hunter, “Matplotlib: A 2D graphics environment,” *Comput. Sci. Eng.*, vol. 9, no. 3, pp. 90–95, 2007.

References for Chapter 6

[6.1] E. M. Purcell, “Spontaneous emission probabilities at radio frequencies,” *Phys. Rev.*, vol. 69, p. 681, 1946.

[6.2] F. De Martini, G. Innocenti, G. R. Jacobovitz, and P. Mataloni, “Anomalous spontaneous emission time in a microscopic optical cavity,” *Phys. Rev. Lett.*, vol. 59, no. 26, p. 2955, 1987.

[6.3] A. Kreuter, C. Becher, G. P. T. Lancaster, A. B. Mundt, C. Russo, H. Häffner, C. Roos, J. Eschner, F. Schmidt-Kaler, and R. Blatt, “Spontaneous emission lifetime of a single trapped Ca+ ion in a high finesse cavity,” *Phys. Rev. Lett.*, vol. 92, no. 20, p. 203002, 2004.

[6.4] A. Haase, B. Hessmo, and J. Schmiedmayer, “Detecting magnetically guided atoms with an optical cavity,” *Opt. Lett.*, vol. 31, no. 2, pp. 268–270, 2006.

[6.5] D. Wang, H. Kelkar, D. Martin-Cano, D. Rattenbacher, A. Shkarin, T. Utikal, S. Götzinger, and V. Sandoghdar, “Turning a molecule into a coherent two-level quantum system,” *Nat. Phys.*, p. 1, 2019.

[6.6] E. Orgiu, J. George, J. Hutchison, E. Devaux, J. F. Dayen, B. Doudin, F. F. Stellacci, C. Genet, J. Schachenmayer, C. Genes, G. Pupillo, P. Samori, and T. W. Ebbesen, “Conductivity in organic semiconductors hybridized with the vacuum field,” *Nat. Mater.*, vol. 14, pp. 1123 – 1129, 2015.

[6.7] J. Schachenmayer, C. Genes, E. Tignone, and G. Pupillo, “Cavity-enhanced transport of excitons,” *Phys. Rev. Lett.*, vol. 114, p. 196403, 2015.

[6.8] J. Feist and F. J. Garcia-Vidal, “Extraordinary exciton conductance induced by strong coupling,” *Phys. Rev. Lett.*, vol. 114, p. 196402, 2015.

[6.9] D. Hagenmüller, J. Schachenmayer, S. Schütz, C. Genes, and G. Pupillo, “Cavity-enhanced transport of charge,” *Phys. Rev. Lett.*, vol. 119, p. 223601, 2017.

[6.10] D. Hagenmüller, S. Schütz, J. Schachenmayer, C. Genes, and G. Pupillo, “Cavity-assisted mesoscopic transport of fermions: Coherent and dissipative dynamics,” *Phys. Rev. B*, vol. 97, p. 205303, 2018.

[6.11] X. Zhong, T. Chervy, S. Wang, J. George, A. Thomas, J. Hutchinson, E. Devaux, C. Genet, and T. W. Ebbesen, “Non-radiative energy transfer mediated by hybrid light-matter states,” *Angew. Chem.*, vol. 55, no. 21, p. 6202, 2016.

[6.12] X. Zhong, T. Chervy, L. Zhang, A. Thomas, J. George, C. Genet, J. Hutchinson, and T. W. Ebbesen, “Energy transfer between spatially separated entangled molecules,” *Angew. Chem.*, vol. 56, p. 9034, 2017.

[6.13] J. A. Hutchison, T. Schwartz, C. Genet, E. Devaux, and T. W. Ebbesen, “Modifying chemical landscapes by coupling to vacuum fields,” *Angew. Chem. Int. Ed.*, vol. 51, no. 7, pp. 1592–1596, 2012.

[6.14] F. G.-V. J. Galego and J. Feist, “Suppressing photochemical reactions with quantized light fields,” *Nat. Commun.*, vol. 7, p. 13841, 2017.

[6.15] D. Plankensteiner, C. Sommer, H. Ritsch, and C. Genes, “Cavity antiresonance spectroscopy of dipole coupled subradiant arrays,” *Phys. Rev. Lett.*, vol. 119, no. 9, p. 093601, 2017.

[6.16] P. R. Rice and R. J. Brecha, “Cavity induced transparency,” *Opt. Commun.*, vol. 126, no. 4–6, pp. 230 – 235, 1996.

[6.17] C. Sames, H. Chibani, C. Hamsen, P. A. Altin, T. Wilk, and G. Rempe, “Antiresonance phase shift in strongly coupled cavity QED,” *Phys. Rev. Lett.*, vol. 112, p. 043601, 2014.

[6.18] D. Wang, H. Kelkar, D. Martin-Cano, T. Utikal, S. Götzinger, and V. Sandoghdar, "Coherent coupling of a single molecule to a scanning Fabry-Perot microcavity," *Phys. Rev. X*, vol. 7, p. 021014, 2017.

[6.19] J. Pellegrino, R. Bourgain, S. Jennewein, Y. R. P. Sortais, A. Browaeys, S. D. Jenkins, and J. Ruostekoski, "Observation of suppression of light scattering induced by dipole-dipole interactions in a cold-atom ensemble," *Phys. Rev. Lett.*, vol. 113, p. 133602, 2014.

[6.20] R. J. Bettles, S. A. Gardiner, and C. S. Adams, "Cooperative ordering in lattices of interacting two-level dipoles," *Phys. Rev. A*, vol. 92, p. 063822, 2015.

[6.21] R. J. Bettles, S. A. Gardiner, and C. S. Adams, "Cooperative eigenmodes and scattering in one-dimensional atomic arrays," *Phys. Rev. A*, vol. 94, p. 043844, 2016.

[6.22] R. J. Bettles, S. A. Gardiner, and C. S. Adams, "Enhanced optical cross section via collective coupling of atomic dipoles in a 2D array," *Phys. Rev. Lett.*, vol. 116, p. 103602, 2016.

[6.23] E. Shahmoon, D. S. Wild, M. D. Lukin, and S. F. Yelin, "Cooperative resonances in light scattering from two-dimensional atomic arrays," *Phys. Rev. Lett.*, vol. 118, p. 113601, 2017.

[6.24] J. Perczel, J. Borregaard, D. E. Chang, H. Pichler, S. F. Yelin, P. Zoller, and M. D. Lukin, "Topological quantum optics in two-dimensional atomic arrays," *Phys. Rev. Lett.*, vol. 119, p. 023603, 2017.

[6.25] S. D. Jenkins and J. Ruostekoski, "Metamaterial transparency induced by cooperative electromagnetic interactions," *Phys. Rev. Lett.*, vol. 111, p. 147401, 2013.

[6.26] T. Botter, D. W. C. Brooks, S. Schreppler, N. Brahms, and D. M. Stamper-Kurn, "Optical readout of the quantum collective motion of an array of atomic ensembles," *Phys. Rev. Lett.*, vol. 110, p. 153001, 2013.

[6.27] E. Shahmoon, M. D. Lukin, and S. F. Yelin, "Collective motion of an atom array under laser illumination," *arXiv:1810.01063*, 2018.

[6.28] E. Shahmoon, M. D. Lukin, and S. F. Yelin, "Quantum optomechanics of a two-dimensional atomic array," *arXiv:1810.01052*, 2018.

[6.29] H. Habibian, S. Zippilli, and G. Morigi, "Quantum light by atomic arrays in optical resonators," *Phys. Rev. A*, vol. 84, p. 033829, 2011.

[6.30] D. S. Wild, E. Shahmoon, S. F. Yelin, and M. D. Lukin, "Quantum nonlinear optics in atomically thin materials," *Phys. Rev. Lett.*, vol. 121, p. 123606, 2018.

[6.31] D. Plankensteiner, L. Ostermann, H. Ritsch, and C. Genes, “Selective protected state preparation of coupled dissipative quantum emitters,” *Sci. Rep.*, vol. 5, p. 16231, 2015.

[6.32] G. Facchinetti, S. D. Jenkins, and J. Ruostekoski, “Storing light with subradiant correlations in arrays of atoms,” *Phys. Rev. Lett.*, vol. 117, p. 243601, 2016.

[6.33] R. Lehmberg, “Radiation from an N-atom system. I. General formalism,” *Phys. Rev. A*, vol. 2, no. 3, p. 883, 1970.

[6.34] P. M. Alsing, D. A. Cardimona, and H. J. Carmichael, “Suppression of fluorescence in a lossless cavity,” *Phys. Rev. A*, vol. 45, pp. 1793–1803, 1992.

[6.35] S. Zippilli, G. Morigi, and H. Ritsch, “Suppression of Bragg scattering by collective interference of spatially ordered atoms with a high-Q cavity mode,” *Phys. Rev. Lett.*, vol. 93, no. 12, p. 123002, 2004.

[6.36] Q. Xu and K. Mølmer, “Intensity correlations near a cavity QED antiresonance,” *J. Phys. B*, vol. 50, no. 3, p. 035502, 2017.

[6.37] H. Zoubi and H. Ritsch, “Bright and dark excitons in an atom-pair–filled optical lattice within a cavity,” *Europhys. Lett.*, vol. 82, no. 1, p. 14001, 2008.

[6.38] H. H. Jen, “Directional subradiance from helical-phase-imprinted multiphoton states,” *Sci. Rep.*, vol. 8, no. 1, p. 7163, 2018.

[6.39] R. H. Dicke, “Coherence in spontaneous radiation processes,” *Phys. Rev.*, vol. 93, pp. 99–110, 1954.

[6.40] M. Hebenstreit, B. Kraus, L. Ostermann, and H. Ritsch, “Subradiance via entanglement in atoms with several independent decay channels,” *Phys. Rev. Lett.*, vol. 118, no. 14, p. 143602, 2017.

[6.41] M. B. Plenio, “Logarithmic negativity: a full entanglement monotone that is not convex,” *Phys. Rev. Lett.*, vol. 95, no. 9, p. 090503, 2005.

[6.42] L. Ostermann, D. Plankensteiner, H. Ritsch, and C. Genes, “Protected subspace Ramsey spectroscopy,” *Phys. Rev. A*, vol. 90, p. 053823, 2014.

[6.43] A. Asenjo-Garcia, M. Moreno-Cardoner, A. Albrecht, H. J. Kimble, and D. E. Chang, “Exponential improvement in photon storage fidelities using subradiance and “selective radiance” in atomic arrays,” *Phys. Rev. X*, vol. 7, no. 3, p. 031024, 2017.

[6.44] J. D. Hunter, “Matplotlib: A 2D graphics environment,” *Comput. Sci. Eng.*, vol. 9, no. 3, pp. 90–95, 2007.

[6.45] S. Krämer, D. Plankensteiner, L. Ostermann, and H. Ritsch, “Quantumoptics.jl: A Julia framework for simulating open quantum systems,” *Comput. Phys. Commun.*, vol. 227, pp. 109–116, 2018.

[6.46] C. Gardiner and P. Zoller, *Quantum noise: a handbook of Markovian and non-Markovian quantum stochastic methods with applications to quantum optics*, vol. 56. SSBM, 2004.

References for Chapter 7

[7.1] R. Lehmberg, “Radiation from an N-atom system. I. General formalism,” *Phys. Rev. A*, vol. 2, no. 3, p. 883, 1970.

[7.2] M. Gross and S. Haroche, “Superradiance: An essay on the theory of collective spontaneous emission,” *Phys. Rep.*, vol. 93, no. 5, pp. 301 – 396, 1982.

[7.3] H. Zoubi and H. Ritsch, “Bright and dark excitons in an atom-pair–filled optical lattice within a cavity,” *Europhys. Lett.*, vol. 82, no. 1, p. 14001, 2008.

[7.4] A. Asenjo-Garcia, M. Moreno-Cardoner, A. Albrecht, H. J. Kimble, and D. E. Chang, “Exponential improvement in photon storage fidelities using subradiance and ”selective radiance” in atomic arrays,” *Phys. Rev. X*, vol. 7, p. 031024, 2017.

[7.5] S. D. Jenkins, J. Ruostekoski, N. Papasimakis, S. Savo, and N. I. Zheludev, “Many-body subradiant excitations in metamaterial arrays: Experiment and theory,” *arXiv preprint arXiv:1611.01509*, 2016.

[7.6] M. O. Scully, “Collective lamb shift in single photon dicke superradiance,” *Phys. Rev. Lett.*, vol. 102, no. 14, p. 143601, 2009.

[7.7] D. Plankensteiner, L. Ostermann, H. Ritsch, and C. Genes, “Selective protected state preparation of coupled dissipative quantum emitters,” *Sci. Rep.*, vol. 5, p. 16231, 2015.

[7.8] H. Zoubi and H. Ritsch, “Optical properties of collective excitations for an atomic chain with vacancies,” *The European Physical Journal D*, vol. 66, no. 11, p. 292, 2012.

[7.9] L. Ostermann, H. Zoubi, and H. Ritsch, “Cascaded collective decay in regular arrays of cold trapped atoms,” *Optics express*, vol. 20, no. 28, pp. 29634–29645, 2012.

[7.10] W. Guerin, M. O. Araújo, and R. Kaiser, “Subradiance in a large cloud of cold atoms,” *Phys. Rev. Lett.*, vol. 116, no. 8, p. 083601, 2016.

[7.11] H. Zoubi and H. Ritsch, “Metastability and directional emission characteristics of excitons in 1d optical lattices,” *Europhys. Lett.*, vol. 90, no. 2, p. 23001, 2010.

[7.12] H. Zoubi and H. Ritsch, “Hybrid quantum system of a nanofiber mode coupled to two chains of optically trapped atoms,” *New Journal of Physics*, vol. 12, no. 10, p. 103014, 2010.

[7.13] L. Ostermann, C. Meignant, C. Genes, and H. Ritsch, “Super-and subradiance of clock atoms in multimode optical waveguides,” *arXiv preprint arXiv:1811.05851*, 2018.

[7.14] M. L. Brongersma, J. W. Hartman, and H. A. Atwater, “Electromagnetic energy transfer and switching in nanoparticle chain arrays below the diffraction limit,” *Phys. Rev. B*, vol. 62, no. 24, p. R16356, 2000.

[7.15] A. Serafini, S. Mancini, and S. Bose, “Distributed quantum computation via optical fibers,” *Phys. Rev. Lett.*, vol. 96, no. 1, p. 010503, 2006.

[7.16] R. E. Blankenship, *Molecular mechanisms of photosynthesis.* John Wiley & Sons, 2014.

[7.17] N. Nelson and A. Ben-Shem, “The complex architecture of organice photosynthesis,” *Nat. Rev. Mol. Cell Biol.*, vol. 6, no. 10, p. 818, 2005.

[7.18] R. J. Cogdell, A. Gall, and J. Köhler, “The architecture and function of the light-harvesting apparatus of purple bacteria: from single molecules to in vivo membranes,” *Q. Rev. Biophys.*, vol. 39, no. 3, pp. 227–324, 2006.

[7.19] G. S. Engel, T. R. Calhoun, E. L. Read, T. Ahn, T. Manal, Y.-C. Cheng, R. E. Blankenship, and G. R. Fleming, “Evidence for wavelike energy transfer through quantum coherence in photosynthetic systems,” *Nature*, vol. 446, pp. 782–786, 2007.

[7.20] G. Panitchayangkoon, D. V. Voronine, D. Abramavicius, J. R. Caram, N. H. C. Lewis, S. Mukamel, and G. S. Engel, “Direct evidence of quantum transport in photosynthetic light-harvesting complexes.,” *Proc. Natl. Acad. Sci. U.S.A.*, vol. 108 52, pp. 20908–12, 2011.

[7.21] A. Asenjo-Garcia, J. D. Hood, D. E. Chang, and H. J. Kimble, “Atom-light interactions in quasi-1d nanostructures: a green’s function perspective,” *Phys. Rev. A*, vol. 95, p. 033818, 2017.

[7.22] R. H. Dicke, “Coherence in spontaneous radiation processes,” *Phys. Rev.*, vol. 93, pp. 99–110, 1954.

[7.23] M. Hebenstreit, B. Kraus, L. Ostermann, and H. Ritsch, “Subradiance via entanglement in atoms with several independent decay channels,” *Phys. Rev. Lett.*, vol. 118, no. 14, p. 143602, 2017.

[7.24] S. Krämer, D. Plankensteiner, L. Ostermann, and H. Ritsch, “Quantumoptics.jl: A Julia framework for simulating open quantum systems,” *Comput. Phys. Commun.*, vol. 227, pp. 109–116, 2018.

[7.25] P.-O. Guimond, A. Grankin, D. Vasilyev, B. Vermersch, and P. Zoller, “Subradiant EPR states in distant atomic arrays,” *arXiv preprint arXiv:1901.02665*, 2019.

References for Chapter 8

[8.1] S. M. Tan, "A computational toolbox for quantum and atomic optics," *J. Opt. B: Quantum Semiclassical Opt.*, vol. 1, no. 4, p. 424, 1999.

[8.2] A. Vukics and H. Ritsch, "C++ QED: an object-oriented framework for wave-function simulations of cavity QED systems," *Eur. Phys. J. D*, vol. 44, no. 3, p. 585, 2007.

[8.3] R. Schack and T. A. Brun, "A C++ library using quantum trajectories to solve quantum master equations," *Comp. Phys. Comm.*, vol. 102, no. 1-3, pp. 210–228, 1997.

[8.4] J. R. Johansson, P. D. Nation, and F. Nori, "QuTiP: An open-source Python framework for the dynamics of open quantum systems," *Comp. Phys. Comm.*, vol. 183, no. 8, pp. 1760–1772, 2012.

[8.5] J. R. Johansson, P. D. Nation, and F. Nori, "QuTiP 2: A Python framework for the dynamics of open quantum systems," *Comp. Phys. Comm.*, vol. 184, no. 4, pp. 1234–1240, 2013.

[8.6] S. Behnel, R. Bradshaw, C. Citro, L. Dalcin, D. Seljebotn, and K. Smith, "Cython: The best of both worlds," *Comput. Sci. Eng.*, vol. 13, no. 2, pp. 31 –39, 2011.

[8.7] J. Bezanson, S. Karpinski, V. B. Shah, and A. Edelman, "Julia: A fast dynamic language for technical computing," *arXiv preprint arXiv:1209.5145*, 2012.

[8.8] J. Bezanson, A. Edelman, S. Karpinski, and V. B. Shah, "Julia: A fresh approach to numerical computing," *SIAM Rev.*, vol. 59, no. 1, pp. 65–98, 2017.

[8.9] "Homepage of PyPy." https://pypy.org/. Accessed: July 10, 2019.

[8.10] S. K. Lam, A. Pitrou, and S. Seibert, "Numba: A LLVM-based Python JIT Compiler," in *Proceedings of the Second Workshop on the LLVM Compiler Infrastructure in HPC*, LLVM '15, pp. 7:1–7:6, ACM, 2015.

[8.11] "The Julia Language." https://julialang.org. Accessed: July 10, 2019.

[8.12] J. H. Eberly, N. B. Narozhny, and J. J. Sanchez-Mondragon, "Periodic spontaneous collapse and revival in a simple quantum model," *Phys. Rev. Lett.*, vol. 44, pp. 1323–1326, 1980.

[8.13] "GitHub repository for QuantumOptics.jl." https://github.com/qojulia/QuantumOptics.jl. Accessed: July 10, 2019.

[8.14] "GitHub repository for the documentation of QuantumOptics.jl." https://github.com/qojulia/QuantumOptics.jl-documentation. Accessed: July 10, 2019.

[8.15] "Homepage of QuantumOptics.jl." http://qojulia.org/. Accessed: July 10, 2019.

[8.16] “GitHub repository for benchmarks of QuantumOptics.jl, QuTiP and the MATLAB QO Toolbox.” https://github.com/qojulia/QuantumOptics.jl-benchmarks. Accessed: July 10, 2019.

[8.17] C. W. Gardiner and H. Haken, *Quantum noise*, vol. 26. Springer Berlin, 1991.

[8.18] R. Dum, P. Zoller, and H. Ritsch, “Monte Carlo simulation of the atomic master equation for spontaneous emission,” *Phys. Rev. A*, vol. 45, no. 7, pp. 4879–4887, 1992.

[8.19] L. Pitaevskii and S. Stringari, *Bose-Einstein condensation and superfluidity*, vol. 164. OUP, 2016.

[8.20] G. Hechenblaikner, M. Gangl, P. Horak, and H. Ritsch, “Cooling an atom in a weakly driven high-Q cavity,” *Phys. Rev. A*, vol. 58, no. 4, p. 3030, 1998.

[8.21] “GitHub repository for the CorrelationExpansion.jl package.” https://github.com/bastikr/CorrelationExpansion.jl. Accessed: July 10, 2019.

[8.22] “GitHub repository for the CollectiveSpins.jl package.” https://github.com/bastikr/CollectiveSpins.jl. Accessed: July 10, 2019.

[8.23] C. Rackauckas and Q. Nie, “DifferentialEquations. jl–A Performant and Feature-Rich Ecosystem for Solving Differential Equations in Julia,” *JORS*, vol. 5, no. 1, 2017.

[8.24] J. D. Hunter, “Matplotlib: A 2D graphics environment,” *Comput. Sci. Eng.*, vol. 9, no. 3, pp. 90–95, 2007.

References for Chapter 10

[10.1] S. Haroche and J. M. Raimond, *Exploring the Quantum: Atoms, Cavities and Photons*. New York: OUP, 2006.

[10.2] Y. Kaluzny, P. Goy, M. Gross, J. M. Raimond, and S. Haroche, “Observation of self-induced rabi oscillations in two-level atoms excited inside a resonant cavity: The ringing regime of superradiance,” *Phys. Rev. Lett.*, vol. 51, no. 13, pp. 1175–1178, 1983.

[10.3] M. G. Raizen, R. J. Thompson, R. J. Brecha, H. J. Kimble, and H. J. Carmichael, “Normal-mode splitting and linewidth averaging for two-state atoms in an optical cavity,” *Phys. Rev. Lett.*, vol. 63, no. 3, pp. 240–243, 1989.

[10.4] F. Bernardot, P. Nussenzveig, M. Brune, J. M. Raimond, and S. Haroche, “Vacuum rabi splitting observed on a microscopic atomic sample in a microwave cavity,” *Europhys. Lett.*, vol. 17, p. 33, 1992.

[10.5] R. J. Brecha, L. Orozco, M. G. Raizen, M. Xiao, and H. J. Kimble, “Observation of oscillatory energy exchange in a coupled-atom–cavity system,” *J. Opt. Soc. Am. B*, vol. 12, p. 2329, 1995.

[10.6] R. J. Thompson, G. Rempe, and H. J. Kimble, “Observation of normal-mode splitting for an atom in an optical cavity,” *Phys. Rev. Lett.*, vol. 68, no. 8, pp. 1132–1135, 1992.

[10.7] M. Brune, F. Schmidt-Kaler, A. Maali, J. Dreyer, E. Hagley, J. M. Raimond, and S. Haroche, “Quantum rabi oscillation: A direct test of field quantization in a cavity,” *Phys. Rev. Lett.*, vol. 76, no. 11, pp. 1800–1803, 1996.

[10.8] J. J. Childs, K. An, M. S. Otteson, R. R. Dasari, and M. S. Feld, “Normal-mode line shapes for atoms in standing-wave optical resonators,” *Phys. Rev. Lett.*, vol. 77, no. 14, pp. 2901–2904, 1996.

[10.9] C. J. Hood, M. S. Chapman, T. W. Lynn, and H. J. Kimble, “Real-time cavity QED with single atoms,” *Phys. Rev. Lett.*, vol. 80, no. 19, pp. 4157–4160, 1998.

[10.10] A. Boca, R. Miller, K. M. Birnbaum, A. D. Boozer, J. McKeever, and H. J. Kimble, “Observation of the vacuum Rabi spectrum for one trapped atom,” *Phys. Rev. Lett.*, vol. 93, no. 23, p. 233603, 2004.

[10.11] P. Maunz, T. Puppe, I. Schuster, N. Syassen, P. W. H. Pinkse, and G. Rempe, “Normal-mode spectroscopy of a single-bound-atom–cavity system,” *Phys. Rev. Lett.*, vol. 94, no. 3, p. 033002, 2005.

[10.12] M. Brune, P. Nussenzveig, F. Schmidt-Kaler, F. Bernardot, A. Maali, J. M. Raimond, and S. Haroche, “From Lamb shift to light shifts: Vacuum and subphoton cavity fields measured by atomic phase sensitive detection,” *Phys. Rev. Lett.*, vol. 72, no. 21, pp. 3339–3342, 1994.

[10.13] P. Bertet, A. Auffeves, P. Maioli, S. Osnaghi, T. Meunier, M. Brune, J. M. Raimond, and S. Haroche, “Direct measurement of the wigner function of a one-photon fock state in a cavity,” *Phys. Rev. Lett.*, vol. 89, p. 200402, 2002.

[10.14] D. I. Schuster, A. Wallraff, A. Blais, L. Frunzio, R.-S. Huang, J. Majer, S. M. Girvin, and R. J. Schoelkopf, “ac Stark Shift and Dephasing of a Superconducting Qubit Strongly Coupled to a Cavity Field,” *Phys. Rev. Lett.*, vol. 94, no. 12, p. 123602, 2005.

[10.15] D. I. Schuster, A. A. Houck, J. A. Schreier, A. Wallraff, J. M. Gambetta, A. Blais, L. Frunzio, J. Majer, B. Johnson, M. H. Devoret, S. M. Girvin, and R. J. Schoelkopf, “Resolving photon number states in a superconducting circuit,” *Nature*, vol. 445, no. 7127, pp. 515–518, 2007.

[10.16] C. Guerlin, J. Bernu, S. Deléglise, C. Sayrin, S. Gleyzes, S. Kuhr, M. Brune, J. M. Raimond, and S. Haroche, “Progressive field-state collapse and quantum non-demolition photon counting,” *Nature*, vol. 448, no. 7156, pp. 889–893, 2007.

[10.17] B. R. Johnson, M. D. Reed, A. A. Houck, D. I. Schuster, L. S. Bishop, E. Ginossar, J. M. Gambetta, L. DiCarlo, L. Frunzio, S. M. Girvin, and R. J. Schoelkopf, "Quantum non-demolition detection of single microwave photons in a circuit," *Nat. Phys.*, vol. 6, pp. 663–667, 2010.

[10.18] S. Deleglise, I. Dotsenko, C. Sayrin, J. Bernu, M. Brune, J. M. Raimond, and S. Haroche, "Reconstruction of non-classical cavity field states with snapshots of their decoherence," *Nature*, vol. 455, no. 7212, pp. 510–514, 2008.

[10.19] M. Hofheinz, H. Wang, M. Ansmann, R. C. Bialczak, E. Lucero, M. Neeley, A. D. O'Connell, D. Sank, J. Wenner, J. M. Martinis, and A. N. Cleland, "Synthesizing arbitrary quantum states in a superconducting resonator," *Nature*, vol. 459, no. 7246, pp. 546–549, 2009.

[10.20] C. Sayrin, I. Dotsenko, X. Zhou, B. Peaudecerf, T. Rybarczyk, S. Gleyzes, P. Rouchon, M. Mirrahimi, H. Amini, M. Brune, J. M. Raimond, and S. Haroche, "Real-time quantum feedback prepares and stabilizes photon number states," *Nature*, vol. 477, no. 7362, pp. 73–77, 2011.

[10.21] B. Vlastakis, G. Kirchmair, Z. Leghtas, S. E. Nigg, L. Frunzio, S. M. Girvin, M. Mirrahimi, M. H. Devoret, and R. J. Schoelkopf, "Deterministically encoding quantum information using 100-photon schrödinger cat states," *Science*, vol. 342, no. 6158, pp. 607–610, 2013.

[10.22] R. W. Heeres, B. Vlastakis, E. Holland, S. Krastanov, V. V. Albert, L. Frunzio, L. Jiang, and R. J. Schoelkopf, "Cavity State Manipulation Using Photon-Number Selective Phase Gates," *Phys. Rev. Lett.*, vol. 115, no. 13, p. 137002, 2015.

[10.23] E. T. Holland, B. Vlastakis, R. W. Heeres, M. J. Reagor, U. Vool, Z. Leghtas, L. Frunzio, G. Kirchmair, M. H. Devoret, M. Mirrahimi, and R. J. Schoelkopf, "Single-photon-resolved cross-kerr interaction for autonomous stabilization of photon-number states," *Phys. Rev. Lett.*, vol. 115, no. 18, p. 180501, 2015.

[10.24] C. Wang, Y. Y. Gao, P. Reinhold, R. W. Heeres, N. Ofek, K. Chou, C. Axline, M. Reagor, J. Blumoff, K. M. Sliwa, L. Frunzio, S. M. Girvin, L. Jiang, M. Mirrahimi, M. H. Devoret, and R. J. Schoelkopf, "A Schrödinger cat living in two boxes," *Science*, vol. 352, no. 6289, pp. 1087–1091, 2016.

[10.25] J. Gambetta, A. Blais, D. I. Schuster, A. Wallraff, L. Frunzio, J. Majer, M. H. Devoret, S. M. Girvin, and R. J. Schoelkopf, "Qubit-photon interactions in a cavity: Measurement-induced dephasing and number splitting," *Phys. Rev. A*, vol. 74, no. 4, p. 042318, 2006.

[10.26] K. W. Murch, S. J. Weber, C. Macklin, and I. Siddiqi, "Observing single quantum trajectories of a superconducting quantum bit," *Nature*, vol. 502, pp. 211–214, 2013.

[10.27] R. Vijay, C. Macklin, D. H. Slichter, S. J. Weber, K. W. Murch, R. Naik, A. N. Korotkov, and I. Siddiqi, “Stabilizing rabi oscillations in a superconducting qubit using quantum feedback,” *Nature*, vol. 490, no. 7418, pp. 77–80, 2012.

[10.28] N. Roch, M. E. Schwartz, F. Motzoi, C. Macklin, R. Vijay, A. W. Eddins, A. N. Korotkov, K. B. Whaley, M. Sarovar, and I. Siddiqi, “Observation of measurement-induced entanglement and quantum trajectories of remote superconducting qubits,” *Phys. Rev. Lett.*, vol. 112, p. 170501, 2014.

[10.29] C. A. Blockley, D. F. Walls, and H. Risken, “Quantum collapses and revivals in a quantized trap,” *Europhys. Lett.*, vol. 17, no. 6, p. 509, 1992.

[10.30] J. I. Cirac, R. Blatt, A. S. Parkins, and P. Zoller, “Preparation of Fock states by observation of quantum jumps in an ion trap,” *Phys. Rev. Lett.*, vol. 70, no. 6, pp. 762–765, 1993.

[10.31] D. M. Meekhof, C. Monroe, B. E. King, W. M. Itano, and D. J. Wineland, “Generation of nonclassical motional states of a trapped atom,” *Phys. Rev. Lett.*, vol. 76, no. 11, pp. 1796–1799, 1996.

[10.32] C. Monroe, D. M. Meekhof, B. E. King, and D. J. Wineland, “A “Schrödinger Cat” Superposition State of an Atom,” *Science*, vol. 272, pp. 1131–1136, 1996.

[10.33] D. Kienzler, H.-Y. Lo, B. Keitch, L. de Clercq, F. Leupold, F. Lindenfelser, M. Marinelli, V. Negnevitsky, and J. P. Home, “Quantum harmonic oscillator state synthesis by reservoir engineering,” *Science*, vol. 347, pp. 53–56, 2015.

[10.34] H. Häffner, C. Roos, and R. Blatt, “Quantum computing with trapped ions,” *Phys. Rep.*, vol. 469, no. 4, pp. 155–203, 2008.

[10.35] F. Schmidt-Kaler, H. Häffner, S. Gulde, M. Riebe, G. Lancaster, J. Eschner, C. Becher, and R. Blatt, “Quantized AC-Stark shifts and their use for multiparticle entanglement and quantum gates,” *Europhys. Lett.*, vol. 65, pp. 587–593, 2004.

[10.36] C. L. Degen, F. Reinhard, and P. Cappellaro, “Quantum sensing,” *Rev. Mod. Phys.*, vol. 89, p. 035002, 2017.

[10.37] C. Russo, H. G. Barros, A. Stute, F. Dubin, E. S. Phillips, T. Monz, T. E. Northup, C. Becher, T. Salzburger, H. Ritsch, P. O. Schmidt, and R. Blatt, “Raman spectroscopy of a single ion coupled to a high-finesse cavity,” *Appl. Phys. B*, vol. 95, no. 2, pp. 205–212, 2009.

[10.38] A. Stute, B. Casabone, B. Brandstätter, D. Habicher, P. O. Schmidt, T. E. Northup, and R. Blatt, “Toward an ion-photon quantum interface in an optical cavity,” *Appl. Phys. B*, vol. 107, no. 4, pp. 1145–1157, 2012.

[10.39] P. Schindler, D. Nigg, T. Monz, J. T. Barreiro, E. Martinez, S. X. Wang, S. Quint, M. F. Brandl, V. Nebendahl, C. F. Roos, M. Chwalla, M. Hennrich, and

R. Blatt, “A quantum information processor with trapped ions,” *New J. Phys.*, vol. 15, no. 12, p. 123012, 2013.

[10.40] C. Gardiner and P. Zoller, *Quantum Noise: A Handbook of Markovian and Non-Markovian Quantum Stochastic Methods with Applications to Quantum Optics.* Springer Series in Synergetics, Berlin: Springer-Verlag Berlin Heidelberg, 2004.

[10.41] R. J. Glauber, *Optical Coherence and Photon Statistics.* Wiley-VCH Verlag GmbH & Co. KGaA, 2007.

[10.42] I. B. Mekhov, C. Maschler, and H. Ritsch, “Probing quantum phases of ultracold atoms in optical lattices by transmission spectra in cavity quantum electrodynamics,” *Nat. Phys.*, vol. 3, pp. 319–323, 2007.

[10.43] S. Begley, M. Vogt, G. K. Gulati, H. Takahashi, and M. Keller, “Optimized multi-ion cavity coupling,” *Phys. Rev. Lett.*, vol. 116, no. 22, p. 223001, 2016.

[10.44] D. Leibfried, E. Knill, S. Seidelin, J. Britton, R. B. Blakestad, J. Chiaverini, D. B. Hume, W. M. Itano, J. D. Jost, C. Langer, R. Ozeri, R. Reichle, and D. J. Wineland, “Creation of a six-atom “Schrodinger cat” state,” *Nature*, vol. 438, pp. 639–642, 2005.

[10.45] J. R. Johansson, P. D. Nation, and F. Nori, “Qutip: An open-source python framework for the dynamics of open quantum systems,” *Comp. Phys. Comm.*, vol. 183, pp. 1760–1772, 2012.

[10.46] J. R. Johansson, P. D. Nation, and F. Nori, “Qutip 2: A python framework for the dynamics of open quantum systems,” *Comp. Phys. Comm.*, vol. 184, p. 1234, 2013.

[10.47] C. W. Gardiner and A. S. Parkins, “Driving atoms with light of arbitrary statistics,” *Phys. Rev. A*, vol. 50, pp. 1792–1806, 1994.

[10.48] H. J. Carmichael, *Statistical Methods in Quantum Optics 1: Master Equations and Fokker-Planck Equations.* Springer-Verlag Berlin Heidelberg, 1999.

[10.49] A. I. Lvovsky and M. G. Raymer, “Continuous-variable optical quantum-state tomography,” *Rev. Mod. Phys.*, vol. 81, pp. 299–332, 2009.

[10.50] A. Stute, *A Light-Matter Quantum Interface: Ion-Photon Entanglement and State Mapping.* PhD thesis, Leopold-Franzens-Universität Innsbruck, 2012.

[10.51] W. M. Itano, J. C. Bergquist, J. J. Bollinger, J. M. Gilligan, D. J. Heinzen, F. L. Moore, M. G. Raizen, and D. J. Wineland, “Quantum projection noise: Population fluctuations in two-level systems,” *Phys. Rev. A*, vol. 47, pp. 3554–3570, 1993.

[10.52] G. Rempe, R. J. Thompson, H. J. Kimble, and R. Lalezari, “Measurement of ultralow losses in an optical interferometer,” *Opt. Lett.*, vol. 17, no. 5, pp. 363–365, 1992.

[10.53] A. H. Myerson, D. J. Szwer, S. C. Webster, D. T. C. Allcock, M. J. Curtis, G. Imreh, J. A. Sherman, D. N. Stacey, A. M. Steane, and D. M. Lucas, "High-fidelity readout of trapped-ion qubits," *Phys. Rev. Lett.*, vol. 100, no. 20, p. 200502, 2008.

[10.54] R. Noek, G. Vrijsen, D. Gaultney, E. Mount, T. Kim, P. Maunz, and J. Kim, "High speed, high fidelity detection of an atomic hyperfine qubit," *Opt. Lett.*, vol. 38, no. 22, pp. 4735–4738, 2013.

List of publications

- L. Ostermann, D. Plankensteiner, H. Ritsch, C. Genes. Protected subspace Ramsey spectroscopy. *Phys. Rev. A.*, **90**, 053823 (2014).

- D. Plankensteiner, L. Ostermann, H. Ritsch, C. Genes. Selective protected state preparation of coupled dissipative quantum emitters. *Sci. Rep.*, **5**, 16231 (2015).

- D. Plankensteiner, J. Schachenmayer, H. Ritsch, C. Genes. Laser noise imposed limitations of ensemble quantum metrology. *J. Phys. B* **49**, 245501 (2016).

- D. Plankensteiner, C. Sommer, H. Ritsch, C. Genes. Cavity antiresonance spectroscopy of dipole coupled subradiant arrays. *Phys. Rev. Lett.*, **119**, 093601 (2017).

- S. Krämer, D. Plankensteiner, L. Ostermann, H. Ritsch. QuantumOptics. jl: A Julia framework for simulating open quantum systems. *Comp. Phys. Commun.*, **227**, 109 (2018).

- D. Plankensteiner, C. Sommer, M. Reitz, H. Ritsch, C. Genes. Enhanced collective Purcell effect of coupled quantum emitter systems. *Phys. Rev. A*, **99**, 043843 (2019).

- M. Moreno-Cardoner, D. Plankensteiner, L. Ostermann, D. E. Chang, H. Ritsch. Extraordinary subradiance with lossless excitation transfer in dipole-coupled nano-rings of quantum emitters. *arXiv preprint arXiv:1901.10598* (2019).

- M. Lee, K. Friebe, D. A. Fioretto, K. Schüppert, F. R. Ong, D. Plankensteiner, V. Torggler, H. Ritsch, R. Blatt, T. E. Northup. Ion-Based Quantum Sensor for Optical Cavity Photon Numbers. *Phys. Rev. Lett.*, **122**, 153603 (2019).